University of Alberta

ULTRAFAST THIRD-ORDER OPTICAL NONLINEARITIES OF CONJUGATED ORGANIC MOLECULES

By

Aaron David Slepkov

A thesis submitted to the Faculty of Graduate Studies and Research in partial fulfilment of the requirements for the degree of Doctor of Philosophy

Department of Physics

Edmonton, Alberta

Fall 2006

Library and Archives Canada

Published Heritage Branch

395 Wellington Street
Ottawa ON K1A 0N4
Canada

Bibliothèque et Archives Canada

Direction du Patrimoine de l'édition

395, rue Wellington
Ottawa ON K1A 0N4
Canada

Your file Votre référence
ISBN: 978-0-494-23109-8
Our file Notre référence
ISBN: 978-0-494-23109-8

NOTICE:
The author has granted a non-exclusive license allowing Library and Archives Canada to reproduce, publish, archive, preserve, conserve, communicate to the public by telecommunication or on the Internet, loan, distribute and sell theses worldwide, for commercial or non-commercial purposes, in microform, paper, electronic and/or any other formats.

The author retains copyright ownership and moral rights in this thesis. Neither the thesis nor substantial extracts from it may be printed or otherwise reproduced without the author's permission.

AVIS:
L'auteur a accordé une licence non exclusive permettant à la Bibliothèque et Archives Canada de reproduire, publier, archiver, sauvegarder, conserver, transmettre au public par télécommunication ou par l'Internet, prêter, distribuer et vendre des thèses partout dans le monde, à des fins commerciales ou autres, sur support microforme, papier, électronique et/ou autres formats.

L'auteur conserve la propriété du droit d'auteur et des droits moraux qui protège cette thèse. Ni la thèse ni des extraits substantiels de celle-ci ne doivent être imprimés ou autrement reproduits sans son autorisation.

In compliance with the Canadian Privacy Act some supporting forms may have been removed from this thesis.

While these forms may be included in the document page count, their removal does not represent any loss of content from the thesis.

Conformément à la loi canadienne sur la protection de la vie privée, quelques formulaires secondaires ont été enlevés de cette thèse.

Bien que ces formulaires aient inclus dans la pagination, il n'y aura aucun contenu manquant.

Canada

ABSTRACT

We describe the extension of a femtosecond pump-probe experimental layout from one that primarily measures third-order birefringent optical nonlinearities to one that can also characterize the dichroic nonlinearities, such as two-photon absorption (TPA). We use this technique, differential optical Kerr effect (DOKE) detection, to study the 800 nm third-order birefringent and/or dichroic nonlinearities in several series of highly-conjugated chromophores and oligomers.

We have revisited a series of cross-conjugated *iso*-polydiacetylene oligomers (*iso*-PDAs), extending their length past 7 repeat units to a total length of 15 repeat units. Whereas we previously reported a linear increase in the second-hyperpolarizability, γ, as a function of oligomer length for short *iso*-PDAs, the extended oligomers exhibit a superlinear increase in γ. This represents the first report of such an increase in a cross-conjugated oligomer series. We identify in this increase two linear regimes which may indicate the onset of folding to a helical structure at a length between 7-9 repeat units.

We have studied the optical nonlinearities of an extended series of polyynes. Polyynes are linear sp-carbon chains that model the hypothetical carbon allotrope carbyne. As the polyyne length is extended, the corresponding rise in γ is the fastest reported for any oligomer series, showing that these are promising nonlinear optical materials. Furthermore, power law increases in both γ and the absorption onset energy as

a function of oligomer length closely model behaviour predicted for purely one-dimensional materials. We also observe two-photon absorption in the longest of the polyyne oligomers, which suggests a reversal of standard energy-level symmetry alternation.

The third-order optical nonlinearities were also investigated in fullerene-terminated conjugated molecules, where we find evidence for charge-transfer from the conjugated backbone to the fullerenes. Furthermore, whereas pristine C_{60} displays very small nonlinearities, we observe a large nonlinear optical response from fullerene-oligomer hybrids.

We have extensively studied a series of self-similar two-dimensionally conjugated cruciform chromophores and find the nonlinearities to depend drastically on donor/acceptor substitution symmetry about their central benzene core. We obtained the TPA spectra of these molecules with ultrafast z-scan measurements and find that the all-donor species displays considerably higher peak TPA than that found in its donor-acceptor counterparts. We also identify and address excited-state absorption (ESA) and birefringence dynamics in these molecules, as obtained at 800 nm with DOKE.

Finally, we report on the design of an 800 nm pump-white light probe experimental setup. We present preliminary results investigating the non-degenerate TPA and ESA response of a standard (MPPBT) conjugated chromophore.

ACKNOWLEDGMENTS

The decision to re-enlist into the Ph.D. program in the Department of Physics at the University of Alberta was not easy. It required me to abandon some long-standing and long-term plans. I have thoroughly enjoyed my time as a doctoral student. Part of that enjoyment comes from the freedom to learn whatever I want, at my own pace. Another factor, is the unique interactions I am afforded at this terrific department and school. My circle of colleagues and friends makes every single day something that I look forward to. I would like to extend my sincerest gratitude to all of the members of the Physics Department at the University of Alberta for providing such a friendly, hospitable, and stimulating place to work and study. Any of my success in both academics and research required the active support of many people, whom I would presently like to thank.

I give thanks both to and for my beloved wife, Emily, who has given me immense support in my pursuit of this degree; has somehow found the time to complete her own excellent PhD; and has given me the gift of a beautiful daughter. Emily, you truly are an *Eshet chayil*!

I thank Dr. Frank Hegmann for having been an excellent supervisor. He has displayed the patience of Job, and has given me near free reign in my research persuits. Frank has afforded me innumerable opportunities to learn and grow as a physicist and an academic. Thank you Frank, for your patience, promotion, support, and humour.

I thank Dr. Rik Tykwinski for being a great co-supervisor. He has taken an active interest in all of my half-cocked ideas, and has turned most of them down with equanimity. Rik, you have acted as both a sounding board and catalyst for all of my research endeavors, and I thank you for both your wisdom and guidance.

I thank my collaborator and friend, Dr. Kenji Kamada of AIST in Japan, for both his friendship and mentorship. Sensei, I have said it before and I will say it again, every

conversation with you sends me scurrying to the library and vaults my research forward. I have thoroughly enjoyed our discussions, collaborations, and visits.

I would like to thank Dr. John Beamish and Dr. Frank Marsiglio for their support and guidance. They have always kept their door open to me, and have helped me immeasurably throughout my time at the U of A. John and Frank, thank you for your camaraderie, guidance, and wisdom.

I have been very fortunate to collaborate with a superb array of chemists and engineers: I acknowledge Dr. Michael Haley, Laura Shirtcliff and Eric Spitler of University of Oregon for our excellent TPEB collaboration. I acknowledge Dr. Jim Tour of Rice University, for our collaboration on fullerene-OPE hybrids, and my friend and colleague Dr. Yuming Zhao (now at Memorial University) for our fullerene-OPE hybrids, *iso*-PDA, and D/A monomer collaborations. I further thank you, Yuming, for your friendship and support during my transition from Masters student to Ph.D student. I thank Dr. Ray DeCorby and Andrzej Tomalik for our collaboration on the extended-wavelength DOKE system and Chalcogenide glass work. Furthermore, Andre, thank you for your friendship and companionship in the lab. I immensely enjoyed working with you; you deferred to my expertise, and I hope I didn't let you down too often.

Finally, I would like to thank past and present graduate student collegues James Day, Alan MacDairmid, Brad Schultz, Nicole Macdonald, Jianbo Gao, Toby Herman, and Kris Lui who have provided me with support, friendship, stimulating conversation, and laughter these past years. I particularly acknowledge the friendship and support of my office/lab-mate David Cooke. Dave, I thank you for the great (and often protracted) discussions we've shared, the countless arguments, and for the times we just sat quietly drinking our beer.

I would also like to thank previous post-docs Dr. Markus Walther and Dr. Oksana Ostroverkova for their guidance and friendship.

I have personally received generous funding from NSERC, Alberta Ingenuity Fund, the Japan Society for the Promotion of Science, the Ralph Steinhauer Foundation, the Department of Physics, and the University of Alberta. I also acknowledge iCORE for financial support.

To my Bubie and Zadie,

Whose pride in me is the major driving

force of this work

TABLE OF CONTENTS

Dedication
Abstract
Acknowledgements
List of Figures
List of Tables
List of Abbreviations and Symbols

Outline 1

CHAPTER 1: Introduction to Two-Photon Absorption in Conjugated Organic Systems 4
1.1 Introduction 4
1.2 A Survey of Two-Photon Absorption in Conjugated Chromophores 6
1.3 Measurement of Two-Photon Absorption 18
1.4 References 22

CHAPTER 2: Differential Optical Kerr Effect (DOKE) for the Characterization of Nonlinear Absorption Dynamics 28
2.1 Introduction 28
2.2 Differential Optical Kerr Effect Detection 29
2.3 Proof of Principle and Characterization of the DOKE Technique 35
2.4 Summary 46
2.5 References 47

CHAPTER 3: Verification of DOKE-Obtained TPA Cross-Sections by Single-Beam Experiments on MPPBT 49
3.1 References 53

CHAPTER 4: Linear and Nonlinear Optical Characterization of Extended Polyynes: Structural and Optical One-Dimensional Systems 55
4.1 Context 55
4.2 Introduction 56
4.3 Experimental 61
4.4 Results and Discussion 62
4.5 Summary 73
4.6 References 74

CHAPTER 5: Third-Order NLO Dynamics and Two-Photon Absorption in Two-Dimensionally-Conjugated Benzene-core Isomers 78
5.1 Context 78
5.2 Introduction 79
5.3 Experimental 83
5.4 Results and Discussion 85
5.5 Summary 103
5.6 References 106

CHAPTER 6: Optical and Nonlinear Optical Characterization of [60]Fullerene-Oligo(*p*-phenylene ethynylene) Hybrids 110
6.1 Context 110
6.2 Introduction 111
6.3 Experimental 112
6.4 Results and Discussion 113
6.5 Summary 119
6.6 References 121

CHAPTER 7: The Kerr Response of Cross-Conjugated *iso*-Polydiacetylenes 124
7.1 Context 124
7.2 Introduction 125
7.3 Results and Discussion 127
7.4 Conclusion 134
7.5 References 135

CHAPTER 8: Experimental Setup for the Measurement of Nondegenerate Two-Photon Absorption Spectra 139
8.1 Introduction 139
8.2 Continuum Generation in H_2O and Pulse Characterization 145
8.3 Time-resolved Non-degenerate Nonlinear Absorption Measurements in an Organic Material 155
8.4 References 162

CHAPTER 9: Summary and Future Work 165
9.1 References 171

APPENDIX A: Two-Photon Absorption as a Third-Order Nonlinear Phenomena 173
A.1 References 178

APPENDIX B: Concerning DOKE Polarization Conditions 179
B.1 Position-Dependence of the Probe Quarter-Wave Plate 181
B.2 The Four DOKE Polarization Conditions 187
B.3 References 188

APPENDIX C: Concerning Experimental Resolution And Raw Data of the DOKE Technique 189
C.1 References 194

LIST OF TABLES

3.1 Fitting parameters for single-beam nonlinear absorption measurements of MPPBT in DMSO, as presented in Figure 3.1 52

4.1 A summary of optical characteristics for the studied polyynes. λ_{max} is the highest wavelength of absorption maximum corresponding to the energy gap of the compound. *p*-PYs display an additional high-wavelength region of miniscule absorption. λ_{max} of in this region for those compounds are in [brackets]. U.R. corresponds to data that was unresolved; N.C. corresponds to data that was not collected. 66

5.1 Summary of optical and nonlinear optical parameters in TPEBs. Decay rates are obtained from bi-exponential fits of Eqn. 5.1. Underlined are rise times, as opposed to decay times. γ-values obtained at a wavelength of 800 nm are presented relative to that of the solvent THF; $\gamma_{THF}=5.2\times10^{-37}$esu. λ_{max} are the wavelengths of the lowest energy peaks in the peak one-photon absorption spectra; ε is the molar absorptivity corresponding at the peak. N.M: not measured 90

6.1 Low-energy absorption peak wavelengths and molecular third-order hyperpolarizabilities γ and TPA cross sections $\sigma^{(2)}$ measured at 800 nm in OPE compounds 112

7.1 DOKE results for the *iso*–PDA series 129

8.1 A quantitative summary of nondegenerate nonlinear absorption measurements on a 10 mM sample solution of MPPBT in DMSO. 157

B.1 Some symbols and matrix representations for various optical elements. 180

LIST OF FIGURES

1.1 [colour] Schematic representations of molecular two-photon absorption. (a) Standard one-photon absorption (blue; left), degenerate two-photon absorption (red, red; middle), and non-degenerate (green, dark-red; right) two-photon absorption to the same energy level. In many organic systems, identical fluorescence (yellow) is observed from one- and two-photon accessed states.[9,46] (b) A two-level model is often sufficient for modeling TPA in dipolar systems. *g* is the ground state and *e* is the excited-state; E_g and E_e are their energies and μ_g and μ_e are their static dipoles. M_{ge} is the transition dipole between these states. $\sigma^{(2)}$ is the two-photon cross section for this transition, and $\hbar\omega$ is the energy of the incident laser light. (c) A minimum three-level model is needed for explaining TPA in symmetric systems lacking permanent dipoles. The ground state in such chromophores is of *gerade* (A_g) symmetry, as is the two-photon allowed state. The two-photon-forbidden but one-photon-allowed state is of opposite, *ungerade* (B_u), symmetry. [$(E_e$-$E_g)$- $\hbar\omega$] is the detuning factor, and is inversely proportional to $\sigma^{(2)}$ in symmetric systems..... 9

1.2 Representative high two-photon absorbing compounds. High $\sigma^{(2)}$-values were obtained for Distyrylbenzene-based Strehmel-3 and Strehmel-4 using femtosecond two-photon excitation fluorescence spectroscopy.[50] High $\sigma^{(2)}$-values were obtained for diacetylene-based MPPBT using femtosecond z-scan.[51]..... 18

2.1 A schematic of our DOKE experimental layout: PDs A & B: Balanced photodiodes; PD C: reference photodiode; BS: 10:1 beam splitter; λ/4: quarter-wave plate; λ/2: half-wave plate; P: Glan-laser polarizer; A: Wollaston polarizer acting as an analyzer; L: lens (f = 40 cm); CH: chopper operating at 270 Hz; PC: computer; S: 1-mm path length quartz cuvette sample holder..... 31

2.2 Two-photon absorption (TPA) and excited-state absorption (ESA) processes to which DOKE detection is sensitive. DOKE monitors pump-induced absorption in the probe beam, and is thus only sensitive to changes in the probe beam. TPA is measured as an instantaneous response, and ESA is measured at longer probe delay times..... 37

2.3 Nonlinear absorption dynamics in an MPPBT sample. (a) At a probe delay time of 0 ps, an instantaneous TPA signal is seen that follows the cross correlation of the pump and probe pulses. (b) At later times, considerable excited-state absorption is seen, displaying a bi-exponential decay with a prominent and well-resolved 30 ps decay time (inset). A similar decay rate of 40 ps is confirmed by time-resolved fluorescence measurements.[22] Solid line in inset is a bi-exponential fit, with the obtained parameters reported on the plot.. 37

2.4 On-peak (probe delay time of 0 ps) nonlinear absorption DOKE response in **MPPBT**. A linear dependence with pump power is an indication of a pure two-photon absorption process. The typical pump powers used for DOKE experiments are well within this linear range, as shown. Dashed line is a line of best fit to a power-law function. 38

2.5 Pump-dependent nonlinear absorption DOKE response from **MPPBT** at a probe delay time of 5 ps. A square dependence with pump power is indication of a pure two-photon accessed single-excited-state absorption. The typical pump powers used for DOKE experiments are well within this range, as shown. Dashed lines are fits to a power-law function. They have been drawn to extend past their fitting ranges for improved visibility. 38

2.6 Chemical structure of TPA reference samples **AF60** and **AF50**. The two species differ by the length of the pendant alkyl side chains off the fluorene centre. 39

2.7 Time resolved nonlinear absorption signals of **AF60**, and **MPPBT**, and of their respective solvents, obtained using the dichroic polarization condition. The inset shows the signal from the THF solvent. Each trace represents an average of three scans 40

2.8 Raw DOKE scans in the second Polarization Condition for **AF60**, showing A-B and A+B signals. Both signals show peaks at zero probe delay time, reflecting instantaneous TPA, as well as time-delayed tails suggesting Pump-induced excited state absorption. Both signals can be used to obtain $\sigma^{(2)}$ values. The dashed line establishes a baseline for the A+B signal.. 41

2.9 [colour] Transient absorption signals from a tetrakis(phenylethynyl)benzene (***ortho*-TPEB**) sample in THF. The strongest TPA is observed when both the pump and probe beams are parallel *in polarization*, in close agreement with the 3:1 parallel:perpendicular TPA predictions by Birge and Pierce.[29]. 43

2.10 [colour] Whereas the transient absorption measurement differs depending on the pump and probe polarizations, DOKE signals are always the same as the transient absorption experiment with a relative 45° pump-probe angle. The inset shows that this stands for ESA signals as well. The sample investigated is ***ortho*-TPEB** (structure is shown in Fig. 2.9). 44

2.11 Various signals from ***ortho*-TPEB** in the DOKE birefringent polarization condition. A+B signals monitored at 270 Hz and 1kHz detect transient absorption signals, while the A-B signal monitors transient birefringence. Clearly, the birefringence response is different from the absorptive signal, and both of these must be taken into account for the full DOKE analysis. 45

2.12 Longer time signals of those presented in the previous figure. The absolute |A-B| signal is larger than the absorptive A+B signal, and shows better signal-to-noise. The two phenomena also present different exponential decay dynamics in this particular sample. 46

3.1 Single-beam nonlinear absorption measurements on MPPBT in DMSO. The data is fit to an equation (inset) that accounts for a constant reflection at the front-surface of the sample cuvette. The output power was calibrated by a polynomial of order 4, to approximate linearity through the vacant path. All other single-beam runs were normalized to this calibration. Solid lines are free fits to the inset equation. Fitting parameters are reported in Table 3.1.....53

4.1 Various carbon allotropes. While diamond, graphite, and fullerenes are well known, carbyne is relatively obscure and elusive. Carbyne is a homogeneous and linear chain of sp-hybridized carbons, with unknown electronic properties.....56

4.2 Variously conjugated oligomers, for comparison with polyynes (PY). Whereas all of the other oligomers have some sp^2 character in the conjugated backbone, polyynes are composed of an entirely sp-hybridized carbon chain. 59

4.3 A schematic representing how conjugation and p-orbital overlap are disrupted by rotations about single bonds in sp^2 and sp hybridized paths. While polyenes can experience the maximum misalignment of π-orbitals, polyynes experience no more than a 45° misalignment through rotation, and thus always maintains some degree of conjugation.....59

4.4 Structural representation of the oligomeric compounds discussed in this chapter. The full extent of longest polyyne, ***TIPS*-10yne**, is shown for emphasis.....60

4.5 UV-vis absorption spectra of the studied polyynes. (a) ***TIPS*-PY**s. (b) ***p*-PY**s. (c) Selected polyynes re-displayed for an overlay comparison between the two series. ***TIPS*-8yne** and ***TIPS*-10yne** show spectra wherein the vibronic structure of the pure polyyne backbone is dominant. In ***p*-6yne** and ***p*-8yne**, the absorption spectrum is more complex. Black arrows signify λ_{max} in region I (upwards) and region II (downwards), used for further analysis. Inset expands region II absorption in ***p*-8yne**. 65

4.6 Absorption trends in two series re-analyzed from the literature (a),[21,27] and in our studied polyynes (b). Power law decreases in the absorption energy as a function of oligomer size for the polyynes indicate that saturation in the conjugation length has not yet begun (fits are shown by solid lines). Polytriacetylenes (PTAs) and poly(phenylene ethynylene)s (PPEs) also show decreases of the gap energy with length, but they do not follow a strict power-law. The best power-law fit for PPEs is shown.....66

4.7 Power law trends for increasing third-order molecular nonlinearity, γ, with chain length for both of our polyyne series and for two poly-enyne series re-plotted from the literature.[21,27] ***p*-PYs** show a power law that is very similar to that of the *TIPS*-polyynes, which show the largest power-law exponent of any conjugated oligomers system. The solid lines are fits to the form $\gamma = a + bn^c$, where a is an offset due to the end-group effect, b is a constant, and c is the power-law exponent For **PTA** and **PPE**, an offset of $a=0$ was used in in these fits. For ***p*-PY** and ***TIPS*-PY**, $a=8.8\times10^{-36}$ esu and $a=2.2\times10^{-36}$ esu were used, respectively.....69

4.8 A scatter plot of two-photon absorption cross-sections obtained from polyynes at 800 nm. Absolute $\sigma^{(2)}$-values are relative to $\sigma^{(2)}_{MPPBT}=380$ GM (1 Göppert-Mayer (GM) = 10^{-50} $cm^4s^{-1}photon^{-1}molecule^{-1}$).....71

4.9 [colour] Selected time-resolved nonlinear absorption signals. (a) Instantaneous two-photon absorption gives way to longer-lasting excited state absorption. (b) Excited-state absorption in two samples studied at long times show a simple exponential decay fits (solid lines) with two very different relaxation times.....72

5.1 Conjugation routes and general structure of the studied tetrakis(phenylethynyl)benzenes (TPEBs) and the analogous TEE and CEE motifs studied by other groups.[22,28] **TD-TPEB** and ***para*-TPEB** are quadrupolar and lack permanent dipole moments. ***meta*-TPEB** and ***ortho*-TPEB** are the dipolar isomers of ***para*-TPEB** (dipoles are shown as gray-filled arrows). Conjugation in TEE type structures is described in terms of three routes; (a) trans-conjugation (linear), (b) cis-conjugation ('bent'), and (c) geminal (coss-conjugation). Similarly, conjugation paths in TPEBs follow (a) linear conjugation (*para*-linked), (b) bent-conjugation (*ortho*-linked), and (c) cross-conjugated (*meta*-linked).....81

5.2 Two-photon absorption spectra of TPEBs (bottom and left axes). The UV-vis spectrum is overlaid (top and right axes) to match the same total photon energy with TPA. Also included is the sample absorption at experimental concentration (bottom & right axes). (a) dipolar meta-TPEB; (b) dipolar ortho-TPEB; (c) quadrupolar TD-TPEB; (d) quadrupolar para-TPEB.....88

5.3 [colour] Molecular orbital and transition density maps of the lowest lying states/transitions in **TD-TPEB**. Molecular orbital maps were calculated with Gaussian 98 at the B3LYP/6-31G* level of DFT, by Haley *et al.*[2] Transition density maps were sketched by hand by overlapping the appropriate MO maps. Within each map, the two different colors represent different phases of the wavefunction /transition density. A net transition dipole is denoted with a black arrow on the transition density maps.. 91

5.4 [colour] Molecular orbital and transition density maps of the lowest lying states/transitions in ***meta*-TPEB**. Molecular orbital maps were calculated with Gaussian 98 at the B3LYP/6-31G* level of DFT, by Haley *et al.*[2] Transition density maps were sketched by hand by overlapping the appropriate MO maps. Within each map, the two different colors represent different phases of the wavefunction /transition density. A net transition dipole is denoted with a black arrow on the transition density maps.. 91

5.5 [colour] Molecular orbital and transition density maps of the lowest lying states/transitions in ***ortho*-TPEB**. Molecular orbital maps were calculated with Gaussian 98 at the B3LYP/6-31G* level of DFT, by Haley *et al.*[2] Transition density maps were sketched by hand by overlapping the appropriate MO maps. Within each map, the two different colors represent different phases of the wavefunction /transition density. A net transition dipole is denoted with a black arrow on the transition density maps.. 92

5.6 [colour] Molecular orbital and transition density maps of the lowest lying states/transitions in ***para*-TPEB**. Molecular orbital maps were calculated with Gaussian 98 at the B3LYP/6-31G* level of DFT, by Haley *et al.*[2] Transition density maps were sketched by hand by overlapping the appropriate MO maps. Within each map, the two different colors represent different phases of the wavefunction /transition density. A net transition dipole is denoted with a black arrow on the transition density maps.. 92

5.7 [colour] Dichroic DOKE condition measurements of TPEBs. (a) The ultrafast response that is centered about a probe delay time of zero represents the two-photon absorption process. The individual data points of the **TD-TPEB** trace are displayed to indicate the temporal resolution used. (b) The instantaneous TPA process gives way to long-lasting excited-state absorption dynamics. The donor-accepetor isomers show a rise and peak, corresponding to the population of the excited-state from which exponential-rate depopulation takes place.. 95

5.8 [colour] Two-photon-accessed excited-state absorption decays fit to a bi-exponential form (probe delay times >1.5 ps). None of the fits (solid lines) required an offset (term *a* in Eqn. 5.1).....95

5.9 A simple model to account for the observed excited-state dynamics in Donor-Acceptor TPEBs. S_0 is the ground electronic state. State S_1 is the two-photon electronic state with the solvation geometry of the ground state. State S_1^* is the relaxed two-photon state with appropriate solvation geometry. 96

5.10 400 nm pump-800 nm probe transient absorption signals of donor-acceptor TPEB isomers. After the initial excitation (a), a rise to another absorbing excited-state is observed (b), and is especially well resolved in the *ortho*-TPEB sample. (b) Fits to a bi-exponential form (solid lines) required a finite (but very small) offset *a* in Eqn. 5.1. Signals are normalized to the peak absorption value of 1. Decay dynamics are: ***para*-TPEB**, τ_1=1.6 ps (rise), τ_2=21 ps (decay); ***meta*-TPEB**, τ_1=2 ps (rise), τ_2=22.5 ps (decay); ***ortho*-TPEB**, τ_1=2.9 ps (rise), τ_2=35.6 ps (decay).....97

5.11 Refractive DOKE polarization condition TPEB scans—THF solvent response removed. Responses are ultrafast about a the probe's arrival time and represent the ultrafast electronic Kerr response. The subtraction of externally-obtained THF response introduces slight time-shifts and artifacts around the peak. **TD-TPEB**—shown with individual data points to illustrate scan resolution—is the only sample that shows a positive γ value at 800 nm. ***para*-TPEB** displays the lowest response.....98

5.12 [colour] Induced birefringence dynamics fit to a bi-exponential form (solid lines; prode delay times >1.5 ps). A very small offset of $|a| < 0.00015$ was required to fit the signals of ***meta*-TPEB** and ***ortho*-TPEB**. Whereas all other samples display ultrafast and long-lasting nonlinearities of the same sign, ***meta*-TPEB** shows a switch in the sign of the birefringent nonlinearity; a negative on-peak electronic Kerr nonlinearity becomes a positive excited-state birefringent nonlinearity. The decay dynamics obtained from the fits are: **TD-TPEB**, τ_1= 4.4 ps, τ_2=350 ps; ***meta*-TPEB**, τ_1=2.7 ps (rise), τ_2=24 ps; ***ortho*-TPEB**, τ_1=1.6 ps (rise), τ_2=32 ps; ***para*-TPEB**, τ_1=1.2 ps (rise), τ_2=21.5 ps.....101

6.1 Chemical structures of the reported OPE-based compounds. Sample **C$_{60}$-oct-5OPE** was not sufficiently soluble for NLO characterization.. 113

6.2 UV-vis absorption spectra for OPE-precursors and OPE-fullerene hybrids in *o*-dichlorobenzene. Note both the emergence of the long tail and the shift in oscillator strength from the lower-energy peak to the higher-energy peak upon the incorporation of C_{60}.. 114

6.3 [colour] Time-resolved nonlinear absorption response of OPE-based samples in CH_2Cl_2 and MPPBT in DMSO. The MPPBT response has been scaled down by 50% for ease of comparison. a) Two-photon absorption is seen on-peak (t=0 ps) for all samples, while longer time scales represent excited-state absorption (ESA). Note that ESA is absent in the fullerene-terminated OPE **C_{60}-quad-5OPE**. b) (log-linear graph) Excited-state absorption decays, showing that samples **quad-5OPE** and **oct-5OPE** have strikingly similar relaxation dynamics. 117

7.1 Three general *iso*-polydiacetylene frameworks. Structures **3** are the perphenylated *iso*-PDAs discussed herein. 126

7.2 Perphenylated *iso*-polydiacetylene oligomers. The end-group Et_3Si, otherwise known as *TES*, is an electronically inert moiety inserted for improved solubility. For this study, oligomers with n=1, 2, 3, 5, 7, 9, 11, 13, and 15 were investigated. The longest linear-conjugated path for each of the oligomers is shown in bold, highlighting the fact that the maximum fixed-length segment is not present in the monomer, ***iso*-PDA-1**. 126

7.3 [colour] Electronic absorption spectra (ε in $Lmol^{-1}cm^{-1}$) in $CHCl_3$ comparing the effects of oligomer chain for n=2-15 *iso*-PDAs. 128

7.4 [colour] Emission spectra in $CHCl_3$ for full *iso*-PDA series, with excitation at 380 nm. λ_{em} in nm for each oligomer is shown in parentheses. For clarity, legend entries follow the peak signal in order. 128

7.5 Correlation of relative molecular second hyperpolarizibilities (γ/γ_{THF}) as a function of oligomer length n. (a) Linear fit (n = 2–15). (b) power-law fit of the form $\gamma = a + bn^c$ (n = 2–15). (c) Two linear fits (n = 2–7 and n = 9–15). 131

7.6 Minimized structure of tridecameric *iso*-PDA using MM3* force field parameters.[40] Only backbone carbons are displayed as space-filling representation for clarity: (a) View from top; (b) View from side. 131

7.7 Plot of absorbance ratio A_{378}/A_{323} *vs.* chain length (n) in $CHCl_3$ (●) and acetonitrile (■). A_{378} denotes the absorbance intensity at 378 nm, and A_{323} denotes the absorbance intensity at 323 nm. 132

8.1 [colour] A schematic of supercontinuum generation. A collimated incident beam (A) begins to self-focus (B) and eventually forms a self-guiding filament (C). In this region, the intensity of light is immense, generating both a collinear continuum and an angle-dependent conical component (D). Modified from [15] 143

8.2 A schematic of our continuum generation layout and its subsequent use in pump-probe experiments/characterization. All optics optimized for 800 nm unless otherwise specified; BS: beam splitter; λ/2: half-wave plate; P_1: polarizers, P_2: broadband Glan-laser polarizers; CH: optical chopper; L_1: f=300 cm lens; L_2: f=4.5 cm achromat doublet lens; L_3: f=7.5 cm achromat doublet lens; L_4: f=10 cm achromat doublet lens; L_5: f=500 cm lens; FC: 10 mm path-length water flow cell; S: sample position; X trans.: longitudinal translation stage; X-Y trans.: bi-directional in-plane translation stage; Scn: screen for diffuse spectral reflection; Spctr: Ocean Optics fiber-collected spectrometer; PD: amplified silicon photodiode (Thorlabs PDA55).....147

8.3 Spectra of broadband continuum generated from 10 mm H_2O and that of the generating pulse. Spectra are normalized to an irradiance of 1. 147

8.4 The supercontinuum pulse as independent bandwidth-limited quasi-monochromatic pulses, here selected by ultrafast Kerr-response cross-correlation with an 800 nm pump pulse in a glass slide. The scaled full continuum spectrum is presented for comparison.. 148

8.5 Continuum pulse chirp as mapped out by cross-correlating an 800 nm pump pulse in a ~1 mm thick glass slide. Wavelengths are determined from the spectra peaks given in Figure 8.4. The line is an extrapolation/interpolation fit in Origin 6.0 and is of typical shape for SCG from water.[25].....149

8.6 800 nm pump continuum probe Kerr measurements in ~1 mm thick glass; raw, corrected for phtodiode response, and quasi-monochromatic at 900 nm probe. Inset: the spectral response of the Thorlabs PDA55 Si photodiode. 153

8.7 Chirp-intensity correction of single-shot Kerr measurements in glass. The Full continuum intensity as a function of delay time is mapped from the white-light spectrum of Fig. 8.3 and the calibrated chirp of Fig. 8.5. This, in turn, can be used to calibrate the single-shot broadband-probe Kerr response in glass to the actual available light intensity, effectively yielding the probe-frequency dependent Kerr response, where pump delay time correlates to wavelength within the pulse.....154

8.8 Non-degenerate transient absorption measurements of MPPBT at three continuum-filtered probe wavelengths. (a) On-peak two-photon absorption is measured while long decay tails represent excited state absorption of a probe photon from a pump beam 800 nm TPA-access state. The transient signals were shifted in time to give the same peak position for dynamics comparisons. (b) Exponential decay of the excited-state absorption at a probe wavelength of 700 nm, showing a best-fit of 22 ±10 ps mono-exponential decay past 1 ps probe delay time.....161

B.1 [colour] Position dependence of probe quarter-wave plate in the birefringent (Kerr) and dichroic (NLA) DOKE polarization conditions. The Kerr signal from MPPBT in DMSO is seen to be insensitive to the position of the quarter wave-plate, and both position provide identical signals (the big symmetric peaks). For the dichroic condition, however, a pre-sample positioning of the quarter-wave plate yields a strong nonlinear absorption signal from MPPBT in DMSO, while the post-sample positioning yields a null signal that matches that of the pure DMSO solvent. The solvent displays no NLA for any position of the quarter-wave plate, as expected. 186

B.2 The four DOKE polarization conditions, as illustrated experimentally by MPPBT in DMSO. The first and third DOKE conditions are the birefringent polarization conditions, and show signals that are the negative of one another. The second and fourth DOKE conditions are the dichroic polarization conditions, and likewise show opposite responses of one another.....187

C.1 Measurements of THF and a ***TIPS*-10yne** sample solution in the DOKE *birefringent condition*. The THF reference sample displays a near-zero response and is used as a null-response check of the proper pump polarization. Scan resolution is limited somewhat by the temporal scan progression and on-peak noise. Each of the traces represents an average of 3 raw scans. From the shown scans, a value of $\tanh(\phi'') \approx \phi'' = 0.050 \pm 0.001$ was tallied for the ***TIPS*-10yne** sample. 191

C.2 [colour] DOKE *birefringent condition* measurements of ***TIPS*-PY**s and their corresponding **THF** reference scans. **THF** scans were obtained ten minutes apart and were dispersed among the scans of the various samples. The **THF** scans were extremely repeatable, as is evident from their excellent overlap. The polyyne kerr signals must be resolved beyond those of the reference **THF** scans, limiting the ultimate resolution of the DOKE technique. To obtain adequate dynamic range, sample concentrations and pump powers are carefully selected. For these scans, a 1.0 mW pump beam was used. The two different ***TIPS*-10yne** samples were used as a quick check on the concentration dependence. A single A+B trance for a ***TIPS*-10yne** sample is shown to show the sensitivity (or lack thereof) of this signal component to resolve two-photon absorption.....192

C.3 [colour] On-peak scans of **THF** and ***TIPS*-10yne** in the *birefringent DOKE polarization condition*. Straight lines are a running average fit to the data. The calculated standard deviation (spread) of the data is 0.001 mV, 0.001 mV, and 0.0002 mV for the ***TIPS*-10yne** A-B, the **THF** A-B, and the ***TIPS*-10yne** A+B signals, respectively. Clearly the on-peak A-B response is much more noisy than A+B.....192

LIST OF ABBREV. AND SYMBOLS

ABBREVIATIONS AND ACRONYMS (in order of appearance)

Abbrev.	abbreviation(s)
NLO	nonlinear optics
SHG	second harmonic generation
TPA	two-photon absorption
1-D, 2-D, 3-D	one-, two- or three-dimensional
PDT	photo-dynamic therapy
GM	Göppert-Mayers (equivalent to 10^{-50} $cm^4 \cdot s \cdot molecule^{-1} \cdot photon^{-1}$)
SOS	sum-over-states
eV	electron Volt
fs	femtosecond (10^{-15} seconds)
ps	picosecond (10^{-12} seconds)
Eqn.	equation
Fig.	figure
TPEB	tetrakis(phenylethynyl)benzene
D-A	donor and acceptor substituted species
D/A	donor and/or acceptor substituted species
D→A	donor to acceptor
BLA/BOA	bond-length alternation / bond-order alternation
TPEF	two-photon excitation fluorescence
OPEF	one-photon excitation fluorescence
THG	third-harmonic generation
DOKE	differential optical Kerr effect
OHD-OKE	optical heterodyne detection of the optical Kerr effect
THz	terahertz (10^{12} Hz)
(B)PD	(balanced) photo-diodes
THF	tetrahydrofuran

MPPBT	1,4-Bis(2,5-dimethoxy-4-{2-[4-(N-methyl)pyridin-1-iumyl]ethenyl}-phenyl)butadiyne triflate	
DMSO	dimethyl sulfoxide	
NLA	nonlinear absorption	
ESA	excited-state absorption	
AF50	N,N-diphenyl-7-[2-(4-pyridinyl)ethenyl]-9,9-di-n-decylfluorene-2-amine	
AF60	N,N-diphenyl-7-[2-(4-pyridinyl)ethenyl]-9,9-di-ethylfluorene-2-amine	
SPIE	The International Society for Optical Engineering	
PPE	poly-phenyleneethynylene	
PPV	poly-phenylenevinylene	
PA	poly-acetylene	
PY	polyynes	
PP	polyphenylene	
PTA	polytriacetylene	
PT	polythiophene	
TIPS, *i*-Pr_3Si	tri(*iso*-propyl)silyl	$-Si(CH(CH_3)_2)_3$
TES	tri(ethyl)silyl	$-Si(C_2H_5)_3$
TMS	tri(methyl)silyl	$-Si(CH_3)_3$
Me	methyl (CH_3)	
t-Bu / Bu	tert-butyl / butyl	
(Z)INDO	(zero) intermediate neglect of differential orbitals	
HOMO	highest occupied molecular orbital	
LUMO	lowest unoccupied molecular orbital	
RPA	random phase approximation	
UV	ultraviolet	
vis	visible	
IR / NIR	infrared / near-infrared	
AIST	Institute for Advanced Industrial Science and Technology	
TEE	tetra(ethynyl)ethene	
TA	transient absorption	
sym.	symmetry group	
DFT	density functional theory	
OPE	oligo(*p*-phenylene ethynylene)	
quad	quadrupolar	
oct	octupolar	
PDA	polydiacetylene	

ECL	effective conjugation length
SCG	supercontinuum generation
OPA / OPG	optical parametric amplifier / optical parametric generator
a-BBO	alpha-barium borate
KDP	potassium dihydrogen phosphate
BK-7	a particular recipe of borosilicate crown glass
FWM	four-wave mixing
SKS	stimulater Kerr scattering
GVD	group velocity dispersion
FWHM	full width at half maximum
κ	imaginary component of the index of refraction

SYMBOLS (in order of appearance)

σ	absorption cross-section in units of cm^2
$\sigma^{(2)}$	two-photon absorption cross-section in units of $cm^4 \cdot s \cdot molecule^{-1} \cdot photon^{-1}$
α	absorption coefficient in units of cm^{-1}
$\alpha^{(2)}$	two-photon absorption coefficient in units of cm/W
ω	angular frequency in radians
N, N_c	number density in molecules or particles per cm^3
$\hbar$ and h	Planck's constant (1.055×10^{-34} J·s and 6.626×10^{-34} J·s)
z	longitudinal displacement co-ordinate
γ	third-order molecular hyperpolarizability in esu
n, n_0, η_0	index of refraction / n may denote the number of oligomer repeat units
c	speed of light (3×10^8 m/s) / power-law exponent
Im(x)	Imaginary component of x
Re(x)	Real component of x
L^4	Lorentz field factor
Δ	change in
μ_i	permanent dipole moment of state i
M_{ij}	transition dipole between states i and j.
Γ_{ij}	i→j transition linewidth.
E_i	Energy of state i
ψ_i	wavefunction of state i

r	radial co-ordinate
»	much-greater-than
β	second-order molecular hyperpolarizability in esu
D	donor group
A	acceptor group
-π-	conjugated route or path
§	thesis section or subsection
ϕ	optical phase change
$\chi^{(3)}$	third-order nonlinear susceptibility in units of m^2/V^2
λ	wavelength in nanometers
λ/2 ; λ/4	half-wave plate; quarter wave plate
R ; S	reference ; sample
I and I_0	intensity in W/cm^2
$\chi^{(5)}$	fifth-order nonlinear susceptibility in units of m^3/V^3
P and P_0	laser power in W
τ	pulse duration time/exponential relaxation time
R	remainder: denotes any functional end-group (non hydrogen)
M	moles/litre
λ_{max}	highest wavelength of absorption maxima
E_{max}	energy corresponding to λ_{max}
ε	molar absorptivity in $L \cdot mol^{-1} \cdot cm^{-1}$
m	electron mass
→	to (as in from A to B)
ρ	density
S	signal or response

OUTLINE

The following thesis presents a summary of research conducted throughout the course of my Ph.D. program in the Department of Physics at the University of Alberta. The content of this thesis reflects the fact that my work was jointly supervised by Dr. Frank Hegmann in the department of Physics and Dr. Rik. Tykwinski in the department of Chemistry, and involved considerable collaborative work with Dr. Kenji Kamada (AIST, Japan), Dr. Michael Haley (University of Oregon), Drs. Yuming Zhao and Jim Tour (Rice University), and Dr. Ray DeCorby (TRlabs and Department of Electrical Engineering, University of Alberta). Considerable research effort was put into establishing an ultrafast pump-probe detection technique for the characterization of the two-photon absorption and excited-state dynamics in conjugated organic materials. Subsequently, this technique was used for the study of the optical nonlinearities in various oligomeric and chromophoric systems. Although we have communicated most of our findings, there is a considerable body of work that has yet to be published. Furthermore, there are many important experimental details and findings that were omitted from our previous reports, primarily due to a lack of space. The study of each class of molecule, such as cross-conjugated *iso*-polydiacetylenes, fullerene-chromophore hybrids, polyynes, and tetrakis(phenylethynyl)benzenes, is reported independently, each yielding unique conclusions. On the other hand, these studies comprise a consistent and cohesive body of work reporting on the third-order optical nonlinearities of highly-conjugated molecules. To accommodate research thrusts that include both developmental and spectroscopic aspects, this work is presented in a hybrid form that incorporates both traditional and paper-based formats.

This thesis is structured in three parts: Part I is comprised of three chapters. Chapter 1 provides a survey of two-photon absorption (TPA) in conjugated molecules, and includes a brief description of the various experimental techniques used for its

characterization. Chapter 2 describes the use of our differential optical Kerr effect (DOKE) detection layout for the ultrafast time-resolved characterization of both the Kerr nonlinearities and two-photon absorption in organic samples in solution. Chapter 3 illustrates the use of a traditional beam-depletion experiment for the measurement of TPA in a reference sample. This experiment is presented as an independent test of the results obtained by the DOKE technique. Thus, Part I looks to establish the use of DOKE as an appropriate technique for the measurement of the real and imaginary components of third-order optical nonlinearities of isotropic organic samples. Part II reports on the study of four different classes of conjugated organic molecules. Each of the four chapters in this part is prefaced with a "Context" section that describes the collaborative nature of the study and mentions its publication history. Chapter 4 presents the study of the optical and nonlinear optical properties of polyynes; a uniquely one-dimensional class of oligomers. Chapter 5 presents the study of two-dimensionally-conjugated oligomers that differ by their donor/acceptor substitution symmetry across a central benzene ring. These samples were studied both with the DOKE technique and with tunable-wavelength z-scan experiments. Chapter 6 presents the study of the optical and nonlinear optical characteristics of multi-fullerene substituted conjugated oligomers. Chapter 7 reports on the optical nonlinearities of extended cross-conjugated *iso*-polydiacetylene oligomers. Our DOKE detection currently operates at a fixed wavelength of 800 nm. Some of the studies presented in Part II motivate the need to measure optical nonlinearities at various wavelengths across the visible and near-infrared. Part III describes the construction and preliminary characterization of an 800 nm pump white-light probe technique used to obtain non-degenerate TPA spectra of a TPA standard. Appendix A provides further background on the link between two-photon absorption and the nonlinear index of refraction. Appendix B discusses the importance of the sample-arm quarter-wave plate position in the DOKE technique. Finally, Appendix C presents some raw DOKE scans and discusses issues related to the signal resolution performance of the various DOKE polarization conditions. Every Chapter and Appendix contains its own bibliography.

PART I

THE DESCRIPTION AND DETECTION OF TWO-PHOTON ABSORPTION IN ORGANIC SAMPLES

CHAPTER 1:

INTRODUCTION TO TWO-PHOTON ABSORPTION IN CONJUGATED ORGANIC SYSTEMS

1.1 Introduction

With the development of the laser as a source for intense and coherent light, new light-matter interactions have risen to the forefront of the optical sciences in the form of a new discipline—Photonics.[1] Light-intensity-dependent phenomena comprise the field of Nonlinear Optics, which represents the cornerstone of Photonics research. Among the first nonlinear processes to be discovered were the optical Kerr effect, the Pockels effect, and second-harmonic generation (SHG).[2] Each of these phenomena has been utilized to technological advantage. In fact, all three are integral components of modern laser design and amplification.[3] In the last few decades, the myriad nonlinear optical processes have been discovered and investigated, ranging from second- and third-harmonic generation and stimulated Raman scattering, to self-focusing and optical rectification.[2] The advancement of these processes towards technological development has typically relied on maximizing the optical nonlinearity while minimizing light absorption.

Two-photon absorption (TPA) is a third-order nonlinear process that is the absorptive counterpart to the optical Kerr effect (see Appendix A).[2] As shown in Fig 1.1a, in a TPA process, two photons are simultaneously absorbed to promote an excitation at the sum energy,[4] in seeming violation of well-established processes such as the photoelectric effect. This process is intensity-dependent, and is only observable at very large optical fields. Traditionally, TPA in systems of interest was studied with the intention of learning how to minimize the effect; TPA was seen as parasitic in these materials, lowering their merit in technological use.[4,5,6] It is only recently that

absorptive nonlinearities such as two-photon absorption have been studied as the primary process of interest for applications. In the past decade, compounds with large two-photon absorption have been vigorously sought for a slew of technological applications in various fields such as defense,[7,8] bio-photonics and medicine,[9-13] nanotechnology,[14-17] and laser development.[18-20]

Using two-photon absorption is uniquely advantageous for various applications due to the nature of the process. More specifically, TPA can occur at wavelengths far removed from linear absorption so that the onset of absorption can occur only at high light intensities. Applications such as optical limiting are based on this premise.[7,18,21] Optical limiters are materials that are transparent to ambient light, but become opaque if they are illuminated with intense light. Thus, materials for optical limiting are actively sought for various defense applications that seek, for example, to protect fighter-pilot vision during a ground-to-air laser attack.[22] Other optical limiting applications involve passive protection of light sensors.[23]

Because TPA is light-intensity-dependent, it allows for excellent 3-D spatial resolution in the vicinity of a focus. This is the feature that is most widely utilized in TPA-based technologies. Examples of these are 3-D optical storage and micro-fabrication, two-photon fluorescence microscopy, and photodynamic therapy. Micro-fabrication with two-photon sensitizers has allowed for unprecedented three-dimensional sub-micrometer resolution.[14,17] Furthermore, with two-photon absorbing fluorescent dyes, one can now selectively excite a miniscule volume within biological tissue, allowing for nanometer-scale microscopic imaging.[10,24] As in fabrication, data storage, and fluorescent imaging, the application of TPA to photodynamic therapy (PDT) promises great improvement in spatial resolution. In standard photodynamic therapy,[25] a light-absorption-activated drug is injected to the vicinity of a tumor. The tumor cells are then destroyed by illuminating the affected area through the creation of singlet-oxygen.[25] The light used is typically at infrared wavelengths to which skin is somewhat transparent. Two-photon photodynamic therapy acts much in the same way, only in this case a two-photon infrared-absorbing drug is used.[9] Because the absorption—and hence tissue damage—is better localized to the beam focus, two-photon PDT promises significant minimization of unwanted near-by collateral absorption and tissue damage.

1.2 A Survey of Two-Photon Absorption in Conjugated Chromophores

Conjugated Chromophores for TPA applications: Although TPA was first observed in doped ionic crystals,[26] and has since been studied in gas,[27-29] semiconductor,[30-32] and glass systems,[6,34-36] the search for material classes with appropriate characteristics for TPA applications has primarily focused on conjugated organic chromophores.[4] Conjugated chromophores are attractive systems for TPA applications for several crucial reasons: First, current laser technology (especially in communications and medicine) uses wavelengths in the near-infrared, around 800-1500 nm. As their name suggests, *chromophores* absorb light most strongly in the visible range of 300nm-800nm, and are thus ideally suited for the required transparency at the fundamental wavelength of interest, while having the strongest two-photon accessible levels at twice the fundamental energy. Semiconductors, on the other hand, have large oscillator strengths that may lead to large TPA cross-sections, but have (one-photon) band gaps that extend through the wavelength range of fundamental excitation light, and are thus insufficiently transparent for many TPA-based photonic applications. Second, organic synthesis techniques provide a huge range of processibility and versatility, allowing for the engineering of unique compounds for specific applications. This includes ample solubility for applications such as laser dyes, deliverable drugs, spin-coated optical limiting films, etc. Third, although saturated organic frameworks (such as alkanes) display miniscule optical nonlinearities, bond-conjugation allows for large electronic delocalization and charge-transfer, leading to large polarizabilities and hyperpolarizabilities.[37] A conjugated path is one of alternating single and multiple (double, triple) bonds, and thus represents a chain of sp- and/or sp^2-hybridized carbons; each of which possesses π-orbitals that extend laterally to the chain direction. Overlap of these π-orbitals provides extended molecular orbitals that run parallel to the conjugated backbone, and through which considerable electronic delocalization can take place: electrons are delocalized along this route, providing for

considerably increased optical polarizabilities.[38,39] Thus, conjugated organic chromophores, as a materials class, are ideally suited for TPA applications.

TPA cross-section: As with all TPA-based technology, it is important to maximize the two-photon absorption activity so that lower light intensities may be used. In an analogous manner to that of linear absorption, wherein the molecular absorption probability is given as a cross-section,

$$\sigma(\omega) = \frac{\alpha(\omega)}{N}, \qquad 1.1$$

where α is the Beer's-law coefficient of absorption (in cm^{-1}), and N is the molecular species density (in cm^{-3}), so too is TPA activity most often described in terms of a cross-section. The two-photon absorption cross-section, $\sigma^{(2)}$, is given by

$$\sigma^{(2)}(\omega) = \frac{\hbar\omega}{N}\alpha^{(2)}(\omega), \qquad 1.2$$

where $\hbar\omega$ is the photon energy, and $\alpha^{(2)}(\omega)$ is the two-photon absorption coefficient (in cm/W) that defines intensity-dependent beam depletion (along propagation direction, z) according to

$$\frac{\partial I}{\partial z} = -\alpha I - \alpha^{(2)} I^2 . \qquad 1.3$$

Typically, $\sigma^{(2)}$ is reported in units of cm^4-s-$photon^{-1}$-$molecule^{-1}$ or in Göppert-Mayers, GM (1 GM=10^{50} cm^4-s-$photon^{-1}$-$molecule^{-1}$). The value $\sigma^{(2)}$ is a third-order nonlinear parameter, and is related to the second molecular hyperpolarizability (third-order molecular polarizability), γ, via

$$\sigma^{(2)}(\omega) = \frac{3\hbar\omega^2}{2\varepsilon_0 c^2 n_0^2} L^4 \,\mathrm{Im}\left(\gamma(-\omega;\omega,\omega,-\omega)\right), \quad [40,41] \qquad 1.4$$

as is further detailed in Appendix A. In the preceding relationship, γ is given in esu units as are the other parameters.[42] The value L^4 is the local field factor that relates the optical field to the microscopic dielectric environment in the vicinity of the individual molecules. Inspection of Eqn. 1.4 shows that quantitative spectral details of TPA rely on the intimate characteristics of the third-order nonlinear response of each molecular system.

Theoretical Description of TPA: Theoretical studies of TPA in conjugated organic chromophores have contributed a considerable body of knowledge.[41,43-48] Currently, popular expressions for TPA in organic molecules are derived from sum-over-states (S.O.S.) expressions for Im[γ],[44] and provide a means for estimating TPA cross-sections based on such parameters as ground-state polarization and multipolar symmetry, the tuning of photon energies to (virtual) molecular levels, and transition dipole moments. A standard starting point for the description of TPA action in conjugated chromophores is given by:[40]

$$\sigma^{(2)}_{SOS} \approx \frac{(\hbar\omega)^2 L^4}{5n^2c^2\varepsilon_0\hbar} \mathrm{Im}\left[\begin{array}{ll} \dfrac{M_{ge}^2(\mu_e-\mu_g)^2}{(E_e-E_g-\hbar\omega-i\Gamma_{ge})^2(E_e-E_g-2\hbar\omega-i\Gamma_{ge})} & \mathrm{I} \\ -\dfrac{M_{ge}^4}{(E_e-E_g-\hbar\omega-i\Gamma_{ge})^2(E_e-E_g+\hbar\omega-i\Gamma_{ge})} & \mathrm{II} \\ +\sum_{e'}\dfrac{M_{ge}^2M_{ee'}^2}{(E_e-E_g-\hbar\omega-i\Gamma_{ge})^2(E_{e'}-E_e-2\hbar\omega-i\Gamma_{ge'})} & \mathrm{III} \end{array}\right] \qquad 1.5$$

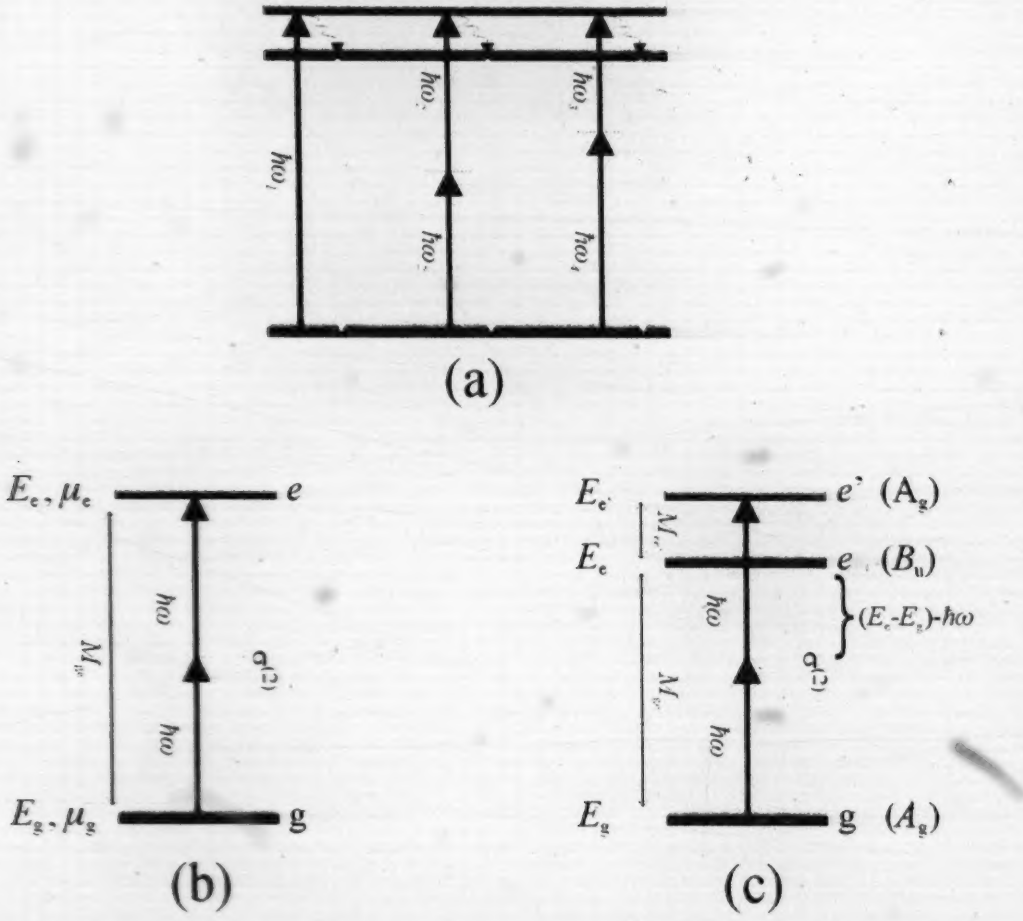

Figure 1.1: [colour] Schematic representations of molecular two-photon absorption. (a) Standard one-photon absorption (blue; left), degenerate two-photon absorption (red, red; middle), and non-degenerate (green, dark-red; right) two-photon absorption to the same energy level. In many organic systems, identical fluorescence (yellow) is observed from one- and two-photon accessed states.[10,49] (b) A two-level model is often sufficient for modeling TPA in dipolar systems. g is the ground state and e is the excited-state; E_g and E_e are their energies and μ_g and μ_e are their static dipoles. M_{ge} is the transition dipole between these states. $\sigma^{(2)}$ is the two-photon cross section for this transition, and $\hbar\omega$ is the energy of the incident laser light. (c) A minimum three-level model is needed for explaining TPA in symmetric systems lacking permanent dipoles. The ground state in such chromophores is of *gerade* (A_g) symmetry, as is the two-photon allowed state. The two-photon-forbidden but one-photon-allowed state is of opposite, *ungerade* (B_u), symmetry. $[(E_e\text{-}E_g)\text{-}\hbar\omega]$ is the detuning factor, and is inversely proportional to $\sigma^{(2)}$ in symmetric systems.

This expression is a simplified version of the full Orr and Ward treatment for the second molecular hyperpolarizability, γ,[44] and assumes degenerate (see Fig. 1.1a) excitation with light that is linearly polarized in the direction of maximal conjugation.[40] The terms in Eqn. 1.5 (denoted I, II, and III) possess three basic parameters on which TPA activity is based. The denominator in all three terms describes the tuning (or detuning) of the photons' energy to various molecular energy levels. $\hbar\omega$ is the photon energy, while E_g, E_e, and $E_{e'}$ are the energy the ground-, one-photon allowed, and two-photon allowed levels, respectively. Γ is the damping factor (linewidth) for the respective transition, and is typically assumed to be 0.1 eV.[40,46,50-53] In reality, Γ values ranging around 0.25 eV have been experimentally determined,[54,55] leading others to use Γ = 0.2 eV in subsequent calculations.[56] The numerators in Eqn. 1.5 describe the ground- and excited-state polarizations, and consist of permanent and transition-dipoles. μ_g and μ_e are the permanent dipole moments of the ground-state and the excited-state, respectively. M_{ge} and $M_{ee'}$ are the transition moments for the ground (g) level to one-photon allowed (e) level transition, and for the one-photon (e) level to the two-photon allowed (e') level, respectively. Transition dipoles represent the transition of electronic density between two states, and are defined as [40,56]

$$\overline{M}_{mn} = \langle m | \overline{\mu} | n \rangle = -e \int \psi_m^*(\bar{r}) \bar{r} \psi_n(\bar{r}) dr . \qquad 1.6$$

In practice, this integration is usually replaced by a summation over atom sites. Like permanent dipole moments, transition dipoles are vector quantities and thus the relative orientation between parameters must be taken into account. Eqn. 1.5 is designed to treat excitations in conjugated systems, most of which have a well-defined (quasi 1-D) axis of conjugation, and for which the transition- and permanent-dipole moments are aligned. In systems of higher dimensionality, these moments may not be aligned, and treatment of TPA in such systems may require slight modifications to Eqn 1.5.[57-59] For a practical example, see the discussion of transition moments in tetrakis(phenylethynyl)benzenes (TPEBs) in Chapter 5. A schematic representation of various two-photon transition schemes annotated with the parameters from Eqn. 1.5 is presented in Fig. 1.1.

Both one-photon and two-photon transitions follow parity selection rules. Thus, in symmetric systems, linear absorption spectroscopy can only access dipole-operator regulated transitions between states with odd parity, and direct two-photon absorption can only occur between states with even parity.[4,53] In asymmetric systems, both one- and two-photon transitions are permitted to the same states, and the TPA spectrum may follow the one-photon absorption spectrum at twice the wavelength. These considerations are also illustrated in Fig. 1.1. There is thus a significant difference between TPA in dipolar molecules and symmetric systems with multipolar (quadrupolar, octupolar) geometries.[48,53]

TPA in Dipolar Molecules: The TPA action of various push-pull dipolar molecules have been investigated by many groups.[20,41,48,53,60-63] For most dipolar molecules, term I in Eqn 1.5 has been shown to dominate the TPA spectrum:[41] Term II describes only one-photon resonances, and thus does not contribute to TPA. It has also been shown that dipolar molecules have miniscule $M_{ge'}$ values, especially compared with M_{ge} and $\mu_e - \mu_g$, and thus the dipolar term II dominates over term III. Accordingly, a 2-state model is typically used to describe two-photon absorption in asymmetric systems, as shown in Fig. 1.1b. With these aforementioned considerations, the peak degenerate TPA cross-section in dipolar molecules may be approximated from Eqn. 1.5 by

$$\sigma^{(2)}_{2-level} \approx \frac{L^4}{5n^2c^2\varepsilon_0\hbar}\frac{M_{ge}^2(\mu_e-\mu_g)^2}{\Gamma_{ge}}, \qquad 1.7$$

where it is assumed that, on-peak, $(E_e\text{-}E_g) \approx 2\hbar\omega$, and $(E_e\text{-}E_g) \gg \Gamma_{eg}$. Furthermore, because of these constraints, this expression is only valid in the immediate vicinity of the TPA peak, and does not describe the TPA *spectrum*. However, it has been shown that in some cases, the one-photon spectrum may be used to predict the TPA spectrum in dipolar molecules.[63]

Equation 1.7 may fail to properly describe two-photon absorption in some dipolar molecules; particularly, those in which strong coupling to higher excited states is present.[64] Those molecules for which a 2-state model is best suited have simple one-

photon absorption spectra that are dominated by a single lowest-energy peak.[41,63] In molecules for which essential-state models are insufficient, such as bis(dioxaborine)-substituted chromophores,[64] term III may provide sizable contributions, and summations over several excited states may become necessary. In general, however, it has been shown that for most dipolar molecules, the peak TPA value may be consistently predicted based on a simple 2-state level, and the main peak in the TPA spectrum follows that of the one-photon spectrum (at half wavelength).

TPA in Symmetric Molecules: Symmetric molecules that lack permanent dipole moments have become the primary focus of recent nonlinear-absorption studies. In particular, molecules/systems with quadrupolar[40,48,50,53,56,61,65,66] and octupolar[46,66-69] symmetries are attracting wide attention both theoretically and experimentally. Unlike dipolar molecules, for which Term I (in Eqn. 1.5) provides the dominant TPA contribution, multipolar systems lack static dipole moments, and TPA in these systems is best described by Term III. TPA between the ground level (g) and final level (e') in these molecules is mediated by at least one intermediate (e). Term III describes TPA through the coupling between intermediate and final levels, through both transition moment terms ($M_{ee'}$) and the tuning of photon energy to that of the intermediate level. The peak degenerate TPA cross-section in symmetric molecules may be approximated from Eqn. 1.5 by

$$\sigma^{(2)}_{3-level} \approx \frac{L^4}{5n^2c^2\varepsilon_0\hbar}\frac{\left(E_{e'}-E_g\right)^2 M_{ge}^2 M_{ee'}^2}{\left[2\left(E_e-E_g\right)-\left(E_{e'}-E_g\right)\right]^2\Gamma_{ge'}}, \qquad 1.8$$

where it is assumed that, on-peak, $(E_{e'}\text{-}E_g) \approx 2\hbar\omega$, and $(E_{e'}\text{-}E_g\text{-}\hbar\omega) \gg \Gamma_{ge'}$.[41] The latter, as well as the functional form of Eqn. 1.8 means that this description is only valid in the absence of double resonance;[41,54,59] i.e, the intermediate level does not lie at precisely half of the energy of the TPA transition. In most organic chromophores, standard symmetry alternation takes place, where the ground-state is of A_g symmetry and the first and second excited states are of B_u and A_g symmetries, respectively.[39,45,70] Unlike dipolar molecules, in which the lowest excited state is both one- and two-photon active,

in quadrupolar molecules two-photon absorption obeys even-parity selection rules, and the lowest one-photon transition is two-photon forbidden,[50] as shown in Fig. 1.1c. Thus, the peak of the TPA *spectrum* of quadrupolar molecules is typically blue-shifted with respect to that of the one-photon absorption spectrum (at the total absorption energy).[53]

In the case of octupolar molecules that possess a three-fold rotation axis (and dendritic systems [71]), there is a sort-of mixing of the two symmetry cases:[67,69] octupolar systems lack permanent dipole moments, thus restricting TPA to transitions of the type described by Term III. On the other hand, they also have relaxed selection rules compared to quadrupolar molecules (which have inversion symmetry), and TPA transitions can occur from the ground state to the lowest one-photon-allowed state.[66-68] Another theoretical approach for describing TPA in octupolar systems considers the structure as being composed of individual dipolar arms that may, or may not, interact via the molecular centre.[46] This approach, known as the exciton model, [46,72] uses both Term III and an expression similar to Term I, but modified to account for tensor component addition within Kleinmann symmetry rules.[37,42] In the case of octupolar (and dendritic) frameworks, choice of the central moiety can lead to molecules in which the dipolar arms are either linked by conjugation,[49,69,71] or are effectively decoupled.[66,67] A strong advantage to using octupolar systems in the design of materials with large TPA lies in a possible link between the second-order molecular polarizability, β, and $\sigma^{(2)}$—a third-order nonlinearity.[67] A linear trend between β and $\sigma^{(2)}$ has been recently identified.[73] Thus, the large body of knowledge of second-order response of octupolar molecules may provide directed guidance for the engineering of molecules with large TPA.[74,75]

Structure-Property Relationships: Considerable research effort has been spent to determine molecular design features that lead to increased TPA activity. This effort has centered on influencing the various parameters of Eqns. 1.7 and 1.8. Maximizing TPA in conjugated chromophores involves a delicate balance between the tuning of various intermediate and final energy levels and the maximizing of permanent and/or transition dipoles. Towards this end, a variety of molecular structure parameters have been studied

by both experimental and theoretical means. Those that have been identified to impact molecular two-photon absorption include molecular geometry and planarity,[40,57,64] Donor/Acceptor substitution and strength,[50,57,65,69] polar/multipolar geometry,[40,46,48,53,66] bond-length alternation,[40,48,76,77] and conjugation scheme/length.[50,51,57,65]

Conjugation length strongly influences TPA.[50,51,57] It has consistently been shown that on-peak $\sigma^{(2)}$ increases rapidly with increasing conjugation length.[50,65] Similar to the case of the second-hyperpolarizability, γ, where the optical nonlinearity scales as a power-law as a function of conjugation length,[38,78] recent calculations predict even steeper power-law increases in $\sigma^{(2)}$ with increasing conjugation length.[47] The impact of increasing the conjugation length is twofold: First, as the length is increased (in oligomers, for example), the optical gap decreases,[38] and thereby tunes the photon energy towards the lowest one-photon allowed transition. This acts to reduce the denominators in Eqn. 1.5.[45,57] Second, increasing conjugation enhances the charge separation within the molecule, and leads to increases in both permanent- and transition-dipoles. In fact, it has been experimentally shown that increased chain length especially increases M_{ge}.[65]

Early TPA studies identified the benefit of substituting π-donors (D) and/or π-acceptors (A) across the conjugated molecule, where it was first shown that end-capping a linear bis(methylstyryl)benzene parent molecule with donors leads to an 80-fold increase in $\sigma^{(2)}$.[50] Subsequently, the effects of D/A strength have been widely studied.[51,57,61,69] In both dipolar and symmetric molecules, functionalizing chromophores with strong donors and/or acceptors increases the ground-state polarization, and thus increases $\sigma^{(2)}$. In the case of dipolar molecules, a D-π-A framework yields large dipole moments. Similarly, in symmetric systems, donor and acceptor strengths correlate with the size of transition dipoles;[51] particularly impacting the $M_{ee'}$ term.[65] Overall, it has been shown that TPA in D-π-D architecture is larger than for A-π-A schemes.[51] This is probably due to the fact that a conjugated centre, especially an aromatic one, acts as a weak electron acceptor;[65] creating a D-π-A-π-D scheme.[50] For a discussion of the effects of donor/acceptor substitution pattern in tetrakis(phenylethynyl)benzenes (TPEBs), see Chapter 5

Planarity and dimensionality in the conjugated framework have also been shown to directly influence TPA. Studies have found that deviations from planarity in the conjugation network/centre adversely affect $\sigma^{(2)}$.[40,57,62] Others, have predicted conformational twisting to have little effect on the TPA activity of certain molecules.[64] Regardless, the type of π-centre seems to be important in TPA.[51,65] Different conjugation schemes can provide varying levels of polarizability,[38] and thus impact both energy tuning and charge separation. In the past, stilbenoid[7,50,65,66] and fluorene[60,79,80] chromophoric centers have shown considerable popularity. Dimensionality impacts $\sigma^{(2)}$ by allowing for conjugation to extend in several directions at once.[46,51] While early studies focused on quasi-one-dimensional structures, recent studies have increasingly explored 2-D conjugation in the form of octupolar and dendritic frameworks. Careful choice of the central linkage can allow for co-operative enhancement between conjugated paths, leading to sizable increases in $\sigma^{(2)}$.[49,69,71] while deviations from both planarity and alignment of (transition)dipoles have been shown to hinder TPA (*vide supra*), the benefit of increased dimensionality does not seem straightforward. In fact, some studies have shown that when $\sigma^{(2)}$ is scaled by the number of arms or the number of multiple bonds, the per-unit cross section is smaller in octupolar and dendritic structures than in sub-structures or the bare unit.[49,66] Thus, structure-property relationships between dimensionality and TPA do not seem to be particularly well defined at present.

Finally, numerous theoretical studies have investigated the relationship between bond-length alternation and two-photon absorption.[40,41,48,76] Quantifiable bond-length alternation (BLA) compares the differences in bond lengths along a conjugated chain.[81] At one extreme lies the covalent, or bond-alternate limit, for which the literal and fixed picture of an alternating single- and multiple-bond sequence is borne out by the actual bond lengths. That is, there is reduced electronic delocalization along the conjugated path, and the electrons of each multiple-bond are dedicated to that location, leading to maximum possible bond-length alternation. At the other extreme lies the cyanine, or bond-equivalent, limit for which near-complete delocalization is present. In this case, each bond along the conjugated path is effectively identical, leading to BLA near zero.[41,81] There is a considerable history to the study of BLA as a defining

parameter for nonlinear optical activity in conjugated systems.[82-85] These studies show that second-order and third-order nonlinearities exhibit disparate dependences on BLA. One might assume that $\sigma^{(2)}$ and γ should show similar trends, since they are both $\chi^{(3)}$-based nonlinearities. Indeed, it has been shown that for dipolar structures, $\sigma^{(2)}$ shows a very similar BLA dependence to that of γ;[48,76] peaking for a finite BLA.[87] Quadrupolar molecules, on the other hand, are expected to exhibit peak TPA at a BLA of zero.[48] The correlation between BLA and TPA response may be well defined, but structure-property relationships for BLA itself are not well established![40] To engineer molecules with a BLA that maximizes TPA, one must increase the ground-state polarization in such a way as to both maximize charge transfer and minimize energy detuning. Minor changes in the detailed chemical structure and environment vary these parameters so strongly that a straightforward way to tune BLA to maximize TPA has not yet been identified.

So much research has focused on the ground-state polarization that a natural question arises: What symmetry class yields the largest TPA cross-sections; dipolar, quadrupolar, or octupolar? As with most structure-property relationship in this area of research, there may not be a straightforward answer. Several studies have specifically looked to directly compare two of these classes.[46,48,51,53,66] All studies that have looked to compare dipolar and quadrupolar geometries claim that quadrupolar is highly favorable over dipolar geometry.[48,51,53] Furthermore, comparisons of octupolar and dipolar geometry give the advantage to octupolar symmetry.[46] Finally, comparisons of octupolar and quadrupolar geometries come out in favor of the latter.[66]

Problems with comparing various geometries extend beyond their peak $\sigma^{(2)}$ values. As previously discussed, the description of TPA in dipolar, quadrupolar, and octupolar molecules employ different selection rules and thus different numerical expressions. While dipolar molecules are well described by Eqn 1.7, quadrupolar and octupolar molecules are oft described by Eqn 1.8. This makes comparisons of their peak TPA problematic. Furthermore, having different selection rules means that the TPA spectra are shifted differently for the various geometries. Since octupolar and dipolar

molecules can support TPA transitions to the lowest excited state, their spectrum can follow that of the one-photon spectrum (at the same total energy). On the other hand, because the lowest excited state is expected to be one-photon-allowed and two-photon-forbidden in quadrupolar molecules, their TPA spectra are blue-shifted with respect to the one-photon spectrum. Thus, quadrupolar and dipolar/octupolar molecules may simply find uses in different TPA applications.[66] Eventually, processibility will become a major concern that may impact the usefulness of one geometry over another. Thus far, the largest experimental cross-sections found in quadrupolar and octupolar molecules are the same within an order of magnitude, giving neither geometry a well-defined advantage. And although dendritic molecules have been found to have TPA cross-sections as large as 11,000GM,[49] their per/unit response does not show them to be particularly superior to their quadrupolar sub-units. Currently, the best TPA cross-sections of single (non-dendritic) molecules measured with femtosecond pulses lie in the order of 2,000-5,000GM.[53,54] Figure 1.2 displays three representative high-$\sigma^{(2)}$ molecules.

Despite numerous studies of two-photon absorption structure-property relationships, no one paramount design feature has been identified, and thus, this area of research is still very active. There are, however, some general trends and guidelines for maximizing TPA in conjugated chromophores. The most immediate way to increase TPA is by extending the overall conjugation path. This will also have the added benefit of moving the TPA spectrum deeper into the near-IR—a desirable feature for practical applications. The superlinear increase of TPA with conjugation (*vide supra*) would be expected to saturate as the effective conjugation length is approached. Thus, careful choice of conjugation scheme must be made in an attempt to find schemes that have sufficient planarity and longer effective conjugation lengths. Quadrupolar geometries appear to be as favorable as dipolar arrangements.(See conclusions arising from TPA in TPEBs; Chapter 5) Furthermore, end-capping with strong donor groups yields larger TPA activity than bis(acceptor) or donor-acceptor substitution. To effect an even better D-π-A-π-D scheme, substitution of acceptor groups as near as possible to the conjugated centre may be beneficial.[40] Keeping the acceptors close to the molecular axis will maintain better alignment between transition dipoles.

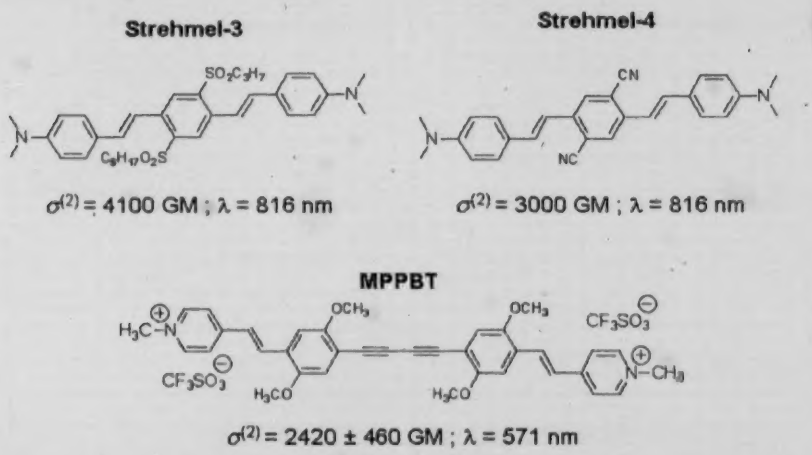

Figure 1.2: Representative high two-photon absorbing compounds. High $\sigma^{(2)}$-values were obtained for Distyrylbenzene-based Strehmel-3 and Strehmel-4 using femtosecond two-photon excitation fluorescence spectroscopy.[53] High $\sigma^{(2)}$-values were obtained for diacetylene-based MPPBT using femtosecond z-scan.[54]

1.3 Measurement of Two-Photon Absorption

The measurement of two-photon absorption is straightforward, and a large number of experimental techniques have been employed for this purpose.[2,4] Each technique has its advantages and disadvantages; whereas some are easy to implement, they may only provide limited information. Others are complex or difficult to analyze, but provide unique information. Currently, though many techniques are in use, four approaches dominate the field: single-beam nonlinear-transmission, two-photon excitation fluorescence spectroscopy, z-scan, and pump-probe transient-absorption based techniques.

The simplest experiment—and one that is still in use for optical limiting measurements—is nonlinear transmission.[2] By passing an intense (focused) laser beam into a sample, one can plot the transmitted power against the incident power. Deviations

from linearity indicate nonlinear absorption. The shape of the curve holds precise information regarding the various nonlinear absorption processes including two-photon and higher-order absorption, saturable absorption, and reverse saturable absorption. When using an ultrashort (fs) pulsed beam, the dominant absorption mechanism is two-photon absorption. Chapter 3 presents results and further background on such single-beam depletion measurements. Other more sophisticated techniques allow for better signal to noise extraction, and may each provide unique information not accessible by the others.

Two-photon excitation fluorescence (TPEF) is a widespread technique that utilizes the fact that many conjugated chromophores display identical fluorescence spectra when excited by one photon or by two-photons at similar sum energies.[88] The two-photon-excitation fluorescence quantum efficiency is typically the same as that for one-photon excitation, and thus normalizing TPEF signals to the one-photon excitation fluorescence (OPEF) spectrum of a standard allows for the calibration of both the quantum efficiency and collection efficiencies.[89] Benefits of TPEF are ease of measurement and signal analysis. One drawback of TPEF is its dependence on quantum efficiency; many materials of interest are non-emissive, or only weakly emissive. Thus, signal resolution is relatively poor in such samples, and uncertainties are large when compared with some other techniques. Furthermore, fluorescence measurements are typically limited to samples in solution, and thus make difficult the characterization of the TPA response in samples such as thin films or single crystals. Overall, however, TPEF is a highly attractive means of measuring $\sigma^{(2)}$ and is therefore quite popular.

A more recent technique that is ideally suited to the measurement of $\sigma^{(2)}$ is the (open aperture) z-scan technique.[90,91] As with the previous two techniques, z-scan is a single-beam measurement that provides degenerate cross-sections. In a typical open

aperture z-scan measurement, a collimated beam is focused into a sample that can be scanned in position through the focus. The total output light is then collected and sent to a photodiode. This technique directly utilizes the intensity dependence of the TPA process. As the sample is scanned through the focus, it experiences a varying intensity such that it absorbs most at the focus, and to a diminishing degree away from the focus. One can then fit the resulting position-dependent attenuation profile to obtain an absolute measurement of $\sigma^{(2)}(\omega)$. Since the fitting depends strongly on the exact laser intensity and temporal profile, complete knowledge of the laser beam and pulse parameters are essential. Even though z-scan obtains absolute TPA cross-sections, signals are typically calibrated against that of a known sample.[91] z-scan has access to the entire TPA spectrum, which may not be the case for TPEF;[92] especially in cases where the lowest excited-state is one-photon forbidden and thus relaxes non-radiatively.[70,93] Of major concern in z-scan are accumulated thermal effects[94] and contributions from excited state absorption, especially in non-ultrafast, high repetition-rate experiments. These effects, however, are often removed by working away from one-photon resonances, lowering the repetition rate, and using femtosecond (fs) pulses.[4]

All three of the aforementioned techniques are single-beam measurements. Over the years, numerous two- and multiple-beam experiments have been used for nonlinear optical characterization. These include optical Kerr gates and ellipsometers, coherent coupling, as well as four-wave mixing layouts.[2,37,95] Such techniques are intrinsically suitable for the measurement of the real (birefringent) part of the optical nonlinearities,[4] but many can be utilized for transient absorption type experiments.[96] A two-beam experiment may be more complicated than the aforementioned single-beam techniques, but it has several crucial and unique benefits: Typical ultrafast pump-probe techniques employ a dual-beam arrangement in which a weak pulsed beam is time-delayed with

respect to a coherent strong pulsed beam. The weak probe beam can then be scanned to measure the temporal-evolution of perturbations made in the sample by the intense pump beam. In applying these experiments to the measurement of nonlinear absorption, the polarizations of the pump and probe beams are set at conditions for which only a dichroic response is measured. In a pump-probe transient absorption experiment, two-photon absorption is detected by the simultaneous absorption of a photon from each of the pump and probe beams. By varying the arrival time of the probe pulses, one can obtain the ultrafast time-evolution of the nonlinear absorption response. Furthermore, the two-beam arrangement allows for the possibility of a 2-colour experiment that can provide the non-degenerate TPA response.[97,98] Traditionally, z-scan, nonlinear transmission measurements, and TPEF have utilized nanosecond or picosecond pulses, and thus must either ignore or account for the possibility of non-instantaneous excited-state absorption (ESA) artifacts.[4] These concerns are far from trivial, and improper accounting for ESA has led to the reporting of nanosecond-pulse-measured $\sigma^{(2)}$ values that are three orders of magnitude higher than those reported with femtosecond pulses![61] With pump-probe measurements, in addition to measuring the instantaneous two-photon absorption, the longer-lasting ESA may be directly measured and characterized (See §2.3).[99] Drawbacks to using pump-probe measurements for the characterization of TPA are the more complex experimental layout, and the relative difficulties is obtaining absolute $\sigma^{(2)}$ values. To account for this, signals are typically referenced to that of a standard sample. The following chapters detail our use of an in-house-designed optical Kerr gate for the measurement of ultrafast time-resolved nonlinear absorption processes in organic samples.

1.4 References

[1] B. E. A. Saleh and M. C. Teich, *Fundamentals of photonics* (Wiley, New York, 1991).

[2] R. L. Sutherland, D. G. McLean, and S. Kirkpatrick, *Handbook of nonlinear optics* (Marcel Dekker, New York, 2003).

[3] W. T. Silfvast, *Laser Fundamentals* (Cambridge University Press, Cambridge, 1996).

[4] S. Kershaw, *Two Photon Absorption*, Chapter 7 in Characterization Techniques and Tabulations for Organic Nonlinear Optical Materials, edited by M. G. Kuzyk and C. W. Dirk (Marcel Dekker, New York, 1998).

[5] G. I. Stegeman and A. Miller, *Photonics in Switching*, in Background and Components, edited by J. E. Midwinter (Academic Press, San Diego, 1993), Vol. I.

[6] J. M. Harbold, F. O. Ilday, F. W. Wise, and B. G. Aitken, IEEE Photon. Technol. Lett. **14**, 822 (2002).

[7] J. E. Ehrlich, X. L. Wu, I. Y. S. Lee, Z. Y. Hu, H. Röckel, S. R. Marder, and J. W. Perry, Opt. Lett. **22**, 1843 (1997).

[8] G. S. He, G. C. Xu, P. N. Prasad, B. A. Reinhardt, J. C. Bhatt, R. Mckellar, and A. G. Dillard, Opt. Lett. **20**, 1930 (1995).

[9] H. Stiel, K. Teuchner, A. Paul, W. Freyer, and D. Leupold, J. Photochem. Photobiol. A **80**, 289 (1994).

[10] W. Denk, J. H. Strickler, and W. W. Webb, Science **248**, 73 (1990).

[11] L. Ventelon, S. Charier, L. Moreaux, J. Mertz, and M. Blanchard-Desce, Angew. Chem. Int. Ed. **40**, 2098 (2001).

[12] J. D. Bhawalkar, N. D. Kumar, C. F. Zhao, and P. N. Prasad, J. Clin. Laser Med. Surg. **15**, 201 (1997).

[13] D. R. Larson, W. R. Zipfel, R. M. Williams, S. W. Clark, M. P. Bruchez, F. W. Wise, and W. W. Webb, Science **300**, 1434 (2003).

[14] S. Kawata, H.-B. Sun, T. Tanaka, and K. Takada, Nature **412**, 697 (2001).

[15] D. A. Parthenopoulos and P. M. Rentzepis, Science **245**, 843 (1989).

[16] J. H. Strickler and W. W. Webb, Opt. Lett. **16**, 1780 (1991).

[17] B. H. Cumpston, S. P. Ananthavel, S. Barlow, D. L. Dyer, J. E. Ehrlich, L. L. Erskine, A. A. Heikal, S. M. Kuebler, I.-Y. S. Lee, D. McCord-Maughon, J. Qin, H. Röckel, M. Rumi, X.-L. Wu, S. R. Marder, and J. W. Perry, Nature **398**, 51 (1999).

[18] G. S. He, J. D. Bhawalkar, C. F. Zhao, and P. N. Prasad, Appl. Phys. Lett. **67**, 2433 (1995).

[19] A. Mukherjee, Appl. Phys. Lett. **62**, 3423 (1993).

[20] A. Abbotto, L. Beverina, R. Bozio, S. Bradamante, C. Ferrante, G. A. Pagani, and R. Signorini, Adv. Mater. **12**, 1963 (2000).

[21] A. A. Said, C. Wamsley, D. J. Hagan, E. W. Van Stryland, B. A. Reinhardt, P. Roderer, and A. G. Dillard, Chem. Phys. Lett. **228**, 646 (1994).

[22] http://www.polymer.kth.se/ytbehandling/ROBERT.HTM

[23] L. W. Tutt and A. Kost, Nature **356**, 225 (1992).

[24] G. A. Blab, P. H. M. Lommerse, L. Cognet, G. S. Harms, and T. Schmidt, Chem. Phys. Lett. **350**, 71 (2001).

[25] B. W. Henderson and T. J. Dougherty, Photochem. Photobiol. **55**, 145 (1992).

[26] W. Kaiser and C. G. B. Garrett, Phys. Rev. Lett. **7**, 229 (1961).

[27] E. J. Cantosaid, D. J. Hagan, J. Young, and E. W. Van Stryland, IEEE J. Quant. Elect. **27**, 2274 (1991).

[28] B. L. Justus, R. J. Tonucci, and A. D. Berry, Appl. Phys. Lett. **61**, 3151 (1992).

[29] F. R. Laughton, J. H. Marsh, D. A. Barrow, and E. L. Portnoi, IEEE J. Quant. Elect. **30**, 838 (1994).

[30] A. Goehlich, T. Kawetzki, and H. F. Dobele, J. Chem. Phys. **108**, 9362 (1998).

[31] D. Descamps, L. Roos, C. Delfin, A. L'Huillier, and C. G. Wahlstrom, Phys. Rev. A **6403** (2001).

[32] W. G. Lawrence and V. A. Apkarian, J. Chem. Phys. **97**, 6199 (1992).

[33] T. D. Krauss and F. W. Wise, Appl. Phys. Lett. **65**, 1739 (1994).

[34] K. S. Bindra, R. Chari, V. Shukla, A. Singh, S. Ida, and S. M. Oak, J. Opt. A. **1**, 73 (1999).

[35] J. N. Chroinin, A. Dragomir, J. G. McInerney, and D. N. Nikogosyan, Opt. Commun. **187**, 185 (2001).

[36] K. Tanaka, Appl. Phys. Lett. **80**, 177 (2002).

[37] P. N. Prasad and D. J. Williams, Introduction to Nonlinear Optical Effects In Molecules & Polymers (Wiley Interscience, New York, 1991).

[38] C. Bubeck, *Nonlinear Optical Properties of Oligomers*, in Electronic Materials-The Oligomer Approach, edited by K. Müllen and G. Wegner (Wiley-VCH, Veinheim, 1998), Chapter 8.

[39] S. Polyakov, F. Yoshino, M. Liu, and G. Stegeman, Phys. Rev. B. **69** (2004).

[40] E. Zojer, D. Beljonne, T. Kogej, H. Vogel, S. R. Marder, J. W. Perry, and J. L. Brédas, J. Chem. Phys. **116**, 3646 (2002).

[41] T. Kogej, D. Beljonne, F. Meyers, J. W. Perry, S. R. Marder, and J. L. Brédas, Chem. Phys. Lett. **298**, 1 (1998).

[42] P. N. Butcher and D. Cotter, *The Elements of Nonlinear Optics* (Cambridge University Press, Cambridge, 1990).

[43] M. Göppert-Mayer, Annalen Der Physik **9**, 273 (1931).

[44] B. J. Orr and J. F. Ward, Mol. Phys. **20**, 513 (1971).

[45] R. R. Birge and B. M. Pierce, J. Chem. Phys. **70**, 165 (1979).

[46] D. Beljonne, W. Wenseleers, E. Zojer, Z. G. Shuai, H. Vogel, S. J. K. Pond, J. W. Perry, S. R. Marder, and J. L. Brédas, Adv. Funct. Mater. **12**, 631 (2002).

[47] P. Norman, Y. Luo, and H. Ågren, Chem. Phys. Lett. **296**, 8 (1998).

[48] M. Barzoukas and M. Blanchard-Desce, J. Chem. Phys. **113**, 3951 (2000).

[49] M. Drobizhev, A. Karotki, A. Rebane, and C. W. Spangler, Opt. Lett. **26**, 1081 (2001).

[50] M. Albota, D. Beljonne, J. L. Brédas, J. E. Ehrlich, J. Y. Fu, A. A. Heikal, S. E. Hess, T. Kogej, M. D. Levin, S. R. Marder, D. McCord-Maughon, J. W. Perry, H. Röckel, M. Rumi, C. Subramaniam, W. W. Webb, X. L. Wu, and C. Xu, Science **281**, 1653 (1998).

[51] C. K. Wang, P. Macak, Y. Luo, and H. Ågren, J. Chem. Phys. **114**, 9813 (2001).

[52] A. M. Masunov and S. Tretiak, J. Phys. Chem. B. **108**, 899 (2004).

[53] B. Strehmel, A. M. Sarker, and H. Detert, ChemPhysChem **4**, 249 (2003).

[54] K. Kamada, K. Ohta, I. Yoichiro, and K. Kondo, Chem. Phys. Lett. **372**, 386 (2003).

[55] N. Pfeffer, P. Raimond, F. Charra, and J. M. Nunzi, Chem. Phys. Lett. **201**, 357 (1993).

[56] R. Kishi, M. Nakano, S. Yamada, K. Kamada, K. Ohta, T. Nitta, and K. Yamaguchi, Chem. Phys. Lett. **393**, 437 (2004).

[57] E. Zojer, D. Beljonne, P. Pacher, and J. L. Brédas, Chem. Eur. J. **10**, 2668 (2004).

[58] P. Cronstrand, Y. Luo, and H. Ågren, Chem. Phys. Lett. **352**, 262 (2002).

[59] M. Drobizhev, Y. Stepanenko, Y. Dzenis, A. Karotki, A. Rebane, P. N. Taylor, and H. L. Anderson, J. Am. Chem. Soc. **126**, 15352 (2004).

[60] B. A. Reinhardt, L. L. Brott, S. J. Clarson, A. G. Dillard, J. C. Bhatt, R. Kannan, L. Yuan, G. S. He, and P. N. Prasad, Chem. Mater. **10**, 1863 (1998).

[61] O.-K. Kim, K.-S. Lee, H. Y. Woo, K.-S. Kim, G. S. He, J. Swiatkiewicz, and P. N. Prasad, Chem. Mater. **12**, 284 (2000).

[61] L. Antonov, K. Kamada, K. Ohta, and F. S. Kamounah, Phys. Chem. Chem. Phys. **5**, 1193 (2003).

[63] P. Feneyrou, O. Doclot, D. Block, P. L. Baldeck, S. Delysse, and J. M. Nunzi, Opt. Lett. **22**, 1132 (1997).

[64] E. Zojer, W. Wenseleers, P. Pacher, S. Barlow, M. Halik, C. Grasso, J. W. Perry, S. R. Marder, and J. L. Brédas, J. Phys. Chem. B. **108**, 8641 (2004).

[65] M. Rumi, J. E. Ehrlich, A. A. Heikal, J. W. Perry, S. Barlow, Z. Hu, D. McCord-Maughon, T. C. Parker, H. Röckel, S. Thayumanavan, S. R. Marder, D. Beljonne, and J. L. Brédas, J. Am. Chem. Soc. **122**, 9500 (2000).

[66] L. Porres, C. Katan, O. Mongin, T. Pons, J. Mertz, and M. Blanchard-Desce, J. Mol. Struct. **704**, 17 (2004).

[67] B. R. Cho, M. J. Piao, K. H. Son, S. H. Lee, S. J. Yoon, S.-J. Jeon, and M. H. Cho, Chem. Eur. J. **8**, 3907 (2002).

[68] O. S. Pyun, W. J. Yang, M. Y. Jeong, S. H. Lee, K. M. Kang, S.-J. Jeon, and B. R. Cho, Tetrahedron Lett. **44**, 5179 (2003).

[69] W. H. Lee, H. Lee, J. A. Kim, J. H. Choi, M. H. Cho, S.-J. Jeon, and B. R. Cho, J. Am. Chem. Soc. **123**, 10658 (2001).

[70] S. Mazumdar, S. Dallakyan, and M. Chandross, Synth. Met. **139**, 769 (2003).

[71] S.-J. Chung, K.-S. Kim, T.-H. Lin, G. S. He, J. Swiatkiewicz, and P. N. Prasad, J. Phys. Chem. B. **103**, 10741 (1999).

[72] M. Y. Lavrentiev, W. Barford, S. J. Martin, H. Daly, and R. J. Bursill, Phys. Rev. B. **59**, 9987 (1999).

[73] H. Le Bozec, T. Le Bouder, O. Maury, A. Bondon, I. Ledoux, S. Deveau, and J. Zyss, Adv. Mater. **13**, 1677 (2001).

[74] J. Zyss, J. Chem. Phys. **98**, 6583 (1993).

[75] J. Zyss and I. Ledoux, Chem. Rev. **94**, 77 (1994).

[76] W. Bartkowiak, R. Zalesny, and J. Leszczynski, Chem. Phys. **287**, 103 (2003).

[77] F. Meyers, S. R. Marder, B. M. Pierce, and J. L. Brédas, J. Am. Chem. Soc. **116**, 10703 (1994).

[78] A. D. Slepkov, F. A. Hegmann, S. Eisler, E. Elliott, and R. R. Tykwinski, J. Chem. Phys. **120**, 6807 (2004).

[79] K. D. Belfield, K. J. Schafer, Y. U. Liu, J. Liu, X. B. Ren, and E. W. Van Stryland, J. Phys. Org. Chem. **13**, 837 (2000).

[80] P. Najechalski, Y. Morel, O. Stephan, and P. L. Baldeck, Chem. Phys. Lett. **343**, 44 (2001).

[81] S. R. Marder, J. W. Perry, B. G. Tiemann, C. B. Gorman, S. Gilmour, S. L. Biddle, and G. Bourhill, J. Am. Chem. Soc. **115**, 2524 (1993).

[82] S. R. Marder, J. W. Perry, G. Bourhill, C. B. Gorman, B. G. Tiemann, and K. Mansour, Science **261**, 186 (1993).

[83] S. R. Marder, L. T. Cheng, B. G. Tiemann, A. C. Friedli, M. Blancharddesce, J. W. Perry, and J. Skindhoj, Science **263**, 511 (1994).

[84] M. Blanchard-Desce, V. Alain, P. V. Bedworth, S. R. Marder, A. Fort, C. Runser, M. Barzoukas, S. Lebus, and R. Wortmann, Chem. Eur. J. **3**, 1091 (1997).

[85] H.-S. Kim, M. H. Cho, and S.-J. Jeon, J. Chem. Phys. **107**, 1936 (1997).

[86] R. R. Tykwinski, U. Gubler, R. E. Martin, F. Diederich, C. Bosshard, and P. Günter, J. Phys. Chem. B. **102**, 4451 (1998).

[87] Note: whereas the second-hyperpolarizability peaks at some finite BLA, at a BLA of zero, it is negative, but overall largest in magnitude. The TPA response is similar in shape to that of the second-hyperpolarizability, but does not go negative. Its magnitude is largest for some finite BLA.

[88] J. P. Hermann and J. Ducuing, Phys. Rev. A **5**, 2557 (1972).

[89] C. Xu and W. W. Webb, J. Opt. Soc. Am. B. **13**, 481 (1996).

[90] M. Sheikbahae, A. A. Said, T. H. Wei, D. J. Hagan, and E. W. Van Stryland, IEEE J. Quant. Elect. **26**, 760 (1990).

[91] P. B. Chapple, J. Staromlynska, J. A. Hermann, T. J. McKay, and R. G. McDuff, J. Nonlinear Opt. Phys. Mater. **6**, 251 (1997).

[92] B. Lawrence, W. E. Torruellas, M. Cha, M. L. Sundheimer, G. I. Stegeman, J. Meth, S. Etemad, and G. Baker, Phys. Rev. Lett. **73**, 597 (1994).

[93] Z. G. Soos, D. S. Galvao, and S. Etemad, Adv. Mater. **6**, 280 (1994).

[94] K. Kamada, K. Matsunaga, A. Yoshino, and K. Ohta, J. Opt. Soc. Am. B. **20**, 529 (2003).

[95] I. Kang, T. Krauss, and F. Wise, Opt. Lett. **22**, 1077 (1997).

[96] Y. Pang, M. Samoc, and P. N. Prasad, J. Chem. Phys. **94**, 5282 (1991).

[97] R. A. Negres, J. M. Hales, D. J. Hagan, and E. W. Van Stryland, IEEE J. Quant. Elect. **38**, 1205 (2002).

[98] V. I. Klimov and D. W. McBranch, Opt. Lett. **23**, 277 (1998).

[99] Y. Zhao, Y. Shirai, A. D. Slepkov, L. Cheng, L. B. Alemany, T. Sasaki, F. A. Hegmann, and J. M. Tour, Chem. Eur. J. **11**, 3643 (2005).

CHAPTER 2:

DIFFERENTIAL OPTICAL KERR EFFECT (DOKE) FOR THE CHARACTERIZATION OF NONLINEAR ABSORPTION DYNAMICS

2.1 Introduction

As outlined in the previous chapter, the characterization of both the real and imaginary contributions to a material's complex third-order optical nonlinearities is advantageous. The real component of the third-order susceptibility gives rise to induced birefringence, and thus can be used for light-modulation. The ultimate goal of such applications is all optical switching, which will require highly nonlinear materials with ultrafast responses on a femtosecond time scale.[1] Applications that require high $Re(\chi^{(3)})$ typically demand near-complete transparency and thus also require the condition of negligible $Im(\chi^{(3)})$. This is the primary reason that the study of the complete $\chi^{(3)}$ response of a sample has been important in the past. In recent years, however, attenuative nonlinearities such as two-photon absorption have leaped to the forefront of photonics research as the primary mechanisms for a variety of technological applications, as discussed in the previous chapter. Thus, the ability to study both the real and imaginary components of the third-order nonlinearities in a sample is an advantage to any experimental technique. Many popular techniques, such as third-harmonic generation (THG) and two-photon excitation fluorescence (TPEF), only access either the real or imaginary component of the optical nonlinearity.[2] Other popular techniques, such as z-scan,[3] which do obtain both components, provide very little information about the temporal dynamics of the optical nonlinearity. Pump-probe experiments, such as the various optical Kerr gate schemes, on the other hand, can be used to study the ultrafast time-resolved response of both the real and imaginary components of $\chi^{(3)}$.[4-7]

2.2 Differential Optical Kerr Effect Detection

The Optical Kerr Gate: In essence, the optical Kerr effect (OKE) describes an optically-induced birefringence. Specifically, polarized light interacts with a medium to modify the index of refraction parallel and perpendicular to the axis of polarization. In a standard homodyne Kerr gate,[4,8-11] an intense, linearly polarized pump pulse induces a birefringence in an isotropic medium. The anisotropy in the index of refraction, $\Delta n = \Delta n_{//} - \Delta n_{\perp}$, induced by the pump pulse can be sampled by a weaker probe pulse that is linearly polarized, for maximum effect, at 45° to the pump polarization. The induced birefringence, Δn, results in a complex phase-retardation in the probe beam that is given by $\phi = \phi' + i\phi''$. The real component of this phase delay, ϕ', represent the Optical Kerr effect, while the imaginary component, ϕ'', manifests as nonlinear absorption (two-photon absorption, for example). In this technique, the absence of Kerr rotation in the sample leads to a null signal on a photodiode placed after the analyzer. On the other hand, rotated probe polarization components will pass through the Kerr gate and provide a photodiode signal. Furthermore, the arrival time of the probe beam may be varied with respect to that of pump pulse, yielding a temporal profile of the induced birefringence. When the pump pulse arrives well before the probe pulse, there is no induced birefringence and no probe light passes through crossed polarizers. Since this detection scheme operates with crossed polarizers, the detected signal is proportional to the square of the pump intensity.[12] As a drawback, a homodyne Kerr gate is unable to separate the real and imaginary components of $\chi^{(3)}$. Furthermore, working about a zero light background means that any unwanted scatter or leakage through the analyzer may be of the same order as the Kerr signal.

In an attempt to separate the real and imaginary components of $\chi^{(3)}$ and to obtain signals that are much larger than the ambient scatter noise, another detection scheme—optical heterodyne detection (OHD-OKE)—is used by the vast majority of optical Kerr effect researchers.[12-15] In this elegant technique, a quarter-wave plate is placed between the probe polarizer and sample such that the long axis of the quarter-wave plate is parallel to the polarizer. By slightly rotating the polarizer, $\pi/2$ out-of-phase light may be added to the probe beam, and the real part of the nonlinear response may be extracted

from the Kerr signal. As an added advantage, the OHD-OKE signal is linear in pump intensity.[12]

We have developed a modified detection scheme that in addition to maintaining the aforementioned attributes of OHD-OKE has simplicity of both analysis and detection as well as robustness of signal as attractive advantages. Furthermore, it provides a larger dynamic range of signal linearity.[5] Our differential optical Kerr effect (DOKE) detection utilizes both the quarter-wave plate and analyzer differently than OHD-OKE. Furthermore, analysis of the complete probe beam with the use of differential detectors establishes DOKE detection as a unique Kerr gate arrangement. DOKE detection is, however, similar to various optical biasing schemes routinely used in free-space electro-optic sampling of THz pulses.[16,17]

Differential Optical Kerr Effect (DOKE): Our Kerr gate, illustrated in Fig. 2.1, is laid out as follows: A multi-pass Ti:sapphire laser amplifier outputs 800 nm, 100 fs, 650 μJ pulses at a repetition rate of 1080 Hz. The beam is split into pump and probe beams, with the beamsplitter providing a 10:1 pump:probe energy ratio. The probe pulse is time-delayed with respect to the pump pulse by a computer controlled retro-reflector delay stage along the probe arm, with 0.7 fs step resolution. The pump pulse is chopped by a 50% duty cycle chopper (CH) at ¼ of the repetition rate (270Hz). Using a half-wave plate, the pump pulse is polarized 45° to the horizontal and is focused onto a 1 mm path-length quartz cuvette that is filled with a sample solution (S). Attenuation control is present for both beams. At the sample, we typically use 0.043 μJ and 0.5-2 μJ pulses for the probe and pump beams, respectively. The weaker probe beam is polarized vertically and then passes through a quarter-wave plate ($\lambda/4$) to produce circularly-polarized probe light. The probe light is focused to overlap in the sample with the near-collinear pump beam ($\theta<5°$). The probe beam is focused more tightly than the pump beam to ensure uniform pump intensity over the probe beam area. Typical spot diameters (and incident powers) at the sample are ~250 μm (approx. 0.8 GW/cm^2) and ~490 μm (approx. 2.5-10 GW/cm^2) for the probe and pump beams, respectively. The pump beam is blocked after the sample, while the probe light is allowed to travel to a Wollaston polarizer acting as the analyzer. Here, the two polarization-separated transmitted beams are directed to

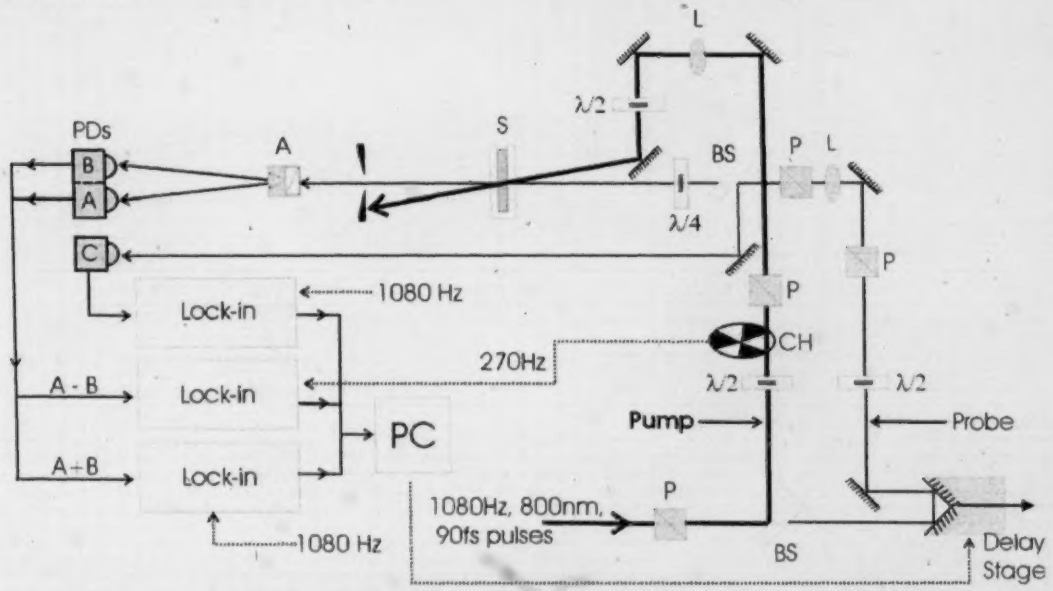

Figure 2.1: A schematic of our DOKE experimental layout: PDs A & B: Balanced photodiodes; PD C: reference photodiode; BS: 10:1 beam splitter; λ/4: quarter-wave plate; λ/2: half-wave plate; P: Glan-laser polarizer; A: Wollaston polarizer acting as an analyzer; L: lens (f = 40 cm); CH: chopper operating at 270 Hz; PC: computer; S: 1-mm path length quartz cuvette sample holder.

balanced photodiodes (BPD). Photodiode *A* receives the horizontally polarized beam, and photodiode *B* receives the vertically polarized beam. The sum and difference (*A+B* and *A-B*, respectively) of these signals are sent to separate lock-in amplifiers. The *A-B* signal is detected at the chopped pump frequency, and *A+B* is detected at the laser repetition rate frequency. Finally, these signals are sent to a data acquisition board en-route to a personal computer (PC) used for analysis and delay-stage control.

As outlined previously,[5] the key features of the DOKE setup are that *A-B* detection acts as our Kerr effect signal, while in the absence of nonlinear absorption, *A+B* acts as a probe beam reference. In the presence of nonlinear absorption, *A+B* acts as a direct and independent detection of such processes. The photodiodes are calibrated so that in the absence of any birefringence, *A* and *B* signals are equal and *A-B* gives a zero background signal.[18] The real and imaginary components of the sample nonlinearity are obtained with the sequential implementation of two polarization conditions:[5] By setting the

pump polarization either vertical or horizontal (that is, orthogonal to the pre-$\lambda/4$ probe polarization) the dichroic response may be directly obtained. In this case, (known as the *"dichroic DOKE polarization condition"*) the ratio of *A-B* to *A+B* provides us with the imaginary nonlinear phase-shift, ϕ'', which is directly proportional to both the third-order susceptibility, $\mathrm{Im}(\chi^{(3)})$, and the two-photon cross section $\sigma^{(2)}$:[2,5]

$$\frac{A-B}{A+B} = \tanh\phi'', \tag{2.1}$$

$$\phi'' = \frac{3\pi l}{2\varepsilon_0 c\lambda n_0^2} I_{pump}\,\mathrm{Im}\left[\chi^{(3)}\right] = \frac{N_c l}{\hbar\omega}\sigma^{(2)} I_{pump}, \tag{2.2}$$

where l is the cuvette path length, ε_0 is the permittivity of free space, n_0 is the linear index of refraction, c is the speed of light, λ is the probe wavelength, I_{pump} is the pump intensity, N_c is the sample number-concentration, ω is the probe frequency, and $\sigma^{(2)}$ is the two-photon cross-section. Typically, ϕ'' is kept below 0.08 (8 % modulation) and $\tanh\phi'' \approx \phi''$.

Subsequently, by setting the pump polarization at 45° to the vertical, the induced birefringence (Kerr) signal is obtained, and the real component of the nonlinearity may be extracted. In this case (referred to as the *birefringent DOKE polarization condition*), the ratio of *A-B* to *A+B* provides us with a convolution of the real (ϕ') and imaginary (ϕ'') nonlinear phase shift:[5]

$$\frac{A-B}{A+B} = \frac{\sin\phi'}{\cosh\phi''}, \tag{2.3}$$

$$\phi' = \frac{3\pi l}{2\varepsilon_0 c\lambda n_0^2} I_{pump}\,\mathrm{Re}\left[\chi^{(3)}\right], \tag{2.4}$$

And for a dilute sample (solute) in a solvent matrix, the rotationally-averaged molecular second-hyperpolarizability, $\langle\gamma\rangle$, is directly related to the third-order susceptibility by [5]

$$\chi^{(3)} = L^4\left(N_{c(solute)} < \gamma_{solute} >\right) + \chi^{(3)}_{solvent}, \qquad 2.5$$

where $L = (n_0^2+2)/3$ is the Lorentz field factor, which accounts for dielectric modifications to the optical field in microscopic environments.[19]

Thus, by iteration of the birefringent and dichroic polarization conditions, we can separate the real and imaginary nonlinear components. Unlike some other Kerr-gate arrangements, DOKE signals are linear with pump beam intensity, and remain so for a large dynamic range, allowing for simplified analysis. Nonetheless, we typically keep ϕ' to less than 0.15 radians.

As demonstrated above, absolute $\sigma^{(2)}$ and γ values may be obtained with DOKE detection. To effect this, detailed knowledge of laser pulse and focusing parameters are needed. These include the temporal beam profile and the spatial beam parameters at the sample location. In practice, the use of a calibrated reference sample allows relative γ and $\sigma^{(2)}$ values to be obtained, and significantly simplifies the signal analysis.[19] In general, where subscripts R and S denote reference and sample, respectively, $\chi^{(3)}_S$ may be calculated from

$$\mathrm{Re}\left(\chi^{(3)}_S\right) = \mathrm{Re}\left(\chi^{(3)}_R\right)\frac{\phi'_S}{\phi'_R}\frac{l_R}{l_S}\left(\frac{n_{0_S}}{n_{0_R}}\right)^2. \qquad 2.6$$

In the case where the sample is dilute enough to leave the index of refraction unchanged and the path length is the same for the reference and sample,

$$\mathrm{Re}\left(\chi^{(3)}_S\right) = \mathrm{Re}\left(\chi^{(3)}_R\right)\frac{\phi'_S}{\phi'_R}. \qquad 2.7$$

The relative second hyperpolarizability is obtained from this and Eqn 2.5, and is given by

$$\langle \gamma_S \rangle = \langle \gamma_R \rangle \left(\frac{\phi_S'}{\phi_R'} - 1 \right). \qquad 2.8$$

We typically study samples as solutions in tetrahydrofuran (THF). Subsequently, THF is used as a reference for all γ-values studied here, with $\langle \gamma_R \rangle = \gamma_{THF} = 5.2 \times 10^{-37} esu$.[18]

Calculating TPA coefficients is somewhat more complicated. The solvent does not generally display any nonlinear absorption, and thus, an external reference must be used. Unfortunately, there is no common or well-established standard for pump-probe TPA measurements; a different standard/reference is used by each group. Once a reference sample is characterized, however, one may easily calibrate TPA signals to this standard according to

$$\alpha_S^{(2)} = \frac{\phi_S''}{\phi_R''} \alpha_R^{(2)} \qquad 2.9$$

and

$$\sigma_S^{(2)} = \frac{\phi_S''}{\phi_R''} \frac{Nc_R}{Nc_S} \sigma_R^{(2)}. \qquad 2.10$$

THF displays no two-photon absorption at 800 nm, and it is thus only used as a null control for the dichroic polarization condition. Instead, we use a 3.0 mM sample of **MPPBT** in dimethyl sulfoxide (DMSO) as a nonlinear absorption reference. **MPPBT** shows strong TPA across the entire vis-nearIR range, and displays great optical and environmental stability. Furthermore, it has been well-characterized by z-scan measurements and is thus a good choice for a reference material.[21] For 800 nm DOKE measurements we use $\sigma^{(2)}_{MPPBT}$=390 GM.[21] The chemical structure of **MPPBT** is shown in Fig 1.2.

2.3 Proof of Principle and Characterization of the DOKE Technique

We have previously demonstrated our abilities to obtain absolute γ values with DOKE that compare well with those reported in the literature.[5,20] In that work, we also outlined the possibility of using DOKE for the quantitative study of nonlinear absorption (NLA) processes. Here, we present the realization of that potential, and detail the use of DOKE detection to the characterization of two-photon absorption and excited-state absorption dynamics. Raw, time-resolved DOKE scans in both polarization conditions are presented in Appendix C.

Two-Photon Absorption and Excited-State Absorption as Detected by DOKE: Because DOKE detection monitors the probe beam at the pump modulation frequency, it is only sensitive to pump-induced changes in the probe. Subsequently, there are typically two different types of NLA processes measured by DOKE, as shown in Fig. 2.2: Two-photon absorption is an instantaneous process and is detected when one photon from each of the pump and probe beams is simultaneously absorbed. This signal manifests itself as a cross-correlation of the two pulses, centred at zero probe delay time. Furthermore, as the pump beam is strong enough to induce TPA transitions in the absence of the probe beam, subsequent long-lasting probe absorption signals are detected due to two-photon accessed excited-state absorption (ESA).[22] ESA is an important process, the detection of which makes the DOKE technique very useful for the characterization of ultrafast nonlinear absorption dynamics. Figure 2.3 displays long DOKE scans in the dichroic polarization condition for a 3.0 mM sample of **MPPBT** in DMSO that displays considerable excited-state absorption. **MPPBT** displays an ESA exponential decay rate of approximately 30±2 ps, and although the ESA signal is essentially gone by 120 ps, the weight of the ESA signal is large with respect to that of the pure TPA. Other techniques such as z-scan or single-beam attenuation, that measure nonlinear absorption with nanosecond or

picosecond pulses would, therefore, considerably overestimate $\sigma^{(2)}$ from TPA. Thus, studies conducted with ns pulses have often found cross-sections that are up to four orders of magnitude higher than those measured with ultrafast (fs) pulses.[21,23] ESA is not solely a parasitic signal. The nonlinear absorption dynamics may contain information about the dynamics of both the populating and de-populating of the state from which ESA occurs, and thus can provide important information regarding the energetics of the excited state in TPA molecules. The most direct way to confirm that the TPA and ESA responses illustrated in Fig. 2.3 are correctly attributed to the phenomena described in Fig. 2.2 is with power-dependence studies. Inspection of the TPA process shown in Fig. 2.2 shows that the response should scale linearly with both pump and probe powers. Furthermore, the two-photon-accessed excited-state absorption signal should scale with the pump power as I^2_{pump}. These relationships are shown in Figs. 2.4 and 2.5. Figure 2.4 shows that **MPPBT** presents a strictly linear relationship with pump power on the TPA peak; maintaining linearity throughout the range of pump powers we typically use in DOKE experiments. Figure 2.5 shows that **MPPBT** displays a square-dependence of the pump power at a probe delay time of 5 ps. This square dependence is maintained throughout the typical pump powers used in DOKE experiments, but shows behaviour that deviates towards a lower power-dependence at higher pump powers. As mentioned, ESA dynamics in **MPPBT** show bi-exponential decay; with a fast component of ~2.7 ps (see Fig. 2.3). Thus, it is possible that at higher excitation powers, signal from this response is mixing with that of the longer decay time to give deviations from a strictly-quadratic dependence.

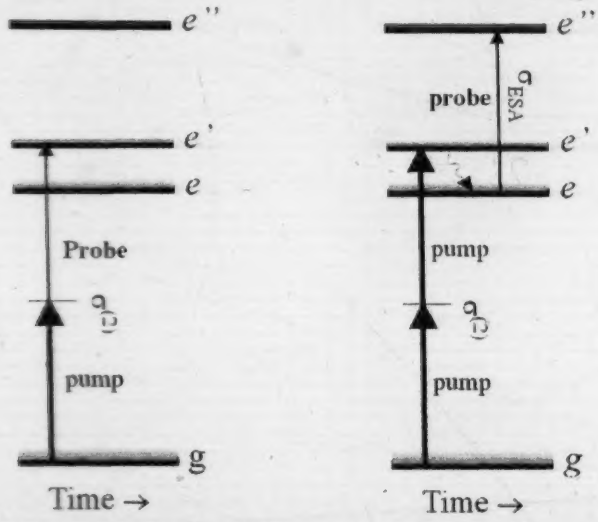

Figure 2.2: Two-photon absorption (TPA) and excited-state absorption (ESA) processes to which DOKE detection is sensitive. DOKE monitors pump-induced absorption in the probe beam, and is thus only sensitive to changes in the probe beam. TPA is measured as an instantaneous response, and ESA is measured at longer probe delay times.

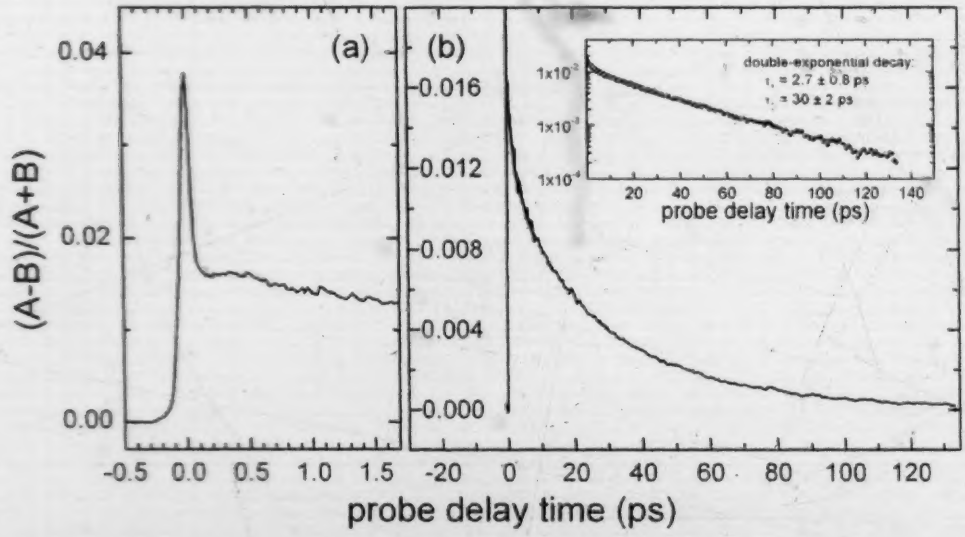

Figure 2.3: Nonlinear absorption dynamics in an **MPPBT** sample. (a) At a probe delay time of 0 ps, an instantaneous TPA signal is seen that follows the cross correlation of the pump and probe pulses. (b) At later times, considerable excited-state absorption is seen, displaying a bi-exponential decay with a prominent and well-resolved 30 ps decay time (inset). A similar decay rate of 40 ps is confirmed by time-resolved fluorescence measurements.[24] Solid line in inset is a bi-exponential fit, with the obtained parameters reported on the plot.

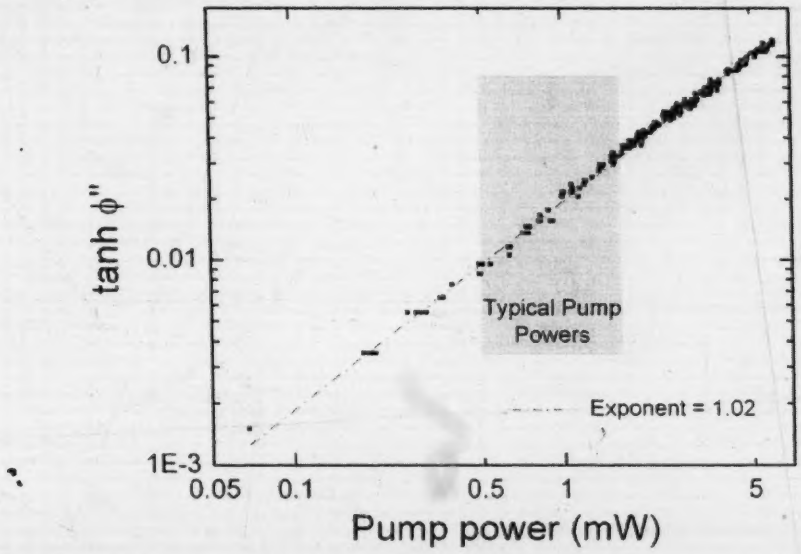

Figure 2.4: On-peak (probe delay time of 0 ps) nonlinear absorption DOKE response in **MPPBT**. A linear dependence with pump power is an indication of a pure two-photon absorption process. The typical pump powers used for DOKE experiments are well within this linear range, as shown. Dashed line is a line of best fit to a power-law function.

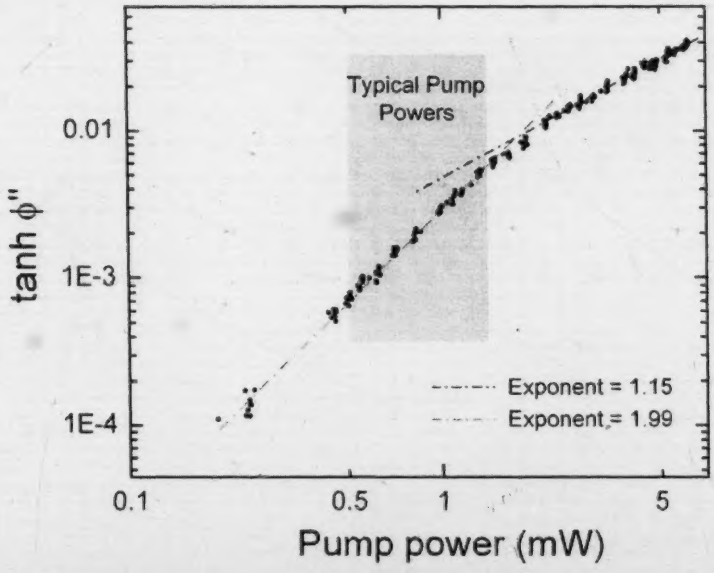

Figure 2.5: Pump-dependent nonlinear absorption DOKE response from MPPBT at a probe delay time of 5 ps. A square dependence with pump power is indication of a pure two-photon accessed single-excited-state absorption. The typical pump powers used for DOKE experiments are well within this range, as shown. Dashed lines are fits to a power-law function. They have been drawn to extend past their fitting ranges for improved visibility.

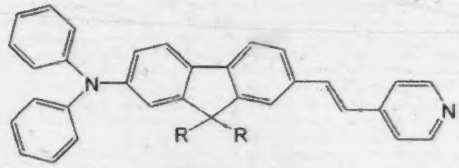

AF60: R=C_2H_5
AF50: R=$C_{10}H_{21}$

Figure 2.6: Chemical structure of TPA reference samples **AF60** and **AF50**. The two species differ by the length of the pendant alkyl side chains off the fluorene center.

Obtaining Absolute $\sigma^{(2)}$ Values as Proof of Principle: We have obtained/synthesized two samples for which the nonlinear absorption characteristics at 800 nm have been reported by other groups. We have subsequently characterized their nonlinearities with the DOKE layout for comparison and their future use as reference samples. The TPA spectrum of **MPPBT** has been extensively studied by Kamada *et al.* with the ultrafast z-scan technique,[21] and we currently use this sample as a TPA standard for all experiments.[25,26] We synthesized **AF60** for the sole purpose of obtaining a secondary calibration of our DOKE analysis. The two-photon absorption response at 800 nm of the AF-X series of molecules has been widely reported by Prasad *et al.*, whom typically use **AF50** as a TPA standard.[23,27,28] As shown in Fig. 2.6, **AF50** and **AF60** have virtually the same structure, and have been shown to have $\sigma^{(2)}$ values that differ by less than 20% when measured by ns pulses,[27] and would be expected to have even closer cross-sections when measured by fs pulses where contribution from excited state absorption can be eliminated. Figure 2.7 presents the raw DOKE signals from **AF60**, **MPPBT**, and their respective solvents of THF and DMSO. From these scans it is evident that THF and DMSO lack measurable resonant TPA at 800nm, while their traces, shown in the figure inset, follow the typical dispersive lineshape of coherent coupling.[29] On the other hand, **MPPBT** and **AF60** both display sizable nonlinear absorption, and provide both two-photon absorption and excited-state absorption signals. The TPA cross-section may be obtained from the peak values in Fig 2.7 together with Eqns. 2.1 and 2.2. We find absolute values of $\sigma^{(2)}$=390±60 GM for **MPPBT** and $\sigma^{(2)}$=60±10 GM for **AF60**. Our DOKE derived **MPPBT** value is in excellent agreement with the literature value of $\sigma^{(2)}$ = 380±40 GM for **MPPBT** in DMSO [1.6 mM] measured with the z-scan method (126 fs,

802 nm, 1kHz pulses).[21] The DOKE-derived **AF60** results are also in excellent agreement with $\sigma^{(2)} = 63\pm11$ GM, as measured by z-scan under the same conditions.[30] Furthermore, comparisons can be made between the DOKE-derived TPA cross-section of **AF60** and that of **AF50** as studied by Kim *et al.*[23] **AF60** differs from **AF50** only in length of alkyl side chains (Fig. 2.6). The reported value of **AF50** in benzene ($\sigma^{(2)}$= 30×10^{-50} GM) measured with femtosecond pulses by the same group is the same order of our value for **AF60** in THF.[23] Furthermore, in subsequent studies, **AF50** exhibited very similar time-resolved beam attenuation behaviour in their ultrafast transient absorption measurements as are present in our $A+B$ signals featured in Fig. 2.8.[28] Figure 2.8 shows the separate $A+B$ and $A-B$ signals from **AF60**: In many ways, $A+B$ measured at the probe repetition rate represents a standard transient absorption measurement, and gives a rough guideline to the nonlinear absorption (NLA) dynamics in the samples. $A-B$ measured at the pump repetition rate presents the dichroic signal, and provides increased signal relative to noise, as can be seen from a comparison of $A+B$ signals in Fig.

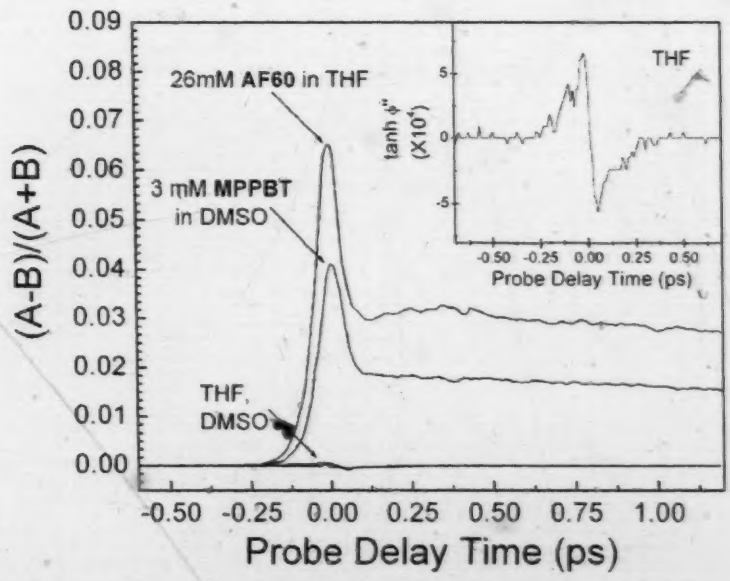

Figure 2.7: Time resolved nonlinear absorption signals of **AF60**, and **MPPBT**, and of their respective solvents, obtained using the dichroic polarization condition. The inset shows the signal from the THF solvent. Each trace represents an average of three scans.

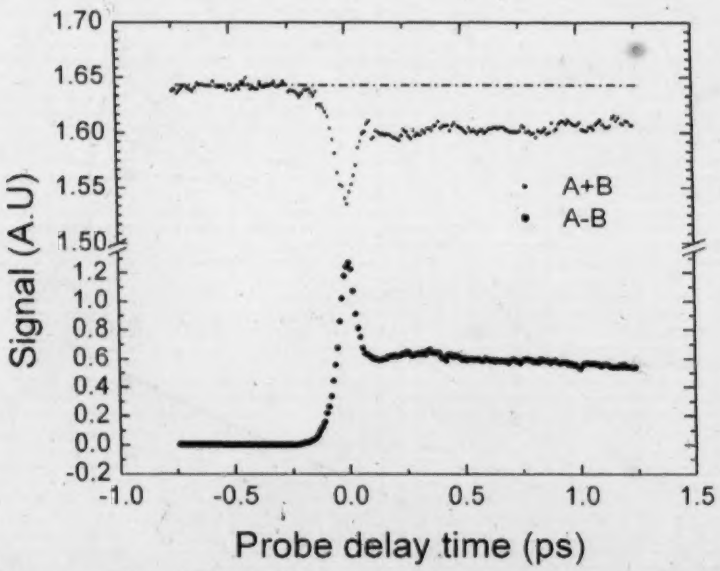

Figure 2.8: Raw scans in the dichroic DOKE condition for **AF60**, showing A-B and A+B signals. Both signals show peaks at zero probe delay time, reflecting instantaneous TPA, as well as time-delayed tails suggesting Pump-induced excited state absorption. Both signals can be used to obtain $\sigma^{(2)}$ values. The dashed line establishes a baseline for the A+B signal.

2.8, *A-B* signals in Fig. 2.8, and the *(A-B)/(A+B)* signals from Fig 2.3. The combination of the two signals gives the *(A-B)/(A+B)* analysis of the DOKE technique. As mentioned in the previous section, the *A+B* signal provides an independent measurement of $\sigma^{(2)}$ through simple beam attenuation analysis. From the signals in Fig 2.8, the *A+B* response estimates a value of $\sigma^{(2)}$=70±20 GM, in agreement with the more precise DOKE analysis. A further comparison of the quantitative values obtained with DOKE detection and the single-beam transmission method is presented in Chapter 3.

Nonlinear Dichroism vs. Nonlinear Absorption: The complete treatment of nonlinear absorption in conjugated molecules must take into account the full polarization relationship of the pump and probe beams. The relative angle of polarization between the pump and probe determines the strength of the various dipole and transition dipole moments, as outlined by Birge and Pierce in 1979.[31] In that study, Birge and Pierce

looked at TPA that is degenerate in energy (but not in polarization) in conjugated polyenes, and found that the relative polarization of the pump and probe beams influences the overall TPA cross-section. This effect directly impacts DOKE-obtained signals, as it would imply that there is a quantitative difference between signals obtained in the DOKE dichroic polarization condition, where the pump beam is linearly polarized and the probe beam is circularly polarized, and standard transient absorption conditions where both beams are linearly polarized.[31] Figure 2.9 shows transient absorption signals from a solution of tetrakis(phenylethynyl)benzene (***ortho*-TPEB**) in THF (see chapter 5 for a full description of this series of 2-dimensionally conjugated isomers). For transient absorption signals, we modified the DOKE layout by removing the quarter-wave plate from the probe arm. For improved signal-to-noise, we monitored the $A+B$ signal at the pump beam frequency of 270 Hz by lock-in detection. Since $A+B$ represents the total probe power, modulations in this signal indicate pump-induced probe depletion, and thus nonlinear absorption. As can be seen from Fig. 2.9, TPA is maximized in this sample when both pump and probe beams are polarized parallel to each other. When they are polarized perpendicular to each other, less TPA takes place—but it is still very much present. At a relative polarization angle of 45° between the pump and probe, an average of the two previous cases is obtained. The ratio of on-peak TPA in the parallel and perpendicular condition is 2.8:1 in this sample. Birge and Pierce predict a ratio of 3:1 for conjugated chromophores when the molecules are assumed in their ideal planar geometry and the dipole and transition dipole moments are aligned parallel to each other. These conditions are expected to hold true for this TPEB sample, as is discussed in Chapter 5. It is interesting to note that the ratio of the dichroic ESA signals is the same as that for TPA. The significance of this is unclear, as Birge and Pierce addressed the dichroism of instantaneous TPA only,[31] and two-photon accessed ESA is effectively a $\chi^{(5)}$ process.[32]

One way in which DOKE detection differs from standard transient absorption is in that the sample is probed with circular polarized light. Figure 2.10 compares the dichroic signals of ***ortho*-TPEB** taken with a linearly polarized pump beam and a circular-

polarized probe beam, and that in which both linearly polarized pump and probe beams are used. Attenuation of $A+B$ signal is identical for both the dichroic and birefringent DOKE polarization conditions. Furthermore, these signals are identical to the case of a 45° relative polarization between the pump and probe beams. This establishes another strong advantage to the DOKE technique: Since the dichroic signal is identical in both DOKE polarization conditions, its polarization dependence can be neglected. On the other hand, standard transient absorption experiments need careful monitoring of the relative polarization between the pump and probe beams. Again, these sentiments follow for the ESA signal as well, which is identical for both of the DOKE polarization conditions as well as for the 45° transient absorption signal, for the entirety of the long, 70 ps, scans.

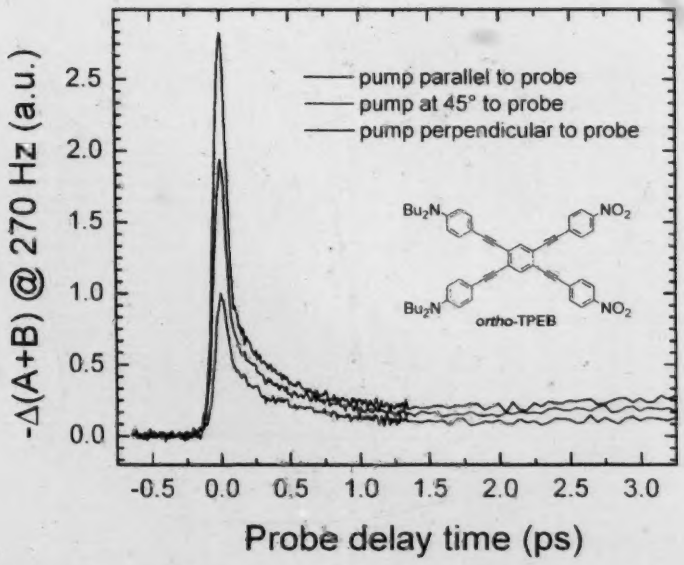

Figure 2.9: [colour] Transient absorption signals from a tetrakis(phenylethynyl)benzene (***ortho*-TPEB**) sample in THF. The strongest TPA is observed when both the pump and probe beams are parallel *in polarization*, in close agreement with the 3:1 parallel:perpendicular TPA predictions by Birge and Pierce.[31]

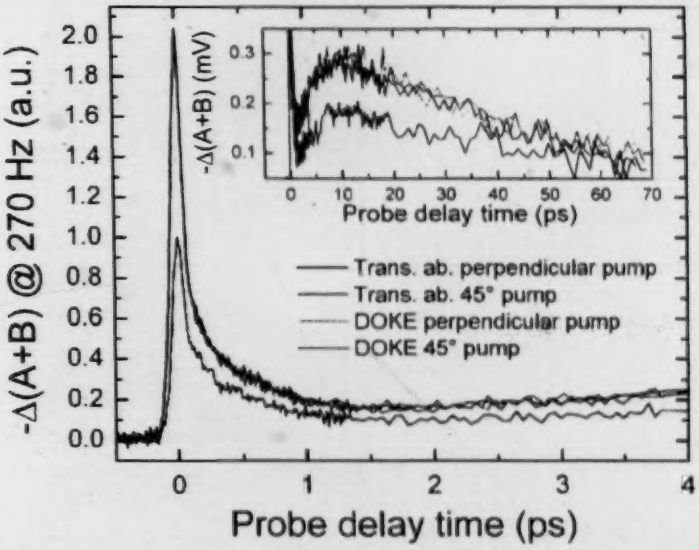

Figure 2.10: [colour] Whereas the transient absorption measurement differs depending on the pump and probe polarizations, DOKE signals are always the same as the transient absorption experiment with a relative 45° pump-probe angle. The inset shows that this stands for ESA signals as well. The sample investigated is ***ortho*-TPEB** (structure is shown in Fig. 2.9).

DOKE vs. Standard Transient Absorption Experiments: The preceding paragraphs may prompt the following question: If DOKE detection provides the same basic information as standard transient absorption experiments, what additional advantages does it possess that warrant its use? The real power behind the DOKE technique is in its ability to extract information about the dynamics of $\mathrm{Re}[\chi^{(3)}]$ in addition to $\mathrm{Im}[\chi^{(3)}]$. That is, DOKE detection can investigate polarization-dependent induced-birefringence responses in conjugated chromophores, in addition to TPA and ESA. To punctuate this point, Fig. 2.11 presents various signals from ***ortho*-TPEB**; the $A+B$ signal detected at the modulated pump frequency of 270 Hz, and representing the transient absorption signals previously shown in Fig. 2.10; the $A+B$ signal detected at 1 kHz and representing both a standard transient absorption signal and an element of DOKE detection; and $A-B$ at 270 Hz, which is the real key to DOKE detection. Furthermore, all of these signals are obtained in the birefringent DOKE condition where the pump beam is polarized at 45° to the pre-$\lambda/4$-plate probe beam. From Fig. 2.11 it can be seen that both $A+B$ signals are

basically the same in shape, and represent a purely absorptive response. The signal *A-B*, on the other hand, appears completely different—as it should—since it mostly represents a birefringent response. In fact, in the absence of gain, the A+B signals will remain positive, while it is possible for γ-derived signals to be negative. Following Eqn. 2.3, for DOKE analysis of the birefringent condition, both the signals of *A-B* signal 270 Hz and *A+B* at 1 kHz are needed. Inspection of Fig. 2.11 clearly suggests that the long-term dynamics of the excited-state dichroism and birefringence are different. This, again, is something that DOKE can extract, as shown in Fig. 2.12. Here, one can see that the differences in long-lasting birefringence and absorption dynamics can be resolved, with the birefringence condition providing far better signal-to-noise than the dichroic signal. This is mainly due to the strength of the signal, as Fig 2.12 is to scale, but Fig 2.11 is not.

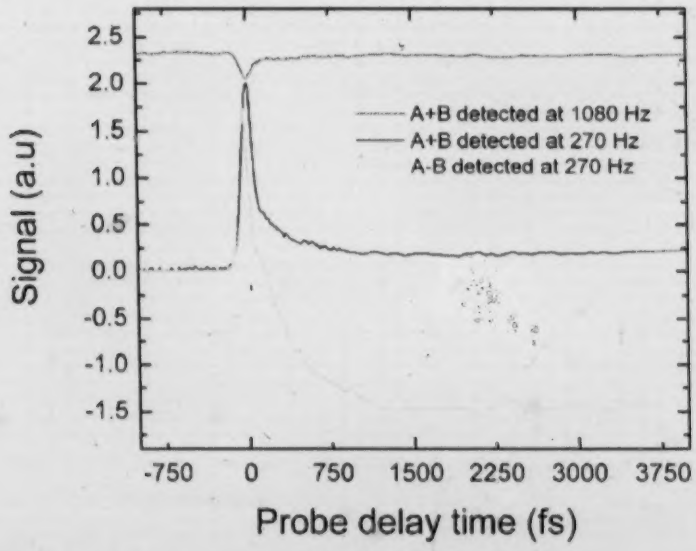

Figure 2.11: Various signals from ***ortho*-TPEB** in the DOKE birefringent polarization condition. A+B signals monitored at 270 Hz and 1 kHz detect transient absorption signals, while the A-B signal monitors transient birefringence. Clearly, the birefringence response is different from the absorptive signal, and both of these must be taken into account for the full DOKE analysis.

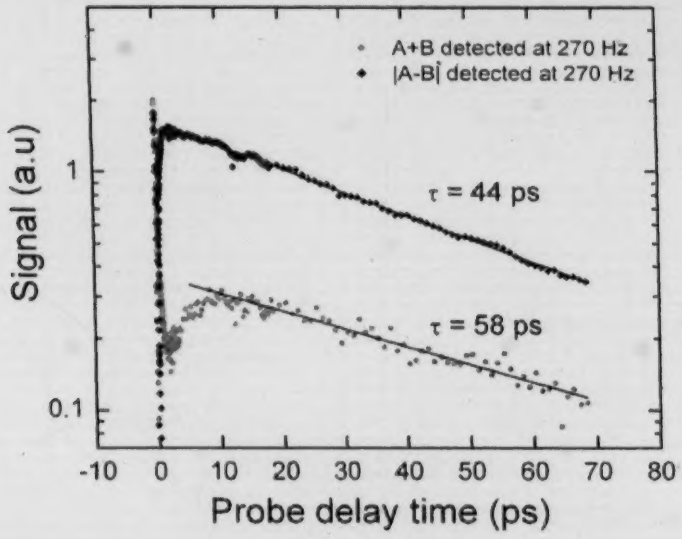

Figure 2.12: Longer time signals of those presented in the previous figure. The absolute |A-B| signal is larger than the absorptive A+B signal, and shows better signal-to-noise. The two phenomena also present different exponential decay dynamics in this particular sample.

2.4 Summary

The preceding chapter lays out the foundation for using the differential optical Kerr effect (DOKE) detection technique for the study of nonlinear absorption dynamics including two-photon absorption (TPA) and two-photon-accessed excited-state absorption (ESA). In previous works, we have established DOKE as a powerful technique for the measurement of the complimentary $\mathrm{Re}[\chi^{(3)}]$ response.[5,20] We have presented comparisons of absolute $\sigma^{(2)}$-values of **MPPBT** and **AF60** to those presented in the literature, and find that the DOKE technique faithfully reproduces both the cross-section and excited-state dynamics of other techniques. Furthermore, we have confirmed some key conditions of DOKE detection such as the linear relationship between pump beam intensity and on-peak TPA and the square dependence of pump beam intensity on off-peak ESA. Specific attention was paid to differences between a standard pump-probe transient absorption experiment and the DOKE technique, showing that DOKE is not sensitive to changes in dichroism as a function of relative pump-probe polarization.

2.5 References

[1] G. I. Stegeman and A. Miller, *Photonics in Switching*, in Background and Components, edited by J. E. Midwinter (Academic Press, San Diego, 1993), Vol. I.

[2] R. L. Sutherland, D. G. McLean, and S. Kirkpatrick, *Handbook of nonlinear optics* (Marcel Dekker, New York, 2003).

[3] M. Sheikbahae, A. A. Said, T. H. Wei, D. J. Hagan, and E. W. Van-Stryland, IEEE J. Quant. Elect. **26**, 760 (1990).

[4] Y. Pang, M. Samoc, and P. N. Prasad, J. Chem. Phys. **94**, 5282 (1991).

[5] A. D. Slepkov, *Third-Order Nonlinearities of Novel iso-Polydiacetylenes Studied by a Differential Optical Kerr Effect Detection Technique*, M.Sc. thesis. University of Alberta, Edmonton, 2001.

[6] I. Kang, T. Krauss, and F. Wise, Opt. Lett. **22**, 1077 (1997).

[7] J. Wang, M. Sheikbahae, A. A. Said, D. J. Hagan, and E. W. Vanstryland, J. Opt. Soc. Am. B. **11**, 1009 (1994)

[8] S. Guha, C. C. Frazier, P. L. Porter, K. Kang, and S. E. Finberg, Opt. Lett. **14**, 952 (1989).

[9] M. G. Kuzyk, R. A. Norwood, J. W. Wu, and A. F. Garito, J. Opt. Soc. Am. B. **6**, 154 (1989).

[10] N. Pfeffer, F. Charra, and J. M. Nunzi, Opt. Lett. **16**, 1987 (1991).

[11] P. P. Ho and R. R. Alfano, Phys. Rev. A **20**, 2170 (1979).

[12] M. E. Orczyk, M. Samoc, J. Swiatkiewicz, and P. N. Prasad, J. Chem. Phys. **98**, 2524 (1993).

[13] D. McMorrow, W. T. Lotshaw, and G. A. Kenney-Wallace, IEEE J. Quant. Elect. **24**, 443 (1988).

[14] M. D. Levenson and G. L. Eesley, Appl. Phys. **19**, 1 (1979).

[15] K. Kamada, M. Ueda, T. Sakaguchi, K. Ohta, and T. Fukumi, Chem. Phys. Lett. **263**, 215 (1996).

[16] K. P. H. Lui and F. A. Hegmann, Appl. Phys. Lett. **78**, 3478 (2001).

[17] Q. Wu, M. Litz, and X. Zhang, Appl. Phys. Lett. **68**, 2924 (1996).

[18] Regardless, it should be noted that instead of *(A-B)*, it is the modulation in *(A-B)* at the chopper frequency that is actually detected; This modulation in *(A-B)* also gives a zero baseline signal in the absence of birefringence

[19] P. N. Butcher and D. Cotter, *The Elements of Nonlinear Optics* (Cambridge University Press, Cambridge, 1990).

[20] A. D. Slepkov, F. A. Hegmann, Y. Zhao, R. R. Tykwinski, and K. Kamada, J. Chem. Phys. **116**, 3834 (2002).

[21] K. Kamada, K. Ohta, I. Yoichiro, and K. Kondo, Chem. Phys. Lett. **372**, 386 (2003).

[22] S. Kershaw, *Two Photon Absorption*, in Characterization Techniques and Tabulations for Organic Nonlinear Optical Materials, edited by M. G. Kuzyk and C. W. Dirk (Marcel Dekker, New York, 1998).

[23] O.-K. Kim, K.-S. Lee, H. Y. Woo, K.-S. Kim, G. S. He, J. Swiatkiewicz, and P. N. Prasad, Chem. Mater. **12**, 284 (2000).

[24] K. Kamada: private communication, 2003.

[25] A. D. Slepkov, J. A. Marsden, J. J. Miller, L. D. Shirtcliff, M. M. Haley, K. Kamada, R. R. Tykwinski, and F. A. Hegmann, in *Nonlinear Optical Transmission and Multiphoton Processes in Organics III,* Proc. of SPIE, **5934**, p. 593405, 2005.

[26] Y. Zhao, Y. Shirai, A. D. Slepkov, L. Cheng, L. B. Alemany, T. Sasaki, F. A. Hegmann, and J. M. Tour, Chem. Eur. J. **11**, 3643 (2005).

[27] R. Kannan, G. S. He, L. Yuan, F. Xu, P. N. Prasad, A. G. Dombroskie, B. A. Reinhardt, J. W. Baur, R. A. Vaia, and L.-S. Tan, Chem. Mater. **13**, 1896 (2001).

[28] J. Swiatkiewicz, P. N. Prasad, and B. A. Reinhardt, Opt. Commun. **157**, 135 (1998).

[29] L. D. Ziegler and X. J. Jordanides, Chem. Phys. Lett. **352**, 270 (2002).

[30] K. Kamada, private communication, 2002. This value is for 10.2 mM of **AF60** in THF.

[31] R. R. Birge and B. M. Pierce, J. Chem. Phys. **70**, 165 (1979).

[32] A. A. Said, C. Wamsley, D. J. Hagan, E. W. Van Stryland, B. A. Reinhardt, P. Roderer, and A. G. Dillard, Chem. Phys. Lett. **228**, 646 (1994).

CHAPTER 3:

VERIFICATION OF DOKE-OBTAINED TPA CROSS-SECTIONS BY SINGLE-BEAM EXPERIMENTS ON MPPBT

In order to further verify the quantitative TPA results obtained with the new DOKE setup, we conducted a simple single-beam absorption experiment.[1,2] In this experiment, we pass a single slightly-focused beam through the sample, carefully monitoring both total input and output powers. By varying the incident power, we can observe intensity-dependent (i.e. nonlinear) absorption in the sample. Analysis of these results is straightforward, but requires complete knowledge of input beam parameters, such as pulse shape, spot-size, and pulse duration.

In a sample that displays both linear and nonlinear absorption, beam depletion may be given by

$$\partial I = -\alpha I \partial z - \alpha^{(2)} I^2 \partial z, \qquad 3.1$$

where z is the beam propagation direction, I is the beam intensity, α is the absorption coefficient, and $\alpha^{(2)}$ is the two-photon absorption coefficient. Integrating over the entire sample, of path length L, the emerging intensity I, is given related to the incident intensity, I_0, by

$$I = \frac{I_0 e^{-\alpha L}}{1 + \left(\alpha^{(2)}/\alpha\right) I_0 - \left(\alpha^{(2)}/\alpha\right) I_0 e^{-\alpha L}}. \qquad 3.2$$

For most application-driven TPA samples, linear absorption is negligible at the wavelengths of interest. For such materials ($\alpha L \ll 1$), and the intensity-dependent absorption is given by

$$I = \frac{I_0 e^{-\alpha L}}{1 + \alpha^{(2)} L I_0}, \tag{3.3}$$

to first order in $\alpha^{(2)}L$. This is simply the linear (Beer's-law reduced) transmission multiplied by a nonlinear transmission term. For pulsed beams in which the time and intensity profiles are Gaussian, and in the absence of linear absorption, the output intensity may be given by [1,3]

$$I = \frac{\ln\left(1 + \alpha^{(2)} L I_0\right)}{\alpha^{(2)} L}. \tag{3.4}$$

Typically, we can directly measure the beam power, P (in Watts), rather than the intensity, I (in W/m^2). The power transmitted through the sample,

$$P = \frac{\ln\left(1 + \alpha'^{(2)} L P_0\right)}{\alpha'^{(2)} L} \tag{3.5}$$

is related to Eqn. 3.4, but yields a $\alpha^{(2)}$, value in W^{-1}m^{-1}, rather than $\alpha^{(2)}$ in m/W. The experimentally-obtained $\alpha'^{(2)}$ is related to the conventionally reported $\alpha^{(2)}$ through

$$\alpha^{(2)} = \frac{\alpha'^{(2)} A \tau R}{2}, \tag{3.6}$$

where A is the Gaussian spot size, R is the pulse repetition rate, and τ is the Gaussian pulse duration (FWHM$\div\sqrt{2}$). The two-photon cross-section, is related to $\alpha^{(2)}$ via

$$\sigma^{(2)} = \frac{\alpha^{(2)}\hbar\omega}{N_0} = \frac{\alpha^{(2)}ch}{N_0\lambda}, \qquad 3.7$$

where c is the speed of light, h is Planck's constant, λ is the incident beam wavelength, and N_0 is the molecular number density (concentration) of the sample, in m^{-3}. $\sigma^{(2)}$ is typically reported in Göppert-Mayers (GM), equivalent to 10^{-50} $cm^4 s^{-1} photon^{-1} molec.^{-1}$. Thus, using Equations 3.6 and 3.7, a convenient form for the experimentally obtained single-beam TPA cross-section, may be given by

$$\sigma^{(2)}(GM) = \frac{\alpha'^{(2)}chA\pi R}{2N_0\lambda} \times 10^8, \qquad 3.8$$

where the entire right-hand side is in SI units.

To verify the $\sigma^{(2)}$-value we obtain from the second DOKE condition, we conducted single-beam measurements on MPPBT samples of various concentrations in dimethylsulfoxide (DMSO). Figure 3.1 presents the input- versus output powers, along with fits to an equation similar to 3.5, but modified to account for an intensity-independent reflection at the front surface of the 1 mm path-length quartz cuvette. Front-surface reflection is easier to account for compared with linear absorption, as it is a single event, and only scales down the input power. The input photodiode deviated slightly from linearity, especially at the lowest and highest powers. To account for this, and in order to resolve the small absorptive signals that manifest as deviations from linearity, the vacant-path run was fit to a polynomial of order 3, and re-normalized for linearity. All subsequent single-beam experiment runs of the same day were calibrated to the same polynomial. These corrected signals are those displayed in Fig. 3.1, and the fitting parameters are reported in Table 3.1. As is evident from Figure 3.1 and Table 3.1, the blank solvent DMSO does not display any nonlinear absorption, but does display a linear trend with a slope smaller than 1. This is evidence of reflection losses at the front (and probably back) surface. The fits for all sample trials yield a reflection coefficient of 0.06-0.07 (6% to 7%), as has been previously measured for our specific sample cuvettes.[4] Fits to the 3 mM MPPBT in DMSO trials yield a nonlinear absorption coefficient of

$(0.110\pm0.017)\times10^{6}$ $m^{-1}W^{-1}$. With a measured (slightly elliptical) spot size of approx. $(5.8)\times10^{-8}$ m^2, and a Gaussian pulse width of 78 fs, we obtain a TPA cross-section of $\sigma^{(2)}_{MPPBT}=340\pm60$ GM, this value is comparable to 380 GM, obtained directly by the DOKE technique [see §2.3]. The more concentrated MPPBT samples yield similar cross sections of $\sigma^{(2)}_{MPPBT}=330\pm40$GM and $\sigma^{(2)}_{MPPBT}=300\pm30$GM for the 10 mM and 20 mM samples, respectively. However, the more concentrated samples experience much larger absorptions, as is evident from Fig 3.1, and thus may be either experiencing saturation of the two-photon signal or undergoing other phenomena.[5] Thus, the best value to compare with our DOKE results are those of the 3 mM sample, as it is this concentration at which we conduct that vast majority of our experiments on MPPBT. Regardless, the results obtained by the single-beam measurement agree with our other results well, confirming our DOKE technique as a good quantitative tool for measuring ultrafast nonlinear absorption phenomena.

Table 3.1. Fitting parameters for single-beam nonlinear absorption measurements of MPPBT in DMSO, as presented in Figure 3.1.

Sample	$\alpha'^{(2)}$ (10^6 $m^{-1}W^{-1}$)	Reflection factor	N_0 (molec./m^{-3})	$\sigma^{(2)}$ (GM)
Blank	0.006±0.003	0.001±0.001		
DMSO	0.008±0.002	0.074±0.001		
MPPBT (3 mM)	0.122±0.002	0.065±0.001	1.81×10^{24}	
	0.098±0.001	0.074[a]	1.81×10^{24}	
average	0.110±0.017		1.81×10^{24}	340±60
MPPBT (10 mM)	0.381±0.004	0.058±0.001	6.02×10^{24}	
	0.333±0.001	0.074[a]	6.02×10^{24}	
average	0.357±0.024		6.02×10^{24}	330±40
MPPBT (20 mM)	0.683±0.004	0.052±0.001	12.04×10^{24}	
	0.612±0.002	0.074[a]	12.04×10^{24}	
average	0.647±0.035		12.04×10^{24}	300±30

[a] Parameter is fixed to match the fitted reflection from DMSO.

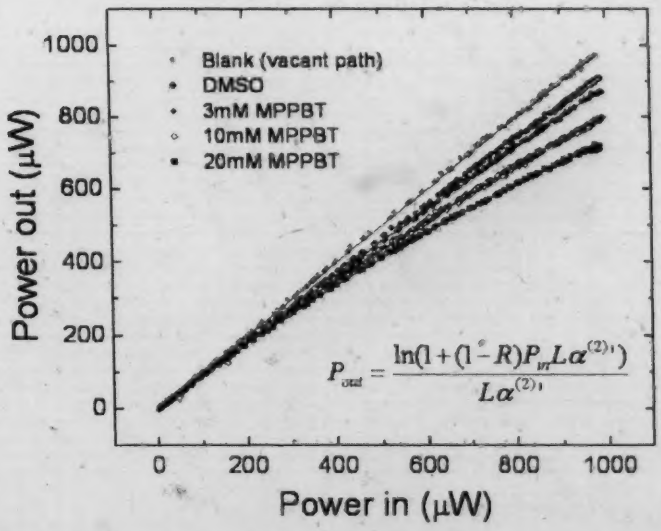

Figure 3.1. Single-beam nonlinear absorption measurements on MPPBT in DMSO. The data is fit to an equation (inset) that accounts for a constant reflection at the front-surface of the sample cuvette. The output power was calibrated by a polynomial of order 3, to approximate linearity through the vacant path. All other single-beam runs were normalized to this calibration. Solid lines are free fits to the inset equation. Fitting parameters are reported in Table 3.1.

3.1 References

[1] G. S. He, L. X. Yuan, N. Cheng, J. D. Bhawalkar, P. N. Prasad, L. L. Brott, S. J. Clarson, and B. A. Reinhardt, J. Opt. Soc. Am. B. **14**, 1079 (1997).

[2] S. Kershaw, Chapter 7: Two-Photon Absorption, in *Characterisation Techniques and Tabulations for Organic Nonlinear Optical Materials*, edited by M. G. Kuzyk and C. W. Dirk (Marcel Dekker, New York, 1998).

[3] B. A. Reinhardt, L. L. Brott, S. J. Clarson, A. G. Dillard, J. C. Bhatt, R. Kannan, L. Yuan, G. S. He, and P. N. Prasad, Chem. Mater. **10**, 1863 (1998).

[4] A. D. Slepkov, *Third-Order Nonlinearities of Novel iso-Polydiacetylenes Studied by a Differential Optical Kerr Effect Detection Technique*, M.Sc. thesis. University of Alberta, Edmonton, 2001.

[5] It may be noted that the fits for the 20 mM MPPBT samples were somewhat less robust than those for the 3 mM and 10 mM samples.

PART II

NLO STUDIES OF MOLECULES WITH VARIOUS CONJUGATION SCHEMES

CHAPTER 4:

LINEAR AND NONLINEAR OPTICAL CHARACTERIZATION OF EXTENDED POLYYNES: STRUCTURAL AND OPTICAL ONE-DIMENSIONAL SYSTEMS

4.1 Context

While diamond, graphite, and fullerenes/nanotubes are well known as allotropes of carbon, carbyne—the hypothetical linear form of entirely sp-hybridized carbon—has presented significant synthetic challenges (See Fig. 4.1).[1] Within these carbon allotropes, the nature of the carbon-carbon bond allows for a wide variation in electronic properties. Although sp^3-hybridization yields insulating carbon in the form of diamond, sp^2-hybridization can lead to conductive properties, such as in graphite, or both the insulating and semiconducting properties of nanotubes and fullerenes. The electronic properties of carbyne remain unknown. The sheer density of delocalized π-electrons within carbyne, however, offers the promise of an interesting electronic landscape. Whether carbyne is insulating, semiconducting, or metallic, remains to be discovered. Polyynes are the oligomeric cousins of carbyne, and it is hoped that the spectroscopic study of polyynes will yield information regarding the optical and electronic properties of carbyne. Thus, our group has synthesized extended polyyne oligomers with up to twenty consecutive sp-hybridized carbons and relatively benign end-groups, in an attempt to glimpse the properties of carbyne. Our optical and nonlinear optical investigations on extended polyynes represent the first of their kind, providing insightful trends as a function of molecular length. Furthermore, while it may not be surprising that polyynes are structurally one-dimensional (as evidenced by X-ray crystallography [2]), we have

found strong evidence that polyynes are model 1-D optical and nonlinear-optical systems. We have published the sum of these finding in two letters,[3,4] an SPIE conference proceedings,[5] and a full article.[2] The following chapter presents an integrated account of the optical and nonlinear optical experimental results on two series of polyyne oligomers. Two-photon and excited-state absorption behaviour of polyynes have not been previously published, and are reported here for the first time.

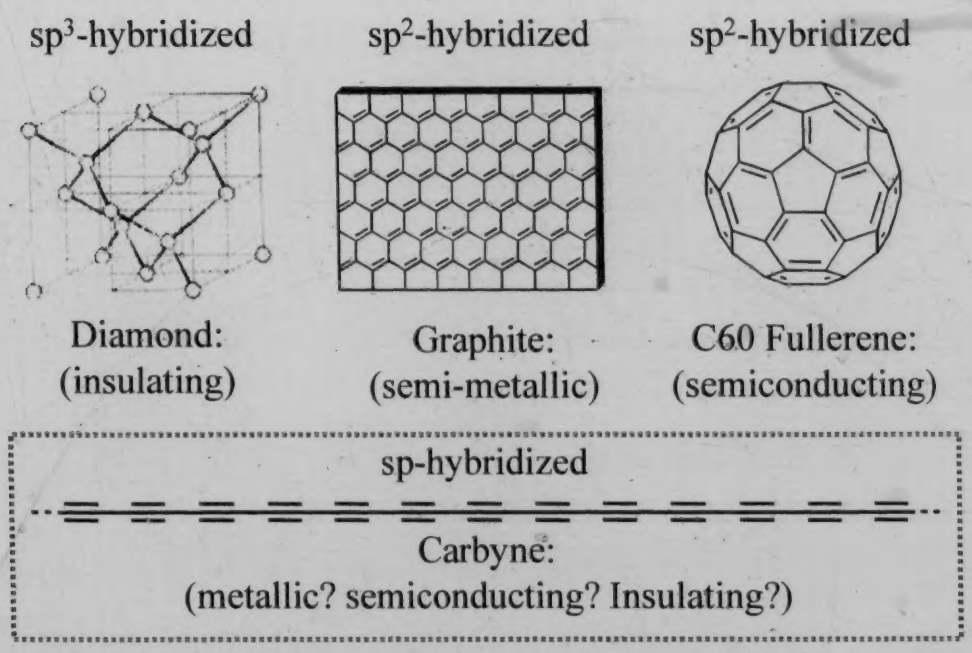

Figure 4.1. Various carbon allotropes. While diamond, graphite, and fullerenes are well known, carbyne is relatively obscure and elusive. Carbyne is a homogeneous and linear chain of sp-hybridized carbons, with unknown electronic properties.

4.2 Introduction

Linearly-conjugated frameworks are at the forefront of research on the nonlinear optical properties of organic materials.[6-8] The high densities of delocalized-electron afforded by the alternation of single- and multiple-bonds in conjugated systems lead to the sizable increases of optical nonlinearities over other non-conjugated frameworks.[7] A central benefit to studying organics as nonlinear optical materials for potential applications lies in the versatility of their structural motifs.[7,8] Therein lies the main question guiding the field of organic nonlinear optics: which conjugation schemes yield the highest optical nonlinearities? It was rapidly discovered, however, that unlike saturated (non-conjugated) molecules such as alkanes,[9] conjugated oligomers yield rapid increases in nonlinear optical activity as a function of molecular size.[6,8] Thus, the central question then becomes: which conjugation scheme yields the most rapid increases in optical nonlinearity with increasing oligomer length (or the number of repeat units)?

For a given series of conjugated oligomers, the magnitude of the third-order nonlinear hyperpolarizability, γ, is known to increase super-linearly as a function of length.[6] For oligomers shorter than the effective conjugation length, theoretical models invariably predict a power-law dependence of $\gamma \sim n^c \sim L^{c'}$, where L is the length of the molecule, n is the number of repeat units, and c (or c') is the power-law exponent.[10-12] Both theoretically and experimentally, the exponent c remains the most commonly used figure of merit for the comparison of third-order optical nonlinearities among different oligomer series.[6] Whereas a constant exponent c is expected for small- to medium-length oligomers, as the chain length approaches the effective conjugation length, the onset of saturation will manifest itself as a decreasing c value.[11] Once saturation is reached, increasing the length of the oligomer does not increase the extent of conjugation, and γ will vary linearly with oligomer length (i.e., $c=1$). Various values of c have been theoretically predicted for organic oligomers, depending on the theoretical model used. In studies that consider a generic model of π-conjugation, predictions range from $c = 5$ for both the "free electron in a box" and the one-electron Hückel models, to $c = 3.2$ for more complex approximations that account for electron-correlation effects.[6,8] Most computational models yield an exponent around $c = 4$.[6]

CHAPTER 4: EXTENDED POLYYNES: ONE-DIMENSIONAL SYSTEMS

In the past several decades, the third-order nonlinear optical properties of various quasi-one-dimensional conjugation schemes have been experimentally investigated. These include, but are not limited to, various oligomers such as carotenoids (polyenes),[13] polytriacetylenes,[14] polythiophenes,[15] oligophenylenes,[16] enynes,[17] polyenes,[11,18] cumulenes,[19] *p*-phenylenevinylenes (PPV),[20] and polyphenyleneethylenes (PPE).[21] Compared with the aforementioned schemes—all of which contain significant sp^2-hybridization in their conjugated backbone—polyynes are composed of a purely sp-hybridized backbone and are a unique class of conjugated oligomer (see Fig. 4.2). As such, polyynes are perhaps the simplest and yet most intriguing of conjugated organic oligomers.[6,22] As truly one-dimensional molecules,[2] polyynes represent a unique model for probing electronic communication free of the configurational limitations often imposed by rotation about single bonds. This characteristic distinguishes polyynes from other typical organic oligomers and polymers, for which bond rotation can result in an interruption in conjugation along the molecular framework (see Fig. 4.3).[23,24] This is, for example, well documented in the case of polydiacetylenes, for which the electronic and optical properties are dependent on solution-state conformation.[25] A strong dependence of the nonlinear optical properties on bond configuration has also been shown for conjugated polyenes.[26]

Compared to other semiconducting organic compounds such as polyenes,[11] polydiacetylenes[17] and polytriacetylenes,[27] polyynes remain the most synthetically challenging and difficult to study.[28-31] To date, formidable synthesis obstacles have meant that although the isolation of both short and extended-polyynes has been reported, the study of electronic, optical, and, in particular, third-order nonlinear optical properties of such systems has been extremely limited. In lieu of sufficient experimental data, the linear and nonlinear optical properties of extended polyyne carbon chains have been widely explored theoretically, often in comparison to other conjugated oligomeric structures.[6] While the molecular structures of the systems vary, these reports consistently predict that the molecular second hyperpolarizability, γ, for polyynes will increase as a power-law with respect to length.[12,32-34] These same studies also suggest that this power-law relationship of γ versus length for polyynes will be inferior to that of polyenes and polyenynes. Experimentally, however, these predictions have been neither challenged nor confirmed.[35]

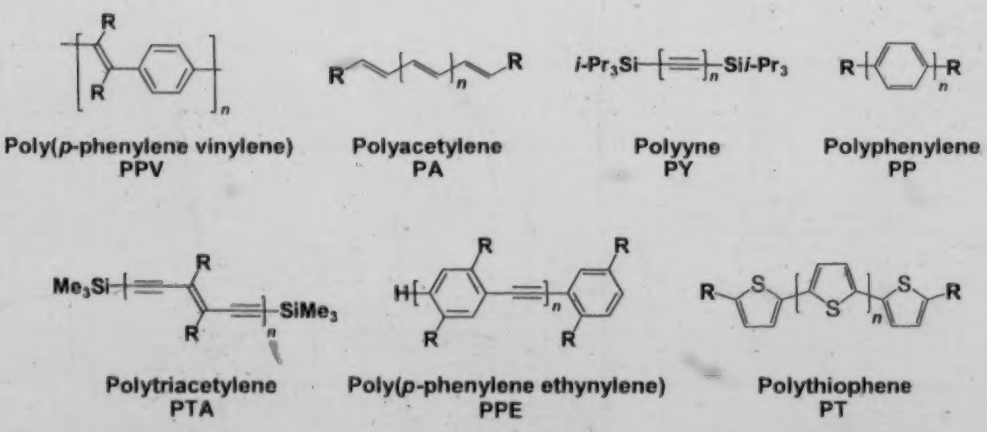

Figure 4.2. Variously conjugated oligomers, for comparison with polyynes (PY). Whereas all of the other oligomers have some sp^2 character in the conjugated backbone, polyynes are composed of an entirely sp-hybridized carbon chain.

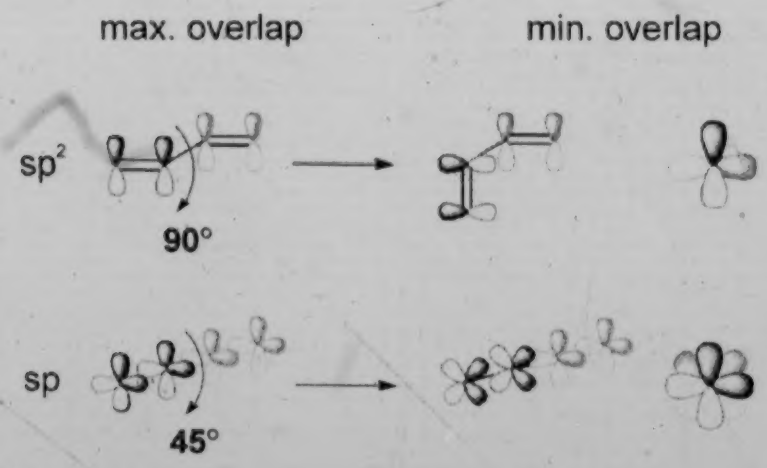

Figure 4.3. A schematic representing how conjugation and p-orbital overlap are disrupted by rotations about single bonds in sp^2 and sp hybridized paths. While polyenes can experience the maximum misalignment of π-orbitals, polyynes experience no more than a 45° misalignment through rotation, and thus always maintains some degree of conjugation.

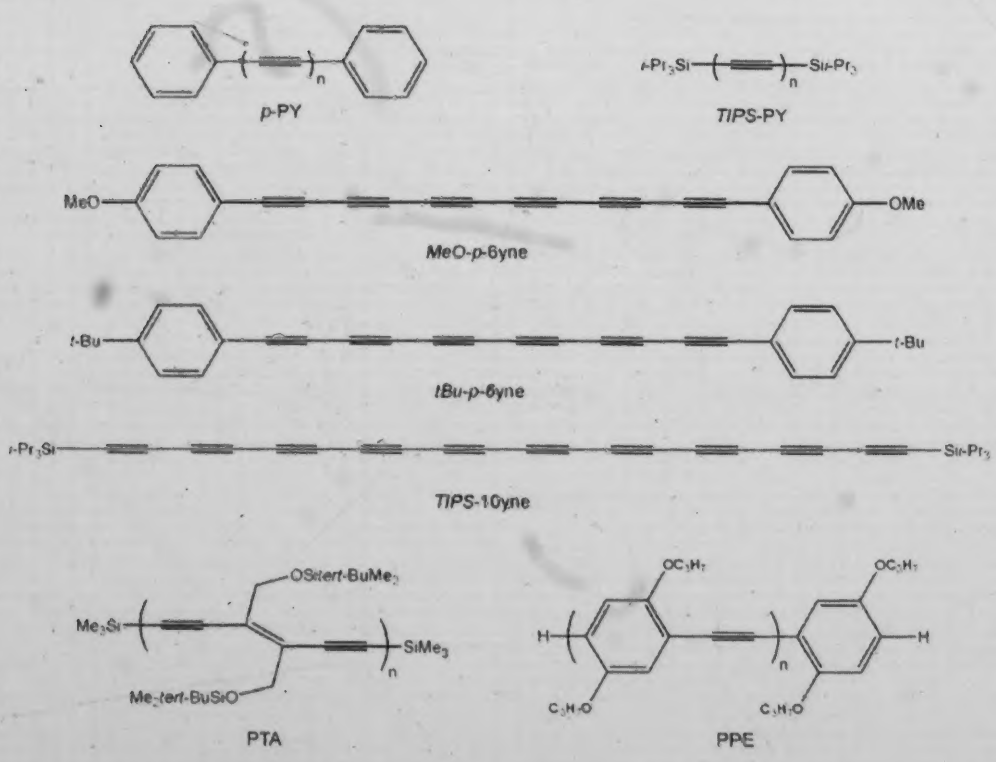

Figure 4.4. Structural representation of the oligomeric compounds discussed in this chapter. The full extent of longest polyyne, ***TIPS*-10yne**, is shown for emphasis.

4.3 Experimental

Compounds: In order to test the aforementioned theoretical predictions, as well as in attempt to glimpse the optical properties of carbyne, a series of extended tri*iso*propylsilyl end-capped polyynes (*TIPS*-PY) with n=2-10 triple bonds [2,3], phenyl end-capped polyynes (*p*-PY) with n=2-8 triple bonds, as well as n=6 bis-substituted tert-butyl-phenyl-hexayne (***tBu-p*-6yne**) and n=6 bis-donor-substituted methoxide-phenyl-hexayne (***MeO-p*-6yne**) were synthesized (see Fig. 4.4).[4] The simple but bulky TIPS moiety has been incorporated for added solubility and stability. It does not dramatically alter the electronic makeup of the carbon chain, nor does it extend conjugation beyond the polyyne backbone,[36] allowing for an analysis of an essentially pure sp-hybridized carbon system.[2]

For UV-vis spectroscopy, polyynes were measured in a Varian Cary 400 spectrometer as dilute solutions in hexanes.[2] For NLO measurements, all samples were investigated as dilute solutions in tetrahydrofuran (THF), and were sufficiently soluble for NLO measurements, with the exception of sample ***MeO-p*-6yne**, which could not be sufficiently solubilized to yield precise γ-measurements. Solubility in this sample was, however, sufficient for nonlinear absorption measurements. NLO characterization at a wavelength of 800 nm was conducted with the ultrafast DOKE detection technique as described in Chapter 2, and elsewhere.[37] All γ-values are referenced to that of THF ($\gamma_{THF}=5.2\times10^{-37}$ esu),[38] and all $\sigma^{(2)}$-values are relative to that of MPPBT ($\sigma^{(2)}_{MPPBT}=380$ GM ; $\lambda=800$ nm).[39] A summary of optical and nonlinear optical values for *TIPS*-PY and *p*-PY are listed in Table 4.1. Raw ***TIPS*-PY** DOKE scans in both polarization conditions are presented and discussed in Appendix C.

4.4 Results and Discussion

Linear Optical Properties: A fair amount of insight into the electronic landscape of polyynes may be achieved by UV-vis spectroscopic characterization. The UV-vis spectra of ***TIPS*-PY**s and ***p*-PY**s are presented in Figure 4.5. In contrast to most other conjugated organic molecules, the high-energy region of the UV spectra (220- 270 nm) of the longest polyynes is nearly transparent. This rare characteristic could allow for interesting optical applications for such compounds within this window of transparency. For the ***TIPS*-PY**s, the vibronic structure is clearly visible, appearing as a series of narrow absorption peaks with steadily increasing intensity toward the visible region. Thus, the highest wavelength of absorption peak, λ_{max}, for each ***TIPS*-PY** oligomer reflects a pure transition from the lowest energy vibrational level in the ground state to the lowest energy vibrational level in the excited state. There is a corresponding increase in the molar absorptivity (ε) as the chain length increases, and the *TIPS* end-capped systems show some of the highest molar absorptivity values measured for polyynes, with octayne ***TIPS*-8yne** at ε = 603,000 $M^{-1}cm^{-1}$ and decayne ***TIPS*-10yne** at ε = 753,000 $M^{-1}cm^{-1}$. A comparison of ε-values at λ_{max} for ***TIPS*-10yne** to that of other known decaynes highlights the dramatic dependence of the oscillator strength on the nature of the end group: a rhenium end-capped decayne shows ε=190,000 $M^{-1}cm^{-1}$,[40] a dendrimer-terminated decayne ε= 605,000 $M^{-1}cm^{-1}$,[30] while a decayne terminated with *t*-Bu groups shows ε= 850,000 $M^{-1}cm^{-1}$.[41] Further highlighting the enhanced oscillator strength of *TIPS* end-capped polyynes is a comparison between the octamers ***TIPS*-8yne** and ***p*-8yne**; where the phenyl end-capped oligomer displays a peak molar absorptivity that is less than one-half that of its TIPS-terminated counterpart (See Table 4.1).

A red-shift in λ_{max} is clearly visible as the conjugation length of these carbon rods is increased, indicating a decrease in the HOMO→LUMO energy gap. It is expected that at a particular chain length, saturation of this effect will occur. Such saturation would represent the effective conjugation length of the oligomers, where the energy gap reaches

a minimum and constant value representative of the theoretical carbon allotrope, carbyne.[42] This property is linked to the bond-order alternation (BOA), or electronic homogeneity of the conjugated backbone (See Chap 1).[43,44] Theoretical studies have predicted various degrees of bond-order alternation in carbyne chains, from sizable values,[45] through extremely small,[43] or even zero.[46] A small BOA in polyynes would imply that all middle-chain carbons are nearly degenerate, and would represent either conduction or a miniscule band-gap in polyynes. Chaquin and coworkers have predicted on the basis of semi-empirical calculations (ZINDO) that saturation ($\Delta\lambda_{max}/\Delta n = 0$) for a polyyne chain will occur at 400 nm.[42] This value is lower than 565 nm [40] and 569 nm [30] predicted based on previous experimental analysis.

If electron correlation effects are taken into consideration, the empirical power-law $1/\lambda_{max}=E_{max}\sim n^{-x}$ best describes the relationship between E_{max}, λ_{max} and n.[6,47] This relationship is well represented in Fig. 4.6b, and portrays the power-law decrease in E_{max} as a function of chain length through at least C_{20} in ***TIPS*-PYs**. Overall, the *TIPS*–protected polyyne oligomers yield a fit of $E_{max}\sim n^{-0.379\pm0.002}$ to high precision. This result contrasts that of Gladysz *et al.* who observed a relationship of $E_{max}\sim n^{-1}$.[40] It is, however, close to the well-established relationship of $E_{max}\sim n^{-0.5}$ observed for many polyenic materials.[20,48] Since the high-precision fit for the ***TIPS*-PY** series includes the longer oligomers, no indication of saturation of the HOMO→LUMO energy is yet observed, as would be indicated by the levelling of E_{max} values as n increases. Thus, a prediction regarding saturation in λ_{max} cannot be made on the basis of these UV-vis results.

Whereas *TIPS*-polyynes have straightforward absorption spectra, with a clear absorption peak corresponding to the gap energy (at λ_{max}), the phenylated polyynes show complex absorption spectra with some barely-resolvable absorption resonances extending past λ_{max} into the low-energy region beyond 340 nm, as can be seen in Fig. 4.5b.[4] Thus, it is difficult to designate a precise and unique λ_{max} value to these samples, for further analysis. Instead, for analysis of the bathocromic shifts in the absorption energy that

indicate increases in conjugation length, we used the leading (small) absorption resonance in the low-energy visible region, as previously described (see Fig 4.5c).[4] Overall, the absorption red-shift in ***p*-PY**s follows a very similar power-law trend to that in ***TIPS*-PY**, yielding $E_g \sim n^{-0.36\pm0.01}$ (see Fig. 4.6).

A comparison of polyynes to similar oligomers is instructive: polytriacetylenes (PTAs) and polyphenyleneethynylenes (PPEs), shown in Fig. 4.4, are close analogues to polyynes. The polytriacetylenes investigated by Martin *et al.* have a conjugated backbone with two sp-hybridized carbons for every sp^2-hybridized carbon.[27] E_g for this series diminishes with oligomers length, but although conjugation is clearly being extended, the trend shown in Fig. 4.6a does not approach a power law. The PPE series investigated by Meier *et al.* has a highly linear conjugated backbone of alternating phenyl rings and sp-hybridized carbons.[21] Again, conjugation is seen to extend, but the gap energy diminishes much more slowly than for the polyynes, with a power-law fit of $E_g \sim n^{-0.14\pm0.01}$. It is probable that deviations from a power-law for these samples may be explained by saturation of the conjugation length. Whereas we see no indication of saturation in our polyyne series—neither in the UV-vis nor in the to-be-discussed nonlinear optical data—Martin *et al.* indicate that saturation has begun by n=6 for the PTA series,[27] and Meier *et al.* suspect that the PPEs behave differently as short n=1,2 chains than they do in extended (n>3 chains).[21]

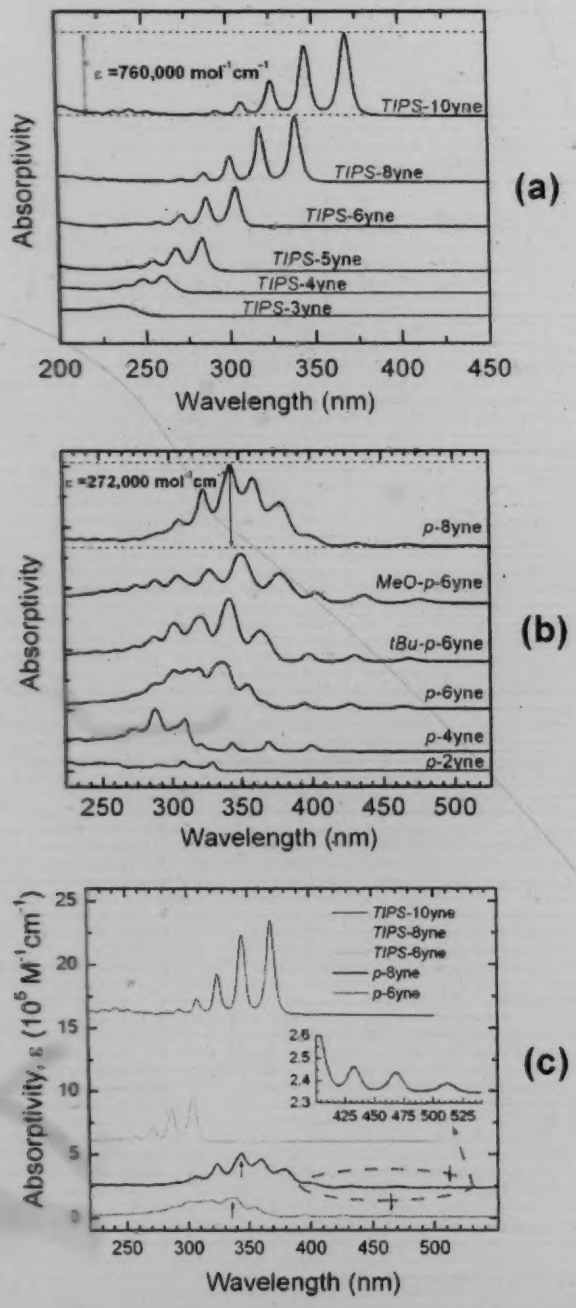

Figure 4.5. UV-vis absorption spectra of the studied polyynes. (a) ***TIPS*-PYs**. (b) ***p*-PYs**. (c) Selected polyynes re-displayed for an overly comparison between the two series. ***TIPS*-8yne** and ***TIPS*-10yne** show spectra wherein the vibronic structure of the pure polyyne backbone is dominant. In ***p*-6yne** and ***p*-8yne**, the absorption spectrum is more complex. Black arrows signify λ_{max} in region I (upwards) and region II (downwards), used for further analysis. Inset expands region II absorption in ***p*-8yne**.

Table 4.1. A summary of optical characteristics for the studied polyynes. λ_{max} is the highest wavelength of absorption maximum corresponding to the energy gap of the compound. *p*-PYs display an additional high-wavelength region of miniscule absorption. λ_{max} of in this region for those compounds are in [brackets]. U.R. corresponds to data that was unresolved; N.C. corresponds to data that was not collected.

Sample	# triple bonds, n	λ_{max} (nm)	γ $\times 10^{-36}$ esu	$\sigma^{(2)}$ (GM)	ε (@ λ_{max}), [ε (@ 400nm)] ($L\ mol^{-1}\ cm^{-1}$)
***TIPS*-2yne**	2	<210	2.75±0.28	N.C	<1,000, [<1,000]
***TIPS*-3yne**	3	234	7.02±0.70	N.C	93,000, [<1,000]
***TIPS*-4yne**	4	260	12.5±2.1	0.34±0.09	157,000, [<1,000]
***TIPS*-5yne**	5	284	35.3±1.2	N.C	293,000, [<1,000]
***TIPS*-6yne**	6	304	64.5±2.9	U.R	359,000, [<1,000]
***TIPS*-8yne**	8	339	238±47	7.6±0.8	603,000, [<1,000]
***TIPS*-10yne**	10	369	646±27	34±3	753,000, [2,000]
***p*-2yne**	2	328	12±2	N.C	30,000, [<1,000]
***p*-4yne**	4	288 (399)	49±18	1.2±0.2	143,000, [21,000]
***p*-6yne**	6	337 (465)	217±10	2.7±0.4	155,000, [6,0 00]
***tBu-p*-6yne**	6	342	300±30	7.6±0.8	206,000, [21,000]
***MeO-p*-6yne**	6	351	U.R	14±2	164,000, [29,000]
***p*-8yne**	8	344 (512)	588±36	68±7	272,000, [37,000]

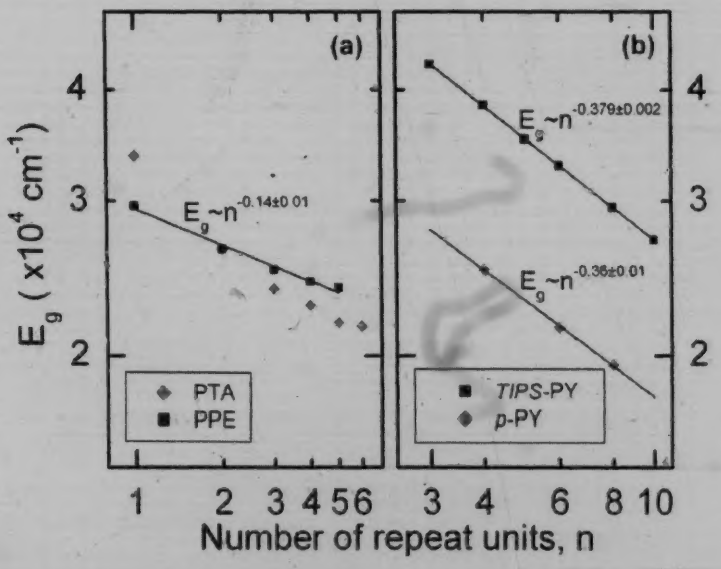

Figure 4.6. Absorption trends in two series re-analyzed from the literature (a),[21,27] and in our studied polyynes (b). Power law decreases in the absorption energy as a function of oligomer size for the polyynes indicate that saturation in the conjugation length has not yet begun (fits are shown by solid lines). Polytriacetylenes (PTAs) and poly(phenylene ethynylene)s (PPEs) also show decreases of the gap energy with length, but they do not follow a strict power-law. The best power-law fit for PPEs is shown.

Kerr Nonlinearity: Molecular second-hyperpolarizabilities for all of the studied polyynes are presented in Table 4.1. With the exception of ***MeO-p*-6yne**, which did not display a large enough Kerr signal be to resolved beyond the THF background at the maximum concentration, all other samples produced strong Kerr signals. As mentioned above, γ is expected to increase as a power-law with increasing chain length for conjugated oligomers. Indeed, as seen in Fig. 4.7, ***TIPS*-PY** and ***p*-PY** display this trend, with exponents of c = 4.3 and 3.8, respectively. Our DOKE signals, obtained with femtosecond pulses, typically yield much lower γ-values than those obtained with nanosecond or picosecond pulses.[49,50] However, when comparing nonlinearities in our polyynes to polyenic materials studied by the same technique, we find that the polyynes already show sizable nonlinearities by the stage of the decamer. For example, β-carotene, a polyene with 22 consecutive sp^2 carbons, shows $\gamma=(7.9\pm0.8)\times10^{-34}$ esu, as measured in THF with our DOKE setup, compared to ***TIPS*-10yne** that has 20 consecutive sp carbons and shows $\gamma=(6.5\pm0.3)\times10^{-34}$ esu.[3]

Although experimentally-obtained γ-values depend dramatically on the detection technique used, the excitation pulse duration and the wavelength of light used, the comparison of power-laws is fairly reliable between sample series reported by different groups.[6,44] The exponent of c = 3.8 obtained for phenylated-polyynes is among the largest non-resonant exponents reported for any oligomer series, while that of the *TIPS*-polyyne is, indeed, the largest. By comparison, Martin *et al.*'s PTA series and Meier *et al.*'s PPE series display much smaller power-law exponents of 2.5 and 2.3 respectively (see Fig 4.7). Various other substituted and unsubstituted polyenes have displayed exponents ranging from c=2.3 to 3.6.[8,11,51] Thus, our results contrast all previous theoretical expectations of lower power-laws for polyynic materials over polyenes. Overall, the phenylated polyynes can be said to behave analogously to that of the TIPS-polyynes, with both the UV-vis absorption and the Kerr nonlinearities paralleling one another. Although the ***p*-PY**s display a slightly slower rise in molecular nonlinearity, the hyperpolarizability of these end-capped polyynes are considerably larger than those of the unsubstituted polyynes. In addition, the bis-donor-substituted phenylated polyyne (***tBu-p*-6yne**) shows a larger nonlinearity than the unsubstituted ***p*-6yne**. Furthermore, as seen in Fig. 4.7, even by the decayne length of the ***TIPS*-PY**s, there is no onset of

saturation for either series. The parallels in linear and nonlinear optical character between the phenyl-capped and the relatively electronically-innert silyl-capped polyynes suggest that, although the phenyl group is a strongly-conjugated moiety, the inhomogeneity it introduces to the π-system in the *p*-PY series may be mitigating stronger power-law increases.

Polyynes as Optical One-Dimensional Systems: In addition to having the fastest rise in γ with extended conjugation length than the quasi-one-dimensional oligoene, polyynes display characteristics predicted for 1-D materials. Recent random phase approximation (RPA) calculations conducted on a variety of materials with various conjugation schemes predict universal power-law trends in the gap energy and longitudinal hyperpolarizability γ_{xxxx}.[47] One-dimensional oligomers would be expected to be dominated by this longitudinal tensor component. With the direct scaling of polyyne length to the number of repeat units, our power-law of $\gamma \sim n^{4.3\pm0.1}$ for the ***TIPS*-PY** series is in almost perfect agreement with the RPA prediction of a universal 1-D $\gamma_{xxx} \sim L^{4.2\pm0.1}$.[47] Furthermore, our power-law trend in absorption energy exactly matches the predicted $E_g \sim n^{-0.38\pm0.02}$.[47] These findings lend credence to the idea that polyynes not only look one-dimensional physically, but also behave so both optically and electronically. Another recent exploration of possible one-dimensional behavior in conjugated systems has yielded a theoretical expression derived from sum-rules. Kuzyk has recently proposed the following expression as the upper limit for γ in linear conjugated organics:[52]

$$\gamma_{xxxx} < 4e^3\hbar^4 m^{-2} N^2 E_g^{-5} \qquad 4.1$$

Where e is the electron charge, m is the electron mass, and N is the number of electrons. Assuming that all of the delocalized electrons come from multiple bonds, N should scale directly with the number of repeat units, n, in our oligomers. With our trend relating the absorption energy and the number of repeat units, we find that Eqn. 4.1 predicts $\gamma_{xxxx} \sim n^{3.9}$ for our ***TIPS*-PY** series and $\gamma_{xxxx} \sim n^{3.8}$ for our ***p*-PY** series. This is in excellent agreement with our direct power-law findings of $\gamma_{TIPS\text{-}PY} \sim n^{4.3}$ and $\gamma_{p\text{-}PY} \sim n^{3.8}$. Indeed, to date, polyynes are the first oligomeric system to approach this limit.[52,53]

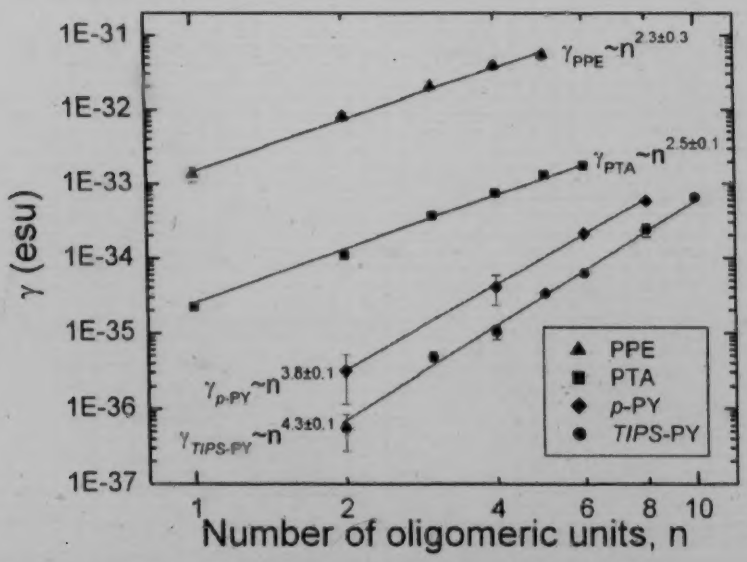

Figure 4.7. Power law trends for increasing third-order molecular nonlinearity, γ, with chain length for both of our polyyne series and for two poly-enyne series re-plotted from the literature.[21,27] ***p*-PYs** show a power law that is very similar to that of the *TIPS*-polyynes, which show the largest power-law exponent of any conjugated oligomers system. The solid lines are fits to the form $\gamma = a + bn^c$, where a is an offset due to the end-group effect, b is a constant, and c is the power-law exponent. For **PTA** and **PPE**, an offset of $a=0$ was used in in these fits. For ***p*-PY** and ***TIPS*-PY**, $a=8.8\times10^{-36}$ esu and $a=2.2\times10^{-36}$ esu were used, respectively.

Two-Photon Absorption: The two-photon absorption (TPA) cross section of polyynes at 800 nm was also investigated. This work is the first report of two-photon and excited-state absorption dynamics in any polyyne oligomers. As with the Kerr nonlinearity, TPA in polyynes increases rapidly with conjugation length. As outlined in Chapter 1, there are many factors that determine the two-photon absorption characteristics of organic samples including symmetry, dimensionality, dipole/multipole strength, and conjugation length.[54-56] Of these, conjugation length has been identified as most influential in increasing the TPA cross-section.[54,55] Furthermore, adding donor and acceptor end-groups has also been identified as beneficial to increasing TPA. With their long and pure conjugation frameworks, substituted polyynes make promising candidate for materials

with large two-photon absorption. On the other hand, polyynes are fairly transparent between 400 nm and 600 nm, and thus may have TPA resonance maxima only at the edge of the visible range. Polyyne two-photon absorption cross-sections are presented in Table 4.1 and are plotted as a function of chain length in Fig. 4.8. The most interesting finding is that the *TIPS*-capped octayne and decayne display nontrivial cross-sections of 7.6 GM and 34 GM at 800 nm despite having negligible absorptivity at or beyond 400 nm. This finding may indicate that extended polyynes posses a rare feature found in extended polyenes, in which the lowest two-photon-allowed state—which, due to selection rules for symmetric molecules, is one-photon forbidden—is below the lowest one-photon level.[57-59] Thus, longer polyynes can be expected to have strong TPA at longer wavelengths, as extended conjugation red-shifts the entire one-photon spectrum, and the lowest two-photon state red-shifts even further.[57]

Some general trends can be discerned from the obtained two-photon absorption cross-sections. Clearly, TPA increases rapidly with conjugation length. This is most evident in the ***p*-PY** series, in which the octamer has a 30 fold increase in $\sigma^{(2)}$ over the hexamer. In general, the phenylated polyynes also show increased two-photon absorption over the *TIPS*-polyynes, with the ***p*-8yne** displaying a 9 fold increased cross-section over the ***TIPS*-8yne**. This difference may indicate that the ***p*-PYs** have longer conjugation lengths than the **TIPS-PY**s, suggesting that the phenyl end groups are, after all, considerably integrated into the conjugated backbone; in seeming contradiction of the discussion in the previous section. On the other hand, because the phenylated polyynes absorb at considerably longer wavelengths compared to the TIPS end-capped polyynes, this increase in TPA may simply indicate enhancements in the detuning factor (denominators) in Eqn. 1.5. The increases in TPA upon bis-donor end-capping are probably not due to these spectral arguments, as the ***tBu-p*-6yne** shows a three-fold increase in $\sigma^{(2)}$ over the unsubstituted ***p*-6yne**, while having a nearly identical UV-vis absorption edge. Bis-donor substitution further raises the cross-section by a factor of two

over the ***tBu-p-*6yne** species. This finding is consistent with the well-established trend that donor-substitution typically affords large increases in TPA (see §1.2 and §5.4).

The prospect of high two-photon absorption in carefully-engineered polyynes is quite promising. By the stage of the octayne, ***p*-PY**s already shows a sizable cross-sections of $\sigma^{(2)}$ = 68±7 GM. With unabated increases in conjugation, longer polyynes substituted with stronger donors and/or acceptors may yield extremely large two-photon cross sections. Of course, there is no reason to believe that the peak of the TPA spectrum resides at 800 nm, and studies at other wavelengths should yield drastic increases in polyyne TPA. In particular, as the one-photon absorption spectra of polyynes are dominated by a single low-energy absorption with a very sharp edge, it may be possible to affect a double-resonance condition that will lead to huge cross-sections.[39,60,61]

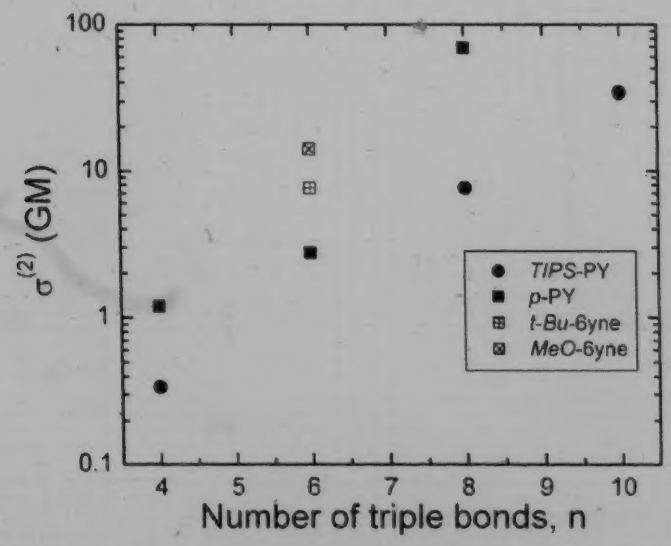

Figure 4.8. A scatter plot of two-photon absorption cross-sections obtained from polyynes at 800 nm. Absolute $\sigma^{(2)}$-values are relative to $\sigma^{(2)}_{MPPBT}$=380 GM (1 Göppert-Mayer (GM) = 10^{-50} $cm^4s^{-1}photon^{-1}molecule^{-1}$).

Nonlinear Absorption Dynamics: A major advantage to using a pump-probe experiment to probe sample nonlinearities is the temporal information it yields.[62] For example, other techniques such as z-scan and nonlinear transmission experiments (see Chapter 3) cannot directly discern between instantaneous TPA and other nonlinear absorption processes such as two-photon mediated excited state absorption.[50,63] This ambiguity often leads to inflated TPA cross-sections reported with nanosecond pulse experiments.[64] Some representative polyyne nonlinear absorption signals are presented in Fig. 4.9. All investigated samples show a sharp peak centered about the arrival time of the probe pulse. This ultrafast signal follows the cross-correlation of the pump and probe pulses and represents the instantaneous TPA. Some samples also exhibit longer-lasting excited state absorption (ESA). This process represents the absorption of a delayed probe photon from a state populated by pump beam two-photon absorption.[63] A simple three-level model suffices for explaining the ESA decays presented in Fig. 4.9b. The two-photon state remains populated for a very long time in the ***p*-8yne** sample, displaying an exponential decay rate of hundreds of picoseconds. By contrast, the bis-donor-substituted ***MeO-p*-6yne** shows a decay rate of only 30 ps, while the unsubstituted ***p*-6yne** does not exhibit resolvable ESA (not shown).

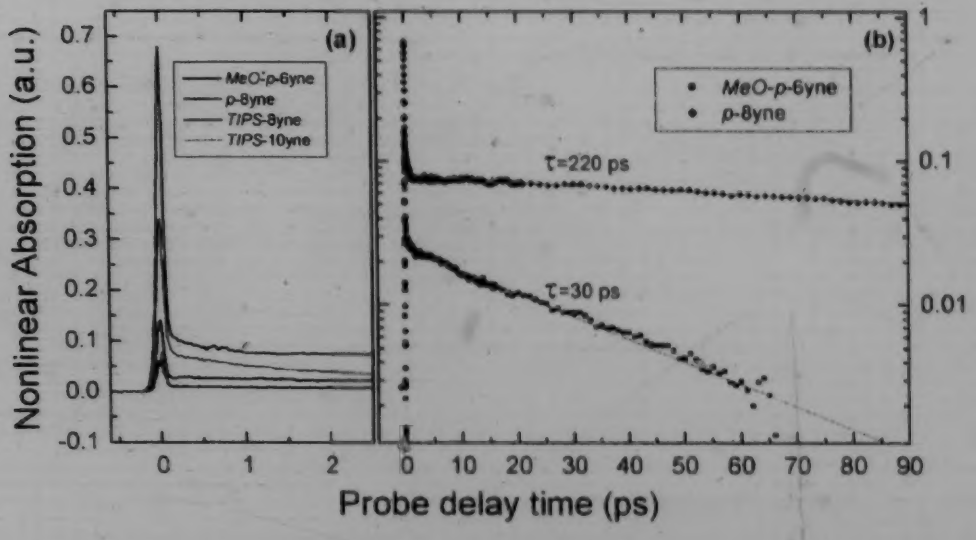

Figure 4.9. [colour] Selected time-resolved nonlinear absorption signals. (a) Instantaneous two-photon absorption gives way to longer-lasting excited state absorption. (b) Excited-state absorption in two samples studied at long times show a simple exponential decay fits (solid lines) with two very different relaxation times.

4.5 Summary

We have used a differential-detection optical Kerr effect scheme to measure the optical and third-order nonlinear optical properties of two series of extended polyynes (PYs). A series of tri*iso*propylsilyl end-capped polyynes with up to 10 triple bonds and a series of phenyl end-capped polyynes with up to 8 triple bonds, in addition to two bis-donor substituted phenyl-hexaynes have been investigated. Polyynes are composed of a pure sp-hybridized carbon backbone and have a very high density of delocalized π-electrons. In addition, polyynes are strictly linear and free of the conformational defects that plague some other conjugated frameworks, such as polyacetylenes. Both the wavelength of absorption (corresponding to the gap energy) and the molecular second-hyperpolarizability increase as a power-law with increasing chain length. For the ***TIPS*-PY** series, the absorption energy increases as $E_g \sim n^{-0.379\pm0.002}$, and the nonlinearities increase as $\gamma \sim n^{4.3\pm0.1}$. The phenyl-polyynes show very similar trends of $E_g \sim n^{-0.36\pm0.01}$ and $\gamma \sim n^{3.9\pm0.1}$. These trends make clear that saturation in the conjugation length has not yet begun at the lengths studied. The power-law exponent for γ in *TIPS*-polyynes is the largest reported for any conjugated oligomer series, a fact that is in direct disagreement with all reported theoretical calculations that predict superior exponents for polyenes and polyenynes than for polyynes. In addition, when compared with theoretical modeling of pure one-dimensional systems, both optical and nonlinear optical results confirm that polyynes behave one-dimensionally. Time-resolved nonlinear absorption measurements show that, for both series, the two-photon absorption cross-section increases dramatically with conjugation length. Furthermore, extending the conjugation with phenyl groups increases TPA in ***p*-PY**s over ***TIPS*-PY**s. Bis-donor and bis-acceptor substitution further increases TPA in polyynes. Overall the ***p*-8yne** sample yielded the largest TPA cross-section of 68±07 GM. There is evidence that, as with extended *polyenes*, the lowest-lying excited state in long polyynes is a one-electron-forbidden two-photon-allowed state.

4.6 References

[1] R. J. Lagow, J. J. Kampa, H. C. Wei, S. L. Battle, J. W. Genge, D. A. Laude, C. J. Harper, R. Bau, R. C. Stevens, J. F. Haw, and E. Munson, Science **267**, 362 (1995).

[2] S. Eisler, A. D. Slepkov, E. Elliott, T. Luu, R. McDonald, F. A. Hegmann, and R. R. Tykwinski, J. Am. Chem. Soc. **127**, 2666 (2005).

[3] A. D. Slepkov, F. A. Hegmann, S. Eisler, E. Elliott, and R. R. Tykwinski, J. Chem. Phys. **120**, 6807 (2004).

[4] T. Luu, E. Elliott, A. D. Slepkov, S. Eisler, R. McDonald, F. A. Hegmann, and R. R. Tykwinski, Org. Lett. **7**, 51 (2005).

[5] A. D. Slepkov, S. Eisler, T. Luu, R. R. Tykwinski, and F. A. Hegmann, in *Linear and Nonlinear Optics of Organic Materials V*, Proc. of SPIE, **5935**, pp. 301-308, 2005.

[6] C. Bubeck, *Nonlinear Optical Properties of Oligomers*, in Electronic Materials-The Oligomer Approach, edited by K. Müllen and G. Wegner (Wiley-VCH, Veinheim, 1998), Chapter 8.

[7] P. N. Prasad and D. J. Williams, Introduction to Nonlinear Optical Effects In Molecules & Polymers (Wiley Interscience, New York, 1991).

[8] Nonlinear optics of organic molecules and polymers, H. S. Nalwa and S. O. Miyata, Eds. (CRC Press, New York, 1997)

[9] J. P. Hermann and J. Ducuing, J. Appl. Phys. **45**, 5100 (1974).

[10] J. L. Brédas, C. Adant, P. Tackx, A. Persoons, and B. M. Pierce, Chem. Rev. **94**, 243 (1994).

[11] I. D. W. Samuel, I. Ledoux, C. Dhenaut, J. Zyss, H. H. Fox, R. R. Schrock, and R. J. Silbey, Science **265**, 1070 (1994).

[12] M. Schulz, S. Tretiak, V. Chernyak, and S. Mukamel, J. Am. Chem. Soc. **122**, 452 (2000).

[13] S. R. Marder, W. E. Torruellas, M. Blanchard-Desce, V. Ricci, G. I. Stegeman, S. Gilmour, J. L. Brédas, J. Li, G. U. Bublitz, and S. G. Boxer, Science **276**, 1233 (1997).

[14] U. Gubler, C. Bosshard, P. Günter, M. Y. Balakina, J. Cornil, J. L. Brédas, R. E. Martin, and F. Diederich, Opt. Lett. **24**, 1599 (1999).

[15] M.-T. Zhao, B. P. Singh, and P. N. Prasad, J. Chem. Phys. **89**, 5535 (1988).

[16] M. Rumi, G. Zerbi, K. Müllen, G. Muller, and M. Rehahn, J. Chem. Phys. **106**, 24 (1997).

[17] H. J. Byrne, W. Blau, R. Giesa, and R. C. Schulz, Chem. Phys. Lett. **167**, 484 (1990).

[18] G. Puccetti, M. Blanchard-Desce, I. Ledoux, J. M. Lehn, and J. Zyss, J. Phys. Chem. **97**, 9385 (1993).

[19] I. Kminek, J. Klimovic, and P. N. Prasad, Chem. Mater. **5**, 357 (1993).

[20] A. Mathy, K. Ueberhofen, R. Schenk, H. Gregorius, R. Garay, K. Müllen, and C. Bubeck, Phys. Rev. B. **53**, 4367 (1996).

[21] H. Meier, D. Ickenroth, U. Stalmach, K. Koynov, A. Bahtiar, and C. Bubeck, Eur. J. Org. Chem. 4431 (2001).

[22] R. E. Martin and F. Diederich, Angew. Chem. Int. Ed. **38**, 1350 (1999).

[23] I. Ledoux, I. D. W. Samuel, J. Zyss, S. N. Yaliraki, F. J. Schattenmann, R. R. Schrock, and R. J. Silbey, Chem. Phys. **245**, 1 (1999).

[24] G. Rossi, R. R. Chance, and R. Silbey, J. Chem. Phys. **90**, 7594 (1989).

[25] Q. Huo, K. C. Russell, and R. M. Leblanc, Langmuir **14**, 2174 (1998).

[26] J. R. Heflin, K. Y. Wong, O. Zamanikhamiri, and A. F. Garito, Phys. Rev. B. **38**, 1573 (1988).

[27] R. E. Martin, U. Gubler, C. Boudon, V. Gramlich, C. Bosshard, J. P. Gisselbrecht, P. Günter, M. Gross, and F. Diederich, Chem. Eur. J. **3**, 1505 (1997).

[28] H. Hopf, in *Classics in Hydrocarbon Synthesis* (Wiley-VCH, Weinheim, 2000), Chapter 8.

[29] S. Szafert and J. A. Gladysz, Chem. Rev. **103**, 4175 (2003).

[30] T. Gibtner, F. Hampel, J. P. Gisselbrecht, and A. Hirsch, Chem. Eur. J. **8**, 408 (2002).

[31] J. Stahl, J. C. Bohling, E. B. Bauer, T. B. Peters, W. Mohr, J. M. Martin-Alvarez, F. Hampel, and J. A. Gladysz, Angew. Chem. Int. Ed. **41**, 1872 (2002).

[32] H. S. Nalwa, J. Mukai, and A. Kakuta, J. Phys. Chem. **99**, 10766 (1995).

[33] I. D. L. Albert, J. O. Morley, and D. Pugh, J. Phys. Chem. A. **101**, 1763 (1997).

[34] W. J. Buma, M. Fanti, and F. Zerbetto, Chem. Phys. Lett. **313**, 426 (1999).

[35] Third-order nonlinear optical coefficients have been reported for shorter polyynes, up to the tetrayne, with insufficient data to fit power-law behaviour. See: J. W. Perry, ACS Symp. Ser. 455, 67 (1991).

[36] M. Traetteberg, P. Bakken, J. F. Liebman, and M. Hulce, J. Mol. Struct. **346**, 101 (1995).

[37] A. D. Slepkov, *Third-Order Nonlinearities of Novel iso-Polydiacetylenes Studied by a Differential Optical Kerr Effect Detection Technique*, M.Sc. thesis. University of Alberta, Edmonton, 2001.

[38] A. D. Slepkov, F. A. Hegmann, Y. Zhao, R. R. Tykwinski, and K. Kamada, J. Chem. Phys. **116**, 3834 (2002).

[39] K. Kamada, K. Ohta, I. Yoichiro, and K. Kondo, Chem. Phys. Lett. **372**, 386 (2003).

[40] R. Dembinski, T. Bartik, B. Bartik, M. Jaeger, and J. A. Gladysz, J. Am. Chem. Soc. **122**, 810 (2000).

[41] E. R. H. Jones, E. E. Lee, and M. C. Whiting, J. Chem. Soc., 3483 (1960).

[42] A. Scemama, P. Chaquin, M. C. Gazeau, and Y. Benilan, Chem. Phys. Lett. **361**, 520 (2002).

[43] A. Abdurahman, A. Shukla, and M. Dolg, Phys. Rev. B. **65**, 115106 (2002).

[44] U. Gubler and C. Bosshard, Adv. Polym. Sci. **158**, 123 (2002).

[45] A. Scemama, P. Chaquin, M. C. Gazeau, and Y. Benilan, J. Phys. Chem. A. **106**, 3828 (2002).

[46] E. J. Bylaska, J. H. Weare, and R. Kawai, Phys. Rev. B. **58**, R7488 (1998).

[47] Y. Luo, P. Norman, K. Ruud, and H. Ågren, Chem. Phys. Lett. **285**, 160 (1998).

[48] G. N. Lewis and M. Calvin, Chem. Rev. **25**, 273 (1939).

[49] P. N. Butcher and D. Cotter, The Elements of Nonlinear Optics (Cambridge University Press, Cambridge, 1990).

[50] R. L. Sutherland, D. G. McLean, and S. Kirkpatrick, *Handbook of nonlinear optics* (Marcel Dekker, New York, 2003).

[51] G. S. W. Craig, R. E. Cohen, R. R. Schrock, R. J. Silbey, G. Puccetti, I. Ledoux, and J. Zyss, J. Am. Chem. Soc. **115**, 860 (1993).

[52] M. G. Kuzyk, Phys. Rev. Lett. **85**, 1218 (2000).

[53] M. G. Kuzyk, Phys. Rev. Lett. **90** (2003).

[54] E. Zojer, D. Beljonne, P. Pacher, and J. L. Brédas, Chem. Eur. J. **10**, 2668 (2004).

[55] M. Albota, D. Beljonne, J. L. Brédas, J. E. Ehrlich, J. Y. Fu, A. A. Heikal, S. E. Hess, T. Kogej, M. D. Levin, S. R. Marder, D. McCord-Maughon, J. W. Perry, H. Röckel, M. Rumi, C. Subramaniam, W. W. Webb, X. Wu, and C. Xu, Science **281**, 1653 (1998).

[56] D. Beljonne, W. Wenseleers, E. Zojer, Z. G. Shuai, H. Vogel, S. J. K. Pond, J. W. Perry, S. R. Marder, and J. L. Brédas, Adv. Funct. Mater. **12**, 631 (2002).

[57] S. Mazumdar, S. Dallakyan, and M. Chandross, Synth. Met. **139**, 769 (2003).

[58] R. R. Birge, J. A. Bennett, B. M. Pierce, and T. M. Thomas, J. Am. Chem. Soc. **100**, 1533 (1978).

[59] M. Rumi, J. E. Ehrlich, A. A. Heikal, J. W. Perry, S. Barlow, Z. Hu, D. McCord-Maughon, T. C. Parker, H. Röckel, S. Thayumanavan, S. R. Marder, D. Beljonne, and J. L. Brédas, J. Am. Chem. Soc. **122**, 9500 (2000).

[60] M. Drobizhev, Y. Stepanenko, Y. Dzenis, A. Karotki, A. Rebane, P. N. Taylor, and H. L. Anderson, J. Am. Chem. Soc. **126**, 15352 (2004).

[61] K. Ohta and K. Kamada, J. Chem. Phys. **124** (2006).

[62] Y. Zhao, A. D. Slepkov, C. O. Akoto, R. McDonald, F. A. Hegmann, and R. R. Tykwinski, Chem. Eur. J. **11**, 321 (2004).

[63] S. Kershaw, *Two Photon Absorption*, in Characterization Techniques and Tabulations for Organic Nonlinear Optical Materials, edited by M. G. Kuzyk and C. W. Dirk (Marcel Dekker, New York, 1998).

[64] K. Kamada, in *Nonlinear Optical Transmission and Multiphoton Processes in Organics II*, Proc. of SPIE, **5516**, pp. 97-105, 2004.

CHAPTER 5:

THIRD-ORDER NLO DYNAMICS AND TWO-PHOTON ABSORPTION IN TWO-DIMENSIONALLY-CONJUGATED BENZENE-CORE ISOMERS

5.1 Context

Tetrakis(phenylethynyl)benzenes (TPEBs) are two-dimensionally-conjugated chromophores that present disparate nonlinear optical response as a function of donor/acceptor substitution symmetry about a central benzene core. TPEBs display large two-photon absorption (TPA) cross-sections across the vis/NIR range, as well as interesting excited-state absorption and Kerr dynamics. We have studied the nonlinear optical properties of this series of constitutional isomers in an effort to link the Kerr nonlinear dynamics as obtained by the birefringent DOKE polarization condition (See Chapter 2) with the excited-state dynamics obtained by the dichroic DOKE polarization condition. Furthermore, we have mapped out the two-photon absorption spectrum in TPEBs with a tuneable-wavelength z-scan setup. The TPEB study comprises a large collaboration between our group at the University of Alberta (DOKE, optical characterization), Dr. Michael Haley's group at the University of Oregon (synthesis/characterization),[1,2] and Drs. Kenji Kamada and Koji Ohta at AIST in Japan (z-scan, theory). I personally obtained the TPEB z-scan measurements reported herein during a brief research stint at AIST in early 2006. The following chapter presents a full description of results obtained from various ultrafast nonlinear-optical characterization experiments conducted on the TPEB isomers. The nonlinear absorption dynamics and two-photon absorption cross-sections measured at 800 nm with the DOKE setup have been previously reported in an SPIE proceedings paper.[3] Linear spectroscopic characterization, molecular orbital plots, and structural considerations have previously been published by Professor Haley's group.[1,2]

5.2 Introduction

Conjugated molecules that utilize an arylated core are widely studied as advanced functional materials for nonlinear optical applications. The majority of these compounds (and oligomers), such as stilbene-,[4-7] fluorene-,[6,8-11] (*p*-phenylene)vinylene-,[8,12,13] diacetylene-,[14,15] and (*p*-phenylene)ethynylene-based chromophores,[16,17] utilize a quasi-one-dimensional axis of conjugation. Recent studies have motivated the investigation of two-dimensionally-conjugated motifs as promising materials for nonlinear optics.[18-21] By extending conjugation in many directions, the delocalized electron density and oscillator strength may be increased, without a corresponding reduction in absorption energy.[22] Furthermore, both quadrupolar and octupolar geometries are garnering support as design motifs for highly-efficient two-photon absorbing chromophores. Thus, there has been a recent flurry of papers reporting on the nonlinear optical response of various two-dimensional compounds that contain conjugated arms substituted about a central benzene core.[3,18,20,23-25] Depending on the substitution symmetry, such molecules range from dipolar, through quadrupolar, to octupolar.[26]

Cross-shaped chromophores are two-dimensionally conjugated structures that have received considerable attention for their usefulness towards studying the effects of donor/acceptor substitution symmetry on (nonlinear)optical properties.[3,22,27-29] Seminal collaborative work, led by Professor Francois Diederich of ETH-Zurich, has studied the contributions of 'linear-', 'bent-', and 'cross-conjugated' donor-acceptor (D→A) intramolecular charge transfer routes across an ethene bridge to the overall molecular second hyperpolarizability, γ. These studies on tetraethynylethene-based (TEE) chromophores (see Fig. 5.1), have been recently, extended to measurements of two-photon absorption.[28]

We endeavor to study the two-photon absorption spectra and nonlinear optical dynamics in chromophores analogous to TEEs, but which contain a central benzene core, as opposed to an ethene bridge. Our tetrakis(phenylethynyl)benzenes (TPEBs) are cross-

shaped molecules with highly conjugated arms extending from a central benzene core, affording them a (quasi)planar geometry (See Fig. 5.1). As illustrated in Fig. 5.1, the TPEBs have conjugation schemes analogous to those in the TEEs, wherein donor - acceptor paths can be either linearly-conjugated (*para*-linked), 'bent-conjugated' (*ortho*-lined), or cross-conjugated (*meta*-linked). In the past, Diederich *et al.* established γ structure-property relationships with non-resonant third-harmonic generation (THG) and degenerate four-wave mixing (DFWM) at one or two wavelengths; with the assumption that the nonlinearities are minimally dispersive away from resonance.[22,27,29] Furthermore, recent reports on the two-photon absorption activity of similar structures were conducted at a single wavelength, and thus did not describe the TPA spectrum of these systems.[28] The optical and nonlinear optical properties of TPEBs (and one-dimensional analogues) are garnering considerable interest.[2,23,26,30-32] Currently, the mechanism for charge-transfer between *meta*-lined arms are attracting attention, as *meta*-linkages are expected to lead to electronic de-coupling in the ground-state.[31-35] The comparatively large and long-lasting excited-state optical activity of some *meta*-linked chromophores—otherwise known as the 'meta-effect'—is drawing interest for various light-emitting diode applications.[30] Despite this interest, a systematic study of the two-photon absorption spectrum and nonlinear-optical dynamics in such systems has, to our knowledge, never been achieved.

The conjugation motif of TPEBs is particularly advantageous for studying TPA in highly-conjugated systems. By varying the peripheral donor/acceptor substitution symmetry, constitutional isomers of various (multi)polar geometries may be created, motivating studies of structure-property relationships between donor/acceptor geometry/substitution and two-photon absorption: Early TPA studies showed that incorporating strong donor (D) and/or acceptor (A) groups across a conjugated backbone can lead to order-of-magnitude increases in the molecular two-photon cross-section, $\sigma^{(2)}$.[36] Subsequently, other studies have looked to establish structure-property relationships for donor-acceptor substitution symmetry, with most studies finding a D-π-D scheme favorable to D-π-A.[6,37-39] Other studies, however, suggest an A-π-D scheme as favorable to D-π-D.[40]

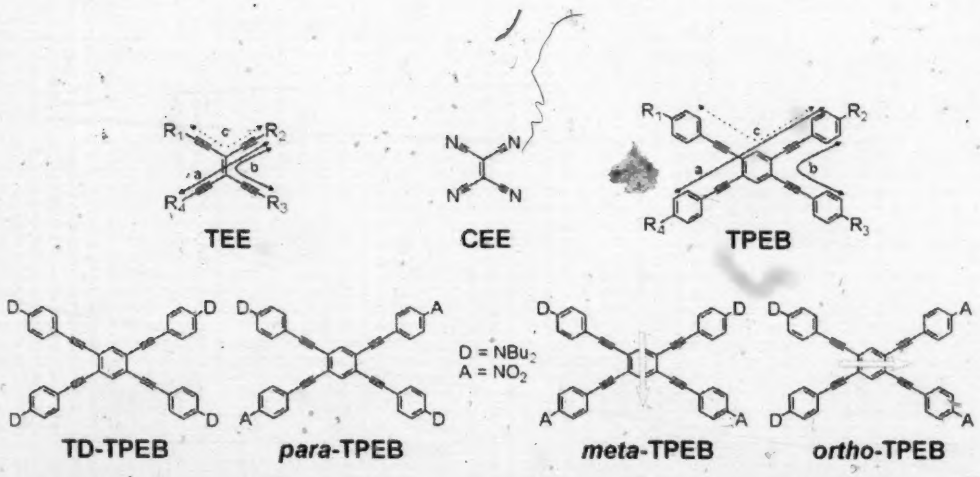

Figure 5.1. Conjugation routes and general structure of the studied tetrakis(phenylethynyl)benzenes (TPEBs) and the analogous TEE and CEE motifs studied by other groups.[22,28] **TD-TPEB** and ***para*-TPEB** are quadrupolar and lack permanent dipole moments. ***meta*-TPEB** and ***ortho*-TPEB** are the dipolar isomers of ***para*-TPEB** (dipoles are shown as gray-filled arrows). Conjugation in TEE type structures is described in terms of three routes; (a) trans-conjugation (linear), (b) cis-conjugation ('bent'), and (c) geminal (coss-conjugation). Similarly, conjugation paths in TPEBs follow (a) linear conjugation (*para*-linked), (b) bent-conjugation (*ortho*-linked), and (c) cross-conjugated (*meta*-linked).

CHAPTER 5: 2-DIMENSIONALLY CONJUGATED TPEBS

It has been shown that TPA in non-symmetric (dipolar) molecules differs considerably from that in symmetric (quadrupolar, for example) systems that lack permanent dipole moments.[38] Furthermore, whereas in dipolar systems two-photon transitions follow the same selection rules as one-photon absorption (OPA), in quadrupolar systems, direct one-photon and two-photon transitions are strictly exclusive.[37,41] Thus, not only is the peak TPA cross-section differently described in dipolar and quadrupolar systems, but they also display differing spectral characteristics.

Whereas recent studies have increasingly explored higher-dimensionality and dendritic systems,[18,20,21,42] most studies have focused on quasi-one-dimensional molecular architectures. Thus, studies that have attempted to draw conclusions about the effect of donor-acceptor substitution on the TPA activity in linear conjugated molecules have had to compare systems of disparate ground-state polarization. For example, several studies have reported that the substitution of π-donors contributes more to $\sigma^{(2)}$ than π-acceptor substitution. As proof of this structure-property relationship, the higher peak $\sigma^{(2)}$-values in D-π-D over D-π-A schemes are typically quoted.[6] However, while the former arrangement is quadrupolar, the latter is dipolar, and thus their TPA activity may have more to do with symmetry and ground-state polarization than with the direct influence of D/A substitution. As illustrated in Fig. 5.1, TPEB geometry allows for studies of both the effects of benzene-core substitution symmetry and (multi)polar geometry on TPA activity. Specifically, in going from the all-donor **TD-TPEB** to the ***para*-TPEB**, one can study the effect of introducing acceptors to an all-donor system, while maintaining quadrupolar geometry. Additionally, comparisons between ***meta*-TPEB** and ***ortho*-TPEB** can study the effects of linear-, bent-, and cross-conjugation through a benzene core on TPA while maintaining dipolar geometry. In the following, we present a study of the two-photon absorption spectra of TPEBs, as obtained by ultrafast z-scan, in addition to femtosecond Kerr and excited-state dynamics measured with the DOKE technique at a wavelength of 800 nm.

5.3 Experimental

Z-scan measurements of TPEBs were conducted in dilute (11 mM) THF solutions. Open-aperture z-scan experiments (see §1.3) were conducted at AIST in Japan on a well-established setup, as detailed elsewhere.[43] For these measurements, amplified 800 nm Ti:Sapphire laser pulses at a 1 kHz repetition rate were sent to an optical parametric amplifier (OPA) for wavelength tunability. The OPA was used for the ranges of 580-750 nm and 855-1130 nm. For the 770-830 nm range, the mode-locked oscillator was tuned to the appropriate wavelength, amplified, and sent directly to the sample; circumventing the OPA. For each wavelength, the pulse duration was monitored and the intensity/photodiode-voltage relationship was calibrated, thus allowing us to obtain absolute TPA cross-sections, $\sigma^{(2)}$. Nonetheless, z-scan TPEB measurements were iteratively compared to MPPBT [44] and/or 1,4-bis(*p*-dibutylaminostyryl)-2,5-dimethoxybenzene, as a reference sample (compound **8** in Ref. 59). For each sample and measurement, global fits to z-scan profiles were obtained at various intensities to guarantee signal linearity and thus purity of the two-photon absorption process. The final TPA spectra of all samples were compared and, when necessary, globally calibrated to that of known MPPBT and 1,4-bis(*p*-dibutylaminostyryl)-2,5-dimethoxybenzene spectra. The UV-vis spectrum of every sample was obtained before and after the z-scan measurements to check for sample degradation. Slight degradation (<<1%, as observed by UV-vis) was observed for the ***ortho*-TPEB** and **TD-TEP** samples over a period of two weeks, but they displayed no perceptible change in TPA activity.

We also measured the (800 nm) ultrafast time-resolved nonlinearities in TPEBs with the DOKE technique. DOKE measurements were conducted in dilute solutions (5 mM – 33 mM) of TPEB in THF. The standard DOKE protocol, as outlined in Chapter 2, was followed. γ-values are referenced to a pure THF sample ($\gamma_{THF}=5.2\times10^{-37}$esu), and $\sigma^{(2)}$-values are relative to that of MPPBT ($\sigma^{(2)}_{MPPBT}=380$ GM; $\lambda=800$ nm). Typical pump

powers of 0.5-1.5 mW were used for the birefringent DOKE conditions, while pump powers as high as 2.0 mW were used for the dichroic DOKE condition. Samples showed good signal linearity at these powers and concentrations. Deviations from DOKE signal linearity were observed at a concentration of 60 mM, possibly indicating photo-degradation or aggregation effects. DOKE measurements were repeated numerous times over a period of four years, and displayed extremely consistent results for sample concentrations below 20 mM and pump powers at or below 2.0 mW.

In order to further investigate the relationship between TPA and OPA in the D/A TPEB isomers, we conducted 400 nm pump-800 nm probe transient absorption (TA) measurements. For transient absorption measurements, the intense (up to 9 mW) 800 nm pump beam was used to generate up to 500 μW of second-harmonic 400 nm light in a 2 mm thick α-BBO crystal. The α-BBO crystal was not optimized for second-harmonic generation at 800 nm, and had to be rotated three-dimensionally to find the maximum generation condition. For TA experiments, 230 μW of the 400 nm light was used as an absorbing pump beam. Transient absorption was measured with the standard DOKE 800 nm probe beam detected at the pump chopping frequency, by monitoring modulation of the total *A-B* signal.

5.4 Results and Discussion

Two-Photon Absorption Spectra: The z-scan-obtained TPA spectra of the four TPEBs are shown in Fig 5.2, overlaid with their one-photon UV-vis spectrum, and actual absorption at the experimental conditions. In all four samples a TPA peak is resolved in the 600-1100 nm range. The tetra-donor sample, **TD-TPEB,** displays the largest peak cross section, $\sigma^{(2)}$=520±30 GM, while ***para*-TPEB** has the lowest, at $\sigma^{(2)}$=240±20 GM. The dipolar samples, ***meta*-TPEB** and ***ortho*-TPEB** show very similar TPA spectra, while the quadrupolar samples, **TD-TPEB** and ***para*-TPEB** show unique spectra. ***meta*-TPEB** and ***ortho*-TEP** have nearly identical cross-section peak values of $\sigma^{(2)}$=400±20 GM, and 440±20 GM, respectively. As discussed in Chapter 1, in the simplest approximation, the TPA peak in dipolar molecules which have a one-photon absorption (OPA) spectrum that is dominated by a single low-energy absorption are often described by a two-level model,[5] given by Eqn. 1.7:

$$\sigma_{2-level}^{(2)} \approx \frac{L^4}{5n^2c^2\varepsilon_0\hbar}\frac{M_{ge}^2\left(\mu_e-\mu_g\right)^2}{\Gamma_{ge}}, \qquad 1.7$$

where L^4 is the local-field factor; μ_e, μ_g, and M_{ge} are the dipole in the two-photon state, the dipole in the ground state, and the transition dipole between the two states, respectively; and Γ_{ge} is the transition linewidth (see §1.2). Because of structural asymmetry, TPA in dipolar molecules may occur to the lowest-lying one-photon level, and thus the two-photon spectrum often follows that of the one-photon spectrum (or UV-vis spectrum).[38,45] Indeed, we see that the TPA spectrum of both ***meta*-TPEB** and ***ortho*-TPEB** follow closely the rise and lowest peak of the OPA spectrum at the same photon sum energy. In the case of the dipolar TPEBs, a claim that the UV-vis spectrum is dominated by a single low-energy absorption is tenuous. Thus, past the low-energy TPA peak (and OPA peak), the TPA spectrum no longer follows that of the OPA spectrum. This is probably due to coupling to higher excited states,[41] and is not unexpected. Related to this coupling is a sharp upturn in the TPA spectrum at higher energies, as the photon-energy approaches that of the absorption edge, as can be seen in Fig. 5.2. Specifically, for the wavelength of 580 nm, there is very little residual one-photon

absorption, but $\sigma^{(2)}$ increases dramatically. This effect has been reported by others for symmetric systems, and is generally referred to as 'double resonance' (see §1.2). Double resonance involves tuning the photon energy to a one-photon level that acts as a virtual level, and is typically attributed to the two-photon Term III in Eqn. 1.5. As mentioned in Chap. 1, and reiterated below, Term III is dominant in symmetric system in which two-photon transitions are exclusive of one-photon transitions. Because dipolar molecules such as ***meta*-TPEB** and ***ortho*-TPEB** are unrestricted by this selection rule, while Term II (in Eqn. 1.5) usually describes the low-energy TPA peak, it is possible for Term III to significantly contribute to TPA activity in the higher-energy region.[5] The fact remains that double-resonance is a phenomenon that is typically observed/predicted in symmetric systems,[11,44,46] and that the observed $\sigma^{(2)}$-enhancement as the absorption edge is approached in ***meta*-TPEB** and ***ortho*- TPEB** may be among the first reported examples of double-resonance in dipolar systems. Further resolution of this feature is hindered by the onset of linear sample absorption that prevents accurate measurements of TPA activity.

Unlike the case for dipolar systems, the low-energy TPA spectra in the quadrupolar **TD-TPEB** and ***para*-TPEB** are considerably blue-shifted with respect to their OPA spectra. In these molecules, the lowest one-photon transition is two-photon allowed, and *vice versa*. Standard energy level alternacy typically has the ground state as *gerade* ($1A_g$) followed by an *ungerade* excited-state ($1B_u$) and a higher *gerade* ($2A_g$) level,[47-49] as discussed in Chapter 1. A simple three-level model, that describes a *gerade-gerade* TPA transition that is mediated by an *ungerade* intermediate level, is typically utilized to describe the low-energy TPA peak in quadrupolar systems. As described in Chapter 1 and in the preceding paragraphs, this three-level model arises through the assumption that Term III in Eqn 1.5 dominates over terms involving linear absorption and (the absent) permanent dipole moments. Peak $\sigma^{(2)}$ values in the three-level model are described by Eqn. 1.8:

$$\sigma^{(2)}_{3-level} \approx \frac{L^4}{5n^2c^2\varepsilon_0\hbar}\frac{\left(E_{e'}-E_g\right)^2 M^2_{ge}M^2_{ee'}}{\left[2\left(E_e-E_g\right)-\left(E_{e'}-E_g\right)\right]^2\Gamma_{ge'}}. \qquad 1.8$$

The lowest-energy TPA peak in ***para*-TPEB** is found between the two lowest one-photon-allowed peaks, indicating that A_g-B_u-A_g alternacy is maintained. This spectral

peak is assumed to correspond to the HOMO → LUMO+1 transition, and is thus well described by the three-level model. In the case of the all-donor **TD-TPEB** the situation is more ambiguous: The lowest-energy TPA peak is found blue shifted with respect to the two (or three)[50] lowest OPA peaks.

Analysis of the TPEB frontier molecular orbital maps, shown in Figs. 5.3-5.6, may explain the unusually large blue-shift in the TPA spectrum of **TD-TPEB**:[2] ***para*-TPEB** is of C_{2h} symmetry, and thus allows for some two-photon transitions within the HOMO-1, HOMO, LUMO, and LUMO+1 orbitals. **TD-TPEB**, on the other hand, is of D_{4h} symmetry, and no TPA paths are allowed within these lowest-lying orbitals.[51] Thus, a simple three-state model is insufficient for describing TPA in **TD-TPEB**. Recently published theoretical studies of TPA in TPEBs have also identified the importance of TPA transitions to high-lying levels, but have not identified any TPA resonances in wavelengths greater than 520 nm.[23] Our results are in clear disagreement with this prediction, as both chromophores display a continuum of two-photon absorption commencing at approximately 900 nm, with large cross-section peaks in the near-IR. Overall, the all-donor species shows the higher cross-section of the two, with a peak cross-section that is more than twice the size of that in ***para*-TPEB**.

As in the case for dipolar ***meta*-TPEB** and ***ortho*-TPEB**, double resonance is observed in quadrupolar **TD-TPEB** and ***para*-TPEB**. This double resonance is particularly strong in ***para*-TPEB**, for which $\sigma^{(2)}$ increases six-fold over a 70 nm spectral range, as can be seen in Fig. 5.2. By a wavelength of 580 nm, ***para*-TPEB** already displays the largest two-photon absorption of any studied TPEB, while still exhibiting the lowest residual one-photon absorption. This upturn in the TPA spectrum is extremely sharp, paralleling the steep absorption edge displayed by the solution at the experimental concentration (shown as hatched gray in Fig. 5.2).

Transition- and Permanent-Dipole Moments in TPEBs: The quantitative theoretical description of TPA in molecular systems according to Eqns. 1.7 and 1.8 requires knowledge of the transition dipole moments $\boldsymbol{M_{ge}}$ and $\boldsymbol{M_{ee'}}$. As was described in Chapter 1, the transition dipole moment is given by Eqn. 1.5: [15,40,52]

$$\overline{M}_{mn} = \langle m | \overline{\mu} | n \rangle = -e \int \psi_m^*(\bar{r}) \bar{r} \psi_n(\bar{r}) d\bar{r} = -e \int \bar{r} \bar{\rho}_{m \to n}(\bar{r}) d\bar{r} . \qquad 1.5$$

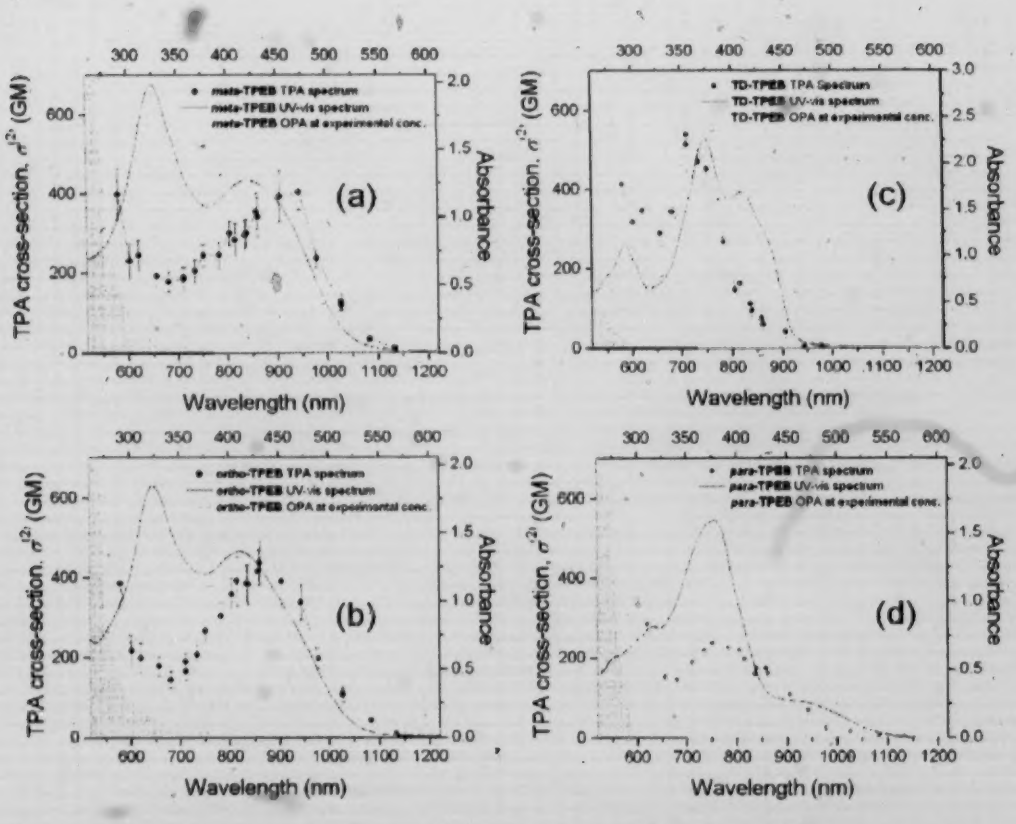

Figure 5.2: Two-photon absorption spectra of TPEBs (bottom and left axes). The UV-vis spectrum is overlaid (top and right axes) to match the same total photon energy with TPA. Also included is the sample absorption at experimental concentration (bottom & right axes). (a) dipolar meta-TPEB; (b) dipolar ortho-TPEB; (c) quadrupolar TD-TPEB; (d) quadrupolar para-TPEB.

Thus, a transition dipole moment may be considered a spatial integral of a transition density map, $\overline{\rho}_{m\to n}(\vec{r})$, where this density map is a product of the wavefunctions of the m and n states between which the transition takes place. Typically, $\overline{\rho}_{m\to n}(\vec{r})$ and $\overline{M}_{mn}$ are calculated by the intermediate neglect of differential overlap (INDO) approximation.[15] In the absence of a rigorous calculation, we have used TPEB molecular orbital maps (wavefunctions) to sketch a qualitatively instructive picture of the transition density for each transition between the HOMO-1 and LUMO+1.[53] In the same way that the molecular orbital maps shown in Figs. 5.3-5.6 provide an indication of the magnitude and direction of permanent dipole moments, the transition density maps (also shown in Figs.

5.3-5.6) provide a glimpse towards the magnitude and direction of the transition dipole moments that contribute to TPA in TPEBs.

Figure 5.3 presents the molecular orbital plots (for HOMO-1 through to LUMO+1)[2] and transition density maps for **TD-TPEB**. The symmetry of the orbital plots in **TD-TPEB** indicates that there are no permanent dipole moments at any of these energy levels, consistent with the centro-symmetry of this molecule. Furthermore, there is not expected to be any transition dipole moment for either the HOMO-1→HOMO or the LUMO→LUMO+1 transitions. Thus, none of these energy levels may be expected to contribute to TPA in **TD-TPEB** according to either Eqns. 1.7 or 1.8. Figure 5.6 presents the orbital and transition density plots for ***para*-TPEB**. As in the case for **TD-TPEB**, ***para*-TPEB** is centrosymmetric, and does not possess any permanent dipole moments. Unlike **TD-TPEB**, however, ***para*-TPEB** does possess transition dipole moments for all three of the lowest transitions. While the HOMO→LUMO transition moment is relatively small, the LUMO→ LUMO+1 (and HOMO-1→HOMO) transition displays large transition density. Overall, however, the two transition dipole moments are oriented at approximately 60° to each other, thus somewhat diminishing their interaction, as described in Chapter 1.

Figures 5.4 and 5.5 present the respective orbital and transition density maps for ***meta*-TPEB** and ***ortho*-TPEB**. Both samples display relatively large dipole moments, with values of 11.1 D and 14.9 D (in the ground state), respectively.[54] From the LUMO orbital maps, the dipoles are seen to be in the opposite direction to those in the HOMO, thereby indicating a very large dipole moment differences, μ_{HOMO}-μ_{LUMO}. The transition density maps indicate a small $M_{HOMO \rightarrow LUMO}$ for ***ortho*-TPEB**, and a larger one for ***meta*-TPEB**. The two-level model of TPA in dipolar systems, is consistent with these plots for explaining the similarities in the TPA spectra between these two chromophores. Slightly larger dipole moments are compensated for by slightly a smaller transition dipole moment in ***ortho*-TPEB**, as compared with ***meta*-TPEB**, thereby indicating a similar peak $\sigma^{(2)}$-value. As indicated in Fig. 5.4, $M_{HOMO \rightarrow LUMO}$ and $M_{LUMO \rightarrow LUMO+1}$ are orthogonal in ***meta*-TPEB**. The relative alignment of transition dipoles in ***meta*-TPEB** may help explain some of the observed Kerr and ESA dynamics in these systems, as obtained by DOKE.

	$\lambda_{max1}(\varepsilon_1)$	$\lambda_{max2}(\varepsilon_2)$	$\sigma^{(2)}(\lambda_{peak})$	μ	sym.	γ/γ_{THF} @800nm	Decay Rates, Kerr	Decay Rates, NLA	Decay Rates, TA
	nm ($mol^{-1}cm^{-1}L$)	nm ($mol^{-1}cm^{-1}L$)	GM (nm)	D			ps	ps	ps
TD-TPEB	373 (119,500)	414 (94,300)	520±30 (710)	0	D_{4h}	670±60	4.4, 350	9, 306	N.M.
***meta*-TPEB**	325 (72,800)	426 (50,100)	400±20 (940)	11.3	C_{2v}	-450±100	<u>2.7</u> , 24	<u>2.1</u> , 21	<u>2</u> , 22.5
***ortho*-TPEB**	323 (61,800)	417 (45,200)	440±20 (860)	14.9	C_{2v}	-600±150	<u>1.6</u> , 32	<u>3.5</u> , 39	<u>2.9</u> , 36
***para*-TPEB**	379 (90,100)	466 (15,000)	240±20 (750)	0	C_{2h}	-100±150	<u>1.2</u> , 21.5	<u>1</u> , 30.5	<u>1.6</u> , 21

Table 5.1. Summary of optical and nonlinear optical parameters in TPEBs. Decay rates are obtained from bi-exponential fits of Eqn. 5.1. Underlined are rise times, as opposed to decay times. γ-Values obtained at a wavelength of 800 nm are presented relative to that of the solvent THF; $\gamma_{THF}=5.2\times10^{-37}$esu. λ_{max} are the wavelengths of the lowest energy peaks in the peak one-photon absorption spectra; ε is the molar absorptivity corresponding at the peak. N.M, not measured.

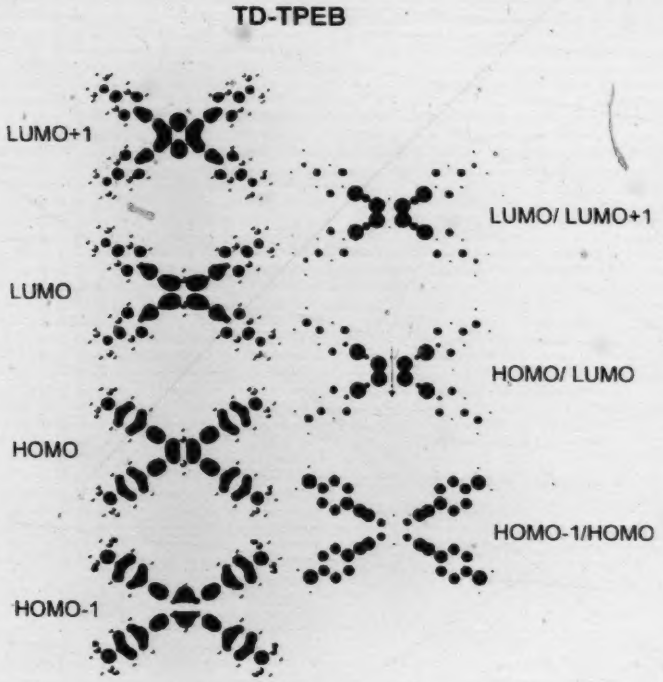

Figure 5.3. [colour] Molecular orbital and transition density maps of the lowest lying states/transitions in **TD-TPEB**. Molecular orbital maps were calculated with Gaussian 98 at the B3LYP/6-31G* level of DFT, by Haley *et al.*[2] Transition density maps were sketched by hand by overlapping the appropriate MO maps. Within each map, the two different colors represent different phases of the wavefunction /transition density. A net transition dipole is denoted with a black arrow on the transition density maps.

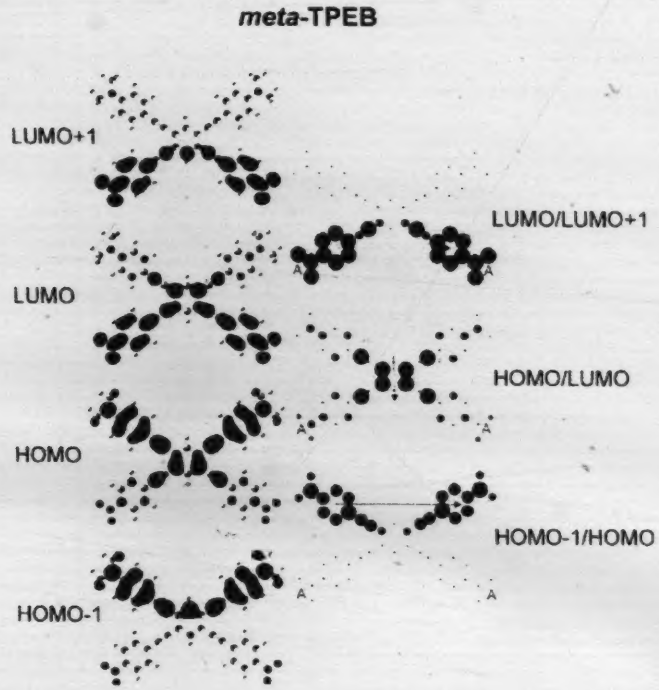

Figure 5.4. [colour] Molecular orbital and transition density maps of the lowest lying states/transitions in ***meta*-TPEB**. Molecular orbital maps were calculated with Gaussian 98 at the B3LYP/6-31G* level of DFT, by Haley *et al.*[2] Transition density maps were sketched by hand by overlapping the appropriate MO maps. Within each map, the two different colors represent different phases of the wavefunction /transition density. A net transition dipole is denoted with a black arrow on the transition density maps.

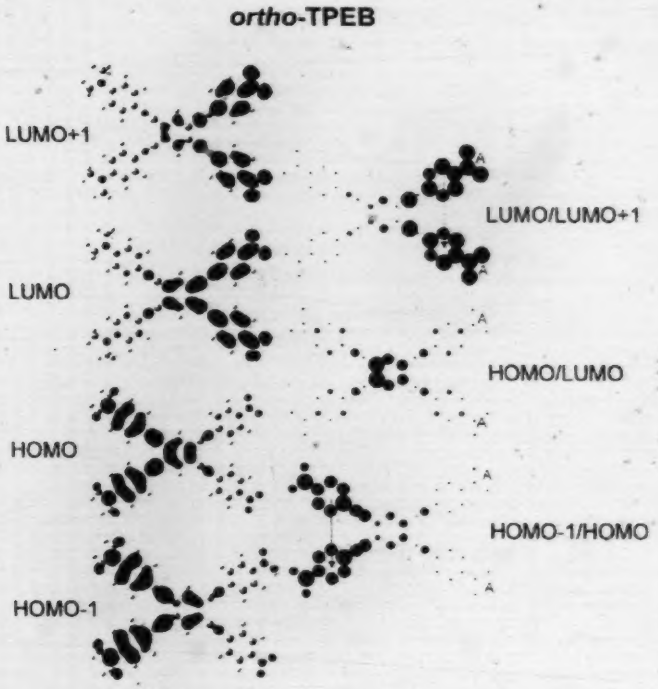

Figure 5.5. [colour] Molecular orbital and transition density maps of the lowest lying states/transitions in ***ortho*-TPEB**. Molecular orbital maps were calculated with Gaussian 98 at the B3LYP/6-31G* level of DFT, by Haley *et al.*[2] Transition density maps were sketched by hand by overlapping the appropriate MO maps. Within each map, the two different colors represent different phases of the wavefunction /transition density. A net transition dipole is denoted with a black arrow on the transition density maps.

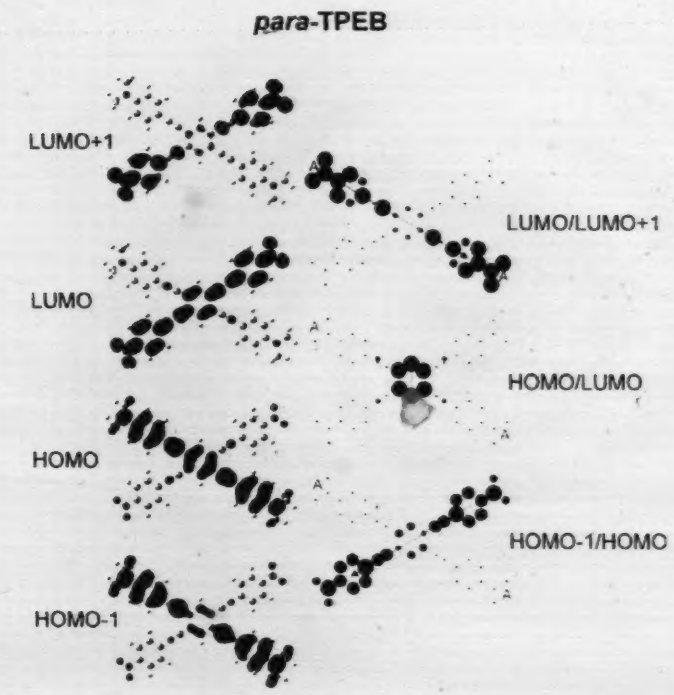

Figure 5.6. [colour] Molecular orbital and transition density maps of the lowest lying states/transitions in ***para*-TPEB**. Molecular orbital maps were calculated with Gaussian 98 at the B3LYP/6-31G* level of DFT, by Haley *et al.*[2] Transition density maps were sketched by hand by overlapping the appropriate MO maps. Within each map, the two different colors represent different phases of the wavefunction /transition density. A net transition dipole is denoted with a black arrow on the transition density maps.

DOKE-Obtained Nonlinear Absorption Dynamics at 800 nm: The time-resolved nonlinear absorption dynamics of the TPEB series are presented in Fig. 5.7. All four samples display an instantaneous nonlinear absorption component that closely follows the cross-correlation of the 800 nm pump and probe pulses. This component is attributed to two-photon absorption in which one photon is absorbed from each of the pump and probe beams. At 800 nm, ***ortho*-TPEB** displays the largest TPA of the four samples. ***para*-TPEB** and ***meta*-TPEB** show relatively similar responses, which are approximately 60% that of ***ortho*-TPEB**. TD-TPEB shows the lowest TPA at this wavelength, with a cross-section that is ≈35% that of ***ortho*-TPEB**. It should be noted that with the exception of ***para*-TPEB**, for which 800 nm is very near the TPA maximum, for all three other TPEBs, 800 nm lies in a strongly dispersive range of the two-photon absorption spectrum, and thus changes (uncertainties) in laser wavelength can lead to significant changes in the measured $\sigma^{(2)}$-values. With this in mind, these DOKE-obtained values are consistent with those obtained by z-scan at 800 nm, as are presented in Fig. 5.2.

In all four samples, TPA gives way to long-lasting excited-state absorption (ESA) dynamics, in which TPA from the pump beam is followed by single-photon absorption from the probe beam, as described in §2.3. Fig. 5.8 presents NLA dynamics in a semi-log scale fitted to bi-exponential rate-equations of the form

$$S(t) = a + be^{-t/\tau_1} + ce^{-t/\tau_2}, \qquad 5.1$$

where $S(t)$ is the amplitude of the measured response ($\tanh\phi''$). For all traces in Fig. 5.8, the fits required no offset ($a = 0$), and included probe delay times longer than 1.5 ps—to avoid any convolution with the TPA response. In the two dipolar species, ***ortho*-TPEB** and ***meta*-TPEB**, there is a rise to an absorbing state that is relatively well separated from the initial TPA transition. A smaller and less-well resolved rise is observed in ***para*-TPEB**. In **TD-TPEB**, however, a separate rise to an absorbing excited-state is not observed, but ESA in this quadrupolar species is considerably larger than in its D/A counterpart, ***para*-TPEB**. For the three D-A isomers, the longer-lasting decays are relatively similar among the three samples, showing rates of 20-40 ps. In **TD-TPEB**, after an initial 9 ps decay, long-lasting residual absorption is observed (τ_{decay}≈300 ps) that

decays with a time considerably longer than the measured range. In general, time-resolved dichroism measurements are sensitive to a host of electronic, solvent and solute dynamics.[55-57] In many cases, the various relaxation mechanism can often be elucidated based on the timescale with which they take place, and in their dependence on temperature/viscosity. As Zhang and Berg have shown in a series of papers on the absorption anisotropy measurements on anthracene in phenol, inertial dynamics on the 100 fs scale are followed by sub-picosecond solvation dynamics, and sub-nanosecond re-orientational diffusion.[55-57] In the case of D/A TPEBs, the ESA peaks at 4-9 ps after the primary TPA excitation are an interesting feature. These peaks represent a transition/relaxation from the TPA state to a lower-energy state from which absorption of 800 nm light can take place. Typically, intraband electronic relaxations would be expected to manifest at times below 100 fs. A slow ps timescale relaxation may indicate an interband transition. The fact that this feature is only observed in the D/A TPEBs, and is most prominent in the dipolar species, may indicate that this peak represents a relaxation to a solvent-stabilized excited-state with lower energy, as is schematically represented in Fig 5.9. In this case, absorption from the ground-state with ground-state solvation geometry (S_0) takes place to a TPA state with ground-state solvation geometry. This excited-state (S_1) can relax to a state with appropriate solvation geometry and lower-energy (S_1^*).[58] Whereas in the non-polar ***para*-TPEB** this appears to occur quickly—within a fitted time of approx. 1 ps—in the dipolar ***meta*-TPEB** and ***ortho*-TPEB** this seems to occurs in 2.1 ps and 3.5 ps, respectively. Other studies that have looked at *meta*- and *para*-substituted donor-π-acceptor paths in bis(ethynyl)benzenes, have reported absorption to a neutral excited state that relaxes to an twisted intramolecular charge transfer (TICT) state. These systems have shown donor-to-acceptor electron transfer times of 4.5-5.5 ps,[30] in good agreement with our reported rise-times in the similarly-structured D/A TPEBs. As mentioned, the **TD-TPEB** sample shows both much longer ESA lifetimes and an apparent absence of picosecond timescale solvation dynamics. This may be linked to the fact that the tetra-donor sample has been shown to display much higher fluorescent activity than the other TPEBs.[2]

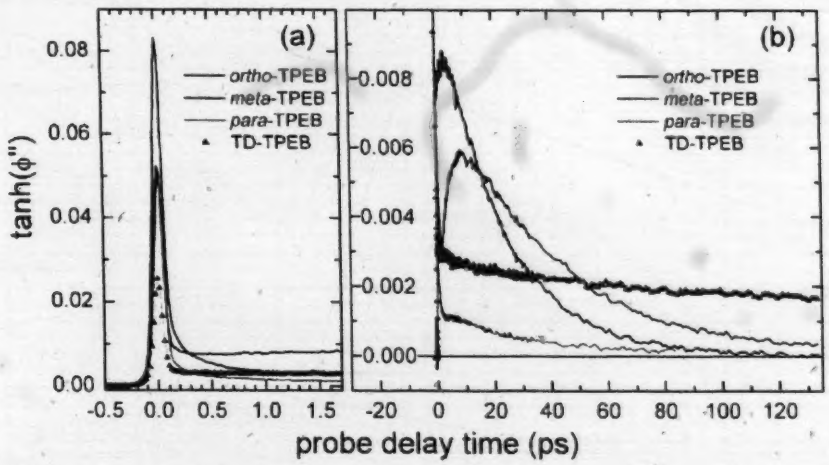

Figure 5.7. [colour] Dichroic DOKE condition measurements of TPEBs. (a) The ultrafast response that is centered about a probe delay time of zero represents the two-photon absorption process. The individual data points of the **TD-TPEB** trace are displayed to indicate the temporal resolution used. (b) The instantaneous TPA process gives way to long-lasting excited-state absorption dynamics. The donor-accepetor isomers show a rise and peak, corresponding to the population of the excited-state from which exponential-rate depopulation takes place.

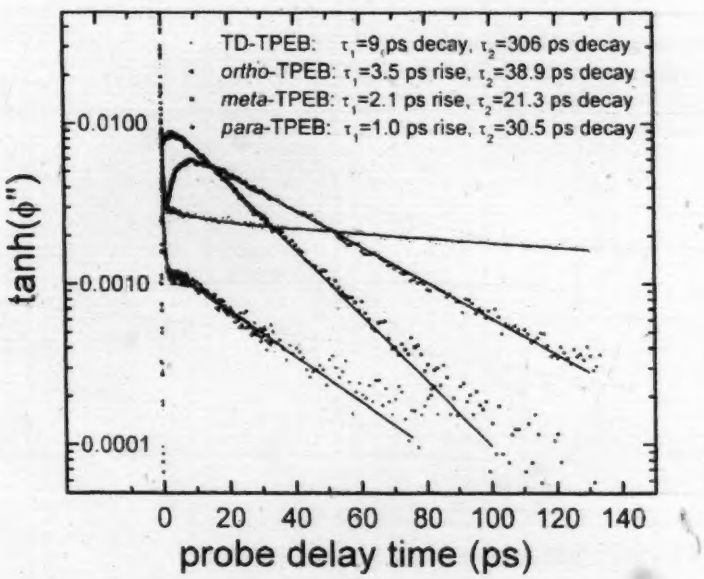
TD-TPEB: τ1=9 ps decay, τ2=306 ps decay
ortho-TPEB: τ1=3.5 ps rise, τ2=38.9 ps decay
meta-TPEB: τ1=2.1 ps rise, τ2=21.3 ps decay
para-TPEB: τ1=1.0 ps rise, τ2=30.5 ps decay
tanh(ϕ")
probe delay time (ps)

Figure 5.8. [colour] Two-photon-accessed excited-state absorption decays fit to a bi-exponential form (probe delay times >1.5 ps). None of the fits (solid lines) required an offset (term *a* in Eqn. 5.1).

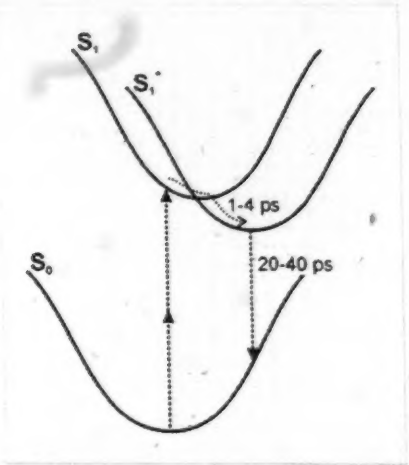

Figure 5.9. A simple model to account for the observed excited-state dynamics in Donor-Acceptor TPEBs. S_0 is the ground electronic state. State S_1 is the two-photon electronic state with the solvation geometry of the ground state. State S_1^* is the relaxed two-photon state with appropriate solvation geometry.

400 nm Pump-800 nm Probe Transient Absorption Dynamics: The investigated TPEBs have their low-energy one-photon absorption peak in the vicinity of 400 nm, and thus show strong absorption at this wavelength. The transient-absorption (TA) of 800 nm probe light subsequent to 400 nm pump absorption is shown in Fig. 5.10 for the D-A TPEB species. Transient absorption in **TD-TPEB** was not investigated due to the low availability of this sample at the time. As seen in Fig. 5.10, all three donor-acceptor samples show some level of long-lasting excited-state absorption. These traces are similar to those obtained by two-photon excitation at 800 nm, as discussed above. A rise to a temporally-distinct level is observed in all three samples, but is clearest in ***ortho*-TPEB**. As in the case of 800 nm-pumped NLA (Fig. 5.8), the TA signals shown in Fig. 5.10 were fit to the form of Eqn. 5.1. For ***ortho*-TPEB** and ***meta*-TPEB**, the same rise and decay times were found as for those excited by TPA. ***ortho*-TPEB** shows a 2.9 ps rise followed by a 35.5 ps exponential decay. ***meta*-TPEB** shows a 1.5 ps rise followed by a 22.5 ps exponential decay. Compared with the decay dynamics observed from 800 nm-pumped TPA state, ***para*-TPEB** shows a slightly lower decay rate of 21 ps from the 400 nm-pumped excited-state. Again, the 400 nm-excited transient absorption peaks observed between 2-10 ps in these chromophores are consistent with the aforementioned findings by Thompson et al., for the approximate charge transfer rate in the excited-state of molecules with similar D→A conjugation paths.[30]

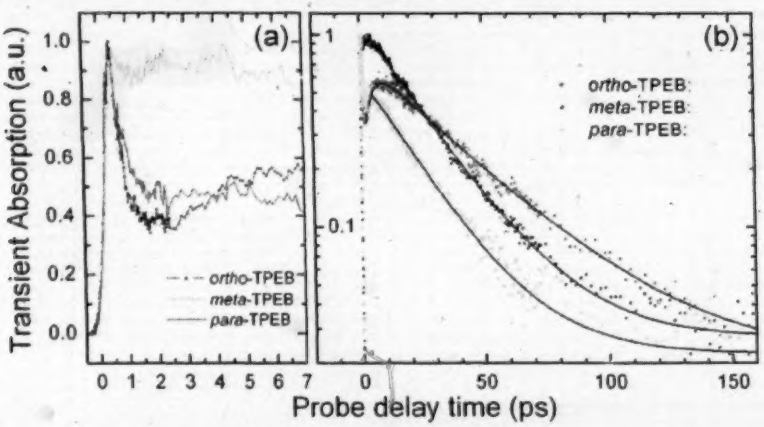

Figure 5.10. 400 nm pump-800 nm probe transient absorption signals of donor-acceptor TPEB isomers. After the initial excitation (a), a rise to another absorbing excited-state is observed (b) and is especially well resolved in the ***ortho*-TPEB** sample. (b) Fits to a bi-exponential form (solid lines) required a finite (but very small) offset *a* in Eqn. 5.1. Signals are normalized to the peak absorption value of 1. Decay dynamics are: ***para*-TPEB**, τ_1=1.6 ps (rise), τ_2=21 ps (decay); ***meta*-TPEB**, τ_1=2 ps (rise), τ_2=22.5 ps (decay); ***ortho*-TPEB**, τ_1=2.9 ps (rise), τ_2=35.6 ps (decay).

The similarities between the one-photon- and two-photon-pumped transient absorption dynamics in the dipolar molecules provide further confirmation that TPA and OPA is occurring to the same state in both ***ortho*-TPEB** and ***meta*-TPEB**. Furthermore, the indication is that the relaxation dynamics from these systems are not governed by the primary excitation process—a finding that is not unexpected. In ***para*-TPEB**, the differences in the secondary (20-30 ps) relaxation times may be a consequence of the fact that, in this sample, TPA does not take place into the lowest OPA level. Thus, it is possible that the 400 nm one-photon-pumped chromophore and the 800 nm two-photon-pumped chromophore have different relaxation routes and dynamics.

Kerr Nonlinearities and Excited-State Birefringence Dynamics: We have measured the birefringent nonlinearities in TPEBs at 800 nm using the birefringent DOKE polarization condition, as described in Chapter 2. All of the TPEB samples display an instantaneous response that follows the pump-probe cross-correlation response, and which is attributed to the ultrafast electronic (Kerr) nonlinearities. As in the case of the nonlinear absorption response measured with the dichroic DOKE polarization condition,

the instantaneous component gives way to a small but long-lasting response. The Kerr response of solutions of **TD-TPEB** in THF is slightly higher than that of the pure THF solvent; representing a positive nonlinearity. In the D/A TPEBs, however, the DOKE response is lower than that of the THF solvent; indicating a negative γ-value at 800 nm. As described in Chapter 2 and Eqn. 2.5, the solvent and solute nonlinearities are additive. Thus, to better elucidate the birefringent dynamics in the TPEB samples, the solvent-subtracted response is studied, as shown in Figure 5.11. For a robust analysis, however, γ-values are obtained from the instantaneous peak of the full solution response, rather than the solvent-subtracted response. This is because a manual subtraction of the externally-obtained solvent response invariably distorts the temporal signal profiles in the vicinity of the peak, as is observed in the subtracted responses of Figure 5.11. At times larger than a few pulse-lengths, these effects become minimal, and the birefringence dynamics of the solutes are elucidated, as shown in Fig. 5.12.

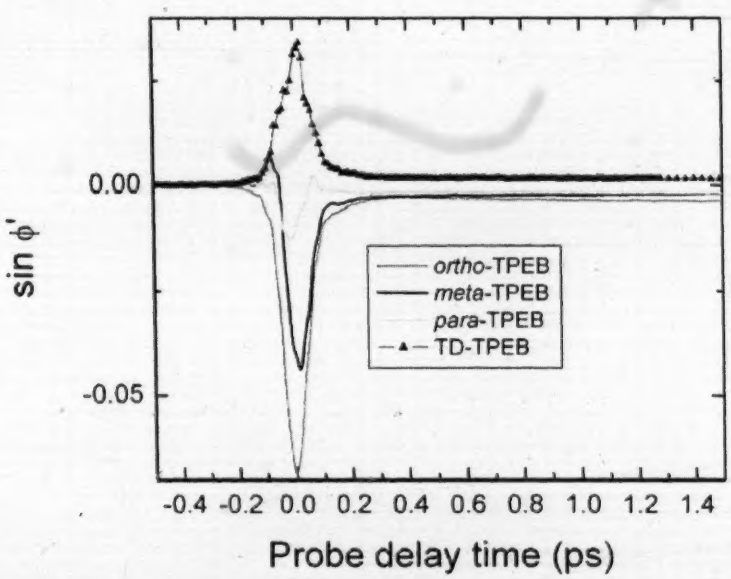

Figure 5.11. Refractive DOKE polarization condition TPEB scans—THF solvent response removed. Responses are ultrafast about a the probe's arrival time and represent the ultrafast electronic Kerr response. The subtraction of externally-obtained THF response introduces slight time-shifts and artifacts around the peak. **TD-TPEB**—shown with individual data points to illustrate scan resolution—is the only sample that shows a positive γ value at 800 nm. ***para*-TPEB** displays the lowest response.

In the vicinity of a strong TPA resonance, the real-component of the nonlinearity becomes very dispersive and follows the dispersive shape of the index of refraction. Unlike the index of refraction, which typically remains positive through the resonance, γ rises to a positive peak at the low-energy side of the absorption, and then becomes negative near the high-energy side of the resonance.[59-61] At the resonant wavelength, γ is zero. A comparison of the spectral position of the TPA peaks in the TPEB samples (Fig. 5.2) shows that 800 nm lies is on the low-energy side of the TPA peak in **TD-TPEB**; while it is on the high-energy side in ***ortho*-TPEB** and ***meta*-TPEB**. In ***para*-TPEB**, the TPA peak is resonant with 800 nm. Thus, the sign of the nonlinearities presented in Fig. 5.11 are consistent with this picture: **TD-TPEB** shows a positive nonlinearity of $\gamma=(670\pm60)\gamma_{THF}$; ***ortho*-TPEB** and ***meta*-TPEB** show negative nonlinearities of $\gamma=(-600\pm150)\gamma_{THF}$ and $\gamma=(-450\pm100)\gamma_{THF}$, respectively; and ***para*-TPEB** shows the lowest-magnitude nonlinearity of $\gamma=(-100\pm150)\gamma_{THF}$. The uncertainty in the size of the nonlinearity in ***para*-TPEB** arises from the fact that although for most scans this sample displayed a small negative nonlinearity, there were some scans where the response was slightly positive or even zero. Again, this is consistent with the idea that the nonlinearities can be expected to nullify in the vicinity of a TPA resonance, and the fact that our nominal 800 nm pulses have a bandwidth that extends through the resonance. The uncertainties in the γ-values of the other TPEBs are also quite large and arise from the large spread of values obtained in the course of approximately a dozen experiments. Thus, the response shown in Fig. 5.11 represents the responses from one particular experiment, and while it does not strictly follow the trend in γ-values reported above, it does agree with these values within our reported uncertainty.

The long-lasting induced birefringence dynamics are an interesting feature of the NLO response of TPEBs at 800 nm: As seen in Fig. 5.12, the ultrafast electronic Kerr response gives way to small but long-lasting pump-induced birefringence. In the case of ***ortho*-TPEB**, ***para*-TPEB**, and **TD-TPEB**, the excited-state nonlinearity is of the same sign as the instantaneous γ-value. Specifically, **TD-TPEB** shows a positive long-lasting birefringence that decays exponentially with $\tau\approx350$ ps, ***ortho*-TPEB** displays a negative birefringence that peaks at ≈2 ps and then decays exponentially with $\tau\approx32$ ps, and ***para*-**

TPEB displays a smaller negative birefringence that peaks at ≈5 ps and then decays exponentially with τ≈21.5 ps. In ***meta*-TPEB**, on the other hand, the initially negative-ultrafast response crosses over and gives way to a positive excited-state birefringent nonlinearity, peaking at approximately 10 ps and decaying exponentially with τ≈24 ps. These decay times are in good agreement with those obtained by the dichroic DOKE condition (Fig. 5.8) and those obtained by 400 nm-pump TA, indicating that the long-lasting Kerr response is due to birefringence of the same excited-states. The curious sign change in ***meta*-TPEB** can be linked to the relative orientation between the HOMO→LUMO and LUMO→LUMO+1 transition dipoles. As discussed in Chapter 2, the linearly polarized pump pulse induces anisotropy in the sample, modifying the index of refraction parallel and perpendicular to the polarization axis. This birefringence ($\Delta n_{//}$ - $\Delta n_{\perp}$) gives rise to the Kerr response in the birefringent DOKE polarization condition. In ***meta*-TPEB** pumped at 800 nm, the ultrafast negative response involves $\boldsymbol{M}_{\text{HOMO}\rightarrow\text{LUMO}}$. For the excited-state birefringence, the optical nonlinearity involves $\boldsymbol{M}_{\text{LUMO}\rightarrow\text{LUMO+1}}$. However, as indicated in Fig. 5.4, $\boldsymbol{M}_{\text{HOMO}\rightarrow\text{LUMO}}$ and $\boldsymbol{M}_{\text{LUMO}\rightarrow\text{LUMO+1}}$ are orthogonal in ***meta*-TPEB**. Thus, if a negative nonlinearity represents $\Delta n_{//} < \Delta n_{\perp}$ for a given transition, it seems reasonable to conjecture that $\Delta n_{//} > \Delta n_{\perp}$ in a subsequent transition for which transition density shifts by 90°, and thus the measured nonlinearities would become positive. Thus, we believe this to be the source of the sign change in the excited-state birefringent nonlinearities of ***meta*-TPEB**. Since this proposed mechanism depends on well-defined molecular orientation, its measurement would be complicated by re-orientational dephasing times.[55] Whereas small molecules (such as CS_2) can display relatively short (≈0.5-5 ps) re-orientational times,[62] TPEBs are much larger rotors, and would be expected to display characteristic re-orientational times in the order of a few hundred picoseconds. Thus, electronic depopulation of the excited-state observed in ***meta*-TPEB** is short compared to the dephasing time, and is primarily monoexponential. The possibility of a sample to display refractive nonlinearities of a given sign on peak and of the opposite side in the excited-state is not new, and has been previously shown (indirectly) by non-time-resolved measurements.[63]

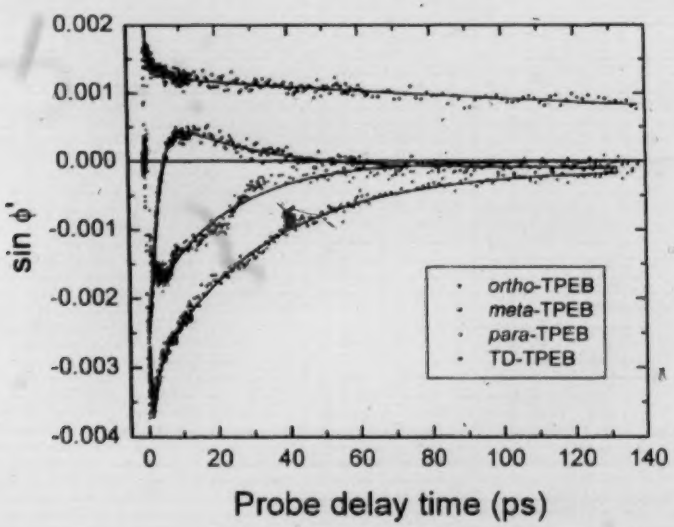

Figure 5.12. [colour] Induced birefringence dynamics fit to a bi-exponential form (solid lines; prode delay times >1.5 ps). A very small offset of $|a| < 0.00015$ was required to fit the signals of ***meta*-TPEB** and ***ortho*-TPEB**. Whereas all other samples display ultrafast and long-lasting nonlinearities of the same sign, ***meta*-TPEB** shows a switch in the sign of the birefringent nonlinearity; a negative on-peak electronic Kerr nonlinearity becomes a positive excited-state birefringent nonlinearity. The decay dynamics obtained from the fits are: **TD-TPEB**, τ_1= 4.4 ps, τ_2=350 ps; ***meta*-TPEB**, τ_1=2.7 ps (rise), τ_2=24 ps; ***ortho*-TPEB**, τ_1=1.6 ps (rise), τ_2=32 ps; ***para*-TPEB**, τ_1=1.2 ps (rise), τ_2=21.5 ps.

Two-Photon Absorption Structure-to-Property Relations: As discussed in Chapter 1, there is growing evidence that in donor/acceptor-substituted conjugated systems, donor substitution impacts $\sigma^{(2)}$ more than acceptor substitution.[6,36] This effect has been shown to be especially strong in molecules that have an aromatic core that can act as a weak acceptor.[64] Comparisons between the TPA spectra of ***para*-TPEB** and **TD-TPEB** provide further evidence for the validity of this structure-property relation. The all-donor substituted **TD-TEP** displays a peak cross-section that is more than twice that of the D/A-substituted ***para*-TEP**. This finding is significant: whereas experiments that look to study the effects of D-π-D vs. D-π-A substitution by using linear chromophores invariably compare TPA between molecules of different polar/multipolar geometry, the 2-D conjugation scheme in TPEBs can provide a comparison between chromophores of the same polarization (quadrupolar, in this case). Considering the benzene core to act as the dominant π-electron accepting region in **TD-TPEB**, this molecule has two large D-π-A-π-D arms (*para*-linked donor arms). On the other hand, the dominant π-electron

accepting region in ***para*-TPEB** resides in the region of the NO_2 moiety, and although this chromophore then has longer D→A conjugated paths than in **TD-TPEB**, it only has two "bent conjugation" paths and two "cross-conjugated" paths. On the other hand, ***meta*-TPEB** and ***ortho*-TPEB** both have long *para*-linked D→A paths, yet they also show smaller TPA activity than the all-donor sample. Thus, our finding that the all-donor **TD-TPEB** species shows the largest TPA of all of the measured TPEBs confirms that donor substitution impacts $\sigma^{(2)}$ more than acceptor substitution, especially for chromophores with an aromatic center.

Another structure-property relation that is hotly debated in the literature is the comparison between peak TPA activity in dipolar and multipolar molecules. [6,18,20,37,38] Whereas most studies find quadrupolar geometry to be favourable to dipolar geometry, [6,37,38] our finding show the opposite trend: Among the three structural isomers, the dipolar molecules (***meta*-TPEB** and ***ortho*-TPEB**) display similar peak $\sigma^{(2)}$-values that are nearly twice as large as that of the quadrupolar species (***para*-TPEB**). Once again, in order to compare dipolar and quadrupolar molecules, most studies have relied on comparisons of molecules which, structurally, are significantly dissimilar. With the cross-shape of the TPEBs, we are able to examine this structure-property relationship by comparing isomers of very similar shape, but of differing polarization geometry.

We would be remiss to claim that our findings indicate that dipolar geometry is superior to quadrupolar geometry. Rather, the TPA behaviour of the TPEBs provides a good example how the details of molecular two-photon absorption depend on specific structural designs. For example, it is likely that TPA in ***meta*-TPEB** and ***ortho*-TPEB** is largely dominated by the *para*-linked D→A paths, and thus, despite having differing alternate D→A conjugated routes, the two molecules show a similar response. ***para*-TPEB**, on the other hand lacks the linear, *para*-linked, D→A path, and can only utilize the aforementioned alternate 'bent' and 'cross-conjugated' routes. This suggestion is consistent with the reported effects of the various conjugation routes in TEEs, where the quasi-linear trans-conjugation was found to dominate that of cross- and the 'bent' cis-conjugation.[28] This has also been previously argued for the case of TPEBs based on trends in the UV-vis spectra.[2]

5.5 Summary

We studied the third-order refractive and absorptive nonlinearities of a two-dimensionally-conjugated series of four tetrakis(phenylethynyl)benzene derivatives. In one species, **TD-TPEB**, all four arms are terminated with NBu_2 donor groups. The other three molecules form a set of structural isomers in which the conjugated arms are terminated with two NO_2 acceptor and two NBu_2 donor groups. These compounds are named according to the respective donor-arm linkages across the central benzene ring; forming ***ortho*-TPEB**, ***meta*-TPEB** and ***para*-TPEB**. **TD-TPEB** and ***para*-TPEB** are both quadrupolar, and therefore lack permanent dipole moments. ***ortho*-TPEB** and ***meta*-TPEB** are dipolar.

We used femtosecond z-scan measurements to obtain the two-photon absorption spectra, and found the low-energy $\sigma^{(2)}$ peak of the four TPEBs. We also used the DOKE technique to time-resolve both the refractive and absorptive nonlinearities of these samples at 800 nm. Finally, we conducted 400 nm pump-800 nm probe transient absorption measurements, resolving the one-photon-accessed excited-state dynamics in these chromophores.

From the z-scan measurements, we find that the all-donor sample shows the highest peak TPA cross section, with $\sigma^{(2)} = 520\pm30$ GM at a wavelength of 710 nm. The total energy of transition at the TPA peak is significantly blue-shifted with respect to the one-photon spectrum. This, together with the molecular symmetry suggests that two-photon transitions to a level higher than LUMO+1 are taking place. The dipolar samples ***ortho*-TPEB** and ***meta*-TPEB** display similar TPA spectra that closely follow the lowest one-photon absorption (in total photon energy), as would be expected in dipolar molecules. ***meta*-TPEB** and ***ortho*-TPEB** yield $\sigma^{(2)} = 440\pm20$ GM at 940 nm, and 400 ± 20 GM at 860 nm, respectively. The similarity in peak $\sigma^{(2)}$-value between these two samples

may arise from the fact that, whereas the ***ortho*-TPEB** has a slightly larger permanent dipole moment, ***meta*-TPEB** has a slightly larger HOMO→LUMO transition dipole moment, and both molecules have very similar UV-vis spectra. Like **TD-TPEB**, ***para*-TPEB** is quadrupolar, and thus shows a blue-shifted TPA spectrum. This sample, however, yields the lowest overall cross-section maximum, with $\sigma^{(2)}$=240±20 GM at 750 nm—nearly half that of the other TPEB samples. These findings help to support the growing belief that adding multiple donor groups at the end of conjugated paths significantly increases TPA activity as compared to adding both donors and acceptors. Furthermore, comparisons between our dipolar and quadrupolar D/A molecules shows that in the case of TPEBs, the dipolar motif yields higher $\sigma^{(2)}$ than a quadrupolar substitution symmetry. This is probably due to a lack of the desirable *para*-conjugated D→A routes in the quadrupolar species.

Pump-probe measurements show that all of the TPEBs display both excited-state absorption and excited-state birefringence at 800 nm. With the exception of **TD-TPEB**, the three isomers show a clear 1-5 ps decay time from the two-photon state to the excited-state from which subsequent 800 nm probe-beam absorption takes place. Absorption from this excited-state is then seen to decay exponentially, with 20-40 ps time scales. The decay times observed in both the birefringent and dichroic signals are similar. Furthermore, these decay rates are consistent with those observed from one-photon pumped transient absorption measurements, indicating that the same excited-state dominates in samples pumped by either two-photon- or one-photon-absorption. Excited-state absorption is also present in **TD-TPEB**, and is seen to decay with a much longer time constant of ≈300 ps.

The third-order molecular hyperpolarizability, γ, of TPEBs was measured with the DOKE technique at 800 nm. The sign of the nonlinearity was found to correlate to the spectral position of the two-photon resonance: **TD-TPEB**, for which 800 nm is on the low-energy side of the TPA transition, yields the positive, and relatively large,[65]

γ=670±60γ_{THF}. In ***meta*-TPEB** and ***ortho*-TPEB**, 800 nm lies on the high-energy side of the TPA transition, and these samples display a negative nonlinearity, with γ=–450±100γ_{THF} and γ=–600±150γ_{THF}, respectively. In ***para*-TPEB**, the two-photon transition is resonant with 800 nm, and this sample displays a small (but zero within error) negative nonlinearity, γ=–100±150γ_{THF}.

In conclusion, TPEBs are excellent two-dimensionally-conjugated systems for investigating both the effects of polar/multipolar geometry and donor-acceptor substitution patterns on nonlinear optical properties. Such structure-to-property relationships are needed for guiding the future design of advanced conjugated materials toward use in technological applications. In this study we have shown that it is *not true that, all things being equal, quadrupolar geometry is superior to dipolar geometry for maximizing TPA*. Furthermore, we have shown that the nonlinear optical activity of molecules with a central benzene core are dependent on the specifics of their structural design, wherein small changes within our series of TPEB isomers lead to significant differences in their Kerr and nonlinear absorption response.

5.6 References

[1] J. J. Miller, J. A. Marsden, and M. M. Haley, Synlett, 165 (2004).

[2] J. A. Marsden, J. J. Miller, L. D. Shirtcliff, and M. M. Haley, J. Am. Chem. Soc. **127**, 2464 (2005).

[3] A. D. Slepkov, J. A. Marsden, J. J. Miller, L. D. Shirtcliff, M. M. Haley, K. Kamada, R. R. Tykwinski, and F. A. Hegmann, in *Nonlinear Optical Transmission and Multiphoton Processes in Organics III,* Proc. of SPIE, **5934**, p. 593405 (2005).

[4] A. M. Masunov and S. Tretiak, J. Phys. Chem. B. **108**, 899 (2004).

[5] T. Kogej, D. Beljonne, F. Meyers, J. W. Perry, S. R. Marder, and J. L. Brédas, Chem. Phys. Lett. **298**, 1 (1998).

[6] C. K. Wang, P. Macak, Y. Luo, and H. Ågren, J. Chem. Phys. **114**, 9813 (2001).

[7] T. C. Lin, G. S. He, P. N. Prasad, and L. S. Tan, J. Mater. Chem. **14**, 982 (2004).

[8] E. Zojer, D. Beljonne, P. Pacher, and J. L. Brédas, Chem. Eur. J. **10**, 2668 (2004).

[9] P. Najechalski, Y. Morel, O. Stephan, and P. L. Baldeck, Chem. Phys. Lett. **343**, 44 (2001).

[10] R. Kannan, G. S. He, L. X. Yuan, F. M. Xu, P. N. Prasad, A. G. Dombroskie, B. A. Reinhardt, J. W. Baur, R. A. Vaia, and L. S. Tan, Chem. Mater. **13**, 1896 (2001).

[11] J. M. Hales, D. J. Hagan, E. W. Van Stryland, K. J. Schafer, A. R. Morales, K. D. Belfield, P. Pacher, O. Kwon, E. Zojer, and J. L. Brédas, J. Chem. Phys. **121**, 3152 (2004).

[12] W. B. Davis, W. A. Svec, M. A. Ratner, and M. R. Wasielewski, Nature **396**, 60 (1998).

[13] A. Mathy, K. Ueberhofen, R. Schenk, H. Gregorius, R. Garay, K. Müllen, and C. Bubeck, Phys. Rev. B. **53**, 4367 (1996).

[14] K. Ohta and K. Kamada, J. Chem. Phys. **124** (2006).

[15] R. Kishi, M. Nakano, S. Yamada, K. Kamada, K. Ohta, T. Nitta, and K. Yamaguchi, Chem. Phys. Lett. **393**, 437 (2004).

[16] H. Meier, D. Ickenroth, U. Stalmach, K. Koynov, A. Bahtiar, and C. Bubeck, Eur. J. Org. Chem., 4431 (2001).

[17] Y. Zhao, Y. Shirai, A. D. Slepkov, L. Cheng, L. B. Alemany, T. Sasaki, F. A. Hegmann, and J. M. Tour, Chem. Eur. J. **11**, 3643 (2005).

[18] D. Beljonne, W. Wenseleers, E. Zojer, Z. G. Shuai, H. Vogel, S. J. K. Pond, J. W. Perry, S. R. Marder, and J. L. Brédas, Adv. Funct. Mater. **12**, 631 (2002).

[19] U. Gubler, R. Spreiter, C. Bosshard, P. Günter, R. R. Tykwinski, and F. Diederich, Appl. Phys. Lett. **73**, 2396 (1998).

[20] L. Porres, C. Katan, O. Mongin, T. Pons, J. Mertz, and M. Blanchard-Desce, J. Mol. Struct. **704**, 17 (2004).

[21] M. Drobizhev, A. Karotki, A. Rebane, and C. W. Spangler, Opt. Lett. **26**, 1081 (2001).

[22] R. R. Tykwinski, U. Gubler, R. E. Martin, F. Diederich, C. Bosshard, and P. Günter, J. Phys. Chem. B. **102**, 4451 (1998).

[23] X.-B. Zhang, J.-K. Feng, A.-M. Ren, and C.-C. Sun, Opt. Mater., doi:10.1016/ j.optmat.2006.01.026.

[24] H. Meier, Angew. Chem. Int. Ed. **44**, 2482 (2005).

[25] B. R. Cho, M. J. Piao, K. H. Son, S. H. Lee, S. J. Yoon, S. J. Jeon, and M. H. Cho, Chem. Eur. J. **8**, 3907 (2002).

[26] K. Kondo, S. Yasuda, T. Sakaguchi, and M. Miya, J. Chem. Soc., Chem. Comm. 55 (1995).

[27] U. Gubler and C. Bosshard, Adv. Polym. Sci. **158**, 123 (2002).

[28] N. N. P. Moonen, W. C. Pomerantz, R. Gist, C. Boudon, J. P. Gisselbrecht, T. Kawai, A. Kishioka, M. Gross, M. Irie, and F. Diederich, Chem. Eur. J. **11**, 3325 (2005).

[29] J. C. May, J. H. Lim, I. Biaggio, N. N. P. Moonen, T. Michinobu, and F. Diederich, Opt. Lett. **30**, 3057 (2005).

[30] A. L. Thompson, T. S. Ahn, K. R. J. Thomas, S. Thayumanavan, T. J. Martinez, and C. J. Bardeen, J. Am. Chem. Soc. **127**, 16348 (2005).

[31] S. Lee, K. R. J. Thomas, S. Thayumanavan, and C. J. Bardeen, J. Phys. Chem. A. **109**, 9767 (2005).

[32] K. M. Gaab, A. L. Thompson, J. J. Xu, T. J. Martinez, and C. J. Bardeen, J. Am. Chem. Soc. **125**, 9288 (2003).

[33] A. Stockmann, J. Kurzawa, N. Fritz, N. Acar, S. Schneider, J. Daub, R. Engl, and T. Clark, J. Phys. Chem. A. **106**, 7958 (2002).

[34] H. E. Zimmerman, J. Am. Chem. Soc. **117**, 8988 (1995).

[35] F. D. Lewis and J. S. Yang, J. Am. Chem. Soc. **119**, 3834 (1997).

[36] M. Albota, D. Beljonne, J. L. Brédas, J. E. Ehrlich, J. Y. Fu, A. A. Heikal, S. E. Hess, T. Kogej, M. D. Levin, S. R. Marder, D. McCord-Maughon, J. W. Perry, H. Röckel, M. Rumi, C. Subramaniam, W. W. Webb, X. L. Wu, and C. Xu, Science **281**, 1653 (1998).

[37] M. Barzoukas and M. Blanchard-Desce, J. Chem. Phys. **113**, 3951 (2000).

[38] B. Strehmel, A. M. Sarker, and H. Detert, ChemPhysChem **4**, 249 (2003).

[39] O.-K. Kim, K.-S. Lee, H. Y. Woo, K.-S. Kim, G. S. He, J. Swiatkiewicz, and P. N. Prasad, Chem. Mater. **12**, 284 (2000).

[40] E. Zojer, D. Beljonne, T. Kogej, H. Vogel, S. R. Marder, J. W. Perry, and J. L. Brédas, J. Chem. Phys. **116**, 3646 (2002).

[41] E. Zojer, W. Wenseleers, P. Pacher, S. Barlow, M. Halik, C. Grasso, J. W. Perry, S. R. Marder, and J. L. Brédas, J. Phys. Chem. B. **108**, 8641 (2004).

[42] S.-J. Chung, K.-S. Kim, T.-H. Lin, G. S. He, J. Swiatkiewicz, and P. N. Prasad, J. Phys. Chem. B. **103**, 10741 (1999).

[43] K. Kamada, K. Matsunaga, A. Yoshino, and K. Ohta, J. Opt. Soc. Am. B. **20**, 529 (2003).

[44] K. Kamada, K. Ohta, I. Yoichiro, and K. Kondo, Chem. Phys. Lett. **372**, 386 (2003).

[45] P. Feneyrou, O. Doclot, D. Block, P. L. Baldeck, S. Delysse, and J. M. Nunzi, Opt. Lett. **22**, 1132 (1997).

[46] M. Drobizhev, Y. Stepanenko, Y. Dzenis, A. Karotki, A. Rebane, P. N. Taylor, and H. L. Anderson, J. Am. Chem. Soc. **126**, 15352 (2004).

[47] S. Polyakov, F. Yoshino, M. Liu, and G. Stegeman, Phys. Rev. B. **69** (2004).

[48] S. Mazumdar, S. Dallakyan, and M. Chandross, Synth. Met. **139**, 769 (2003).

[49] R. R. Birge and B. M. Pierce, J. Chem. Phys. **70**, 165 (1979).

[50] A mostly-unresolved lowest-energy peak may be present at approximately 450 nm in TD-TPEB

[51] K. Ohta, private communication, 2006.

[52] E. Zojer, W. Wenseleers, M. Halik, C. Grasso, S. Barlow, J. W. Perry, S. R. Marder, and J. L. Brédas, ChemPhysChem **5**, 982 (2004).

[53] Molecular Orbitals and Dipole calculations were performed with the Gaussian 98 suite of programs at the B3LYP/6-31G* level of DFT. Gaussian 98: Frisch, M. J.;

Trucks, G. W.; Schlegel, H. B.; Scuseria, G. E.; Robb, M. A.; Cheeseman, J. R.; Zakrzewski, V. G.; Montgomery, J. A., Jr.; Stratmann, R. E.; Burant, J. C.; Dapprich, S.; Millam, J. M.; Daniels, A. D.; Kudin, K. N.; Strain, M. C.; Farkas, O.; Tomasi, J.; Barone, V.; Cossi, M.; Cammi, R.; Mennucci, B.; Pomelli, C.; Adamo, C.; Clifford, S.; Ochterski, J.; Petersson, G. A.; Ayala, P. Y.; Cui, Q.; Morokuma, K.; Malick, D. K.; Rabuck, A. D.; Raghavachari, K.; Foresman, J. B.; Cioslowski, J.; Ortiz, J. V.; Stefanov, B. B.; Liu, G.; Liashenko, A.; Piskorz, P.; Komaromi, I.; Gomperts, R.; Martin, R. L.; Fox, D. J.; Keith, T.; Al-Laham, M. A.; Peng, C. Y.; Nanayakkara, A.; Gonzalez, C.; Challacombe, M.; Gill, P. M. W.; Johnson, B.; Chen, W.; Wong, M. W.; Andres, J. L.; Gonzalez, C.; Head-Gordon, M.; Replogle, E. S.; Pople, J. A.; Revision A.6 ed.; Gaussian: Pittsburg, PA, 1998.

[54] Dr. Michael Haley and Laura Shirtcliff, 2005. Personal communication superceding the previously published values in J. A. Marsden, J. J. Miller, L. D. Shirtcliff, and M. M. Haley, J. Am. Chem. Soc. 127, 2464 (2005).

[55] Y. Zhang, M. I. Sluch, M. M. Somoza, and M. A. Berg, J. Chem. Phys. **115**, 4212 (2001).

[56] Y. Zhang and M. A. Berg, J. Chem. Phys. **115**, 4231 (2001).

[57] Y. Zhang, J. Jiang, and M. A. Berg, J. Chem. Phys. **118**, 7534 (2003).

[58] D. Rendell, D. J. Mowthorpe, and ACOL (Project), *Fluorescence and phosphorescence spectroscopy* (Published on behalf of ACOL, London by Wiley, Chichester [West Sussex] ; New York, 1987).

[59] N. Bloembergen, *Nonlinear Optics* (World Scientific, 2002).

[60] M. P. Cifuentes, C. E. Powell, M. G. Humphrey, G. A. Heath, M. Samoc, and B. Luther-Davies, J. Phys. Chem. A. **105**, 9625 (2001).

[61] R. Rangel-Rojo, S. Yamada, H. Matsuda, H. Kasai, H. Nakanishi, A. K. Kar, and B. S. Wherrett, J. Opt. Soc. Am. B. **15**, 2937 (1998).

[62] B. J. Loughnane, A. Scodinu, R. A. Farrer, J. T. Fourkas, and U. Mohanty, J. Chem. Phys. **111**, 2686 (1999).

[63] A. A. Said, C. Wamsley, D. J. Hagan, E. W. Van Stryland, B. A. Reinhardt, P. Roderer, and A. G. Dillard, Chem. Phys. Lett. **228**, 646 (1994).

[64] M. Rumi, J. E. Ehrlich, A. A. Heikal, J. W. Perry, S. Barlow, Z. Hu, D. McCord-Maughon, T. C. Parker, H. Röckel, S. Thayumanavan, S. R. Marder, D. Beljonne, and J. L. Brédas, J. Am. Chem. Soc. **122**, 9500 (2000).

[65] See Chapter 4 for a comparison to the hyperpolarizability of extended polyynes and beta-carotene.

CHAPTER 6:

OPTICAL AND NONLINEAR OPTICAL CHARACTERIZATION OF [60]FULLERENE-OLIGO(*P*-PHENYLENE ETHYNYLENE) HYBRIDS

6.1 Context

As new carbon allotropes discovered in 1985, fullerenes draw continuing attention to their optical and electronic properties.[1,2] [60]fullerenes (denoted either "C_{60}" or "fullerene") are three-dimensional soccer-ball-shaped conjugated molecules that are relatively compact and contain a high-density of π-electrons. Various forms of C_{60} have been shown to display a range of electronic and optical properties depending on their processing and surroundings.[3,4] As such, fullerenes have drawn considerable interest to their nonlinear optical characteristics and their subsequent potential for use in emerging NLO-based technologies, such as all-optical limiting.[5-7] While early studies indicated that fullerenes have very large nonlinear optical response, recent studies on the nonlinear optical properties of pristine C_{60} have shown them to yield disappointingly small or even negligible instantaneous nonlinearities.[8-11] Nonetheless, it is presumed that properly integrating fullerenes into other conjugated materials may yield novel materials with strong optical nonlinearities at wavelengths of interest. However, synthesis of hybrid materials in which fullerenes are directly integrated into/onto a conjugated chromophore has proven problematic.[12,13] This chapter reports on the study of three oligo(*p*-phenylene ethynylene) (OPE) based chromophores, one of which consists of an OPE-(bis)fullerene hybrid. The results of this study, comprising a collaboration between Dr. Hegmann's ultrafast spectroscopy group at the U of A, and Dr. Tour's synthetic organic chemistry group at Rice university, have been published in Chemistry (Chem. Eur. J.).[14] This represented a landmark study for us, as it was our first publication to report on quantitative two-photon and excited-state absorption obtained with the DOKE detection layout.

6.2 Introduction

Possessing a dense network of delocalized π-electrons, as well as high-transparency in the near- and mid-infrared, fullerenes are appealing candidates for NLO applications.[15,16] NLO research on pristine C_{60} has proved disappointing, as unfunctionalized fullerenes display miniscule hyperpolarizabilites and poor solubility.[9-11] Functionalized fullerenes, however, have been shown to yield large γ and $\sigma^{(2)}$ values.[17-20] By bonding fullerenes to conjugated oligomers such as OPEs, the electronic characteristics of both components are altered, thus modifying the hybrid's overall NLO properties. Therefore, it is of particular interest to shed light on the fullerene-controlled third-order NLO behavior as well as respective structure-property relationships. From a geometric standpoint, the OPE symmetries investigated in this work are also of particular interest for NLO research, with the roles of both extended conjugation and polar/multipolar symmetries on the NLO properties of molecular systems being investigated.[21-31] In the OPE-based compounds studied herein, both quadrupolar and octupolar systems with similarly conjugated backbones are studied. Our preliminary efforts to investigate short fullerene-OPE chains and pristine C_{60} failed due to their low solubility in organic solvents. The inability to resolve nonlinearities of dilute C_{60} solutions is consistent with prior findings that pristine fullerenes display extremely small nonlinearites.[8-11] On the other hand, fullerenes bonded to long-chain OPEs should be more soluble and were primarily targeted in our study. Compounds **C_{60}-oct-5OPE** and **C_{60}-quad-5OPE** were selected as potential candidates for NLO investigation, since they represent not only multiple-fullerene derivatives but also two different types of molecular dimensionalities. To determine the effects of fullerene terminal groups in governing the third–order NLO properties, the corresponding OPE compounds **oct-5OPE** and **quad-5OPE** were also investigated (See Fig. 6.1).

6.3 Experimental

Compounds: All OPE compounds were synthesized at Rice University in the Tour lab (see Fig. 6.1). For this study, the UV-vis and third-order nonlinear optical properties of four oligo(*p*-phenyleneethynylene)-based compounds were investigated. For UV-vis characterization, OPE samples were measured as dilute solution in *o*-dichlorobenzene. For NLO studies, all samples were analyzed in CH_2Cl_2 solutions. Both compounds **C_{60}-quad-5OPE** and **C_{60}-oct-5OPE** are only weakly soluble in CH_2Cl_2. However, whereas a dilute solution of **oct-5OPE** (<2 mM)[32] gave detectable signals, **C_{60}-oct-5OPE** was not sufficiently soluble for accurate measurements, with a saturated solution (approximately 0.5 M) yielding an irresolvable response. Although CS_2 is a better solvent for fullerene compounds, CH_2Cl_2 displays both smaller and faster γ-nonlinearites that allow for the extraction of small solute-derived signals with far better resolution.[33]

NLO characterization at a wavelength of 800 nm was conducted with the ultrafast DOKE detection technique as described in Chapter 2 and elsewhere.[33] All γ-values are referenced to that of THF ($\gamma_{THF}=5.2\times10^{-37}$esu),[34] and all $\sigma^{(2)}$-values are relative to that of MPPBT ($\sigma^{(2)}_{MPPBT}$=380GM; λ=800 nm).[35] A summary of optical and nonlinear optical values for the studied OPEs are listed in Table 6.1.

Table 6.1. Low-energy absorption peak wavelengths and molecular third-order hyperpolarizabilities γ and TPA cross sections $\sigma^{(2)}$ measured at 800 nm in OPE compounds.

Compound	Concentration (mM)	λ_{max} (nm)	γ (10^{-34} esu)	$\sigma^{(2)}$ (10^{-50} cm^4 s)
quad-5OPE	20	430	5. 7 ± 0.4	65 ± 10
Oct-5OPE	20	415	4.4 ± 0.2	28 ± 8
C_{60}-quad-5OPE	2	425	10 ± 3	140 ± 40

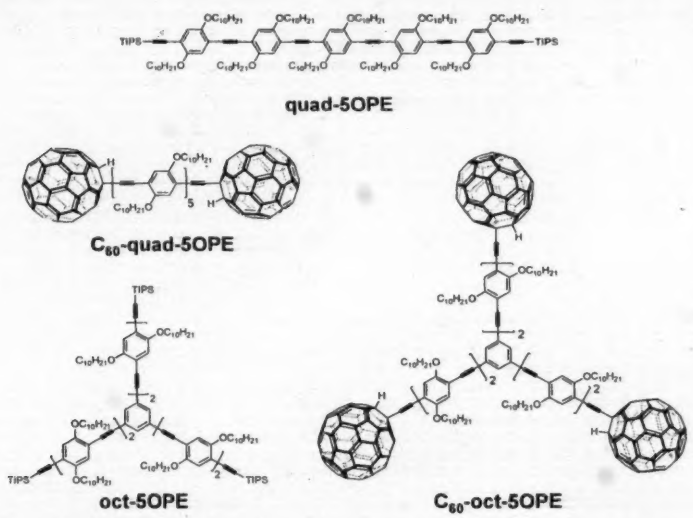

Figure 6.1. Chemical structures of the reported OPE-based compounds. Sample **C_{60}-oct-5OPE** was not sufficiently soluble for NLO characterization.

6.4 Results and Discussion

Linear Optical Properties: The UV-vis spectra of the OPE-based samples are presented in Fig. 6.2. The absorption spectra of the OPE samples are dominated by two features; a higher-energy peak located between 300-325 nm, and a lower-energy peak located between 400-430 nm. Furthermore, samples **C_{60}-oct-5OPE** and **C_{60}-quad-5OPE** display long absorption tails that range from 450-600 nm and are characteristic of fullerene-containing chromophores.[36]

A red-shifting of the highest-wavelength of maximal absorption, λ_{max}, is observed in going from sample **oct-5OPE** to **quad-5OPE.** Although both samples have an arm-to-arm length of 5 OPE units, the quadrupolar **quad-5OPE** is fully linearly-conjugated across all five repeat units, whereas in the octupolar molecule **oct-5OPE,** conjugation is broken by the *meta*-linkage across the central phenyl ring (see Chapter 5). Thus, this bathochromic shift of approximately 15 nm is most likely due to an increased conjugation length. A similar red-shift is seen in the fullerene-capped OPE samples, where λ_{max} is approx. 405 nm for **C_{60}-oct-5OPE** and 425 nm for **C_{60}-quad-5OPE**, respectively. This shift is thus also attributed to a difference in conjugation length, and not to the difference in the number of terminal fullerenes.

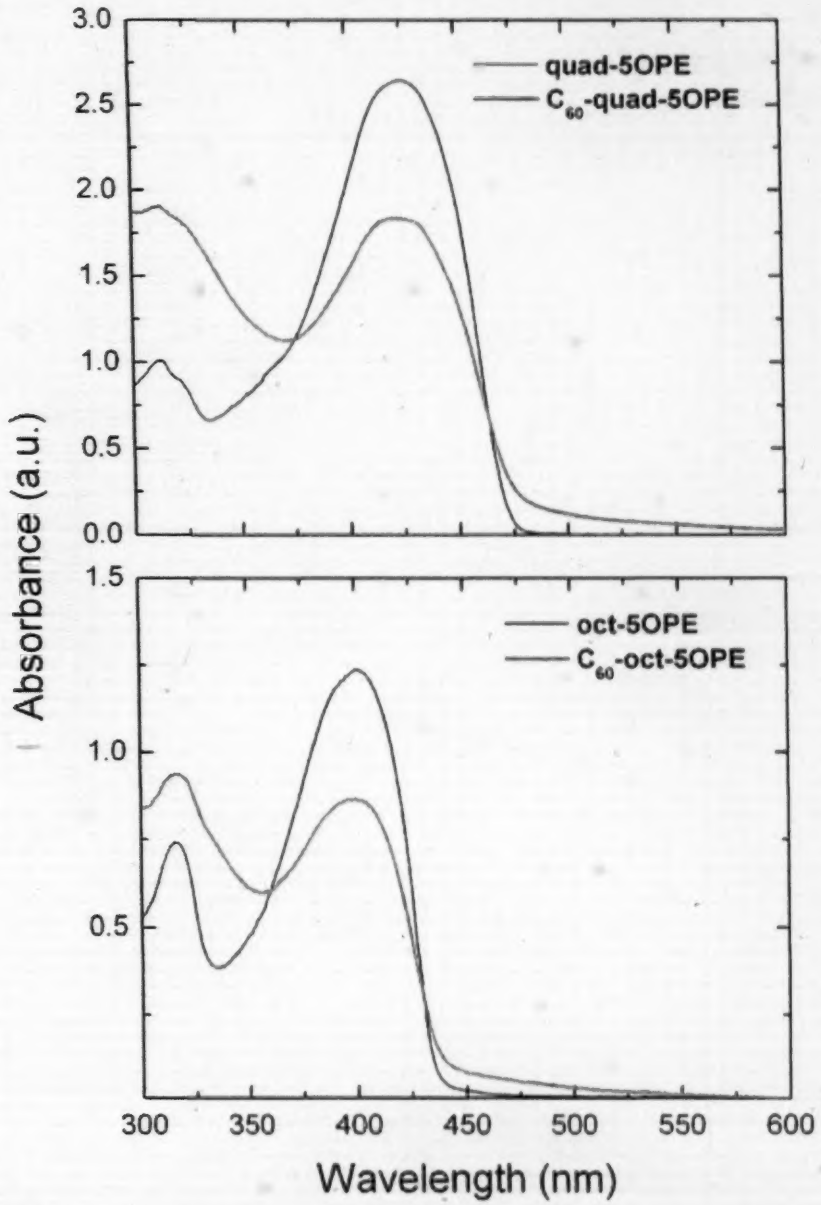

Figure 6.2. UV-vis absorption spectra for OPE-precursors and OPE-fullerene hybrids in *o*-dichlorobenzene. Note both the emergence of the long tail and the shift in oscillator strength from the lower-energy peak to the higher-energy peak upon the incorporation of C_{60}.

A significant redistribution in oscillator strength is observed upon end-capping with fullerenes, as can be seen from comparisons of the spectra in Fig. 6.2. While the absorptivity in the vicinity of λ_{max} in OPE oligomers **oct-5OPE** and **quad-5OPE** is much larger than in **C_{60}-oct-5OPE** and **C_{60}-quad-5OPE**, the oscillator-strength is seen to shift to the higher-energy peak in the latter compounds. In fact, the molar absorptivity at the higher-energy region is larger than that at λ_{max} for the fullerene-OPE hybrids. It is reasonable to believe that this enhancement is due to the contribution from fullerene groups; most likely due to an electronic transition from the orbitals of OPE to those of the fullerene cages.[14] However, despite being connected by a conjugated OPE bridge, an absorption band from intramolecular electronic interaction between the fullerene groups is not detected, and thus, electronic communication between the conjugated fullerene moieties and OPE backbone is not borne by the UV-vis spectra.

Third-order optical nonlinearities and two-photon absorption properties: In Table 6.1, γ- and $\sigma^{(2)}$-values for the OPE sample series are listed. Fullerene-terminated sample **C_{60}-quad-5OPE** displays the largest molecular hyperpolarizability; $\gamma=10\times10^{-34}$ esu ($\approx2000\gamma_{THF}$). This is a relatively large non-resonant nonlinearity for a conjugated molecule in solution, investigated by femtosecond Kerr spectroscopy, and compares well with other ultrafast third-order NLO studies of single-fullerene/polyaminonitrile hybrids.[9,19] Of the OPE compounds studied, **C_{60}-quad-5OPE** also has the largest TPA cross-section, with $\sigma^{(2)}=140\times10^{-50}$ GM ($\approx0.4\sigma^{(2)}_{MPPBT}$). This value is large for a non-polymeric compound studied with femtosecond pulses, and displays a value that compares well with the only other fullerene-derivative two-photon absorption results reported in the literature,[18,25,37] but studied with nanosecond pulses.[38] We find several interesting trends in our data: Fullerene-terminated OPE **C_{60}-quad-5OPE** shows a γ-value that is nearly twice that of its OPE precursor **quad-5OPE**. Likewise, a two-fold enhancement in $\sigma^{(2)}$ is observed, when comparing these two compounds. A similar doubling of the two-photon coefficients of conjugated chromophores upon attaching a terminal fullerene is reported by Chiang *et al.*[18] Considering that pristine fullerenes display negligible nonlinearities, it is possible that this enhancement of γ and $\sigma^{(2)}$ for **C_{60}-**

quad-5OPE compared to **quad-5OPE** is due to periconjugation effects and/or charge transfer from OPE to fullerene in the excited state.[14] In previous works, Chiang *et al.*, as well as others, attribute the sizable TPA response of functionalized fullerenes to charge transfer from the conjugated backbone to the terminal fullerene that acts as an electron acceptor.[8,9,18,39-41] This explanation is consistent with our NLO and UV-vis results. That same study, however, found that an octupolar conjugated backbone geometry displays larger $\sigma^{(2)}$-values than a linear conjugated quadrupolar conjugated backbone.[18] In contrast, we find that the quadrupolar **quad-5OPE** displays a larger TPA cross section than the octupolar **oct-5OPE**. This is perhaps not surprising when we consider that although the through-centre arms of these compounds have the same number of OPE units, in the octupolar geometry linear conjugation is interrupted by the *meta*-linked central phenyl ring (i.e., cross-conjugation), whereas the quadrupolar molecule is fully conjugated along its length.[28] On the other hand, other groups have synthesized octupolar molecules with an amide core that has been shown to allow some degree of conjugation through the center.[28,42,43] Moreover, the superiority of the γ-values of **quad-5OPE** over **oct-5OPE** further suggests that the degree of π-delocalization plays a more crucial role than the (multi)polar symmetry in controlling the NLO behavior of the molecules synthesized here—especially when considering that **oct-5OPE** is the larger molecule.

In addition to instantaneous two-photon absorption, the *TIPS*-terminated OPEs also display excited-state absorption (ESA).[44,45] Because DOKE detection is only sensitive to changes in the probe beam, TPA is recorded when one photon is absorbed from each of the pump and probe beams. This can only occur when the beams are overlapped temporally. For excited-state absorption, two photons are simultaneously absorbed from the intense pump beam to a high-lying two-photon state, as described in Chapter 2. After relaxation to a lower-lying excited state, a photon may be absorbed from the probe beam. This process will depend on the relaxation dynamics from the two-photon and lower excited-state as well as the transition probability of the excited state from which the subsequent absorption is to take place.

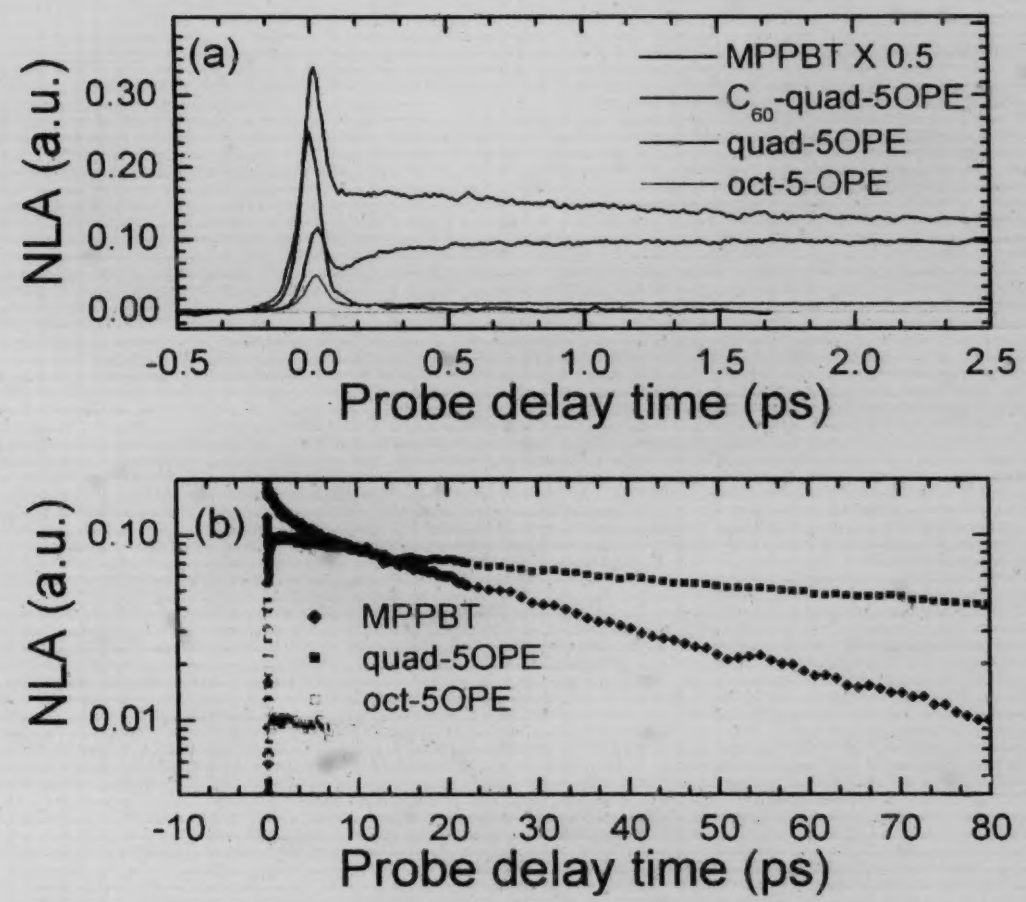

Figure 6.3. [colour] Time-resolved nonlinear absorption response of OPE-based samples in CH_2Cl_2 and MPPBT in DMSO. The MPPBT response has been scaled down by 50% for ease of comparison. a) Two-photon absorption is seen on-peak (t=0 ps) for all samples, while longer time scales represent excited-state absorption (ESA). Note that ESA is absent in the fullerene-terminated OPE **C_{60}-quad-5OPE**. b) (log-linear graph) Excited-state absorption decays, showing that samples **quad-5OPE** and **oct-5OPE** have strikingly similar relaxation dynamics.

Figure 6.3 presents the time-resolved nonlinear absorption responses of **oct-5OPE**, **quad-5OPE**, **C_{60}-quad-5OPE**, and **MPPBT**. CH_2Cl_2, lacking TPA at 800 nm, only displays a very small transient grating signal typical of coherent coupling (not shown; See Fig. 2.7 for a similar response in THF).[46] Whereas both OPE compounds **oct-5OPE**, **quad-5OPE** display a measure of excited-state absorption, the fullerene-terminated **C_{60}-quad-5OPE** shows only instantaneous TPA. When NLA in **MPPBT** is shown for comparison, it becomes clear how similar the excited-state dynamics of both the quadrupolar OPE and octupolar OPE are (Fig. 6.3b). This is somewhat surprising as the electronic levels in these systems are expected to be closely governed by the transition dipoles and geometry. For example, the lowest lying energy state in the centrosymmetric **quad-5OPE** is expected to be two-photon forbidden, while having a higher-energy state that is one-photon forbidden but two-photon allowed. On the other hand, the noncentrosymmetric **oct-5OPE** is expected to have both a one- and two-photon allowed first excited state.[27,28] Because the band-gap wavelength (λ_{max}=415-430 nm) of these samples is longer than the two-photon wavelength, (1/2 λ_{laser} = 400 nm), it is possible that the TPA is occurring to a high-lying excited state. Accordingly, from the UV-Vis spectra and time-resolved ESA dynamics, it is reasonable to suggest that it is the OPE chromophore units themselves, rather than the multipolar geometry that regulates the excited-state behavior of samples **oct-5OPE** and **quad-5OPE**. The fact that the OPE precursor **quad-5OPE** displays excited-state absorption while the fullerene-terminated **C_{60}-quad-5OPE** does not, is further consistent with a charge-transfer mechanism, in which relaxations from the two-photon-accessed level to the ground state take place without significant population of the intermediate excited state that is observed in **quad-5OPE** and **oct-5OPE**.[18] However, in the absence of two-photon induced fluorescence spectroscopy data it is difficult to conclusively map out the electronic states in these samples.[47]

6.5 Summary

A new synthesis route has made available multiple-fullerene functionalized conjugated-chromophore hybrids.[12] The spectroscopic characterization of such materials is of considerable interest, as researchers seek to realize the benefits of incorporating the highly π-electron-rich fullerenes into conjugated frameworks. In this context, we studied a multiple-fullerene oligo(*p*-phenyleneethynylene) (OPE) hybrid, **C_{60}-quad-5OPE,** together with its quadrupolar OPE precursor, **quad-5OPE,** and another structurally-related octupolar OPE, **quad-5OPE**. We investigated the third-order NLO and nonlinear-absorption properties of the OPE-based compounds using the DOKE detection technique. The measured third-order nonlinear-optical coefficients for fullerene derivative **C_{60}-quad-5OPE** are approximately double those of its OPE precursor **quad-5OPE** at 800 nm, while nonlinearities for pristine C_{60} are negligible. **C_{60}-quad-5OPE** displays significant two-photon absorption at 800 nm, with $\sigma^{(2)}$=140±40 GM, compared with $\sigma^{(2)}$=65±10 GM and $\sigma^{(2)}$=28±8 GM for **quad-5OPE** and **oct-5OPE**, respectively. The molecular second-hyperpolarizability at 800 nm is also non-negligible for these compounds, ranging from $(5.7\pm0.4)\times10^{-34}$ esu for **quad-5OPE** and $(4.4\pm0.2)\times10^{-34}$ esu for **oct-5OPE,** to $(10\pm3)\times10^{-34}$ esu for **C_{60}-quad-5OPE**. Whereas the doubling of γ and $\sigma^{(2)}$ in **C_{60}-quad-5OPE** could typically be explained by increases in conjugation length commensurate with a significant red-shifting of λ_{max}, no such shift is observed in the absorption spectra in going from **quad-5OPE** to **C_{60}-quad-5OPE**. In fact, a slight blue-shifting of approximately 5 nm is measured. Therefore, the differences in optical nonlinearities between the pure OPEs and the OPE-fullerene hybrids are not due to any extension of conjugation beyond the OPE backbone. Thus, the NLO results suggest a synergistic interaction between the conjugated OPE backbone and terminal fullerenes. Evidence for this is further supported by cyclic voltammetry studies presented elsewhere.[14] Other groups have attributed similar findings to the formation of a charge-

transfer species in which excited electrons pass from the conjugated backbone to the terminal fullerene. This proposed mechanism is further supported by the comparisons of the excited-state absorption dynamics of the compounds. Whereas both of the pure OPE frameworks display similar excited-state absorption, end-capping with fullerene (in **C_{60}-quad-5OPE**) yields a compound that only displays instantaneous two-photon absorption. Finally, this fullerene-terminated OPE displays sizable γ- and $\sigma^{(2)}$-values that are consistent with other C_{60} derivatives reported in the literature. Thus, our findings are potentially instructive to guiding the molecular design and engineering of organic-based electronic and nonlinear optical materials.

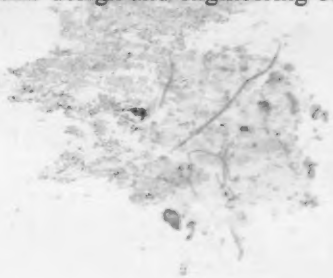

6.6 References

[1] W. E. Billups and M. A. Ciufolini, *Buckminsterfullerenes* (Vch, New York, 1993).

[2] R. Taylor, *The chemistry of fullerenes* (World Scientific, Singapore ; River Edge, NJ, 1995).

[3] D. M. Guldi and M. Prato, Acc. Chem. Res. **33**, 695 (2000).

[4] P. V. Kamat, D. M. Guldi, and K. M. Kadish, *Fullerenes : the exciting world of nanocages and nanotubes : proceedings of the International Symposium on Fullerenes, Nanotubes and Carbon Clusters* (Electrochemical Society, Pennington, NJ, 2002).

[5] Y. Sun and J. E. Riggs, International Reviews in Physical Chemistry **18**, 43 (1999).

[6] L. W. Tutt and A. Kost, Nature **356**, 225 (1992).

[7] S. Couris, E. Koudoumas, A. A. Ruth, and S. Leach, Journal of Physics B-Atomic Molecular and Optical Physics **28**, 4537 (1995).

[8] R. Lascola and J. C. Wright, Chem. Phys. Lett. **269**, 79 (1997).

[9] J. Li, S. Wang, H. Yang, Q. Gong, X. An, H. Chen, and D. Qiang, Chem. Phys. Lett. **288**, 175 (1998).

[10] L. Geng and J. C. Wright, Chem. Phys. Lett. **249**, 105 (1996).

[11] S. J. A. vanGisbergen, J. G. Snijders, and E. J. Baerends, Phys. Rev. Lett. **78**, 3097 (1997).

[12] Y. Shirai, Y. Zhao, L. Cheng, and J. M. Tour, Org. Lett., **6**, 2129 (2004).

[13] R. Taylor, *Lecture notes on fullerene chemistry: a handbook for chemists* (Imperial College Press, River Edge, NJ, 1999).

[14] Y. Zhao, Y. Shirai, A. D. Slepkov, L. Cheng, L. B. Alemany, T. Sasaki, F. A. Hegmann, and J. M. Tour, Chem. Eur. J. **11**, 3643 (2005).

[15] W. J. Blau, H. J. Byrne, D. J. Cardin, T. J. Dennis, J. P. Hare, H. W. Kroto, R. Taylor, and D. R. M. Walton, Phys. Rev. Lett., **67**, 1423 (1991).

[16] M. F. Yung and K. Y. Wong, Applied Physics B-Lasers and Optics **66**, 585 (1998).

[17] Q. Chen, L. Kuang, E. H. Sargent, and Z. Y. Wang, Appl. Phys. Lett. **83**, 2115 (2003).

[18] L. Y. Chiang, P. A. Padmawar, T. Canteenwala, L. S. Tan, G. S. He, R. Kannan, R. Vaia, T. C. Lin, Q. D. Zheng, and P. N. Prasad, Chem. Commun., 1854 (2002).

[19] S. Wang, W. Huang, R. Liang, Q. Gong, H. Li, H. Chen, and D. Qiang, Phys. Rev. B. **6315** (2001).

[20] B. L. Yu, H. P. Xia, C. S. Zhu, and F. X. Gan, Appl. Phys. Lett. **81**, 2701 (2002).

[21] W. H. Lee, H. Lee, J. A. Kim, J. H. Choi, M. H. Cho, S.-J. Jeon, and B. R. Cho, J. Am. Chem. Soc. **123**, 10658 (2001).

[22] C.-K. Wang, P. Macak, Y. Luo, and H. Ågren, J. Chem. Phys. **114**, 9813 (2001).

[23] A. Abbotto, L. Beverina, R. Bozio, S. Bradamante, C. Ferrante, G. A. Pagani, and R. Signorini, Adv. Mater. **12**, 1963 (2000).

[24] M. Albota, D. Beljonne, J. L. Brédas, J. E. Ehrlich, J. Y. Fu, A. A. Heikal, S. E. Hess, T. Kogej, M. D. Levin, S. R. Marder, D. McCord-Maughon, J. W. Perry, H. Röckel, M. Rumi, C. Subramaniam, W. W. Webb, X. Wu, and C. Xu, Science **281**, 1653 (1998).

[25] B. A. Reinhardt, L. L. Brott, S. J. Clarson, A. G. Dillard, J. C. Bhatt, R. Kannan, L. Yuan, G. S. He, and P. N. Prasad, Chem. Mater. **10**, 1863 (1998).

[26] M. Barzoukas and M. Blanchard-Desce, J. Chem. Phys. **113**, 3951 (2000).

[27] E. Zojer, D. Beljonne, P. Pacher, and J. L. Brédas, Chem. Eur. J. **10**, 2668 (2004).

[28] D. Beljonne, W. Wenseleers, E. Zojer, Z. Shuai, H. Vogel, S. J. K. Pond, J. W. Perry, S. R. Marder, and J. L. Brédas, Adv. Funct. Mater. **12**, 631 (2002).

[29] M. Rumi, J. E. Ehrlich, A. A. Heikal, J. W. Perry, S. Barlow, Z. Hu, D. McCord-Maughon, T. C. Parker, H. Röckel, S. Thayumanavan, S. R. Marder, D. Beljonne, and J. L. Brédas, J. Am. Chem. Soc. **122**, 9500 (2000).

[30] M. Drobizhev, A. Karotki, A. Rebane, and C. W. Spangler, Opt. Lett. **26**, 1081 (2001).

[31] B. R. Cho, M. J. Piao, K. H. Son, S. H. Lee, S. J. Yoon, S.-J. Jeon, and M. H. Cho, Chem. Eur. J. **8**, 3907 (2002).

[32] In a 2mM solution of **C_{60}-oct-5OPE** in CH_2Cl_2, some undissolved residue was observed. The quantity of this particulate was extremely small and should not impact the concentration. If, however, the concentration were lower than reported, the molecular nonlinearities reported herein for **C_{60}-oct-5OPE** would only be greater than reported.

[33] A. D. Slepkov, *Third-Order Nonlinearities of Novel iso-Polydiacetylenes Studied by a Differential Optical Kerr Effect Detection Technique*, M.Sc. thesis. University of Alberta, Edmonton, 2001.

[34] A. D. Slepkov, F. A. Hegmann, Y. Zhao, R. R. Tykwinski, and K. Kamada, J. Chem. Phys. **116**, 3834 (2002).

[35] K. Kamada, K. Ohta, I. Yoichiro, and K. Kondo, Chem. Phys. Lett. **372**, 386 (2003).

[36] Y. Murata, M. Ito, and K. Komatsu, J. Mater. Chem. **12**, 2009 (2002).

[37] G. S. He, J. D. Bhawalkar, C. F. Zhao, and P. N. Prasad, Appl. Phys. Lett. **67**, 2433 (1995).

[38] Nonlinear absorption measurements conducted with ns pulses often show signals that are orders of magnitude higher than those conducted with fs pulses. This is mainly due to signals from excited-state absorption mixing with pure TPA signals. However, comparisons of the same "AFX" compounds' TPA cross-sections have been done by the same group at both pulse duration regimes. We have also studied an "AFX" compound, AF60 (See Chapter 2) that allows for scaling of our fs results for comparisons with ns results.

[39] L. Kuang, Q. Chen, E. H. Sargent, and Z. Y. Wang, J. Am. Chem. Soc. **125**, 13648 (2003).

[40] C. Zhan, D. Li, D. Wang, D. Zhang, Y. Li, W. Xu, Z. Lu, L. Zhao, Y. Nie, and D. Zhu, Chem. Phys. Lett. **347**, 410 (2001).

[41] D. M. Guldi, G. Torres-Garcia, and J. Mattay, J. Phys. Chem. A. **102**, 9679 (1998).

[42] S.-J. Chung, K.-S. Kim, T.-H. Lin, G. S. He, J. Swiatkiewicz, and P. N. Prasad, J. Phys. Chem. B. **103**, 10741 (1999).

[43] G. S. He, J. Swiatkiewicz, Y. Jiang, P. N. Prasad, B. A. Reinhardt, L.-S. Tan, and R. Kannan, J. Phys. Chem. A. **104**, 4805 (2000).

[44] S. Kershaw, *Two Photon Absorption*, Chapter 7 in Characterization Techniques and Tabulations for Organic Nonlinear Optical Materials, edited by M. G. Kuzyk and C. W. Dirk (Marcel Dekker, New York, 1998).

[45] S. Polyakov, F. Yoshino, M. Liu, and G. Stegeman, Phys. Rev. B. **69** (2004).

[46] L. D. Ziegler and X. J. Jordanides, Chem. Phys. Lett. **352**, 270 (2002).

[47] R. L. Sutherland, *Handbook of Nonlinear Optics* (Marcel Dekker, New York, 1996).

CHAPTER 7:

THE KERR RESPONSE OF CROSS-CONJUGATED *ISO*-POLYDIACETYLENES

7.1 Context

iso-Polydiacetylens (*iso*-PDAs) are a novel class of oligo-enynes in which repeat units are linked via cross-conjugated bridges. Because *iso*-PDAs are not linearly conjugated, their nonlinearities may not be expected to increase superlinearly as a function of oligomers length, but rather, each unit may simply contribute additively to the molecular nonlinearity. On the other hand, cross-conjugated *iso*-PDAs have as high a concentration of π-electrons as linearly-conjugated compounds such as typical polydiacetylenes, and may thus be expected to yield large Kerr nonlinearities. This study set out to investigate whether there is sufficient electronic delocalization through the cross-conjugated bridge to yield a superlinear increase in Kerr response as a function of oligomers length. The results of this study have been published in two preliminary articles and one full article.[1-3] The following is a summary of the *iso*-PDA work, and is a reworked excerpt from Y. Zhao, A. D. Slepkov, C. O. Akoto, R. McDonald, F. A. Hegmann, and R. R. Tykwinski, **"Synthesis, structure, and nonlinear optical properties of cross-conjugated perphenylated *iso*-polydiacetylenes"**, *Chem:-Eur. J.* **11**, pp. 321-329, 2004.

Synthesis, linear spectroscopy and molecular modeling of the *iso*-PDA samples were conducted by Dr. Yuming Zhao and Clement Akoto in Dr. Tykwinski's lab. X-ray crystallography was provided by Dr. McDonald, at the University of Alberta.

7.2 Introduction

In the past several decades, molecules with extensive π–delocalization have been investigated for use in third-order NLO applications.[4,5] Conjugated oligomers are also attractive as nonlinear optical materials due to their extended π–electron systems.[6,7] For example, polyynes (PY),[8,9] polyacetylenes (PAs),[10,11] polydiacetylenes (PDAs),[12] polytriacetylenes (PTAs),[13] as well as many others have been explored.[14-18] While linearly-conjugated frameworks are highly attractive for the sheer magnitude of their nonlinear-optical responses, they do have drawbacks.[7] A major disadvantage to most linearly-conjugated oligomers is the dramatic red-shift of maximum electronic absorption wavelength (λ_{max}) towards the visible region of the spectrum as the oligomer chain length is increased. This results in longer oligomers with considerably decreased transparency in the visible region of the spectrum, hindering their technological potential.[19-21] To circumvent this "transparency-nonlinearity trade-off", alternatives to linear conjugation have been explored, such as two-dimensional conjugation[22,23] and the substitution of functional groups in the oligomer backbones.[24,25]

This study looks to investigate cross-conjugation as a way to increase optical nonlinearities without suffering loss of transparency. In this context, cross-conjugated enyne oligomers[26] have been examined with the following motives in mind: First, the red-shift of λ_{max} can be mediated, on account of the attenuated π–electron delocalization via a cross-conjugated framework, giving relatively unmodified transparency, even for extended oligomers. Second, cross-conjugated oligomers remain rich in π–electron density, which is necessary for providing a large third-order molecular and bulk nonlinear optical susceptibility.

Oligomers with a cross-conjugated enyne framework, such as *iso*–polydiacetylenes **1** and **2**[27,28] (shown in Fig. 7.1) and *iso*–polytriacetylenes (*iso*–PTAs)[29-31] show electron communication along the cross-conjugated enyne frameworks, while maintaining high transparency in the visible region of the spectrum.[32] In search of cross-conjugated oligomers suitable for the study of third-order NLO behavior, a series of perphenylated *iso*–PDA oligomers **3** was synthesized, wherein the perphenylation allows for high solubility necessary for NLO measurements.[3]

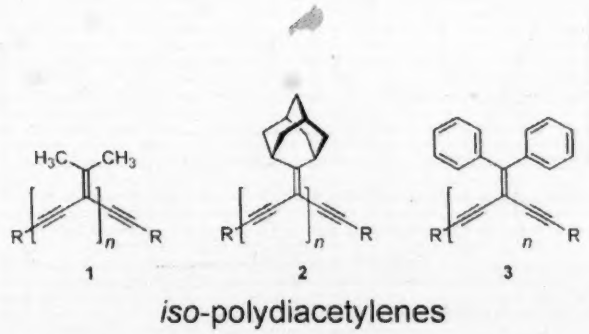

Figure 7.1. Three general *iso*-polydiacetylene frameworks. Structures **3** are the perphenylated *iso*-PDAs discussed herein.

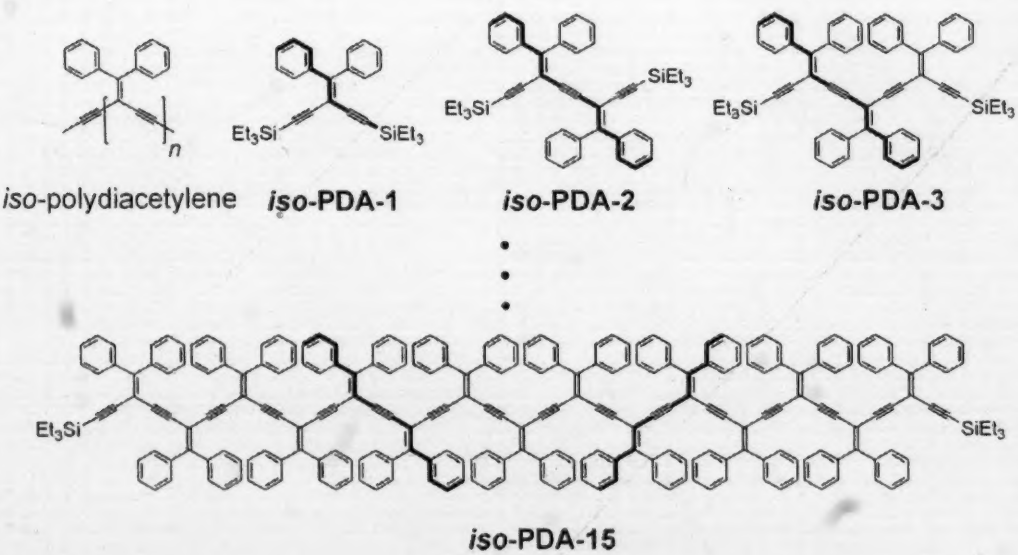

Figure 7.2. Perphenylated *iso*-polydiacetylene oligomers. The end-group Et_3Si, otherwise known as *TES*, is an electronically inert moiety inserted for improved solubility. For this study, oligomers with n=1, 2, 3, 5, 7, 9, 11, 13, and 15 were investigated. The longest linear-conjugated path for each of the oligomers is shown in bold, highlighting the fact that the maximum fixed-length segment is not present in the monomer, ***iso*-PDA-1**.

7.3 Results and Discussion

Electronic Absorption and Emission: The electronic absorption characteristics of dimer ***iso*-PDA-2** through pentadecamer ***iso*-PDA-15** were investigated by UV-vis spectroscopy, and are shown in Fig. 7.2. A prominent aspect of the UV/Vis spectra is the steadily increasing molar absorptivity as the oligomeric chain length is extended, which ultimately reaches ε= 160,000 $M^{-1}cm^{-1}$ for ***iso*–PDA-15**. The electronic absorption spectrum of the dimer shows two distinct absorptions at 373 nm and 323 nm. In the absence of a significant contribution from cross conjugation, the major absorptions for *iso*–PDAs are expected to come from the longest linearly-conjugated framework, the ene-yne-ene segment shown in bold in Fig. 7.2.[33] Previous work with cyclic *iso*–PDAs suggests that the lower-energy absorption (373 nm) results from the HOMO→LUMO transition for the ene-yne-ene segment. The absorption at 323 nm, however, is predicted to arise from the HOMO→LUMO+1 transition of the cisoid conformer, a transition that is formally symmetry forbidden for the transoid conformer. The spectrum of trimer ***iso*-PDA-3** shows a similar absorption profile to that of the dimer, with distinct absorptions at 375 and 324 nm. In the spectrum of the pentamer, the low-energy absorption at 377 nm becomes the only resolved characteristic, as the higher-energy absorption peak at 324 nm merges into a barely-distinguishable shoulder. From the heptamer ***iso*-PDA-7** to pentadecamer ***iso*-PDA-15**, the electronic absorption profiles show a similarly broad and featureless peak at a maximum absorption energy of λ_{max} = 378 nm. Overall, a very small red-shifting of λ_{max} is observed as one progresses from the dimer (λ_{max} = 373 nm) to pentadecamer **25** (λ_{max} = 378 nm). This effect has, however, already reached saturation by the length of approximately n = 7–9,[34] similar to that observed in other *iso*–PDAs.[27,28]

Emission spectra ([*iso*-PDA] < 1.5 M), have been measured in degassed $CHCl_3$ with an excitation wavelength of 380 nm (Figure 7.4), and the perphenylated *iso*–PDAs show enhanced emission when compared to their alkylidene analogues **1** and **2**. The *iso*–PDA oligomers (n = 2-15) consistently show only one broad emission peak, and the relative emission intensity steadily increased with chain length n. The maximum emission wavelength (λ_{em}) shifts toward the lower-energy region from dimer ***iso*-PDA-2** (λ_{em} = 468 nm) to heptamer ***iso*-PDA-7** (λ_{em} = 503 nm). From heptamer to pentadecamer ***iso*-PDA-15**, λ_{em} is constant. This trend concurs with that discussed above for the UV/Vis absorption data, suggesting an effective conjugation length (ECL) of $n \approx 7$.

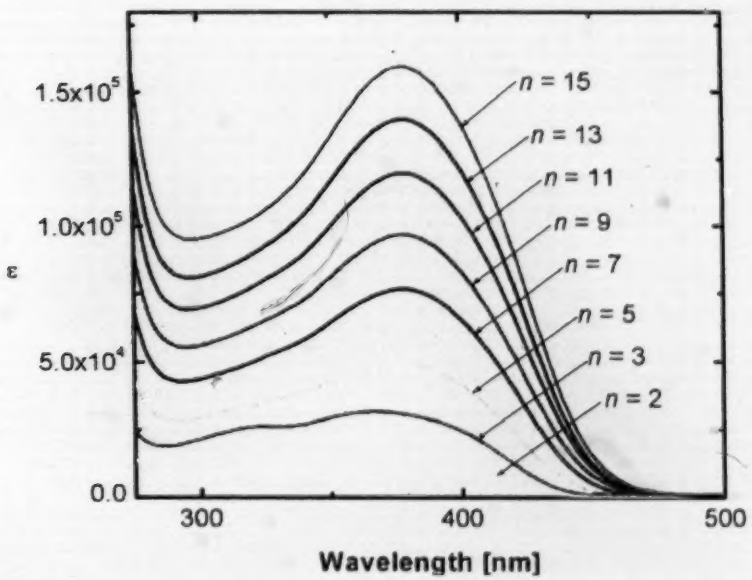

Figure 7.3. [colour] Electronic absorption spectra (ε in $Lmol^{-1}cm^{-1}$) in $CHCl_3$ comparing the effects of oligomer chain for *n*=2-15 *iso*-PDAs.

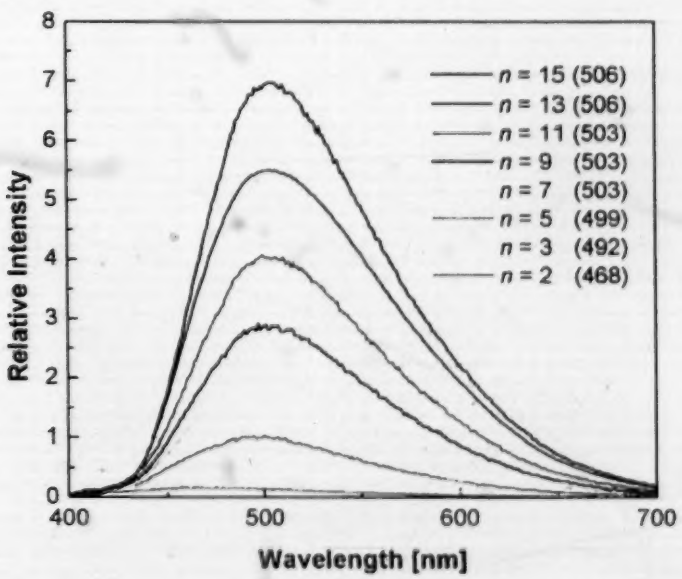

Figure 7.4. [colour] Emission spectra in $CHCl_3$ for full *iso*-PDA series, with excitation at 380 nm. λ_{em} in nm for each oligomer is shown in parentheses. For clarity, legend entries follow the peak signal in order.

Table 7.1. DOKE results for the *iso*–PDA series.[a]

Entry	*n*	Concentration (M)	γ ($\times 10^{-36}$ esu)	γ_s / γ_{THF}
***iso*-PDA-1**	1	0.23	9.2±0.4	17.7±0.8
***iso*-PDA-2**	2	0.15	30.3±0.3	58.2±0.5
***iso*-PDA-3**	3	0.13	48±4	94±7
***iso*-PDA-5**	5	0.12	70±5	134±9
***iso*-PDA-7**	7	0.10	94±4	181±9
***iso*-PDA-9**	9	0.12	123±8	240±15
***iso*-PDA-11**	11	0.054	177±18	347±35
***iso*-PDA-13**	13	0.054	208±10	408±20
***iso*-PDA-15**	15	0.035	308±8	603±16

[a] γ and γ_{THF} are the third-order hyperpolarizabilities of the oligomer samples and THF reference, respectively. *n* is the number of repeat units in the oligomer.

Nonlinear Optical Properties: Because of their significant optical transparency, an appealing aspect of *iso*–PDA oligomers is their potential use as third-order NLO materials. Molecular second hyperpolarizabilities, γ, for the *iso*–PDA samples were determined by differential optical Kerr effect (DOKE) experiments. In these experiments, the oligomer samples, from monomer ***iso*-PDA-1** to pentadecamer ***iso*-PDA-15**, were prepared as THF solutions of 0.035-0.23 M. The γ-values were then obtained as described in Chapter 2 and elsewhere.[35] All γ-values are referenced to that of THF (γ_{THF}). As depicted by the values in Table 7.1, the *iso*–PDA series shows an order of magnitude increase in γ from the dimer to pentadecamer. Overall, however, the γ-values themselves remain quite modest (when compared to those of linearly conjugated polyenes, for example [4]). On the basis of the absorption and emission data, conventional wisdom dictates that electronic communication would be limited across a cross-conjugated bridge. Thus, increasing the number of monomer units of an *iso*–PDA oligomer would simply increase the number of fixed-length linearly-conjugated paths (shown in bold, Figure 7.2). In the absence of significant cross-conjugated π–

delocalization, a linear increase in γ-values as a function of chain length would be expected. Indeed, a linear trend for shorter *iso*–PDA oligomers (n = 2–7) was observed and reported.[1,2] The investigation of longer oligomers, however, reveals markedly different behavior as shown in Fig. 7.5, where the oligomer nonlinearities clearly deviate from linearity with increasing chain length (n).

A superlinear increase in γ-values as a function of chain length is typically encountered in both theoretical and experimental studies of the electronic hyperpolarizabilities of linearly conjugated oligomers. Such studies have shown that optical nonlinearities generally increase with conjugation length according to a power-law relationship, $\gamma \sim n^c$, where c is the power law exponent.[7,36,37] Thus, a nonlinear increase in γ as a function of oligomer length may indicate increased electronic communication along a conjugated backbone. While theories predict power law exponents of c = 2 – 4 for linearly conjugated systems,[7,38] there are currently no theoretical predictions for cross-conjugated systems. This is, arguably, because no electronic delocalization is expected to occur through cross-conjugated linkages. Figure 7.5b presents the γ-values of the entire *iso*–PDA series (with the exclusion of the monomer, ***iso*-PDA-1**)[39] fit to a power law function of the form $\gamma = a + bn^c$, where a and b are constants. Considering the entire data series, this analysis provides a superior fit to that of a simple straight line, and yields a power of c=2.0±0.3. Although the data adequately fits a power-law, the correlation is not ideal.

A third possible relationship, consisting of two linearly increasing regimes, is also considered, and is shown in f 7.5c. The γ-values show a good linear fit spanning n=2–7 and a second linear fit with a steeper slope over the range of n=9–15. Overall, the two-line analysis, with a distinct change in slope at $n \approx 9$, provides the best description of the data. The analyses in Figs. 7.5b,c represent two different phenomena. A power-law relationship between γ and oligomer length (Fig. 7.5b) would presumably arise from increased π–electron delocalization, an unlikely prospect considering only the minute red-shifting seen UV/Vis absorption and emission data. A two-regime linear increase in nonlinearities with a distinct change in slope, however, could arise from the onset of ordering of the sample in solution, such as folding. This prospect is discussed below.

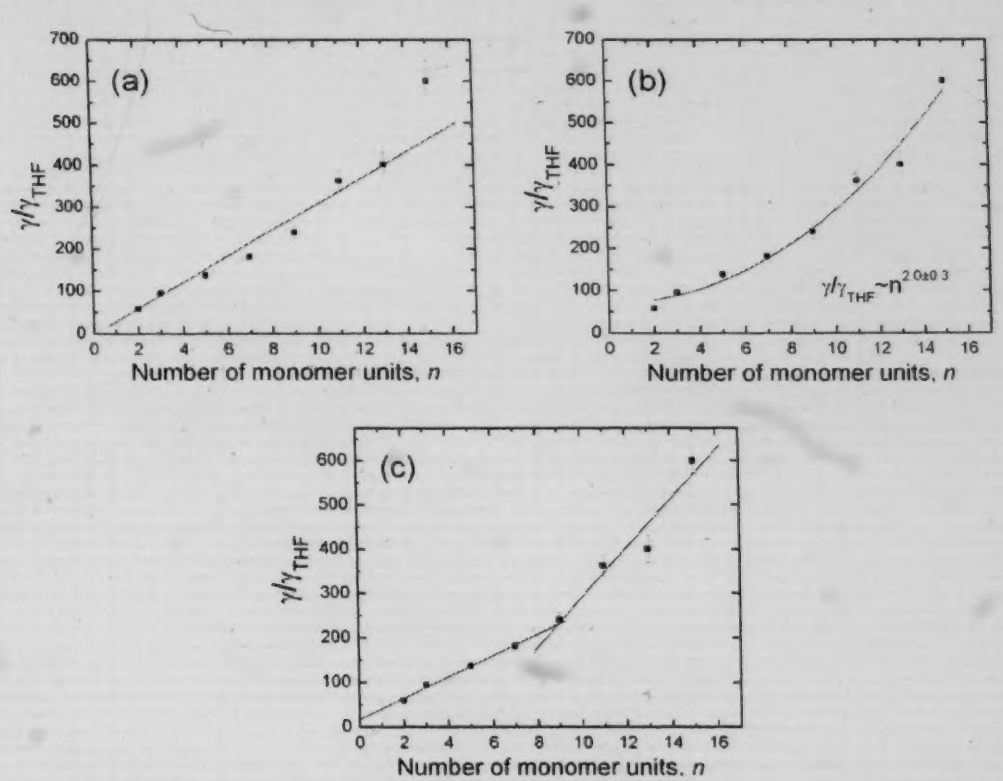

Figure 7.5. Correlation of relative molecular second hyperpolarizibilities (γ/γ_{THF}) as a function of oligomer length *n*. (a) Linear fit (n = 2–15). (b) power-law fit of the form $\gamma = a + bn^c$ (n = 2–15). (c) Two linear fits (n = 2–7 and n = 9–15).

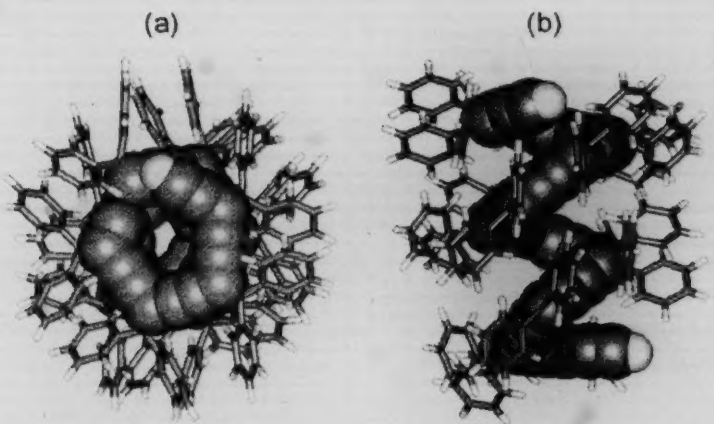

Figure 7.6. Minimized structure of tridecameric *iso*-PDA using MM3* force field parameters.[40] Only backbone carbons are displayed as space-filling representation for clarity: (a) View from top; (b) View from side

Solution state folding of *iso*–PDAs: Perphenylated *iso*–PDA oligomers may prefer a specific, folded, conformation in the solution state, especially in the case of longer oligomers ($n > 7$). In addition to the NLO evidence for structural changes at a length between n=7 and n=9, crystallographic analysis of trimer ***iso*-PDA-3** further supports this hypothesis; where the pseudo-*cis* orientation between enediyne segments allows the neighboring phenyl groups to approach close enough to effect π-π interactions, which could become the dominant feature in the longer oligomers. To further probe the prospect of folding, the geometry of *iso*–PDA oligomers of various length was analyzed computationally (by Dr. Y. Zhao).[40] When the initial oligomer geometry adopts an all-*cisoid* conformation (n>7), the minimized structure consistently achieved a helical conformation with a "folded" enyne framework, which is demonstrated in Fig. 7.6 for the tridecamer (minus *TIP*S end-groups). The phenyl rings of neighboring alkylidene units each participate in π–stacking, contributing to the stabilization of the folded conformation, as can be seen in Figure 7.6b. The pitch angle for the helix is calculated to be approximately 40°.

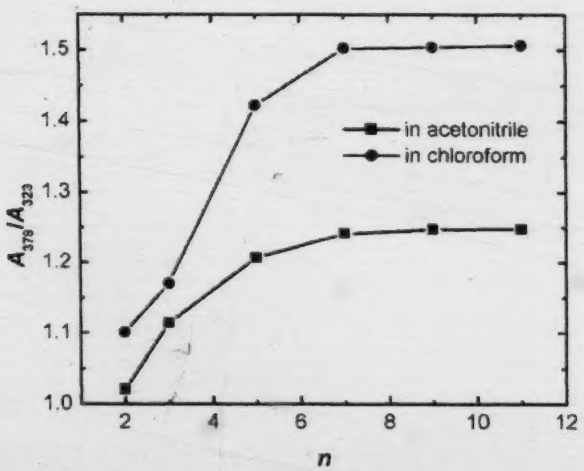

Figure 7.7. Plot of absorbance ratio A_{378}/A_{323} *vs.* chain length (n) in $CHCl_3$ (●) and acetonitrile (■). A_{378} denotes the absorbance intensity at 378 nm, and A_{323} denotes the absorbance intensity at 323 nm.

Folding of the *iso*–PDA oligomers is further supported by UV/Vis spectroscopic analysis. Previous work on *iso*–PDAs provide for the following assumptions in the present study: First, the HOMO→LUMO+1 transition at approximately 323 nm is symmetry allowed for the cisoid conformation and forbidden for the transoid conformation,[27,28] and, secondly, the HOMO→LUMO transition for the cisoid ene-yne-ene chromophore occurs at slightly higher energy than that of the transoid conformer (although both are observed as a combined absorption band at approximately 378 nm in the present case).[27,28,41] The ratio of these two absorbances (denoted as A_{378}/A_{323}) could therefore be an indicator of a conformational change, and a plot of this indicator versus chain length n is presented in Figure 7.7. In both $CHCl_3$ and acetonitrile, the ratio of A_{378}/A_{323} steadily increases from dimer ***iso*-PDA-2** to heptamer ***iso*-PDA-7**, and then reaches a constant value for the longer oligomers ($n \geq 7$). This behaviour is consistent with a conformational change for the longer oligomers. In an effort to provide additional support of a folded conformation for *iso*–PDAs, circular dichroism (CD) spectroscopy in the presence of chiral guests (such as pinene) was explored.[42,43] These studies, unfortunately, did not give conclusive evidence for (or against) solution-state folding, as a biased twist sense could not be achieved.

7.4 Conclusion

The optical, structural and nonlinear optical properties of perphenylated cross-conjugated *iso*-polydiacetylene oligomers, with n=1-15 repeat units, were studied. Their electronic absorption behavior indicates an effective conjugation length of approximately n≈7–9. The *iso*–PDA oligomers show steadily increasing fluorescence intensity as a function of chain length, and the emission wavelength red-shifts slightly from 468 nm (in dimer ***iso*-PDA-2**) to 503 nm (in heptamer ***iso*-PDA-7**). Beyond the length of the heptamer, the emission energy remains essentially constant. The third-order NLO properties of the *iso*–PDAs in THF solutions were studied by differential optical Kerr effect (DOKE) experiments, at a wavelength of 800 nm. The molecular second hyperpolarizabilities display a super-linear increase as a function of chain length. The best fit to the NLO data shows two linear regimes, suggesting an increased order in the system, likely helical folding. While definitive proof of a folded conformation for extended *iso*–PDAs remains elusive, empirical evidence of this conformational presence is provided by molecular modeling studies as well as UV/Vis and NLO spectroscopy. The superlinear increase in γ as a function of oligomer length is the first of its kind reported for (through-carbon) cross-conjugated systems. The 15-repeat-unit ***iso*-PDA-15** showed the largest nonlinearity, with γ=603±16γ_{THF}.

7.5 References

[1] A. D. Slepkov, F. A. Hegmann, Y. Zhao, R. R. Tykwinski, and K. Kamada, J. Chem. Phys. **116**, 3834 (2002).

[2] A. D. Slepkov, F. A. Hegmann, K. Kamada, Y. Zhao, and R. R. Tykwinski, J. Opt. A. **4**, S207 (2002).

[3] Y. Zhao, A. D. Slepkov, C. O. Akoto, R. McDonald, F. A. Hegmann, and R. R. Tykwinski, Chem. Eur. J. **11**, 321 (2004).

[4] U. Gubler and C. Bosshard, Adv. Polym. Sci. **158**, 123 (2002).

[5] R. R. Tykwinski, U. Gubler, R. E. Martin, F. Diederich, C. Bosshard, and P. Günter, J. Phys. Chem. B. **102**, 4451 (1998).

[6] R. E. Martin and F. Diederich, Angew. Chem. Int. Ed. **38**, 1350 (1999).

[7] C. Bubeck, *Nonlinear Optical Properties of Oligomers*, in Electronic Materials-The Oligomer Approach, edited by K. Müllen and G. Wegner (Wiley-VCH, Veinheim, 1998), Chapter 8.

[8] A. D. Slepkov, F. A. Hegmann, S. Eisler, E. Elliott, and R. R. Tykwinski, J. Chem. Phys. **120**, 6807 (2004).

[9] S. Eisler, A. D. Slepkov, E. Elliott, T. Luu, R. McDonald, F. A. Hegmann, and R. R. Tykwinski, J. Am. Chem. Soc. **127**, 2666 (2005).

[10] S. Hahn, D. Kim, and M. H. Cho, J. of Phys. Chem. B **103**, 8221 (1999).

[11] A. Kiehl, A. Eberhardt, M. Adam, V. Enkelmann, and K. Müllen, Angew. Chem. Int. Ed., **31**, 1588 (1992).

[12] M. P. Carreon, L. Fomina, S. Fomine, D. V. G. L. N. Rao, F. J. Aranda, and T. Ogawa, Photon. Optoelectron. Polym., **672**, 199 (1997).

[13] R. E. Martin, U. Gubler, J. Cornil, M. Balakina, C. Boudon, C. Bosshard, J. P. Gisselbrecht, F. Diederich, P. Günter, M. Gross, and J. L. Brédas, Chem. Eur. J. **6**, 3622 (2000).

[14] L. Kuang, Q. Chen, E. H. Sargent, and Z. Y. Wang, J. Am. Chem. Soc. **125**, 13648 (2003).

[15] M. Wong, Z. Li, M. Shek, M. Samoc, A. Samoc, and B. Luther-Davies, Chem. Mater. **14**, 2999 (2002).

[16] K. Ogawa, T. Q. Zhang, K. Yoshihara, and Y. Kobuke, J. Am. Chem. Soc. **124**, 22 (2002).

[17] P. Siemsen, U. Gubler, C. Bosshard, P. Günter, and F. Diederich, Chem. Eur. J. **7**, 1333 (2001).

[18] H. Meier, D. Ickenroth, U. Stalmach, K. Koynov, A. Bahtiar, and C. Bubeck, Eur. J. Org. Chem., 4431 (2001).

[19] M. Blanchard-Desce, J. B. Baudin, L. Jullien, R. Lorne, O. Ruel, S. Brasselet, and J. Zyss, Opt. Mater. **12**, 333 (1999).

[20] C. R. Moylan, R. D. Miller, R. J. Twieg, K. M. Betterton, V. Lee, T. J. Matray, and C. Nguyen, Chemistry of Materials **5**, 1499 (1993).

[21] I. Ledoux, J. Zyss, A. Jutand, and C. Amatore, Chem. Phys. **150**, 117 (1991).

[22] U. Gubler, R. Spreiter, C. Bosshard, P. Günter, R. R. Tykwinski, and F. Diederich, Appl. Phys. Lett. **73**, 2396 (1998).

[23] C. Bosshard, R. Spreiter, P. Günter, R. R. Tykwinski, M. Schreiber, and F. Diederich, Adv. Mater. **8**, 231 (1996).

[24] S. Concilio, I. Biaggio, P. Günter, S. P. Piotto, M. J. Edelmann, J. M. Raimundo, and F. Diederich, J. Opt. Soc. Am. B. **20**, 1656 (2003).

[25] U. Gubler, S. Concilio, C. Bosshard, I. Biaggio, P. Günter, R. E. Martin, M. J. Edelmann, J. A. Wytko, and F. Diederich, Appl. Phys. Lett. **81**, 2322 (2002).

[26] R. R. Tykwinski and Y. Zhao, Synlett, 1939 (2002).

[27] Y. Zhao and R. R. Tykwinski, J. Am. Chem. Soc. **121**, 458 (1999).

[28] Y. Zhao, K. Campbell, and R. R. Tykwinski, J. Org. Chem. **67**, 336 (2002).

[29] Y. Zhao, R. McDonald, and R. R. Tykwinski, J. Org. Chem. **67**, 2805 (2002).

[30] Y. Zhao, R. McDonald, and R. R. Tykwinski, Chem. Comm. 77 (2000).

[31] E. Burri, F. Diederich, and M. B. Nielsen, Helv. Chim. Act. **85**, 2169 (2002).

[32] M. Bruschi, M. G. Giuffreda, and H.-P. Lüthi, Chem. Eur. J. **8**, 4216 (2002).

[33] It is worth noting, however, that a fully planar conformation is not easily achieved in longer oligomers due to steric repulsion, as demonstrated by crystallographic analyses. Accordingly, it is possible that electron delocalization could be, on average, mediated to a more limited segment than that shown in bold.

[34] Electronic absorption spectra of ***iso*-PDA-7** and ***iso*-PDA-9** were recorded at varied concentrations (from 10-5 to 10-7 M) in $CHCl_3$ in order to probe the possibility of aggregation in solution. These results showed consistent profiles and nearly identical extinction coefficients, suggesting little or no aggregation over the accessible range of concentrations.

[35] A. D. Slepkov, *Third-Order Nonlinearities of Novel iso-Polydiacetylenes Studied by a Differential Optical Kerr Effect Detection Technique*, M.Sc. Thesis. University of Alberta, Edmonton, 2001.

[36] U. Gubler, C. Bosshard, P. Günter, M. Y. Balakina, J. Cornil, J. L. Brédas, R. E. Martin, and F. Diederich, Opt. Lett. **24**, 1599 (1999).

[37] I. D. W. Samuel, I. Ledoux, C. Dhenaut, J. Zyss, H. H. Fox, R. R. Schrock, and R. J. Silbey, Science **265**, 1070 (1994).

[38] Nonlinear optics of organic molecules and polymers, H. S. Nalwa and S. O. Miyata, Eds. (CRC Press, New York, 1997).

[39] For consistency, the data for the monomer, ***iso*-PDA-1** is ignored in the analysis of the relationship between the molecular hyperpolarizability and conjugation length, because the monomer does not contain a complete linearly-conjugated segment (see Fig. 7.2). This segment is complete by the stage of the dimer, and only with extending the oligomeric series past this stage do we add fixed numbers of this segment.

[40] Molecular mechanics software *Macromodel 7.0*, using the implemented MM3* force field parameters; the silyl groups were excluded to minimize computational time. Calculations conducted by Yuming Zhao, 2003.

[41] S. Eisler and R. R. Tykwinski, Angew. Chem. Int. Ed. **38**, 1940 (1999).

[42] J. C. Nelson, J. G. Saven, J. S. Moore, and P. G. Wolynes, Science **277**, 1793 (1997).

[43] C. R. Ray and J. S. Moore, Adv. Polym. Sci. **177**, 91 (2005).

PART III

EXTENDING WAVELENGTH CAPABILITIES WITH A SUPERCONTINUUM PROBE

CHAPTER 8:

EXPERIMENTAL SETUP FOR THE MEASUREMENT OF NONDEGENERATE TWO-PHOTON ABSORPTION SPECTRA

8.1 Introduction

All of the time-resolved measurements described in preceding chapters measured degenerate sample nonlinearities, wherein pump and probe wavelengths are the same. Our laser outputs 800 nm light, as defined by our Ti:Sapphire oscillator. For various experiments, we often desire pump or probe beams of wavelengths different than 800 nm. Such experiments include one- or two-colour transient absorption and pump-probe two photon absorption measurements. As outlined in preceding chapters, the need for characterizing optical nonlinearities at various wavelengths is becoming increasingly clear. This is especially true for absorptive nonlinearities, where two-photon absorption (TPA) *spectra* provide immeasurably more information than cross-sections at a single wavelength. Theoretical expressions that describe a compound's two-photon activity depend on parameters at the TPA spectrum peak and on oscillator strengths and absorption line-widths.[1-3] Our experience with a series of self-similar two-dimensional tetrakis(phenylethynyl)benezene (TPEB) compounds provides a good example for illustrating the importance of measuring the entire TPA spectrum, as opposed to measurements at a single wavelength (see Chapter 5). For several years we only had access to measurements of TPEB nonlinearities at 800 nm. We spent considerable time attempting to analyze trends in the optical nonlinearities of these compounds, but found that without knowledge of the position of the TPA peaks themselves, any conclusions would have to be tentative at best. Upon obtaining the (vis-NIR) two-photon absorption spectra of these compounds, it became clear that the true ordering of TPA activity was

very different than that presented at 800 nm; some compounds had TPA peaks at shorter-wavelengths, and were thus decreasing at 800 nm, while others were increasing TPA activity to peaks at longer wavelengths. While these z-scan spectral measurements were extremely useful for the description of TPA processes in the TPEBs, they were nonetheless conducted without time-resolution capabilities. Thus, we have a clear and urgent need for a broadband laser source for pump-probe experiments.

In the past, we have used a frequency-doubling crystal such as α-BBO or KDP for the generation of 400 nm light for use in such experiments. However, this process still limits our spectral capabilities to two wavelengths; namely, 800 nm and 400 nm. For the past 15 years, the most widely used source for wavelength-tunable laser light has been the optical parametric generator, OPG (or amplifier: OPA). A typical OPG/OPA can convert intense monochromatic laser beam to a much-weaker monochromatic beam at a different wavelength. We have a Quantronix TOPAS OPA, which we have used for wavelength-tunable pump-probe experiments, with intermittent success.[4] The TOPAS specifications list its output range to be from 250 nm to 20 μm, using 8 different generation/doubling crystals. The conversion efficiency for the OPA depends on the output wavelength, and ranges from 20% to 0.2% efficiency in the visible. In practice, we have found the TOPAS efficiency to be considerably lower than this. We have mainly used the OPA for generating infrared pulses with wavelengths greater than 800 nm, and thus, outside of the visible range. We have also found the OPA output to be very noisy, with large pulse-to-pulse fluctuation. This is a major problem for pump-probe experiments, and especially those like the Kerr effect that exhibit a quadratic dependence on laser power. Furthermore, the TOPAS can only output one wavelength at a time, and needs alignment (often considerable) to tune each individual wavelength. Thus, there is considerable downside to using the OPA as a source for broadband tunable laser light for pump-probe experiments.

Supercontinuum ("white-light") generation (SCG) is a well-established, but fairly recent technique for obtaining broadband coherent laser light. Alfano and Shapiro first discovered SCG by focusing intense picosecond pulses into BK-7 glass.[5] Since then, the technique has been extended to ultrashort femtosecond pulses and a variety of media, including simple liquids such as water and benzene;[6] glasses; crystalline solids such as

LiF and sapphire;[7] modified optical fibers;[8,9] and gasses.[10] It is not surprising that SCG was among the last NLO phenomena to be discovered because this process requires extremely high field intensities. In fact, all white-light generation shows thresholding behaviour, a universal characteristic of SCG that may be a clue to its origins.[10,11] It has become clear that regardless of the exact chain of events, the creation of new wavelengths in SCG involves nonlinear optical processes. This conclusion is made from the high threshold powers needed to sustain the phenomenon combined with the low attenuation levels of the incident pulse. Somehow, the intense light is interacting with the medium to convert incident radiation into new wavelengths. For this to occur, a time-varying phase change must exist such that the creation of new frequencies is given by:[11]

$$\Delta\omega(t) = -\frac{\partial \phi_{NL}}{\partial t}. \qquad 8.1$$

This phase change (ϕ_{NL}) may, for example, be brought about by a third-order Kerr-type index modulation where the index of refraction is intensity dependent.

$$\phi_{NL}(t) = \frac{\omega n_2 L I(t)}{c}. \qquad 8.2$$

Thus, self-phase modulation as the generation mechanism predicts a continuum bandwidth that depends on the third-order optical nonlinearities of the generating material;[12]

$$\Delta\omega(t) = -\frac{\omega L n_2}{c}\frac{\partial I(t)}{\partial t} \propto \chi^{(3)}. \qquad 8.3$$

This correlation, however, is nearly universally absent and may, in fact, be reversed.[6,7,11] Processes that are easily identified with these expressions, such as self-phase modulation (SPM),[8,12] four-wave mixing (FWM),[6] and self-focusing [10,13-

17] were among the first to be nominated as the key mechanisms responsible for SCG. Other processes such as Raman-enhanced four-wave mixing (FWM) and stimulated Raman scattering (SRC) have been shown to play a key roll in the SCG of some materials,[6] while novel phenomena such as stimulated reorientational Kerr-scattering (SKS) and Raman-induced Kerr effect have been proposed to explain anomalous features of SCG in other materials.[6] Finally, processes that take into account the large intensities of incident light, such as multi-photon excitation or electron-plasma production,[18] have provided convincing arguments to explain key features of many SCG spectra. Amidst a multitude of white-light spectra, generated by different samples or seeded by different pulses, it is easy to find trends to support any given generation theory. However, there is also enough evidence to shed doubt of any one nonlinear phenomenon as the sole mechanism for supercontinuum generation. In all probability, SCG involves multiple competing nonlinear processes, yielding complex and highly variant broadband spectra.

Generation of The Supercontinuum: In practice, the generation of coherent supercontinuum light is trivial. High-intensity laser light is incident (either focused or not) on a sample, and the out-going light is collimated for analysis or use. The intricacies of SCG lie in the fact that every initial parameter—including sample type, sample length, incident pump wavelength, incident pulse length, and maximum pulse intensity—gives rise to different white-light spectra. The commonality in all of the experiments lies in the depletion of pump light to create a continuum of other wavelengths. These new frequencies may lie on either or both of the high-frequency, low-wavelength (anti-Stokes), or on the low-frequency, high-wavelength (Stokes) side of the incident spectrum. What makes the supercontinuum exciting is not in the creation of other distinct wavelengths—since these are achievable by established means such as Stimulated Raman Scattering (SRS), and sum- or difference-frequency mixing—but in the *continuous creation of new frequencies*. The supercontinuum may be symmetric, where $\Delta\omega$ is equal on each side of the incident frequency, or it may be asymmetric, with either $\Delta\omega_+ > \Delta\omega_-$ or $\Delta\omega_- < \Delta\omega_+$ (where + signifies the anti-Stokes side and – signifies the Stokes side).[19] The case of dominant Stokes continuum is relatively rare. The notation of "Stokes" and "anti-Stokes" does not mean that the process necessarily involves Raman modes, as is clear from the possibility that $\Delta\omega_+ > \Delta\omega_-$. Furthermore, the supercontinuum spectrum may be extremely wide with $\Delta\omega \approx \omega_0$, making it particularly useful for broad-band spectroscopy.[20,21]

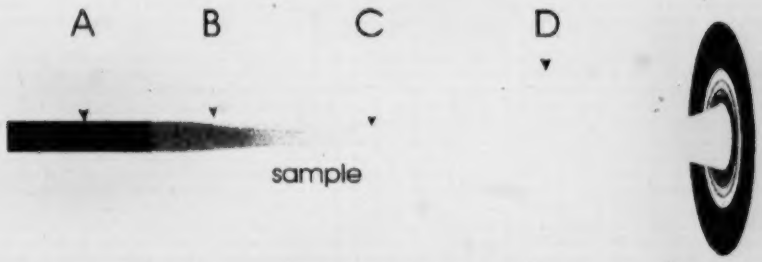

Figure 8.1. [colour] A schematic of supercontinuum generation. A collimated incident beam (A) begins to self-focus (B) and eventually forms a self-guiding filament (C). In this region, the intensity of light is immense, generating both a collinear continuum and an angle-dependent conical component (D). Modified from [15]

In a typical SCG setup, the out-going white light has three essential components, as illustrated in Fig. 8.1:[7,15] The majority of the energy lies in the undepleted pump pulse at the original frequency. Collinear with this light, is the supercontinuum. This light has a modulated spectrum, and is *iso*-polarized with the pump beam, with its anti-Stokes component typically lagging temporally behind its Stokes component.[22] With the vast spectral differences between the pump and supercontinuum beams, one might expect complete spatio-temporal collapse of the supercontinuum beam. However, despite these spectral characteristics, the supercontinuum beam is nearly unaltered spatio-temporally, displaying a homogeneous temporal broadening.[10] The third feature is a conical emission that slightly diverges from the main beam. This emission has a wavelength-dependent angle, increasing in divergence with decreasing wavelength. Thus, it appears as an inverted rainbow when projected on a screen. Simple scattering (diffraction) processes would yield the opposite wavelength-emission angle dependence, suggesting that the conical component is distinct from the collinear component. This feature also represents a coherent supercontinuum. However, the term supercontinuum is often reserved for the white-light that is collinear with the pump beam.[11] This notation will be used for the remainder of this work, where supercontinuum or white-light will refer only to the collinearly generated component.

CHAPTER 8: ESTABLISHING A WHITE-LIGHT PROBE SETUP

A further attribute of SCG is the phase coherence of the white light, making it ideal for spectroscopy. This aspect of SCG may be surprising, especially when considering the various proposed competing mechanisms that bring about its creation. Despite all of these attributes, it is important to note that regardless of the technique used for generation, the process is quite inefficient, with the best free-space conversion efficiencies on the order of 10% pump depletion, and in most cases under 2% conversion! However, since creating white light typically takes intensities on the order of 10^7-10^{15} W/cm^2, even a few percent of white light is sufficient for spectroscopic and amplification-seeding purposes. Furthermore, contrary to expectation, the low conversion efficiency does not arise from absorption, since in most cases the total absorption losses are less than 5%.[11]

Towards the end of establishing capabilities for the ultrafast time-resolved characterization of nonlinear absorption processes in organic samples, I have endeavoured to set up an 800 nm-pump continuum-probe experiment. The goal was to establish proof-of-principle that a usable continuum beam may be created in our lab, and further, that this beam may be suitable for studying the nondegenerate two-photon absorption (TPA) cross-section and excited-state dynamics of condensed-matter samples.

8.2 Continuum Generation in H_2O and Pulse Characterization

Continuum Generation in H2O: After preliminary investigation of SCG from H_2O and heavy water in 1 mm path-length cuvettes, as well as from thin sapphire windows, we found that a longer, 10 mm path-length, water cell produces an adequately strong and broad continuum. In all of the generating media that we investigated, we found large pulse-to-pulse intensity and spectrum fluctuations. These fluctuations are mostly due to the formation of trapped bubbles in thin cells and from damage in sapphire windows. In an attempt to reduce these fluctuations, we constructed a 10 mm path-length (square profile) quartz flow-cell to flush out any bubbles. A temperature-controlled liquid pump is used to circulate the water through the flow-cell. The output light shows good pulse-to-pulse and long term stability, both in the spectrum and the intensity. Thus, we currently generate our continuum by focusing 800 nm light into distilled water in a 10 mm path length quartz flow-cell.

The experimental layout for both the supercontinuum generation and its subsequent characterization is presented in Fig. 8.2. For the white-light generation, polarized 100 μJ, 800 nm amplified laser pulses are focused with an f = 7.5 cm lens into distilled water flowing through a 10 mm path-length quartz cell. The emerging continuum diverges rapidly and shows typical conical emission in addition to a central 'white-light' beam. The conical emission, as well as approximately 10% of the continuum beam is removed with an iris acting as a window. The flow cell is on a translation stage, allowing us to vary the position of the focus within the cell. It is found that the most intense, stable, and broad light is obtained when one can see the generation of white light very near the entrance window, about ½ to 1 mm from the window. This also creates the most diverging beam, which is somewhat of a problem. After generation and near-collimation, the continuum beam may be filtered to remove the large 800 nm pump component and to select other wavelengths, before passing through a polarizer and

analyzer gating pair. Slightly uncrossing the analyzer allows for a small amount of continuum light to proceed to a scattering screen for spectral measurements. Figure 8.3 presents the continuum spectrum in comparison to the generating 800 nm beam. The generated spectrum is of typical asymmetric shape,[7] with the majority of spectral weight present near the generating wavelength, and extending further on the Stokes side than the anti-Stokes side. Spectrometer detection resolution effectively cuts off detection at 350 nm and 1000 nm, but the continuum is expected to extend to longer wavelengths. It is not expected to extend beyond 400 nm to lower wavelengths. Considerable pump depletion takes place, yet the majority of the outgoing beam consists of undepleted 800nm light. Typical generating values, which admittedly change slightly from day to day, are as follows: 800 nm generating beam power is 100 mW; the total out-coming light is 70 mW; the total stokes-side light when a 750 nm short-pass filter is used is 5-10 mW. Thus the generating efficiency is 5%-10%, ignoring the sizable >800 nm light component. At any given wavelength, however, the power is small. For example, with the aforementioned generating conditions, the total 634 nm light present is 300 μW when using an efficient bandpass filter, and only 50 μW at 700 nm when using an inefficient one. These powers are ample for probing nonlinearities in pump-probe measurements, but are insufficient for use as pump sources.

When describing the generating parameters in SCG, it is crucial to detail the input powers and focal parameters of the beam. Because self-focusing is such an important factor in the generation process, slight changes in either the z-position of the cell, the generating beam intensity, the generating beam size, or the pulse's temporal width will all change the output spectrum and its intensity. Thus, it is also important to maintain consistent generating parameters throughout an experiment. 100 mW input power and a 300 mm focal length lens were selected for moderate (but not strong) white-light generation to avoid possible complications from significant filamenting that may occur with intense generating pulses.[23,24]

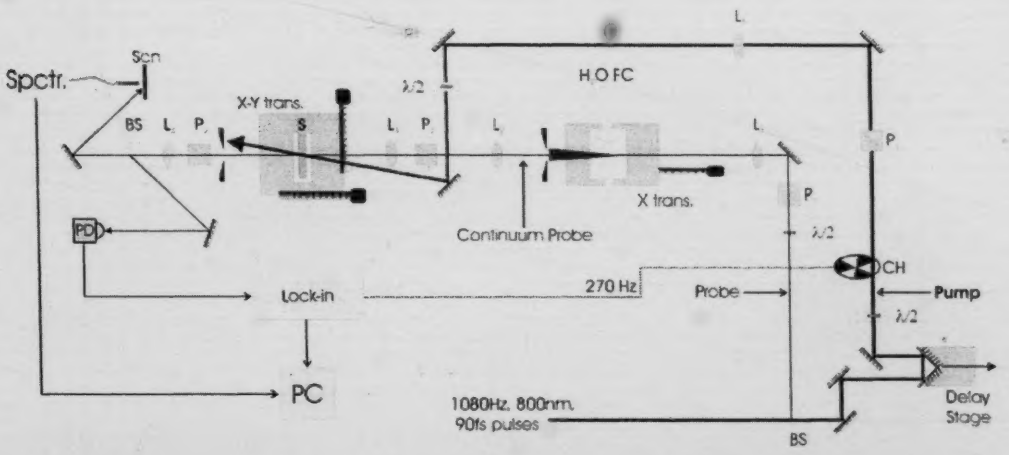

Figure 8.2. A schematic of our continuum generation layout and its subsequent use in pump-probe experiments/characterization. All optics optimized for 800 nm unless otherwise specified; BS: beam splitter; λ/2: half-wave plate; P_1: polarizers, P_2: broadband Glan-laser polarizers; CH: optical chopper; L_1: f=300 cm lens; L_2: f=4.5 cm achromat doublet lens; L_3: f=7.5 cm achromat doublet lens; L_4: f=10 cm achromat doublet lens; L_5: f=500 cm lens; FC: 10 mm path-length water flow cell; S: sample position; X trans.: longitudinal translation stage; X-Y trans.: bi-directional in-plane translation stage; Scn: screen for diffuse spectral reflection; Spctr: Ocean Optics fiber-collected spectrometer; PD: amplified silicon photodiode (Thorlabs PDA55).

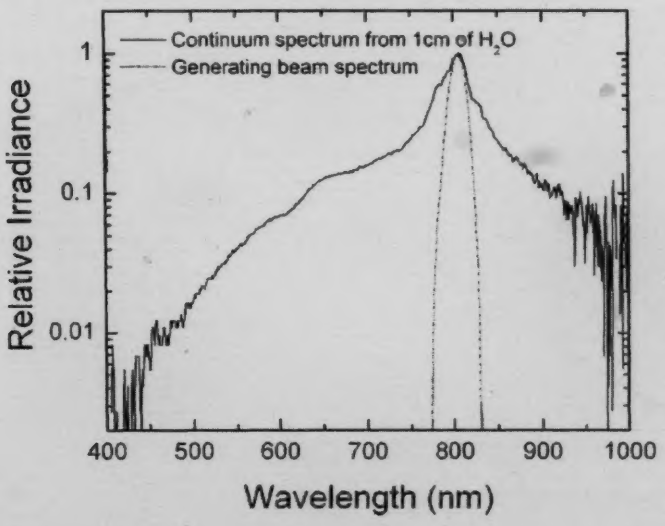

Figure 8.3. Spectra of broadband continuum generated from 10 mm H_2O and that of the generating pulse. Spectra are normalized to an irradiance of 1.

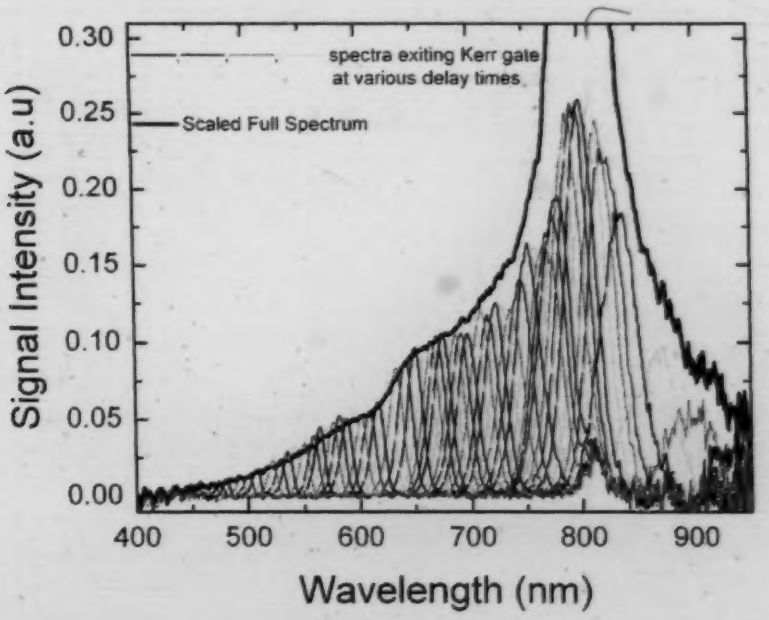

Figure 8.4. The supercontinuum pulse as independent bandwidth-limited quasi-monochromatic pulses, here selected by ultrafast Kerr-response cross-correlation with an 800 nm pump pulse in a glass slide. The scaled full continuum spectrum is presented for comparison.

Need for Chirp Correction: As mentioned above, the white-light pulse is created with its use for ultrafast broadband spectroscopy in mind. There are a couple of ways in which the continuum pulse may be used. In the first, the entire continuum may to be used in single-shot (spectral, not temporal) experiments, thereby utilizing the entire wavelength range. The generating process, however, seriously affects the temporal characteristics of the pulse, and complicates its use as a single-shot probe. Because of group velocity dispersion (GVD), the continuum beam displays considerable chirp; that is, different wavelengths are spread in time within the continuum pulse envelope. A chirp will seriously impact time-dependent (pump-probe) measurements with a continuum probe. To circumvent this problem, researchers have introduced serious further GVD, in an attempt to extrinsically increase the chirp to a point where colors can no longer be thought to overlap/interact.[20] Alternately, others have sought to disperse the supercontinuum spectrum spatially, thus using a sort of ultrafast rainbow for spectroscopic measurements.[21] Ultimately, however, neither of these approaches yields a satisfactory approach for single-shot white-light pump-probe spectroscopy.

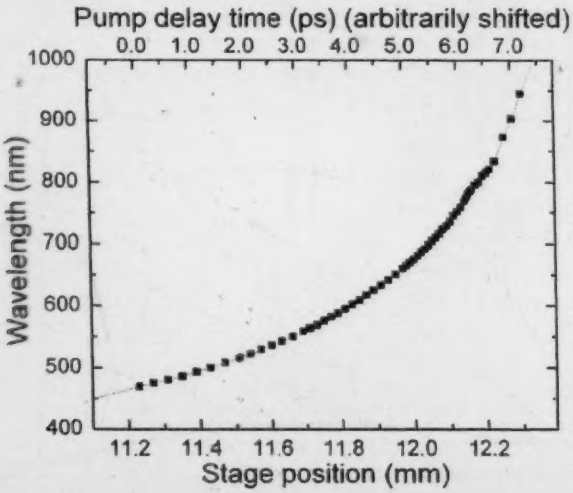

Figure 8.5. Continuum pulse chirp as mapped out by cross-correlating an 800 nm pump pulse in a ~1 mm thick glass slide. Wavelengths are determined from the spectra peaks given in Figure 8.4. The line is an extrapolation/interpolation fit in Origin 6.0 and is of typical shape for SCG from water.[25]

The most widespread approach to continuum-probe spectroscopy involves filtering the spectrum to various specific narrow-bandwidth or quasi-monochromatic pulses.[25-27] This approach treats the continuum pulse as a source of tunable single-wavelength light, much like one would an optical parametric generator, but with strong advantages: First, unlike when using an OPG, the ultrafast continuum does not need realignment/tuning for each wavelength. Second, to access a wide range of wavelengths with an OPG several different crystals must be used, each requiring unique optimized alignment. Furthermore, even the smallest OPGs require considerably larger bench space than a white-light generating cell or crystal. Thus, a well-characterized supercontinuum pulse can be a handy source of tunable monochromatic light.

As previously mentioned, the generating process introduces a considerable chirp in the continuum pulse, thereby broadening it in time. For example, our ~100 fs 800 nm generating pulse creates a ~10 ps continuum pulse from 1.0 cm of H_2O. Such considerable broadening may seem to render the continuum pulse unusable for ultrafast (fs) spectroscopy, but this is not the case. In general, our continuum pulse may be viewed

as a train of noninteracting bandwidth-limited probe pulses.[20,27] Each of these pulses is thought to have narrow Gaussian spatial, temporal, and spectral profiles. With this approximation, the continuum pulse may be treated as a source of tunable ultrafast monochromatic pulses. Tunability is obtained by narrow-band filtering the spectrum and time-varying the arrival time of the pulse to correct for chirp. To confirm the validity of this approximation, we have set up a standard Kerr gate, and conducted cross-correlation measurements between a coherent 800 nm pump pulse and the continuum pulse.[28-30] The experimental layout is presented in Fig. 8.2. For quantitative optical Kerr measurements, it is important to have high Kerr-gate extinction ratios, in order to maintain a strict square dependence on pump power.[28,31] This may be somewhat difficult to achieve with a broadband pulse, as even the best "broadband" Glan-laser polarizers are somewhat dispersive. Thus, it should be noted that extinction ratios of only about 300:1 are obtained, and that one orientation of the polarizer yields better extinction than that 180° removed. Kerr measurements in a ~1 mm-thick glass slide are output to both an amplified Si photodiode and to a fiber-coupled spectrometer for chirp analysis. Data collection from the spectrometer is not automated, so the time delay is moved manually for about 50 different stage positions (pump time delays) and the spectrum at each position is measured. Figure 8.4 presents this data, which represents a spectral view of the chirp present in the continuum beam. From Fig. 8.4, the validity of treating the continuum pulse as noninteracting bandwidth-limited pulses becomes apparent, as at any given delay time, the gated portion of the continuum follows a typical Gaussian profile. All of the selected 'continuum pulse slices' appear Gaussian, with some broadening at longer wavelengths. 460 nm pulses are 7 nm wide (FWHM), while 950 nm pulses are 50 nm wide. Figure 8.5 presents a more traditional way of looking at the pulse chirp. Here, the pulse wavelength increases with increased pump pulse delay time (top axis), or alternatively, with pump delay stage position (bottom axis). Clearly, white-light generation in water does not yield a linearly chirped pulse, and the curve in Fig. 8.5 is quite steep. As expected from GVD in water, the red portion of the pulse arrives before

the blue portion, and the entire spectrum is thus spread from 100 fs to over 7 ps. In order to obtain quantitative spectroscopic results with a white-light continuum pulse, it is important to calibrate signals for this chirp. This is equally important for both the single-shot measurements and for incremented quasi-monochromatic measurements. [20,25,27] We fit the measured chirp curve by extrapolation/interpolation, and use this for future calibration to account for pulse chirp.

Photodiode Spectral Response Calibration and Single-Shot Kerr Measurements in Glass: Kerr response from silica glass is known to have an nearly instantaneous time response. Thus obtaining the Kerr response with the entire continuum probe beam proves to be instructive for understanding the difficulties facing single-shot continuum spectroscopy. Because the probe pulse is considerably chirped, the typically symmetric 130 fs FWHM Kerr response is replaced with an asymmetric drawn out curve that follows both the wavelength-dependent material nonlinear response and the photodiode spectral response. Since the glass slide should only display ultrafast electronic nonlinearities,[28] we are still operating in the noninteracting bandwidth-limited probe pulse regime. Thus, the spreading of the Kerr response is primarily due to the pulse chirp. Nonetheless, the intensity of the response varies depending on $\chi^{(3)}(\omega)$. Furthermore, the amplified Si photodiode also has a nonuniform spectral response which must be calibrated. Figure 8.6 presents the 800 nm pump-full-bandwidth probe and the 800 nm pump-900 nm filtered probe Kerr responses from a ~1 mm glass slide. The inset in Figure 8.6 shows the spectral response of the Si photodiode.[32] As can be seen in this figure, the Kerr response with a continuum-filtered 900 nm probe pulse is the typically symmetric, 130 fs (FWHM), response. The full-continuum response, however, is stretched in time, and appears to have a flattened peak profile, that may be a tell-tale sign of group velocity dispersion and pump-pulse walk-off.[33]

Correcting for photodiode spectral response only provides a minor correction to the raw Kerr signal. A much larger experimental artifact—and one that proves to be

considerably more problematic—is the calibration of the Kerr signal to the continuum probe's spectral intensity. Figure 8.7 overlays the photodiode response-corrected broadband-probe Kerr signal with the chirp-calibrated continuum spectrum. Hence, the spectrum is actually visualized here as light intensity as a function of pump delay time, much as the Kerr response is obtained. The Kerr response is a nonlinear optical process and is thus intensity dependent. For this experimental setup, the Kerr response should display a linear increase with probe intensity. Thus, we need to correct the full-continuum Kerr response in glass to the actual incident light intensity present at each delay time. Figure 8.7 presents the chirp-intensity corrected Kerr signal, showing that this calibration introduces a far more significant modification to the raw signal. Because the continuum intensity profile is so sharply peaked at a pump delay time of 2 ps (or 800 nm)—having a large un-depleted generating pulse component—this calibration has a large degree of uncertainty. Small error in delay time will cause large artifacts in the corrected signal. In the case of Fig. 8.7, the spectral intensity and Kerr signal were obtained hours apart, and may represent a slight drift in beam position and thus a drift in the precise delay time. It is likely that the post-correction features found between 1.8 ps and 2.5 ps may simply be correction artifacts. Also, it is possible that the spectrometer was saturating at the peak wavelength of 800 nm, and thus calibration at this range is unreliable.

The fully-calibrated Kerr signal displayed in Fig. 8.7, seems to show very small dispersion of $\chi^{(3)}(\omega)$ in glass in the 780-450 nm range. This, of course, assumes that the Kerr response is instantaneous at this range. The absorption edge for silica glass is in the near-UV range and these measurements are thus far removed from resonance; supporting the idea of a mildly-dispersive response at the continuum-probe's spectral range. This feature was, perhaps, directly confirmed in Fig. 8.4, where the spectrum remained scaled to the spectrometer-detected pulse slices from around 750 nm to 450 nm. Again, the sharp downturn in response seen around 800 nm in Fig. 8.7, may be inferred from the scale mismatch at this position in Fig. 8.4.

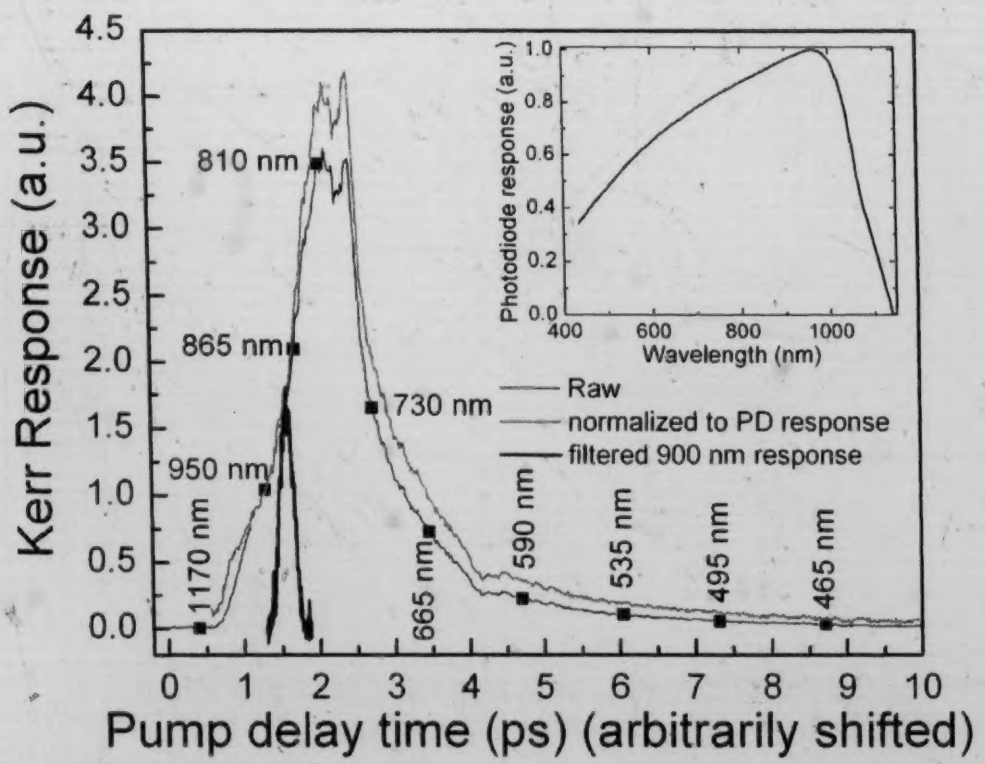

Figure 8.6: 800 nm pump continuum probe Kerr measurements in ~1 mm thick glass; raw, corrected for phtodiode response, and quasi-monochromatic at 900 nm probe. Inset: the spectral response of the Thorlabs PDA55 Si photodiode.

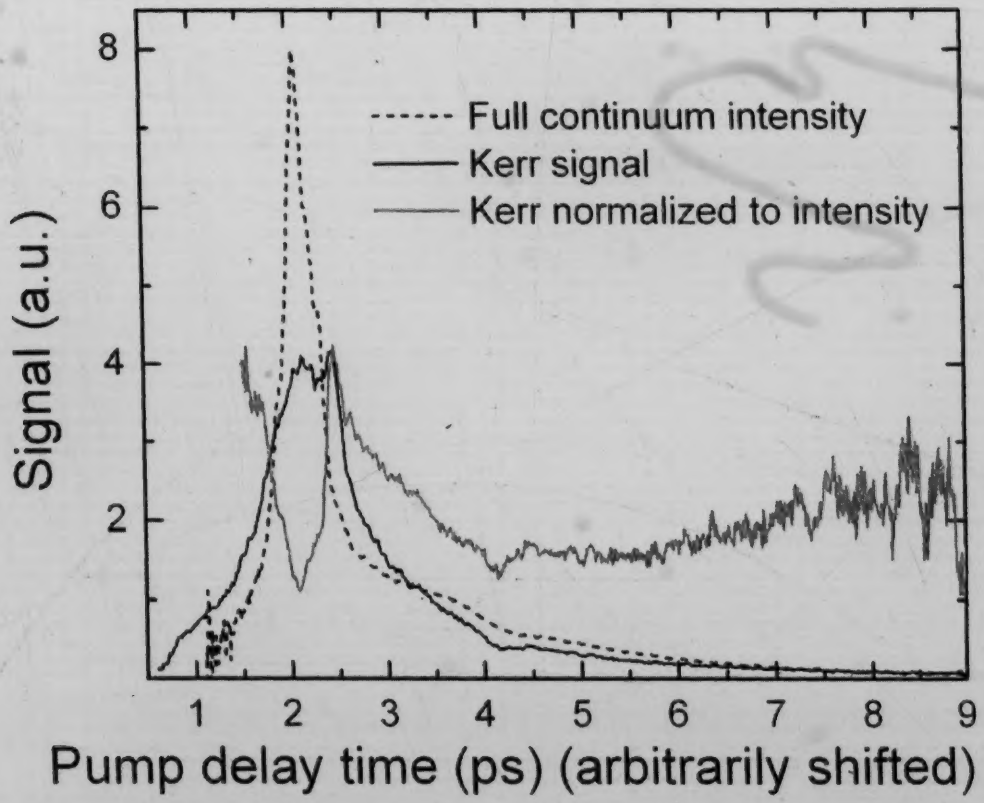

Figure 8.7: Chirp-intensity correction of single-shot Kerr measurements in glass. The Full continuum intensity as a function of delay time is mapped from the white-light spectrum of Fig. 8.3 and the calibrated chirp of Fig. 8.5. This, in turn, can be used to calibrate the single-shot broadband-probe Kerr response in glass to the actual available light intensity, effectively yielding the probe-frequency dependent Kerr response, where pump delay time correlates to wavelength within the pulse.

8.3 Time-resolved Non-degenerate Nonlinear Absorption Measurements in an Organic Material:

The primary goal of setting up the continuum-generation experiment is to obtain a tool for the time-resolved measurement of the two-photon absorption (TPA) spectra of various samples. Ultimately, one would be able to use an intense continuum beam for both pump and probe arms, and thus have complete spectral control, allowing for both degenerate and non-degenerate measurements. In the context of TPA, degenerate measurements refer to the absorption of two like-wavelength photons; for example, two 700 nm photons to promote a 3.5 eV transition. One photon would come from the pump beam and one from the probe beam. In a nondegenerate TPA experiment, the pump and probe wavelengths are different, allowing for, say, an 800 nm pump photon and a 620 nm probe photon to be simultaneously absorbed to promote a 3.5 eV transition. Theoretically, the probability of transition (TPA cross-section) could be considerably different for these two mechanisms, as each of the wavelengths may couple differently to intermediate virtual states.[3,34] Thus, nondegenerate TPA measurements yield more complex TPA spectra, but may also allow for more complete investigation of the excited-state energetics of a given sample. With our DOKE system, we are currently set-up to conduct non-degenerate TPA measurements only, because our intense pump pulse is fixed at 800 nm.

Non-Degenerate Two-Photon Absorption in MPPBT: We have attempted to measure the time-resolved nonlinear absorption (NLA) dynamics in an MPPBT sample at various continuum-derived filtered probe wavelengths. Obtaining the precise non-degenerate $\sigma^{(2)}(\omega_1,\omega_2)$ values requires considerable calibration that goes far beyond that described in the previous (sub)section. However, observing a qualitative difference in NLA signal at various wavelengths represents proof-of-principle for illustrating the power and usefulness of the continuum-probe for ultrafast spectroscopy. For nonlinear absorption

measurements, we use A 10 mM sample solution of MPPBT in DMSO in a 1.0 mm path-length quartz cuvette. We conduct a typical transient absorption experiment: First, the pump and probe polarization are set parallel with each other, to remove any Kerr signal (which is typically measured when the pump polarization is 45° to the probe). Next, the gate is slightly uncrossed, so that a small amount of baseline probe light can be detected on both the photodiode and spectrometer, as pictured in Fig. 8.2. The probe signal from the photodiode is detected by the lock-in amplifier at the pump-chopped frequency of 270 Hz, thereby allowing for the selective measurement of only pump-induced effects. By allowing a small amount of leakage light to pass to the spectrometer, we are able to monitor the spectrum of the filtered continuum probe pulse while also maintaining a constant intensity of probe light incident on the sample. We fix the amount of leakage light, as detected by the spectrometer by careful attenuation of the pre-sample probe light. Thus, unlike for the Kerr measurements described in the previous (sub)section, there is no need for the drastic continuum-chirp-intensity correction in these NLA measurements. Ultimately, a probe reference detector arm should be set up for real-time pulse intensity monitoring and subsequent calibration. We conducted measurements at five continuum-filtered probe wavelengths; 634 nm, 700 nm, 750 nm, 800 nm, and 850 nm. The raw transient absorption signals from MPPBT at wavelengths of 800 nm, 700 nm, and 634 nm, are presented in Fig. 8.8a. The measurement at 800 nm essentially represents a degenerate TPA measurement, and should conform to numerous measurements conducted on this sample with the DOKE setup; providing for an independent calibration of $\sigma^{(2)}$(800 nm). A quantitative summary of non-degenerate NLA measurements on MPPBT are presented in Table 8.1.

Table 8.1: A quantitative summary of nondegenerate nonlinear absorption measurements on a 10 mM sample solution of MPPBT in DMSO.

λ_{probe} (nm)	λ_{degen} [a] (nm)	τ [b] (ps)	FWHM (fs)	TPA Signal (raw) (a.u)	Signal (photodiode response corrected)	$\sigma^{(2)}$ [c] (calibrated to 800 nm) (GM)	$\sigma^{(2)}$ [d] (previous, degenerate) (GM)
634	707	None	190	2.7	3.6	931	475 ± 60
700	747	22 ± 10	270	4.5	5.3	1361	930 ± 90
750	774	>5 ps	330	2.4	2.6	670	750 ± 75
800	800	>5 ps	330	2.4	2.5	645	645 ± 80
850	824	Exists	410	1.4	1.4	360	410 ± 60

[a] Equivalent wavelength for degenerate TPA measurements

[b] Excited-state absorption (ESA) exponential decay times. None: no ESA observed. Exists: ESA is present, but decay dynamics are unresolved.

[c] Photodiode signals have been scaled to give the same $\sigma^{(2)}$ values for 800 nm non-degenerate and degenerate measurements. Uncertainty value is considerable and as of yet unaccounted for.

[d] Most recent $\sigma^{(2)}$ values for MPPBT as measured with z-scan.

There are a number of factors that complicate the quantitative assignment of precise $\sigma^{(2)}$-values from our nondegenerate pump-probe experiments. As described previously, photodiode spectral response must be accounted for. This is done as described for Fig. 8.6. Accounting for the different spectral intensities of the continuum, as well as for the transmission efficiency of the various band-pass filters used to select the probe wavelength, can be done pre-measurement, by direct attenuation of the probe light before it passes through the sample. The largest uncertainty, however, arises from group velocity dispersion (GVD) and pump-probe pulse walk-off effects.[20,27,33] In a degenerate pump-probe experiment, such as our DOKE experiments, the pump and probe pulses have the same wavelength, and thus maintain a constant phase (difference) as they pass through the sample. For example, at an assigned "pump delay time of 0 ps", the pump and probe beam arrive at the entrance surface of the sample cell at the same time, and travel together throughout the sample. Thus the probe beam experiences a maximal cumulative cross-phase modulation. In non-degenerate pump-probe experiments, the simple dispersion in index of refraction of the sample will make the pump and probe pulses travel at different speeds. Thus, the assigned "pump delay time of 0 ps" can only truly correspond to a unique time and location in the sample; the pump and probe beams do not travel with a constant phase difference in the sample. The pump beam will either run away from the probe pulse or will lag behind. This effect necessarily leads to diminished cross-phase modulation and a decrease in any nonlinear optical signal, including TPA action.[35] We estimate that in a 1 mm path-length dilute sample in DMSO, the time lag may be as large as 30 fs. Ziolek *et al.* estimate a lag as large as 100 fs for a 400 nm pump-600 nm probe experiment in 1.0 mm of water.[33] For Gaussian pulse cross-correlation, this may lead to a considerable decrease in integrated signal.[27] Simple GVD-affected pulse walk-off can create considerable changes to both the intensity of light transmitted and to the measured temporal response in a transient absorption experiment. Considerable GVD can broaden, flatten, and shift the detected NLO response to longer times.[27] Thus, GVD must be corrected for, even for rudimentary comparisons of our non-degenerate two-photon absorption signals. Ziolek *et*

al. have derived and provided expressions for universal GVD correction for femtosecond pump-probe experiments assuming that the laser beam parameters are known, that the beam chirp is well mapped out, and that one knows the linear dispersion of their optically active material.[33]

The dispersion in the nonlinear optical index of refraction also introduces pulse walk-off issues, but is expected to be orders of magnitude smaller than linear GVD.[20]

Setting aside GVD correction, there are other direct issues that impact the comparison of degenerate and non-degenerate TPA cross-sections. The complete sum-over-states description of two-photon absorption accounts for the use of many (all) states to act as virtual states for intermediate transitions.[34,36-38] Thus, the coupling between any one photon and a virtual state will intimately involve the photon energy. For degenerate TPA, both photons are of the same energy. However, for non-degenerate TPA, each photon has a unique energy that may be differently resonant with various levels. Thus, two-photon absorption action is not expected to be the same between, say, a 700 nm pump–probe experiment and a 620 nm pump–800 nm probe experiment. In fact, non-degenerate TPA spectra are best compared between experiments with the same pump wavelength. On the other hand, assuming that for these continuum-probe measurements the pump and probe wavelengths are sufficiently close as to yield roughly the same trends as those for degenerate measurements at the average energy, we can see that the measurements of TPA from MPPBT roughly follow previously established trends in degenerate $\sigma^{(2)}(\omega)$. The nondegenerate $\sigma^{(2)}(\omega)$ values given in Table 8.1 follow the same trends as the degenerate values, with the exception of the 800 nm pump-634 nm probe trial. The 700 nm probe experiment yields the largest TPA, and is compared with a degenerate wavelength of 747 nm. The 850 nm probe experiment yields the lowest TPA, and is compared with a degenerate wavelength of 824 nm. It is, perhaps, not surprising that the 634 nm probe experiments deviate the most from their degenerate analogues since GVD effects (and sum-over-states detuning conditions) would be largest for the greatest pump-probe mismatch.

Excited-State Absorption Dynamics: In addition to demonstrating the ability to measure the ultrafast non-degenerate TPA response of an organic sample, we are also able to measure the TPA-accessed excited-state absorption dynamics of the samples. An example of this is shown in Fig. 8.8b for MPPBT probed at 700 nm. Here, we measure absorption of 700 nm probe light after initial excitation by an intense 800 nm pump beam. Similar measurements with the DOKE setup have shown MPPBT to re-absorb 800 nm light after initial TPA at the same pump wavelength. DOKE measurements have shown this excited-state absorption to decay exponentially, with a decay time of 30±2 ps (see Chaper 2). Similarly, in the continuum-filtered probe experiment, excited state absorption is detected. The 700 nm probe ESA shows a decay rate of with a rate of 22±10 ps, as shown in Fig. 8.8b. The large uncertainty is due to noise, which may be preventing the extraction of longer decay times in the 800 nm and 750 nm probe responses. Thus, the continuum-probe dynamics are in good agreement with our DOKE results, and demonstrate that the white-light setup can be used for further measurements of excited-state absorption processes in materials of interest. In addition, most of the calibration issues that hinder the analysis of instantaneous two-photon absorption do not impact longer-lived excited-state absorption dynamics. For example, a pulse walk-off of 100 fs, that may seriously affect TPA measurements, does not drastically change the 22 ps decay rate of ESA in MPPBT. Furthermore, if one is interested in decay dynamics, the exact intensity of the signal is of secondary concern, and thus other calibrations, such as the photodiode's spectral response, become irrelevant. The power of this technique is immediately evident by the stark difference in ESA dynamics as MPPBT is probed with various wavelengths. While 800 nm and 700 nm probe yield a strong ESA signal that display essentially the same decay, at the highest investigated probe energy, 634 nm, no ESA is observed at all. This seems counterintuitive, as one expects a multitude of energy levels above the TPA access state, one of which should be sufficiently resonant as to allow for absorption of 2.0 eV. Clearly, measurements of the non-degenerate absorption dynamics of organic materials can probe new phenomena that are inaccessible by typical degenerate pump-probe techniques. Within this framework, an H_2O generated continuum is a great source for broadband probe light.

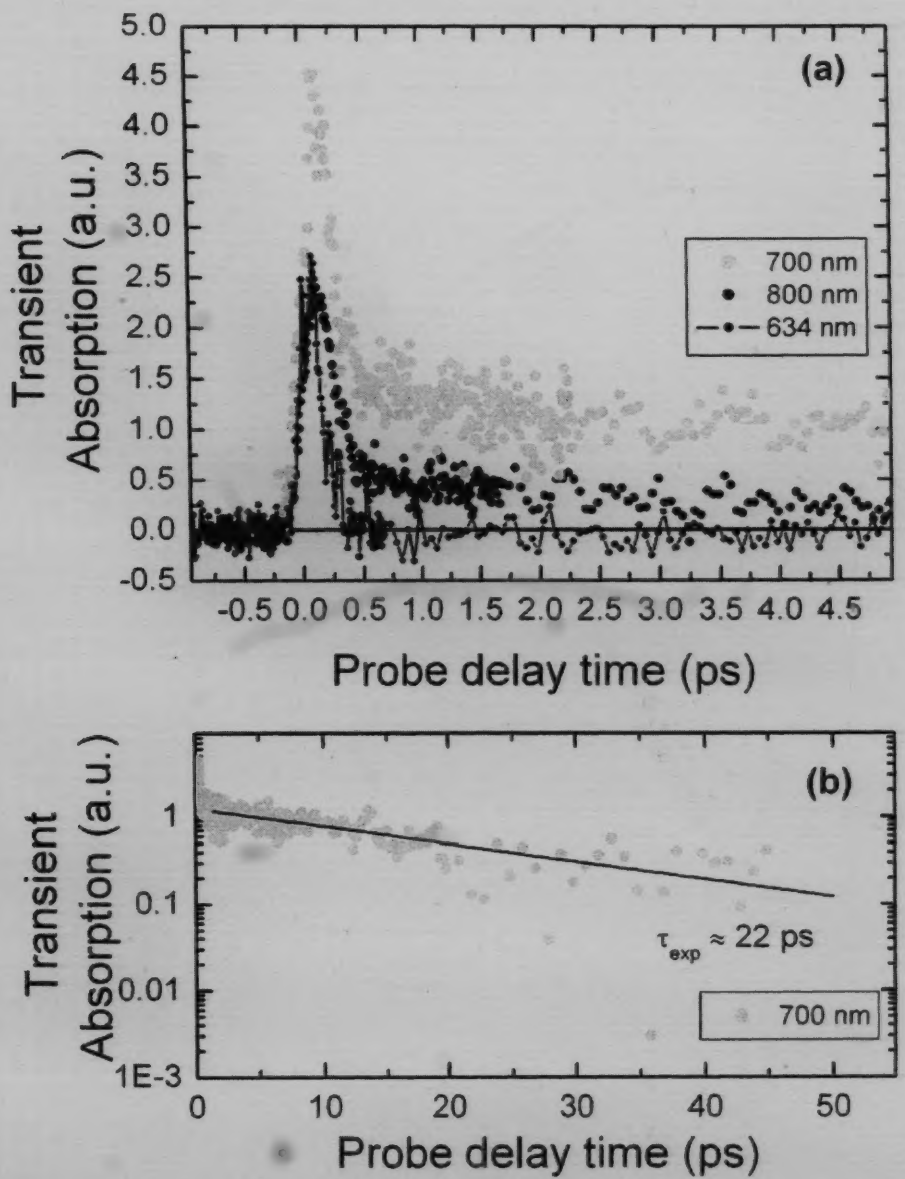

Figure 8.8: Non-degenerate transient absorption measurements of MPPBT at three continuum-filtered probe wavelengths. (a) On-peak two-photon absorption is measured while long decay tails represent excited state absorption of a probe photon from a pump beam 800 nm TPA-access state. The transient signals were shifted in time to give the same peak position for dynamics comparisons. (b) Exponential decay of the excited-state absorption at a probe wavelength of 700 nm, showing a best-fit of 22 ±10 ps mono-exponential decay past 1 ps probe delay time.

8.4 References

[1] M. Albota, D. Beljonne, J. L. Brédas, J. E. Ehrlich, A. A. Heikal, S. E. Hess, T. Kogej, M. D. Levin, S. R. Marder, D. McCord-Maughon, J. W. Perry, H. Röckel, M. Rumi, C. Subramaniam, W. W. Webb, X. L. Wu, and C. Xu, Science **281**, 1653 (1998).

[2] E. Zojer, W. Wenseleers, P. Pacher, S. Barlow, M. Halik, C. Grasso, J. W. Perry, S. R. Marder, and J. L. Brédas, J. Phys. Chem. B. **108**, 8641 (2004).

[3] K. Kamada, K. Ohta, I. Yoichiro, and K. Kondo, Chem. Phys. Lett. **372**, 386 (2003).

[4] A. Tomalik, R. G. DeCorby, A. D. Slepkov, F. A. Hegmann, A. Major, P. W. Smith, and S. Aitchison, J., in *Photonic Applications in Nonlinear Optics, Nanophotonics, and Microwave Photonics*, Proc. SPIE, **5971**, pp. 74-82, 2005.

[5] R. R. Alfano and S. L. Shapiro, Phys. Rev. Lett. **24**, 592 (1970).

[6] G. S. He, G. C. Xu, Y. P. Cui, and P. N. Prasad, Appl. Opt. **32**, 4507 (1993).

[7] A. Brodeur and S. L. Chin, Phys. Rev. Lett. **80**, 4406 (1998).

[8] J. K. Ranka, R. S. Windeler, and A. J. Stentz, Opt. Lett. **25**, 25 (2000).

[9] T. A. Birks, W. J. Wadsworth, and P. S. Russell, Opt. Lett. **25**, 1415 (2000).

[10] P. B. Corkum, C. Rolland, and T. Srinivasanrao, Phys. Rev. Lett. **57**, 2268 (1986).

[11] A. Brodeur and S. L. Chin, J. Opt. Soc. Am. B. **16**, 637 (1999).

[12] M. Bellini and T. W. Hansch, Opt. Lett. **25**, 1049 (2000).

[13] J. E. Rothenberg, Opt. Lett. **17**, 583 (1992).

[14] D. Strickland and P. B. Corkum, J. Opt. Soc. Am. B. **11**, 492 (1994).

[15] E. T. J. Nibbering, P. F. Curley, G. Grillon, B. S. Prade, M. A. Franco, F. Salin, and A. Mysyrowicz, Opt. Lett. **21**, 62 (1996).

[16] A. L. Gaeta, Phys. Rev. Lett. **84**, 3582 (2000).

[17] A. A. Zozulya, S. A. Diddams, A. G. Van Engen, and T. S. Clement, Phys. Rev. Lett. **82**, 1430 (1999).

[18] Q. Feng, J. V. Moloney, A. C. Newell, E. M. Wright, K. Cook, P. K. Kennedy, D. X. Hammer, B. A. Rockwell, and C. R. Thompson, IEEE J. Quant. Elect. **33**, 127 (1997).

[19] The Supercontinuum Laser Source, R. R. Alfano, Ed. (Springer-Verlag, Berlin, 1989).

[20] R. A. Negres, J. M. Hales, D. J. Hagan, and E. W. Van Stryland, IEEE J. Quant. Elect. **38**, 1205 (2002).

[21] G. S. He, T.-C. Lin, and P. N. Prasad, Opt. Express **10**, 566 (2002).

[22] Q. X. Li, T. Jimbo, P. P. Ho, and R. R. Alfano, Appl. Opt. **25**, 1869 (1986).

[23] A. Brodeur, F. A. Ilkov, and S. L. Chin, Opt. Commun. **129**, 193 (1996).

[24] Dr. David Hagan and Michaela Balu, University of Central Florida, private communication. 2005.

[25] V. I. Klimov and D. W. McBranch, Opt. Lett. **23**, 277 (1998).

[26] M. Balu, J. Hales, D. J. Hagan, and E. W. Van Stryland, Opt. Express **12**, 3820 (2004).

[27] R. A. Negres, J. M. Hales, A. Kobyakov, D. J. Hagan, and E. W. Van Stryland, Opt. Lett. **27**, 270 (2002).

[28] A. D. Slepkov, *Third-Order Nonlinearities of Novel iso-Polydiacetylenes Studied by a Differential Optical Kerr Effect Detection Technique*, M.Sc. Thesis. University of Alberta, Edmonton, 2001.

[29] P. P. Ho and R. R. Alfano, Phys. Rev. A **20**, 2170 (1979).

[30] S. Yamaguchi and H. O. Hamaguchi, Appl. Spectosc. **49**, 1513 (1995).

[31] P. N. Prasad and D. J. Williams, Introduction to Nonlinear Optical Effects In Molecules & Polymers (Wiley Interscience, New York, 1991).

[32] As obtained from an interpolation of the digitized curve from the manufacturer's online catalogue. Photodiode is Thorlabs Inc. PDA55. Interpolation was done in Origin ver. 6.1.

[33] M. Ziolek, M. Lorenc, and R. Naskrecki, Appl. Phys. B: Lasers Opt. **72**, 843 (2001).

[34] E. Zojer, D. Beljonne, T. Kogej, H. Vogel, S. R. Marder, J. W. Perry, and J. L. Brédas, J. Chem. Phys. **116**, 3646 (2002).

[35] A. Maciejewski, R. Naskrecki, M. Lorenc, M. Ziolek, J. Karolczak, J. Kubicki, M. Matysiak, and M. Szymanski, J. Mol. Struct. **555**, 1 (2000).

[36] P. Cronstrand, Y. Luo, and H. Ågren, Chem. Phys. Lett. **363**, 198 (2002).

[37] P. Cronstrand, Y. Luo, and H. Ågren, Chem. Phys. Lett. **352**, 262 (2002).

[38] P. Feneyrou, O. Doclot, D. Block, P. L. Baldeck, S. Delysse, and J. M. Nunzi, Opt. Lett. **22**, 1132 (1997).

CHAPTER 9:
SUMMARY AND FUTURE WORK

Materials with large ultrafast third-order optical nonlinearities are desireable for a variety of technological applications. Traditionally, materials with large birefringent (Kerr-like) and negligible absorptive (two-photon, for example) nonlinearities have been sought for all-optical switching applications.[1] Recently, however, two-photon absorption (TPA) has emerged as a technological process of interest in its own right, and has sparked considerable interest towards finding materials with large nonlinear absorption activity.[2] The birefringent and absorptive nonlinearities correspond to the real and imaginary components of the complex third-order susceptibility, $\chi^{(3)}$. Many commonly-used nonlinear optics (NLO) techniques, such as heterodyne Kerr gates, third-harmonic generation (THG), two-photon excitation fluorescence (TPEF) and single-beam attenuation, can only measure either the birefringent or absorptive nonlinear component. For the complete analysis of third-order optical nonlinearities, there is need for simple techniques that can obtain both the real and imaginary components of $\chi^{(3)}$. Furthermore, the incorporation of femtosecond time-resolution is desirable for the study of $\chi^{(3)}$ (and higher order[3,4]) dynamics. We have designed an ultrafast differential optical Kerr effect (DOKE) detection technique to be able to time-resolve both the real and imaginary optical nonlinearities of various sample systems. We have previously outlined the development and use of the DOKE technique for studying the Kerr nonlinearities in organic compounds.[5] In the current work, we have further outlined the extension of DOKE to the measurement of TPA and TPA-accessed excited-state absorption dynamics in a variety of organic samples. While all materials possess third-order nonlinearities, organic compounds with extended conjugation paths (an alternation of single and multiple bonds) are at the forefront of ultrafast NLO research due to their large electronic

nonlinearities. Organic compounds, however, provide an immense versatility of design. Thus, the engineering of compounds suitable for use in technological applications will require specific knowledge of structure-property relationships.[6,7] Towards this end, among others, we have studied the nonlinear optical properties of several classes of organic compounds with a variety of conjugation schemes.

We have used the DOKE technique at 800 nm to study both the birefringent nonlinearities and two-photon absorption of a class of sp-hybridized polyyne oligomers. We have found power-law trends in both the decreasing absorption energy and increasing third-order molecular hyperpolarizability, γ, as a function of oligomer length (and hence, conjugation length). Neither trend shows any signs of the onset of saturation by the size of the longest oligomer (decayne; 20 consecutive carbons). The largest polyyne investigated, ***TIPS*-10yne**, yields the largest hyperpolarizability of $\gamma \approx 650 \times 10^{-36}$ esu. The hyperpolarizability increases with the number of repeat units n according to $\gamma \sim n^{4.3}$, which is the largest exponent reported for any quasi-one-dimensional conjugated compound. This finding is contrary to all reported theoretical findings, which predict poly(yne) power-law exponents to be lower than those of pol(eyne)s and/or poly(enyne)s. Our reported polyyne power-law trend in γ, combined with that of the absorption energy, compares extremely well with recent theoretical predictions regarding the linear and nonlinear optical behaviour of strictly 1-D systems. Thus, polyynes, which are extremely linear geometrically, are also so optically and electronically. We have further shown that the optical nonlinearities can be increased considerably by end-capping the polyynes with phenyl groups—without detrimental changes in the power-law trends. Furthermore, 800 nm studies of two-photon absorption in polyynes has suggested a reversal of standard chromophore energy-level ordering, indicating a two-photon accessible, one-photon forbidden, level below the lowest one-photon allowed level.

We have extensively studied the third-order nonlinear optical properties of two-dimensionally conjugated cruciform donor/acceptor-substituted tetrakis(phenyl-ethynyl)benzenes (TPEBs). We have utilized an ultrafast z-scan technique to measure the TPA spectra from 580nm-1150nm. We used DOKE detection at 800 nm to probe the dynamics of both the real and imaginary parts of the third-order nonlinear response. We also used 400 nm pump-800 nm probe transient absorption measurements to further study the absorption dynamics in these compounds. In one species, **TD-TPEB**, all four arms

are donor-terminated. The other three molecules form a set of structural isomers in which the conjugated arms are terminated with two acceptors and two donors. These compounds are named according to the respective donor-arm linkages across the central benzene ring; forming ***ortho*-TPEB**, ***meta*-TPEB** and ***para*-TPEB**. **TD-TPEB** and ***para*-TPEB** are both quadrupolar, and therefore lack permanent dipole moments. ***ortho*-TPEB** and ***meta*-TPEB** are dipolar. From the z-scan measurements, we find that the all-donor sample shows the highest peak TPA cross section, with $\sigma^{(2)}$ = 520±30 GM at a wavelength of 710 nm. The total energy of transition at the TPA peak is significantly blue-shifted with respect to the lowest one-photon transitions, as seen from the UV-vis spectrum. The dipolar samples ***ortho*-TPEB** and ***meta*-TPEB** display similar TPA spectra that closely follow the lowest one-photon absorption (in total photon energy), as would be expected in dipolar molecules. ***meta*-TPEB** and ***ortho*-TPEB** yield $\sigma^{(2)}$ = 440±20 GM at 940 nm, and 400±20 GM at 860 nm, respectively. Like **TD-TPEB**, ***para*-TPEB** is quadrupolar, and thus shows a blue-shifted TPA spectrum. This sample, however, yields the lowest overall cross-section maximum, with $\sigma^{(2)}$=240±20 GM at 750 nm—nearly half that of the other TPEB samples. These findings help to support the growing belief that adding multiple donor groups at the end of conjugated paths significantly increases TPA activity as compared to adding both donors and acceptors. Furthermore, comparisons between our dipolar and quadrupolar D/A molecules shows that in the case of TPEBs, the dipolar motif yields higher $\sigma^{(2)}$ than a quadrupolar substitution symmetry. This is probably due to a lack of the desirable *para*-conjugated D→A routes in the quadrupolar species. Pump-probe measurements show that all of the TPEBs display both excited-state absorption and excited-state birefringence at 800 nm. With the exception of **TD-TPEB**, the three isomers show a clear 1-5 ps decay time from the two-photon state to the excited-state from which subsequent 800 nm probe-beam absorption takes place. Absorption from this excited-state is then seen to decay exponentially, with 20-40 ps time scales. The decay times observed in both the birefringent and dichroic signals are similar. Furthermore, these decay rates are consistent with those observed from one-photon pumped transient absorption measurements, indicating that the same excited-state dominates in samples pumped by either two-photon- or one-photon-absorption. Excited-state absorption is also present in **TD-TPEB**, and is seen to decay with a much longer time constant of ≈300 ps. In 800 nm DOKE studies of the real component of the nonlinearity, its sign was found to correlate to the spectral position of the two-photon

resonance, with ***meta*-TPEB** and ***ortho*-TPEB** displaying negative electronic nonlinearities, ***para*-TPEB** displaying negligible nonlinearities, and **TD-TPEB** showing a positive γ-value. We have shown that TPEBs are excellent two-dimensionally-conjugated systems for investigating both the effects of polar/multipolar geometry and donor-acceptor substitution patterns on nonlinear optical properties. We have shown that it is not generally true that quadrupolar geometry is superior to dipolar geometry for maximizing TPA. Furthermore, we have shown that the nonlinear optical activity of molecules with a central benzene core are dependent on the specifics of their structural design, wherein small changes within our series of TPEB isomers lead to significant differences in their Kerr and nonlinear absorption response.

We investigated the third-order NLO and nonlinear-absorption properties of a bis-fullerene-terminated conjugated oligomer using the DOKE detection technique. The measured third-order nonlinear-optical coefficients for quadrupolar fullerene derivative **C_{60}-quad-5OPE** are approximately double those of its OPE precursor **quad-5OPE** at 800 nm, while nonlinearities for pristine C_{60} are negligible. **C_{60}-quad-5OPE** displays significant two-photon absorption at 800 nm, with $\sigma^{(2)}$=140±40 GM, compared with $\sigma^{(2)}$=65±10 GM and $\sigma^{(2)}$=28±8 GM for **quad-5OPE** and a *meta*-linked octupolar copmpound **oct-5OPE**, respectively. The molecular second-hyperpolarizability at 800 nm is also non-negligible for these compounds, ranging as high as $(10\pm3)\times10^{-34}$ esu for **C_{60}-quad-5OPE**. Whereas the doubling of γ and $\sigma^{(2)}$ in **C_{60}-quad-5OPE** could typically be explained by increases in conjugation length commensurate with a significant red-shifting of λ_{max}, no such shift is observed in the absorption spectra in going from **quad-5OPE** to **C_{60}-quad-5OPE**. Therefore, the differences in optical nonlinearities between the pure OPEs and the OPE-fullerene hybrids suggest a synergistic interaction between the conjugated OPE backbone and terminal fullerenes. Evidence for charge transfer from the conjugated backbone to the terminal fullerenes is further supported by the comparisons of the excited-state absorption dynamics of the compounds. Whereas both of the pure OPE frameworks display similar excited-state absorption, end-capping with fullerene (in **C_{60}-quad-5OPE**) yields a compound that only displays instantaneous two-photon absorption. Finally, this fullerene-terminated OPE displays sizable γ- and $\sigma^{(2)}$-values that are consistent with other C_{60} derivatives reported in the literature. Thus, our findings are potentially instructive to guiding the molecular design and engineering of organic-based electronic and nonlinear optical materials.

CHAPTER 9: SUMMARY AND FUTURE WORK

We have studied the structural, optical, and nonlinear optical properties of per-phenylated cross-conjugated *iso*-polydiacetylene oligomers, with up to n=15 repeat units. Their electronic absorption behavior indicates an effective conjugation length of approximately n≈7–9. The *iso*–PDA oligomers show steadily increasing fluorescence intensity as a function of chain length, and the emission wavelength red-shifts slightly from the dimer to the heptamer. Beyond the length of the heptamer, the emission energy remains essentially constant. The third-order NLO properties of the *iso*–PDAs were studied by the DOKE technique at a wavelength of 800 nm. the *iso*-PDA oligomers display a super-linear increase in γ-value as a function of chain length. The best fit to the NLO data shows two linear regimes, suggesting an increased order in the system, likely due to helical folding. While we have not established definitive proof of a folded conformation for extended *iso*–PDAs, empirical evidence of this conformational presence is provided by molecular modeling studies as well as UV/Vis and NLO spectroscopy. The superlinear increase in γ as a function of oligomer length is the first of its kind reported for (through-carbon) cross-conjugated systems. Compared with the γ-values obtained from the polyynes, the *iso*-PDA oligomers are relatively poor NLO materials. The 15-repeat-unit ***iso*-PDA-15** showed the largest nonlinearity, with $\gamma \approx 310\times10^{-36}$ esu. This nonlinearity is only half as large as in the n=10 polyyne ***TIPS*-10yne**, yet the *iso*-PDA is approximately 10 times as heavy

Finally, in an effort to extend the wavelength capability of our DOKE technique beyond the single wavelength of 800 nm, we have conducted preliminary research into establishing an 800 nm pump-white-light probe layout. The use of a stable 450-1100 nm supercontinuum beam generated from a 10 mm path-length water flow-cell has been shown for ultrafast pump-probe measurements of optical nonlinearities in a glass slide and a two-photon absorbing standard. We have outlined the necessary calibrations to pulse-chirp, photodiode spectral response, and continuum spectral intensity. Other issues, such as (linear and nonlinear) the effects of group velocity dispersion on pump-probe temporal walk-off remain to be properly addressed. Ultimately, this experimental setup will be used to probe the nondegenerate two-photon absorption spectra of organic chromophores. Our preliminary results on the nondegenerate TPA response of MPPBT are quite promising.

CHAPTER 9: SUMMARY AND FUTURE WORK

Much of the work presented in this thesis has already been either published or submitted for publication. There are, however, several unresolved issues and avenues of research that should be explored in the near future: First, we are working to obtain the two-photon spectra of extended polyyne oligomers. Our preliminary TPA findings on these compounds suggest that the longer polyynes show a reversal of standard level-symmetry ordering. It would be very interesting to investigate this issue further, and to establish the polyyne size at which this cross-over occurs. These results would speak directly to previous studies of this effect in polyenic systems,[8] further strengthening our optical comparisons between the two oligomer classes. Furthermore, even at a strongly detuned wavelength of 800 nm the longer polyynes show moderate TPA cross-sections. These values are bound to increase with decreased detuning, and may display very large double-resonance enhancement as the one-photon energy is approached. In this way, the fairly sharp absorption edge of the ***TIPS*-PY** species may be utilized to give large TPA action while retaining relatively good one-photon transparency.

A second issue that remains to be address in the future is the proper way to analyze the absorption energy as a function of oligomer length. Through our polyyne work, we have shown that these compounds follow a power-law decrease in absorption energy edge as a function of repeat unit, with an exponent of c=-0.38. While it has been traditionally common to fit this trend to a c=-0.5 or a c=-1 behavior, Bubeck *et al.* have suggested,[9] and we have confirmed, that a free fit to a power-law provides far superior agreement with experimental data. We have re-analyzed (re-plotted) the absorption behavior of several previously reported polyynes, and find that most oligoynes follow a strict power law behavior with little or no saturation. We further find these compounds to fall into two distinct groups: those that display a $c\approx$-0.48 (very close to 0.5) exponent and those that follow a $c\approx$-0.37 exponent. We plan to explore these curious preliminary findings in the future.

A third avenue for future work should involve the development of the 800 nm-pump-supercontinuum-probe technique for studying the nondegenerate two-photon absorption activity of various samples. Ideally, a way to conduct single-shot experiment will be developed. Such an advancement would see immediate and emphatic impact in the NLO spectroscopy community.

9.1 References

[1] G. I. Stegeman and A. Miller, *Photonics in Switching*, in Background and Components, edited by J. E. Midwinter (Academic Press, San Diego, 1993), Vol. I.

[2] M. Albota, D. Beljonne, J. L. Brédas, J. E. Ehrlich, J. Y. Fu, A. A. Heikal, S. E. Hess, T. Kogej, M. D. Levin, S. R. Marder, D. McCord-Maughon, J. W. Perry, H. Röckel, M. Rumi, C. Subramaniam, W. W. Webb, X. L. Wu, and C. Xu, Science **281**, 1653 (1998).

[3] A. A. Said, C. Wamsley, D. J. Hagan, E. W. Van Stryland, B. A. Reinhardt, P. Roderer, and A. G. Dillard, Chem. Phys. Lett. **228**, 646 (1994).

[4] Y.-F. Chen, K. Beckwitt, F. W. Wise, B. G. Aitken, J. S. Sanghera, and I. D. Aggarwal, J. Opt. Soc. Am. B. **23**, 347 (2006).

[5] A. D. Slepkov, *Third-Order Nonlinearities of Novel iso-Polydiacetylenes Studied by a Differential Optical Kerr Effect Detection Technique*, M.Sc. thesis. University of Alberta, Edmonton, 2001.

[6] R. R. Tykwinski, U. Gubler, R. E. Martin, F. Diederich, C. Bosshard, and P. Günter, J. Phys. Chem. B. **102**, 4451 (1998).

[7] U. Gubler and C. Bosshard, Adv. Polym. Sci. **158**, 123 (2002).

[8] S. Mazumdar, S. Dallakyan, and M. Chandross, Synth. Met. **139**, 769 (2003).

[9] C. Bubeck, *Nonlinear Optical Properties of Oligomers*, in Electronic Materials-The Oligomer Approach, edited by K. Müllen and G. Wegner (Wiley-VCH, Veinheim, 1998), Chapter 8.

APPENDICES

APPENDIX A:

TWO-PHOTON ABSORPTION AS A THIRD-ORDER NONLINEAR PHENOMENA

In this appendix, the relationship between various coefficients used to describe third-order nonlinearities is presented. In particular, the mathematical description of two-photon absorption is introduced through analogy to linear absorption, showing how it relates to the complex (nonlinear) index of refraction. Because the DOKE technique is used to obtain the real component of the third-order susceptibility in addition to the imaginary (absorptive) component, the relationships between coefficients that are used to describe the Kerr nonlinearities and TPA are presented.

Deviations from linear optical behavior are observed when intense laser light is incident on a dielectric. Second-order nonlinearities are absent in symmetric and isotropic systems.[1] Furthermore, second-order effects give rise to optical responses at either twice the incident frequency (second-harmonic generation, for example), or manifest as a zero-frequency component known as optical rectification.[2] Third-order nonlinearities can yield optical responses at higher frequencies (i.e. third-harmonic generation) or they can modify the outgoing signal at the incident frequency. Thus, third-order nonlinearities may be detected by monitoring the sample response at the original frequency, ω.[3] One manifestation of this nonlinear response is the modification of the dielectric index of refraction, $\eta(\omega)$.

In the absence of optical nonlinearities, the index of refraction is typically defined as

$$\eta_0^2(\omega) = \varepsilon(\omega) = 1 + \chi^{(1)}(\omega), \qquad \text{A.1}$$

where ε is the dielectric constant and $\chi^{(1)}(\omega)$ is the first-order optical susceptibility; usually referred to as $\chi(\omega)$. The index of refraction is a complex quantity;

$$\eta_0(\omega) = n(\omega) + i\kappa(\omega), \qquad \text{A.2}$$

Where n is the real component of the index of refraction and κ is the imaginary component that gives rise to the absorption coefficient, $\alpha(\omega)$, through

$$\kappa(\omega) = \frac{c}{2\omega}\alpha(\omega). \qquad \text{A.3}$$

In this case, α is simply the Beer's-law absorption coefficient that describes beam attenuation according to

$$I = I_0 e^{-\alpha L}, \qquad \text{A.4}$$

where L is the optical path length, and I_0 and I are the incident and transmitted optical intensities, respectively. Through third-order optical nonlinearities, the index of refraction is modified to become intensity dependent:[3,4]

$$\eta(\omega) = \eta_0(\omega) + \eta_2(\omega)I. \qquad \text{A.5}$$

Thus, the optical nonlinearities represent a small perturbation that grows with laser intensity. Squaring Eqn. A.5:

$$\begin{aligned} \eta^2(\omega) &= (\eta_0(\omega) + \eta_2(\omega)I)^2 \\ &= \eta_0^2(\omega) + 2\eta_0(\omega)\eta_2(\omega)I + \eta_2^2(\omega)I^2, \\ &\cong \eta_0^2(\omega) + 2\eta_0(\omega)\eta_2(\omega)I \end{aligned} \qquad \text{A.6}$$

to first order in η_2. This approximation will typically hold, given the fact that for standard NLO response and intensities, $\eta_2 I \leq 0.01\,\eta_0$.[5] In analogy to Eqn. A.1,[3]

$$\begin{aligned}\eta^2(\omega) &= 1 + \chi_{eff}(\omega) \\ &= 1 + \chi^{(1)}(\omega) + \frac{3}{2c\varepsilon_0 n_0(\omega)}\chi^{(3)}(-\omega;\omega,-\omega,\omega)I \\ &= \eta_0^2 + \frac{3}{2c\varepsilon_0 n_0(\omega)}\chi^{(3)}(-\omega;\omega,-\omega,\omega)I\end{aligned} \qquad \text{A.7}$$

where ε_0 is the permittivity of free-space, c is the speed of light, I is the incident light intensity and $\chi^{(3)}(-\omega;\omega,-\omega,\omega)$ is the degenerate third-order susceptibility; a fourth-rank tensor.[4] It may be noted that in the case of third-harmonic generation, a modified susceptibility is accessed, namely $\chi^{(3)}(3\omega;\omega,\omega,\omega)$.[1] The nonlinear index of refraction may thus be extracted from Eqns. A.6 and A.7:

$$\eta^2(\omega) - \eta_0^2(\omega) = \frac{3}{2c\varepsilon_0 n_0(\omega)}\chi^{(3)}(-\omega;\omega,-\omega,\omega)I = 2\eta_0(\omega)\eta_2(\omega)I \qquad \text{A.7}$$

and

$$\eta_2(\omega) \cong \frac{3}{4c\varepsilon_0 n_0^2(\omega)}\chi^{(3)}(-\omega;\omega,-\omega,\omega). \qquad \text{A.8}$$

The value $\eta_2(\omega)$ is the nonlinear index of refraction that gives rise to both the optical Kerr effect and two-photon absorption. Like the linear index of refraction, the nonlinear index is a complex quantity that may be given by,

$$\eta_2(\omega) = n_2(\omega) + i\kappa_2(\omega), \qquad \text{A.9}$$

in analogy to Eqn. A.2. Here, the nonlinear index of refraction is proportional to the real component of the third-order susceptibility, and may be obtained (trivially) from Eqn. A.8;

$$n_2(\omega) = \frac{3}{4c\varepsilon_0 n_0^2(\omega)} \mathrm{Re}\left[\chi^{(3)}(-\omega;\omega,-\omega,\omega)\right], \qquad \text{A.10}$$

and the change in the (real) index of refraction is proportional to both $\chi^{(3)}$ and light intensity via,

$$\Delta n = n_2(\omega) I = \frac{3}{4c\varepsilon_0 n_0^2(\omega)} \mathrm{Re}\left[\chi^{(3)}(-\omega;\omega,-\omega,\omega)\right] I; \qquad \text{A.11}$$

defining the optical Kerr effect.[4]

Likewise, by analogy to linear absorption and Eqn. A.3, the two-photon absorption coefficient emerges as a third-order nonlinearity via,

$$\kappa_2(\omega) = \frac{3}{4c\varepsilon_0 n_0^2(\omega)} \mathrm{Im}\left[\chi^{(3)}(-\omega;\omega,-\omega,\omega)\right] = \frac{c}{2\omega}\alpha^{(2)}(\omega); \qquad \text{A.12}$$

and

$$\alpha^{(2)}(\omega) = \frac{3\omega}{2c^2\varepsilon_0 n_0^2(\omega)} \mathrm{Im}\left[\chi^{(3)}(-\omega;\omega,-\omega,\omega)\right], \qquad \text{A.13}$$

where $\kappa_2(\omega)$ (unlike the unitless $\kappa(\omega)$) has units of m^2/W. This absorption coefficient describes intensity-dependent absorption as intense light propagates through a dielectric. Beam depletion in the presence of TPA is given by

$$\frac{\partial I}{\partial l} = -\alpha I - \alpha^{(2)} I^2. \qquad \text{A.14}$$

Note that in the absence of TPA, this reduces to Beer's law (Eqn. A.4). Thus, $\alpha^{(2)}$ (with units of m/W) is analogous to α (in units of m^{-1}). Implication of Eqn. A.14 to the direct measurement of TPA are expanded on in Chapter 3.

n_2 and $\alpha^{(2)}$ are bulk properties. In order to describe structure-property relationships, the intrinsic NLO response of individual molecules needs to be described. To do this, microscopic—or molecular—coefficients are used most often. For birefringent nonlinearities, γ is most often used.[2] This, the second hyperpolarizability (or alternatively the "second molecular hyperpolarizability", or "third-order hyperpolarizability") scales n_2 by the molecular number density and local field factors, such that

$$\langle \gamma(-\omega;\omega,-\omega,\omega)\rangle = \frac{\mathrm{Re}\left[\chi^{(3)}(-\omega;\omega,-\omega,\omega)\right]}{L^4 N_c}. \qquad \text{A.15}$$

where $<\gamma>$ is the rotationally-averaged second molecular hyperpolarizability,[2] L^4 is the Lorentz field factor that accounts for the optical field in the (dielectric) vicinity of the molecules ($L=(n^2+2)/3$) and N_c is the molecular concentration. γ is typically reported in esu units, where $\chi^{(3)}$ is also in esu units and N_c is in cm^{-3}.

For absorptive nonlinearities, the TPA cross-section, $\sigma^{(2)}(\omega)$, is the most commonly reported coefficient, where

$$\sigma^{(2)}(\omega) = \frac{\hbar\omega}{N_c}\alpha^{(2)}(\omega), \qquad \text{A.16}$$

and is further related to $\chi^{(3)}$ by

$$\sigma^{(2)}(\omega) = \frac{3(\hbar\omega)^2}{2\varepsilon_0 c^2 \hbar n_0^2(\omega) N_c}\mathrm{Im}\left[\chi^{(3)}(-\omega;\omega,-\omega,\omega)\right], \text{ [6]} \qquad \text{A.17}$$

where $\sigma^{(2)}(\omega)$ is typically reported in units of cm^4-s-photon^{-1}-molecule^{-1} or Göppert-Mayers, GM (1 GM = 10^{-50} cm^4-s-photon^{-1}-molecule^{-1}).

A.1 References

[1] P. N. Butcher and D. Cotter, The Elements of Nonlinear Optics (Cambridge University Press, Cambridge, 1990).

[2] P. N. Prasad and D. J. Williams, Introduction to Nonlinear Optical Effects In Molecules & Polymers (Wiley Interscience, New York, 1991).

[3] A. D. Slepkov, *Third-Order Nonlinearities of Novel iso-Polydiacetylenes Studied by a Differential Optical Kerr Effect Detection Technique*, M.Sc. thesis. University of Alberta, Edmonton, 2001.

[4] R. L. Sutherland, D. G. McLean, and S. Kirkpatrick, *Handbook of nonlinear optics* (Marcel Dekker, New York, 2003).

[5] H. S. Nalwa, *Chapter 11: Organic Materials for Third-Order Nonlinear Optics*, in Nonlinear optics of organic molecules and polymers, edited by H. S. Nalwa and S. O. Miyata (CRC Press, New York, 1997), pp. 571-609.

[6] E. Zojer, D. Beljonne, T. Kogej, H. Vogel, S. R. Marder, J. W. Perry, and J. L. Brédas, J. Chem. Phys. **116**, 3646 (2002).

APPENDIX B:

CONCERNING DOKE POLARIZATION CONDITIONS

In a previous work, we used Jones matrix notation to derive the standard DOKE equations; namely, Eqns. 2.1 and 2.3.[1] Third-order nonlinearities induce a complex phase delay in the probe beam, given by $\phi = \phi' + i\phi''$. A linearly polarized pump beam will induce a different nonlinearity parallel and perpendicular to its polarization. Thus, in choosing coordinates x and y to denote the two polarization directions, we can delineate the more rigorously defined nonlinear phase *difference* between the two polarizations. Hence, ϕ is composed of ϕ_x and ϕ_y. By defining ϕ_x as the common phase, we describe the nonlinearities in terms of the induced phase difference, $\Delta\phi_{xy} = \phi_y - \phi_x$. These quantities remain complex, with the real component providing birefringent-induced polarization changes and the imaginary component providing dichroic polarization changes.

Some of the abbreviations used in the following treatment are found in Table B.1. Note that brackets after a matrix symbol denote angle of alignment or the angle of pumping polarization. For example, $\lambda/4(45)$ represents a quarter-wave plate oriented with the fast axis at 45° to the horizontal; while S(90) represents a sample pumped with a vertically polarised pump beam. All angles are with respect to the horizontal, where positive angles denote counter-clockwise rotation when looking along the beam propagation direction.

Table B.1: Some symbols and matrix representations for various optical elements.

Symbol	Description	Matrix Representation	Notes
λ/4(45)	Quarter-Wave Plate	$\begin{bmatrix} i & 0 \\ 0 & 1 \end{bmatrix}$	Fast axis aligned 45 degrees to horizontal
P	Polarizer	$\begin{bmatrix} 0 \\ 1 \end{bmatrix}$	Allows only, y (vertical light) through
DA	Differential Analyser (Wollaston Prism)	$\begin{bmatrix} 1 & 1 \end{bmatrix}$	Separates the horizontal from the vertical light.
S	Sample	$e^{i\phi_x}\begin{bmatrix} 1 & 0 \\ 0 & e^{i\Delta\phi_{xy}} \end{bmatrix}$	Sample is a retarder, allowing a relative phase retardation between the *x* and *y* polarized light
R(45)	Rotation Matrix	$\frac{1}{\sqrt{2}}\begin{bmatrix} 1 & -1 \\ 1 & 1 \end{bmatrix}$	Rotation of 45 degrees
R(δ)	Rotation Matrix	$\begin{bmatrix} \cos\delta & -\sin\delta \\ \sin\delta & \cos\delta \end{bmatrix}$	General rotation matrix

B.1 Position-Dependence of the Probe Quarter-Wave Plate

As mentioned in §2.2, DOKE detection employs a quarter-wave plate in the probe arm, which is set to circularize the probe polarization; a practice similar to that used in free-space electro-optic sampling.[2,3] However, the differential detection schemes employed in free-space electro-optic sampling experiments routinely place the quarter-wave plate after the sample (or equivalent position), whereas the DOKE technique always utilizes the quarter-wave plate in the probe arm *before* the sample. In the following section we show that although the birefringent polarization condition is insensitive to the position of this optical component, for proper detection in the dichroic polarization condition, it is imperative that the quarter-wave plate be placed before the sample.

The First Birefringent DOKE Condition With the Quarter-Wave Plate Before the Sample: This experimental setup involves pumping the sample at 45° to the horizontal. Furthermore, the probe is circularly polarized with a quarter-wave plate with its long axis is oriented at 45° to the at-present vertically polarized probe beam. Such an arrangement is described by P(90)-λ/4(45)-S(45)-DA(0). In this case, the detector signal matrix is given by

$$D = \frac{1}{2} e^{i\phi_x} \begin{bmatrix} 1 & 1 \\ -1 & 1 \end{bmatrix} \begin{bmatrix} 1 & 0 \\ 0 & e^{i\Delta\phi_{xy}} \end{bmatrix} \begin{bmatrix} 1 & 0 \\ 0 & i \end{bmatrix} \begin{bmatrix} 1 & -1 \\ 1 & 1 \end{bmatrix} \begin{bmatrix} 0 \\ 1 \end{bmatrix}, \tag{B.1}$$

$$D = \begin{bmatrix} D_x \\ D_y \end{bmatrix} = \frac{1}{2} e^{i\phi_x} \begin{bmatrix} -1 + ie^{i\Delta\phi_{xy}} \\ 1 + ie^{i\Delta\phi_{xy}} \end{bmatrix}. \tag{B.2}$$

Separating the *x* and *y* components with a (Wollaston) differential polarizer yields,

APPENDIX B: CONCERNING DOKE POLARIZATION CONDITIONS

$$I_x = D_x D_x^* = \frac{1}{4} e^{-2\phi_x''} \left(-1 + ie^{-i\Delta\phi_{xy}'}\right)\left(-1 - ie^{-i\Delta\phi_{xy}^*}\right)$$

$$= \frac{1}{4} e^{-2\phi_x''} \left(1 + ie^{-i\Delta\phi_{xy}'} e^{-\Delta\phi_{xy}''} - ie^{i\Delta\phi_{xy}'} e^{-\Delta\phi_{xy}''} + e^{i\Delta\phi_{xy}' - \Delta\phi_{xy}'' - i\Delta\phi_{xy}' - \Delta\phi_{xy}''}\right)$$

$$= \frac{1}{4} e^{-2\phi_x''} \left(1 + ie^{-\Delta\phi_{xy}''} \left(e^{-i\Delta\phi_{xy}'} - e^{i\Delta\phi_{xy}'}\right) + e^{-2\Delta\phi_{xy}''}\right)$$

$$= \frac{1}{4} e^{-2\phi_x''} \left(1 - 2i^2 \sin\Delta\phi_{xy}' e^{-\Delta\phi_{xy}''} + e^{-2\Delta\phi_{xy}''}\right)$$

$$\boxed{I_x = \frac{1}{4} e^{-2\phi_x''} \left(1 + e^{-2\Delta\phi_{xy}''}\right) + \frac{1}{2} e^{-2\phi_x''} \sin\Delta\phi_{xy}' e^{-\Delta\phi_{xy}''}} \qquad \text{B.3}$$

$$I_y = D_y D_y^* = \frac{1}{4} e^{-2\phi_x''} \left(1 + ie^{i\Delta\phi_{xy}'}\right)\left(1 - ie^{-i\Delta\phi_{xy}^*}\right)$$

$$= \frac{1}{4} e^{-2\phi_x''} \left(1 - ie^{-i\Delta\phi_{xy}'} e^{-\Delta\phi_{xy}''} + ie^{i\Delta\phi_{xy}'} e^{-\Delta\phi_{xy}''} + e^{i\Delta\phi_{xy}' - \Delta\phi_{xy}'' - i\Delta\phi_{xy}' - \Delta\phi_{xy}''}\right)$$

$$= \frac{1}{4} e^{-2\phi_x''} \left(1 + ie^{-\Delta\phi_{xy}''} \left(-e^{-i\Delta\phi_{xy}'} + e^{i\Delta\phi_{xy}'}\right) + e^{-2\Delta\phi_{xy}''}\right)$$

$$\boxed{I_y = \frac{1}{4} e^{-2\phi_x''} \left(1 + e^{-2\Delta\phi_{xy}''}\right) - \frac{1}{2} e^{-2\phi_x''} e^{-\Delta\phi_{xy}''} \sin\Delta\phi_{xy}'} \qquad \text{B.4}$$

$$I_x + I_y = \frac{1}{2} e^{-2\phi_x''} \left(1 + e^{-2\Delta\phi_{xy}''}\right) = \frac{1}{2} e^{-\Delta\phi_{xy}''} e^{-2\phi_x''} \left(e^{\Delta\phi_{xy}''} + e^{-\Delta\phi_{xy}''}\right) = e^{-2\phi_x''} e^{-\Delta\phi_{xy}''} \cosh\Delta\phi_{xy}''$$

$$I_x - I_y = e^{-2\phi_x''} e^{-\Delta\phi_{xy}''} \sin\Delta\phi_{xy}'$$

$$\boxed{\frac{I_x - I_y}{I_x + I_y} = \frac{\sin\Delta\phi_{xy}'}{\cosh\Delta\phi_{xy}''}} \qquad \text{B.5}$$

Differential detection yields the simplified expression in Eqn. B.5. In the absence of absorptive terms, $\Delta\phi_{xy}''=0$, and the first DOKE condition reduces to

$$\boxed{\frac{I_x - I_y}{I_x + I_y} = \sin\Delta\phi_{xy}' \approx \Delta\phi_{xy}'} \qquad \text{B.6}$$

for small typical nonlinear response sizes.

The First Dichroic DOKE Condition— With the Quarter-Wave Plate Before the Sample: In the case of two-photon absorption terms, $\Delta\phi_{xy}^{''} \neq 0$ and there is a need to separate the imaginary components from the real ones in Eqn. B.5. To accomplish this, the polarization of the pump may be rotated so that it is parallel to the initial polarisation the probe. Now, the arrangement is described by P(90)-λ/4(45)-S(90)-DA(0). The detector signal matrix is given by

$$D = \frac{1}{2}e^{i\phi_x}\begin{bmatrix}1 & 0\\ 0 & e^{i\Delta\phi_{xy}}\end{bmatrix}\begin{bmatrix}1 & 1\\ -1 & 1\end{bmatrix}\begin{bmatrix}1 & 0\\ 0 & i\end{bmatrix}\begin{bmatrix}1 & -1\\ 1 & 1\end{bmatrix}\begin{bmatrix}0\\ 1\end{bmatrix}, \tag{B.7}$$

$$D = \begin{bmatrix}D_x\\ D_y\end{bmatrix} = \frac{1}{2}e^{i\phi_x}\begin{bmatrix}-1+i\\ e^{i\Delta\phi_{xy}} + ie^{i\Delta\phi_{xy}}\end{bmatrix}. \tag{B.8}$$

Separating the *x* and *y* components with a (Wollaston) differential polarizer yields,

$$\begin{aligned} I_x &= D_x D_x^* = \frac{1}{4}e^{-2\phi_x^{''}}(-1+i)(-1-i) = \frac{1}{4}e^{-2\phi_x^{''}}(1+i-1+1)\\ I_x &= \frac{1}{2}e^{-2\phi_x^{''}} \end{aligned} \tag{B.9}$$

$$\begin{aligned} I_y = D_y D_y^* &= \frac{1}{4}e^{-2\phi_x^{''}}\left(e^{i\Delta\phi_{xy}} + ie^{i\Delta\phi_{xy}}\right)\left(e^{-i\Delta\phi_{xy}^*} - ie^{-i\Delta\phi_{xy}^*}\right)\\ &= \frac{1}{4}e^{-2\phi_x^{''}}\left(e^{i\Delta\phi_{xy}^{'}-i\Delta\phi_{xy}^{''}} + ie^{i\Delta\phi_{xy}^{'}-i\Delta\phi_{xy}^{''}} - ie^{i\Delta\phi_{xy}^{'}-i\Delta\phi_{xy}^{''}} + e^{i\Delta\phi_{xy}^{'}-i\Delta\phi_{xy}^{''}}\right)\\ &= \frac{1}{4}e^{-2\phi_x^{''}}\left(2e^{i\Delta\phi_{xy}^{'}-\Delta\phi_{xy}^{''}-i\Delta\phi_{xy}^{'}-\Delta\phi_{xy}^{''}}\right) = \frac{1}{2}e^{-2\phi_x^{''}}e^{-2\Delta\phi_{xy}^{''}} \end{aligned} \tag{B.10}$$

$$\begin{aligned} I_x - I_y &= \frac{1}{2}e^{-2\phi_x^{''}} - \frac{1}{2}e^{-2\phi_x^{''}}e^{-2\Delta\phi_{xy}^{''}} = \frac{1}{2}e^{-2\phi_x^{''}}e^{-\Delta\phi_{xy}^{''}}\left(e^{\Delta\phi_{xy}^{''}} - e^{-\Delta\phi_{xy}^{''}}\right)\\ &= e^{-2\phi_x^{''}}e^{-\Delta\phi_{xy}^{''}}\sinh\Delta\phi_{xy}^{''} \end{aligned} \tag{B.11}$$

$$I_x + I_y = \frac{1}{2}e^{-2\phi_x''} + \frac{1}{2}e^{-2\phi_x''}e^{-2\Delta\phi_{xy}''} = \frac{1}{2}e^{-2\phi_x''}e^{-\Delta\phi_{xy}''}\left(e^{\Delta\phi_{xy}''} + e^{-\Delta\phi_{xy}''}\right) \qquad \text{B.12}$$
$$= e^{-2\phi_x''}e^{-\Delta\phi_{xy}''}\cosh\Delta\phi_{xy}''$$

$$\boxed{\frac{I_x - I_y}{I_x + I_y} = \tanh\Delta\phi_{xy}''} \qquad \text{B.13}$$

Clearly, if there are no absorptive terms, this expression is zero, as is intuitively expected from a sample pumped with light polarised parallel to the probe beam. Since this expression only has $\Delta\phi_{xy}''$ terms, it may be used together with Eqn. B.5 to extract the real component of the nonlinearity. Thus, the prescribed DOKE detection technique leads to simple expressions in the phase retardation and allows for easy separation of the real and imaginary terms.

The First Birefringent DOKE Condition—With the Quarter-Wave Plate After the Sample: Such an arrangement is described by P(90)-S(45)-λ/4(45)-DA(0). In this case, the detector signal matrix is given by

$$D = \frac{1}{2}e^{i\phi_x}\begin{bmatrix}1 & 1\\ -1 & 1\end{bmatrix}\begin{bmatrix}1 & 0\\ 0 & i\end{bmatrix}\begin{bmatrix}1 & 0\\ 0 & e^{i\Delta\phi_{xy}}\end{bmatrix}\begin{bmatrix}1 & -1\\ 1 & 1\end{bmatrix}\begin{bmatrix}0\\ 1\end{bmatrix}, \qquad \text{B.14}$$

$$D = \begin{bmatrix}D_x\\ D_y\end{bmatrix} = \frac{1}{2}e^{i\phi_x}\begin{bmatrix}-1 + ie^{i\Delta\phi_{xy}}\\ 1 + ie^{i\Delta\phi_{xy}}\end{bmatrix}. \qquad \text{B.15}$$

This is exactly the same as Eqn. B.2. Thus, the position of the quarter-wave plate relative to the sample is immaterial for the birefringent DOKE condition. This, however, is not the case for the dichroic DOKE condition.

APPENDIX B: CONCERNING DOKE POLARIZATION CONDITIONS

The First Dichroic DOKE Condition—With the Quarter-Wave Plate After the Sample: This arrangement is described by P(90)-S(90)-λ/4(45)-DA(0). In this case, the detector signal matrix is given by

$$D = \frac{1}{2} e^{i\phi_s} \begin{bmatrix} 1 & 1 \\ -1 & 1 \end{bmatrix} \begin{bmatrix} 1 & 0 \\ 0 & i \end{bmatrix} \begin{bmatrix} 1 & -1 \\ 1 & 1 \end{bmatrix} \begin{bmatrix} 1 & 0 \\ 0 & e^{i\Delta\phi_w} \end{bmatrix} \begin{bmatrix} 0 \\ 1 \end{bmatrix}, \tag{B.16}$$

$$D = \begin{bmatrix} D_x \\ D_y \end{bmatrix} = \frac{1}{2} e^{i\phi_s} \begin{bmatrix} -1+i \\ 1+i \end{bmatrix}. \tag{B.17}$$

Separating the x and y components with a (Wollaston) differential polarizer yields,

$$\begin{aligned} I_x = D_x D_x^* &= \frac{1}{4} e^{-2\phi_s^*} (-1+i)(-1-i) e^{-2\Delta\phi_w^*} \\ &= \frac{1}{2} e^{-2\phi_s^*} e^{-2\Delta\phi_w^*} \end{aligned} \tag{B.18}$$

$$\begin{aligned} I_y = D_y D_y^* &= \frac{1}{4} e^{-2\phi_s^*} (1+i)(1-i) e^{-2\Delta\phi_w^*} \\ &= \frac{1}{2} e^{-2\phi_s^*} e^{-2\Delta\phi_w^*} \end{aligned} \tag{B.19}$$

$$\because I_x = I_y$$

and so,

$$\boxed{\frac{I_x - I_y}{I_x + I_y} = 0} \tag{B.20}$$

Thus, DOKE detection would prove useless for the dichroic detection of TPA *when the quarter-wave plate is placed after the sample*, as is routine in free-space electro-optic sampling techniques.

APPENDIX B: CONCERNING DOKE POLARIZATION CONDITIONS

The preceding treatment has also been tested in the lab on samples of MPPBT in DMSO, as shown in Fig. B.1. This figure presents six temporal DOKE traces with the two aforementioned polarization conditions, as the position of the probe quarter-wave plate is varied: As expected, the Kerr response—obtained from the birefringent DOKE polarization condition—is insensitive to the position of the quarter-wave plate relative to the sample, and the two responses are identical. Furthermore, as predicted, the nonlinear absorption (NLA) response—obtained from the dichroic DOKE polarization condition—is well-resolved when the probe quarter-wave plate is placed before the sample, but is nullified when it is placed after the sample. As confirmation, this response is seen to follow that of the pure solvent response—which would not be expected to have any NLA response regardless of quarter-wave plate position. The miniscule response observed for the pure DMSO solvent around a probe delay time of 0 ps is due to imperfect light polarizations and transient grating effects,[4] as was shown in Fig.2.7 for THF.

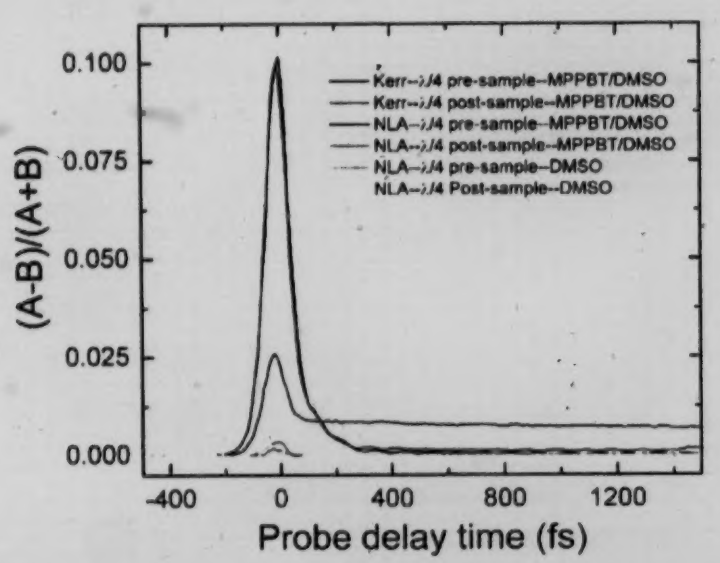

Figure B.1. [colour] Position dependence of probe quarter-wave plate in the birefringent (Kerr) and dichroic (NLA) DOKE polarization conditions. The Kerr signal from MPPBT in DMSO is seen to be insensitive to the position of the quarter wave-plate, and both position provide identical signals (the big symmetric peaks). For the dichroic condition, however, a pre-sample positioning of the quarter-wave plate yields a strong nonlinear absorption signal from MPPBT in DMSO, while the post-sample positioning yields a null signal that matches that of the pure DMSO solvent. The solvent displays no NLA for any position of the quarter-wave plate, as expected.

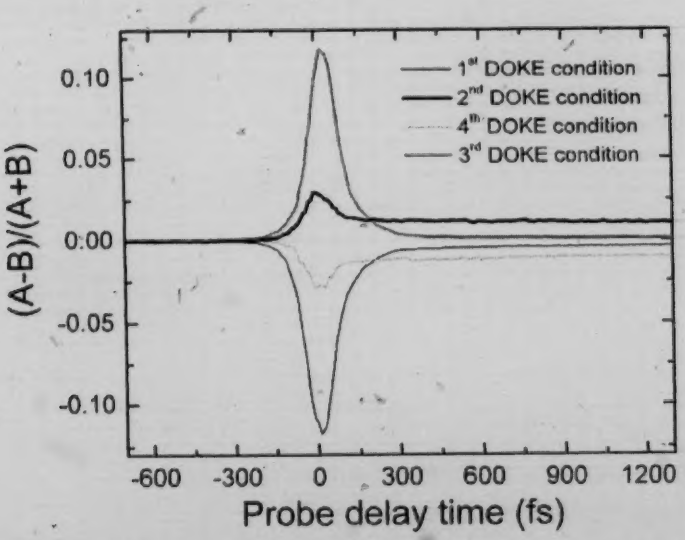

Figure B.2: The four DOKE polarization conditions, as illustrated experimentally by MPPBT in DMSO. The first and third DOKE conditions are the birefringent polarization conditions, and show signals that are the negative of one another. The second and 4th DOKE conditions are the dichroic polarization conditions, and likewise show opposite responses of one another.

B.2 The Four DOKE Polarization Conditions

Two unique polarization conditions have been outlined in the preceding derivations, and throughout the bulk of this work. However, there are actually four useful polarisation conditions in DOKE detection. Pumping at a polarisation 45° to analyser polarization has been shown to yield a signal given by Eqn. B.5. However, it can be shown that pumping at a polarisation -45° to that of the analyser yields a signal that is simply negative that of Eqn. B.5. Pumping with a polarization parallel to that of the analyser was shown to yield a signal given by Eqn. B.13 Likewise, it can be shown that pumping with an orthogonal polarization to the analyser yields a signal that is the negative of Eqn. B.13. Thus, there are four important polarization conditions in the DOKE technique. The signals from these four conditions are shown experimentally in Fig. B.2. We have outlined these four conditions in a previous work.[1] In that work, however, we did not have access to a satisfactory nonlinear absorbing sample, and the dichroic conditions were shown to be degenerately null. Thus, for the sake of completeness, we present Fig. B.2 to show the four conditions for our MPPBT NLA standard.

B.3 References

[1] A. D. Slepkov, *Third-Order Nonlinearities of Novel iso-Polydiacetylenes Studied by a Differential Optical Kerr Effect Detection Technique*, M.Sc. thesis. University of Alberta, Edmonton, 2001.

[2] K. P. H. Lui and F. A. Hegmann, Appl. Phys. Lett. **78**, 3478 (2001).

[3] Q. Wu, M. Litz, and X. C. Zhang, Appl. Phys. Lett. **68**, 2924 (1996).

[4] L. D. Ziegler and X. J. Jordanides, Chem. Phys. Lett. **352**, 270 (2002).

APPENDIX C:

CONCERNING EXPERIMENTAL RESOLUTION AND RAW DATA OF THE DOKE TECHNIQUE

This appendix looks to present some raw DOKE time-resolved signals in an effort to explore some of the experimental details of this new technique. In particular, a frank presentation of issues that lead to a reduction of signal-to-noise performance and experimental uncertainties is attempted.

Fundamentally, the lock-in detection that is used for the extraction of TPA and Kerr signals is only limited to electronic (bit-noise) and background photodiode noise levels, and resolution of signals as low as $\Delta\phi'$ or $\Delta\phi''$ of about 1×10^{-4} rad (as is shown for ϕ'' of THF in the inset of Fig. 2.7) may be expected. In practice, however, there are various effects that significantly limit our detection resolution away from this value. As shown in Fig. 2.7, in the absence of a two-photon absorption signal, any inherent pulse chirp may lead to the measurement of a coherent grating coupling between the pump and probe samples. This artefact is present on top of any measured nonlinear absorption response. When the *dichroic polarization condition* is strictly aligned (a non-trivial procedure), the full transient grating signal is kept to about $\pm5\times10^{-4}$ rad. In practice, it is very difficult to align the pump half-wave plate to yield the precise polarization, and a THF signal of under 15×10^{-4} is considered sufficient to constitute a "null" result. Unlike measurements of the Kerr response in the *birefringent polarization condition*, the two-photon absorption measurements contain no internal offset signal, as the solvents do not exhibit TPA near 800 nm. We generally try to control the sample concentration and pump intensity to levels that yield a measured ϕ'' of between 0.005 and 0.08 rad. The lower limit guarantees proper resolution and confidence, and the upper limit assures that neither the nonlinearity nor the linearity of the DOKE response are near saturation. In general, signals measured in the *dichroic polarization condition* is more noisy than those of the *birefringent polarization condition*. This occurs because in the *dichroic polarization*

condition, the pump beam is aligned along either A or B, and thus may lead to increased scatter-based noise on A-B. The *birefringent condition*, on the other hand works with a pump polarization of 45°, and thus leads to very little scatter noise on A-B; the A and B scatter is roughly equal. The scatter from both polarization conditions can ultimately be removed by careful attention, and thus does not often impact our ultimate scan resolution. A typical *dichroic condition* scan set is shown in Fig. C.1, where the excellent signal-to-noise ratio of the DOKE technique is apparent. Unlike other pump-probe techniques such as z-scan and spectrally-resolved two-beam coupling (SRTBC) that rely on extensive and multiple-parameter fittings to obtain the optical nonlinearities,[1,2] in the DOKE technique we can simply extract the peak signal value. This procedure, of course, relies on the proper and smooth progression of data points, as exemplified by Fig. C.1. From this figure, for example, a value of $\tanh(\phi'')=0.050\pm0.001$ rad would be reported. The uncertainty value is strictly estimated based on the temporal spread in the data points near peak and the smoothness of the peak itself. Increasing the scan resolution would is made possible by increasing the temporal resolution and by fitting the curve to a Gaussian profile. The latter, we find, is unnecessary for the type of resolution we typically require. In the case of the signals shown in Fig. C.1, the noise-to-signal ratio (or uncertainty) in the *TIPS*-10yne trace is approximately 0.01. Efforts are not typically made to reduce this uncertainty, as it is on par or lower than the typical uncertainty in the sample concentration, which is often about 2%. Each trace presented in Figure C.1 is an average of three consecutive scans, all together taking less than five minutes of scanning time. Increasing the number of scans in the average may be used to increase the experimental resolution, but this is only strictly correct on days in which the laser power is not noticeably diminishing over the timeframe of a sample and reference scan pair. As mentioned in Chapter 2, all TPA measurements are referenced to an iterative MPPBT reference scan set. Thus, the ultimate uncertainty in the TPA coefficient is double that of a single scan due to normalization to an MPPBT scan. Furthermore, to obtain a reliable measure of $\sigma^{(2)}$ (and γ) we typically repeat each experiment several times, often months apart. Changes in the operational parameters of the laser and sample concentration can lead to slight variations in inter-run results. These are typically accounted for with a measure of standard-deviation or simple error analysis. In summary, signal noise, various scatter, uncertainty in concentration, repeatability, and reference scan normalization typically lead to an ultimate uncertainty of approximately 10% in $\sigma^{(2)}$. As discussed, signal-to-noise issues are a minor component of this final value.

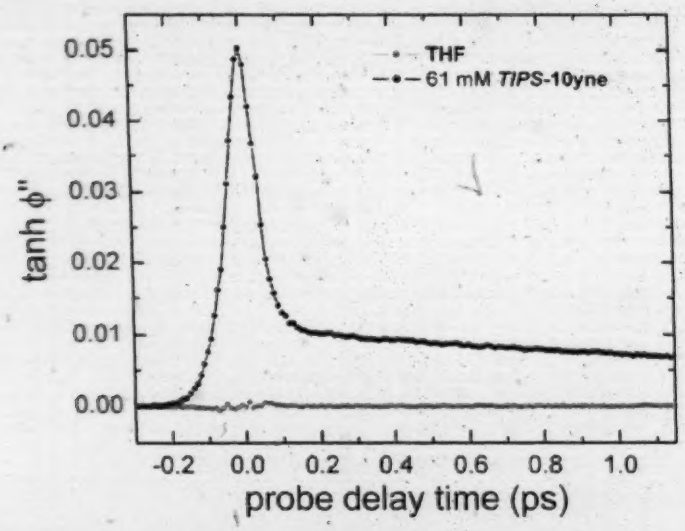

Figure C.1. Measurements of THF and a ***TIPS*-10yne** sample solution in the DOKE *birefringent condition*. The THF reference sample displays a near-zero response and is used as a null-response check of the proper pump polarization. Scan resolution is limited somewhat by the temporal scan progression and on-peak noise. Each of the traces represents an average of 3 raw scans. From the shown scans, a value of $\tanh(\phi'') \approx \phi'' = 0.050 \pm 0.001$ was tallied for the ***TIPS*-10yne** sample.

As discussed in a previous work,[3] the *birefringent polarization condition* suffers from different concerns that lead to an ultimate reduction in experimental resolution. Raw scans of **THF**, ***TIPS*-5yne** and ***TIPS*-10yne** obtained with the DOKE *birefringent polarization condition* are shown in Fig. C.2. Again, each trace represents an average of three scans and takes approximately 5 minutes to obtain. In addition to (A-B)/(A+B) signals, Fig. C.2 shows a typical A+B trace; in this case, of ***TIPS*-5yne**. A slight dip in the A+B trace is seen around the probe arrival time, corresponding to TPA. Clearly, this signal is much harder to resolve than the TPA traces of the *dichroic polarization condition* shown in Fig. C.1. Unlike for the dichroic response, the solvent (in this case THF) displays an inherent Kerr response. As was discussed in Chapter 2, Eqn. 2.5 shows that the Kerr response of a sample in solution is simple a sum of the solvent and solute responses. Thus, we can only resolve that sample response which can be resolved beyond the pure solvent's. This condition leads to a significant reduction in the resolution of DOKE signals in the *birefringent polarization condition* because the resolution of the solvent response itself suffers from all of the aforementioned uncertainties found in the *dichroic polarization condition* (with the exception

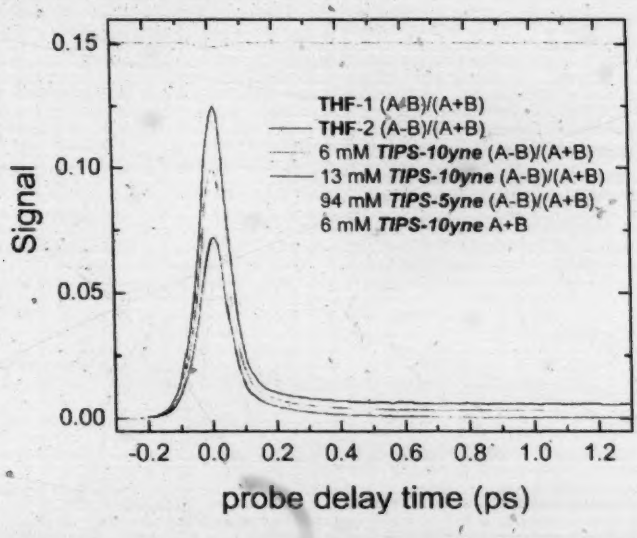

Figure C.2. [colour] DOKE *birefringent condition* measurements of ***TIPS*-PY**s and their corresponding THF reference scans. THF scans were obtained ten minutes apart and were dispersed among the scans of the various samples. The THF scans were extremely repeatable, as is evident from their excellent overlap. The polyyne kerr signals must be resolved beyond those of the reference THF scans, limiting the ultimate resolution of the DOKE technique. To obtain adequate dynamic range, sample concentrations and pump powers are carefully selected. For these scans, a 1.0 mW pump beam was used. The two different ***TIPS*-10yne** samples were used as a quick check on the concentration dependence. A single A+B trance for a ***TIPS*-10yne** sample is shown to show the sensitivity (or lack thereof) of this signal component to resolve two-photon absorption.

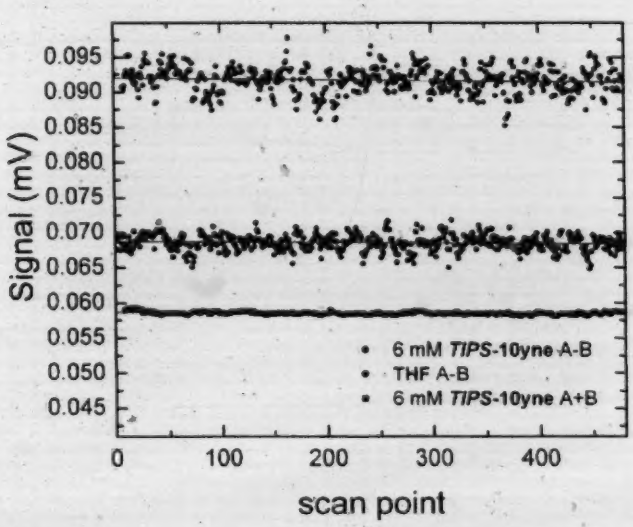

Figure C.1. [colour] On-peak scans of THF and ***TIPS*-10yne** in the *birefringent DOKE polarization condition*. Straight lines are a running average fit to the data. The calculated standard deviation (spread) of the data is 0.001 mV, 0.001 mV, and 0.0002 mV for the ***TIPS*-10yne** A-B, the THF A-B, and the ***TIPS*-10yne** A+B signals, respectively. Clearly the on-peak A-B response is much more noisy than A+B.

of pump beam scatter). This is further exacerbated by the fact that we obtain γ values by analyzing the Kerr response on-peak, but the peak itself is the temporal component with the most noise due to the coherent coupling of the pump and probe beams. Thus, to make the measurement more robust, we often obtained a measurement of 250-500 data points on-peak, for statistical purposes. Figure C.3 presents an on-peak scan of A-B in a ***TIPS-10yne*** sample and its corresponding THF reference. When inspecting this figure, it becomes clear that there is considerable on-peak noise, in the order of about 6%. Obtaining many data points allows for the fitting of the on-peak data and a measure of the standard-deviation in ϕ'. For the scans shown in Fig. C.3 the uncertainty in the peak value is approximately 1%-2% of the signal, as given by the standard deviation. As mentioned, the on-peak noise is considerably greater than off-peak and is not due to standard experimental scatter and noise. This point is punctuated by relatively low noise present on the typical A+B response on-peak (as shown in Fig. C.3). This response has an uncertainty of approximately 0.3%, as given by the standard deviation. The on-peak scans presented in Figure C.3 are single, non-averaged, scans, and take approximately four minutes to obtain. This type of experiment is typically utilized once the temporal response profile, such as given in Fig. C.2, is already obtained. Thus the signal is both properly mapped out temporally and the peak response is properly characterized. This procedure is also utilized in the *dichroic polarization condition* (not shown). Ultimately, the various accumulated experimental uncertainties lead us to typically report γ to within ±10%. Repeating the experiments numerous times with new sample solutions has often lead to only small variations in the obtained γ and $\sigma^{(2)}$ values. In this case, the experimental uncertainty may have been reported as lower than 10% and it represents the statistical spread in the repeated data. There have been cases where repeated measurements do not yield results that are in close agreement with previous ones. In this case, the culprit is often difficulty in making precise concentrations of sample solutions, and the experimental uncertainty has been reported as considerably higher than 10%.

C.1 References

[1] I. Kang, T. Krauss, and F. Wise, Opt. Lett. **22**, 1077 (1997).

[2] M. Sheikbahae, A. A. Said, T. H. Wei, D. J. Hagan, and E. W. Van Stryland, IEEE J. Quant. Elect. **26**, 760 (1990).

[3] A. D. Slepkov, *Third-Order Nonlinearities of Novel iso-Polydiacetylenes Studied by a Differential Optical Kerr Effect Detection Technique*, M.Sc. thesis. University of Alberta, Edmonton, 2001.